Control of passive and active open random media: Theoretical and Experimental investigations

Nicolas Bachelard

UPMC SORBONNE UNIVERSITÉS — ESPCI ParisTech — Institut Langevin ONDES ET IMAGES

THÈSE DE DOCTORAT DE L'UNIVERSITÉ PARIS 6

Spécialité

Physique

Présentée par

Nicolas Bachelard

Pour obtenir le grade de

DOCTEUR de l'UNIVERSITÉ PARIS 6

Sujet de la thèse :

Control of passive and active open random media: Theoretical and Experimental investigations.

Soutenue le 15 Juillet 2014

devant le jury composé de :

Pr.	**Treps**	**Nicolas**	**Président**
Pr.	**Rotter**	**Stefan**	**Rapporteur**
DR	**Robin**	**Kaiser**	**Rapporteur**
Pr.	**Carminati**	**Rémi**	**Examinateur**
Pr.	**Cao**	**Hui**	**Examinateur**
Pr.	**Gigan**	**Sylvain**	**Invité**
DR	**Sebbah**	**Patrick**	**Directeur de Thèse**

Université Pierre & Marie Curie - Paris VI
Bureau de la Scolarité Doctorat
Esc. G, 2^{eme} étage
15 rue de l'École de Médecine
75270 PARIS Cedex 06

Tél Secrétariat : 01 42 34 68 35
Fax : 01 42 34 68 40
Tél pour les étudiants de A à ME : 01 42 34 68 41
Tél pour les étudiants de MG à Z : 01 42 34 68 51
E-mail : scolarite.doctorat@upmc.fr

Remerciements

C'est l'été. De la soutenance, il ne reste plus qu'un vague souvenir et surtout une interminable liste de corrections que je repousse chaque jour un peu plus. Pour me soustraire à cet exercice je décide qu'est venu le temps des remerciements.

Ces quelques lignes, j'avais imaginé les écrire sur une plage de sable blanc en sirotant un "cuba libre" en me laissant brûler par le soleil. Malheureusement la vérité est bien différente. Je suis à Strasbourg à la fin du mois d'août. Je suis enfermé chez moi. Il pleut... Néanmoins, si le cadre diffère, l'envie de remercier les gens, elle, reste intacte.

En premier lieu, j'aimerais remercier les membres de mon jury qui on enduré trois heures de milieux désordonnés dans une salle à 40 degrés. Comme l'a dit un ami dont je tairais l'identité: "Ton jury, c'est la classe".

Chaque thèse est associée à une histoire particulière. Pour la mienne, je dirais qu'elle a commencé par une rencontre un peu singulière. Au cours d'une visite de M2 j'ai rencontré Patrick qui venait alors juste de déménager à l'institut depuis Nice. Son bureau se résumait à un enchevêtrement de cartons et il n'avait qu'un simple poster pour présenter ses travaux. Malgré ce décorum des plus singuliers, le courant est immédiatement passé. Je ne vais pas me lancer dans une liste à la Prévert de ce qu'il m'a apporté, mais simplement souligné que j'ai conscience du chemin parcouru grâce à lui.

Si bonne bouillabaisse rime avec une bonne casserole, je dirais qu'on ne peut pas faire une bonne thèse sans un bon laboratoire. En particulier je remercie chaleureusement les gestionnaires qui font un travail remarquable. Je remercie les différents permanents, notamment Rémi, Romain, Yannick, Sylvain, Geoffroy, Alexandre et bien d'autres qui font leur maximum pour instaurer une ambiance de travail formidable. J'aimerais également avoir une pensée pour les doctorant et post-doctorant de l'institut. Pierre pour son optimisme et sa bonne humeur. Ariadna avec qui j'évolue parallèlement dans le monde de l'optique depuis de nombreuses années maintenant. Marc et Alex avec qui j'ai pu échanger aussi bien sur le plan personnel que scientifique. Je nommerais également pêle mêle: Gautier, Baptiste, Daria, Emilie, Olivier, Khan Van, Miguel, Thomas, Hugo et tout ceux que j'oublie.

Je ne porte pas encore la moustache et ne fume pas non plus la pipe mais j'aimerais, à l'image de Brassens, écrire quelques lignes pour mes amis. Tout d'abord les amis du lycée et en particulier Quentin et Gwen. Quels que soient les kilomètres qui nous séparent, je sais qu'on ne se s'oubliera pas. Les amis de l'ENS: Marion, Bastoun, Laura, Jerem, Patate, Zouzou, Manu. On s'est suivi pendant de nombreuses années. Maintenant que nos chemins divergent, la seule chose qui va changer c'est que nous devrons prendre l'avion à la place du métro pour se voir. A Manu et Zouzou avec qui j'ai cohabité durant plusieurs années, j'aimerais les remercier pour ces belles années. Une mention

spéciale pour Poupette et Loïc (et leur canapé) qui sponsorisent la recherche française en m'hébergeant lors de mes différents séjours à Paris. Si par malheur j'oubliais quelqu'un il serait en droit de me demander de lui payer un coup à boire. Par ce que ce ne sont pas tout à fait des amis comme les autres, j'aimerais chaleureusement remercier la famille Limousin. Je les connais depuis toujours et ils ont et auront toujours une place bien particulière.

Bien évidemment j'aimerais avoir un mot pour ma famille. Tout d'abord mes sœurs et leurs familles respectives: merci pour tout ce que vous m'apportez. Enfin mes parents qui m'ont fait comme je suis: je leur dois tout. Si ils pensent n'y être pour rien et bien ils se trompent...

Et puis y'a Edith, ou mon gros lapin pour les intimes. Elle m'a supporté durant cette longue et rugueuse épreuve qu'a été la rédaction. Sans elle les choses auraient été bien plus compliquées. Elle est et restera ma bouteille d'oxygène (c'est à dire toujours sur mon dos). J'associe aussi à ces remerciements sa famille que je passe mon temps à ennuyer de mon mieux.

Bref, à vous tous merci...

Summary

Light propagation in matter is described by vibration eigenstates, called modes, which characterize the light-matter interaction. In the specific case of random media, according to the strength of the disorder, the modes can be either extended over the whole system or spatially localized. This disorder-based confinement is called Anderson's localization. In the first part, we introduce basic notions used along this manuscript. In particular the light-matter interaction requires a semiclassical approach: The electromagnetic field is described by Maxwell's equations while the quantum nature of matter must be considered. In this thesis open media are studied. In such systems the modal description requires a specific analytic treatment different from closed problems. In the second part, we focus on Anderson-localized modes in open passive random media. Any change of the disorder induces modifications of modes. Therefore, it enables the control over the light properties. Moreover, when inserting an emitter inside an Anderson-localized mode, strong light-matter interaction regimes can be reached. In the third part, active random media, commonly called random lasers, are introduced. Using our experimental achievements, characteristics of random lasers are presented. The notion of mode enables us to describe complex mechanisms involved in the lasing emission. Last, we demonstrate both experimentally and numerically that a non-uniform excitation of random lasers can lead to a control of the properties of the emission. In particular a multimode spectrum for a uniform pumping can be turned into single-mode using an adapted pumping.

Contents

Introduction

In principle, confining light can be easily achieved by two mirrors facing each other. As simple as it might seem, this "classical" cavity is the cornerstone of many physical systems such as Fabry-Perot spectrometer and lasers. In an ideal optical cavity, a photon will remain trapped for ever. The system is isolated from the rest of the universe and said hermitian. The electromagnetic field describing the light oscillates at specific frequencies: These oscillations define the modes of the close cavity. In this ideal description, the modes are independent vibrations. The hermitian cavity allows both to address theoretical questions and to offer interesting prospects. As an illustration, we mention Quantum Electro Dynamic (QED) cavities, where a two-level atom is inserted between two mirrors. On the one hand it offers elementary verification of quantum mechanics. On the other hand, it paves the way to many interesting physical applications, in particular in quantum computational processing. Unfortunately, satisfying hermitian conditions sometimes requires tremendous efforts. For instance, Serge Haroche developed a very high-Q cavity based on two superconducting niobium mirrors at low temperature. Wineland's group used single ions in ultra vacuum between to gold electrodes.

When the dimensions of the cavity are down-scaled, ensuring the hermiticity of the cavity becomes even harder. In contrast, novel science-driven cavities with complex geometries have risen much interest. Among them, we can mention open dielectric micro-disks and micro-spheres or photonic crystal slab defect mode. In all these systems, because of openness or absorption, energy leaks out of the cavity. This energy loss couples the system to the rest of the universe: The system is said non-hermitian. Unfortunately, different theories of hermitian physics, such as Random Matrix Theory, fail badly to describe non-hermitian problems. In non-hermitian system, the electromagnetic field is still described by privileged vibration, commonly referred as resonances. But unlike closed cavity, these non-hermitian modes are no-longer independent vibrations and energy can be transferred from one mode to another. The new Physics involved in non-hermitian systems has triggered strong theoretical interest, raising many questions: Is it possible the adapt or extend standard approaches of hermitian Physics to open systems? What are the specific properties that these open systems may offer?

A random scattering medium is another example of an open system. In such a medium, the photon dwell time is enhanced by multiple scattering. Depending on the disorder strength, light may explore the entire system and escape from it or may be trapped for a long time by the disordered structure. In the first case, the system is said diffusive, whereas in the second case, diffusion is inhibited and the wave is localized. In the last case, if the system is large enough, all the good properties of hermitian systems are recovered. The openness is simply driven by the degree of disorder. A random system is therefore an interesting playground to explore systems ranging from hermitian to non-hermitian. This unique characteristic has led to the exploration of many questions related

to light-matter interaction, such as non-linear physics, QED or lasing. In the work that we present here, some aspects of light-matter interaction in random scattering media have been investigated. Our aim is to exemplify how the complexity of these systems offers new degree of freedom to explore fundamental questions as well as new applications.

The document is organized in four parts and eight chapters, that we briefly introduce.

Part I - From microscopic light-matter interaction to modes in open random media

In Chapter I, we review the basic notions of light-matter interaction in the semiclassical formalism. Starting from microscopic Maxwell's equations, we derive the propagation of light in macroscopic dielectric systems. In particular, we describe the scattering of light by inhomogeneities. The matter is described quantum-mechanically by discrete levels of energy. We review the different mechanisms allowing a transfer from one level to another. More specifically, we consider the two-level and four-level atoms.

In Chapter II, we introduce the concept of modes in non-hermitian systems. Starting from a simple example in physics, modes are defined as a resonance in non-hermitian problems, instead of stationary wave in the hermitian case. We present some fundamental differences between hermitian and non-hermitian modes. Then, we consider the case of open systems. We discuss the conditions allowing to expand the electric field along the modes and the related mathematical formalism. Finally, we introduce modes for the specific case of disordered open systems.

Part II - Managing light-matter interaction in passive random media

In Chapter III, we explore mode interaction and exceptional points in a non-hermitian system. We first derive the evolution with any variation of the dielectric constant of modes in a 2D system. In a general 2D dielectric system, we derive the exact evolution of modes when the permittivity distribution is modified. In the specific case of localization by disorder, we induce the coalescence of two modes for a specific modulation of the disorder. In the vicinity of this so-called exceptional point, we study the mechanism of coalescence and in particular the role played by other modes. We confirm theoretical predictions by numerical simulations.

In Chapter IV, we investigate theoretically the interaction between a two-level atom with a localized mode. For small intensity of the electric field, the interaction is described by a linear polarization of the atom. In contrast, a high intensity gives rise to non-linear polarization. In the linear regime, we study the electric field evolution and recover the strong coupling condition between the emitter and the mode. Then, we investigate the condition of a non-linear response of the emitter. We propose experimental observation of both effects. Our predictions are confirmed by numerical simulations.

Part III - Active random media: The random laser

In Chapter V, we introduce the random laser and present our experimental achievements of microfluidic devices. Starting from a textbook description of a conventional laser, we define the random laser and model it in the diffusion approximation. Then, after describing the technique we developed to make microfluidic lasers, we characterize 1D and 2D devices. We explain why the diffusion model is inadequate to describe such a random laser and conclude that a more accurate description should be based on a modal description

In Chapter VI, we analytically derive the modes of the random laser from the modes of the underlying random structure, the so-called passive system. The presence of a threshold in the lasing emission requires to consider two distinct regimes, namely below and above threshold. Below threshold, we derive the evolution of the modes and a perturbation expansion allows to investigate the linear coupling between modes. Above threshold, we derive the lasing mode using a similar approach and exhibit the linear and non-linear mechanisms involved in the lasing.

Part IV - Control of random lasers

In Chapter VII, we propose a new method to control random laser emission based on the shaping of the pump profile. Using an iterative approach, the spatial distribution of the pump profile is progressively tuned to control the random laser characteristics. We offer some analytical insights to understand the role played by the pump profile on mode mixing and we propose further investigations for a complete description.

In Chapter VIII, we experimentally demonstrate the control of an optofluidic random laser. Using a spatial light modulator, the pump fluence is modulated and an iterative procedure adjusts the pump profile to drive the multimode laser to single-mode operation at a desired wavelength. We investigate the influence of pump profile on linear and non-linear mixing. Finally a similar approach to control the directivity of the random laser emission is proposed.

Part I

From microscopic light-matter interaction to modes in open dielectric random media

Chapter 1

Light-matter interaction: Semiclassical description

Table of Contents

The most complete description of light-matter interaction is provided by a quantum mechanic description, where both electromagnetic field and matter are quantized. However, many phenomena can be understood within the framework of the semiclassical theory of light-matter interaction, where the light is described by a classic electromagnetic field, while the quantum nature of matter is considered.

In this chapter, we introduce basic notions of the semiclassical theory that will be used in this manuscript. Starting from Maxwell's equations, we first derive the propagation equations of the electromagnetic field in media with homogeneous and inhomogeneous refractive index at macroscopic scale. Then, we consider the propagation of the field when scattered by a particle. Finally, we present briefly the quantum description of matter and introduce the different mechanisms of energetic transition.

1.1 Light-Matter interaction: Light propagation in matter

In this section, we remind the evolution of electromagnetic field in 1D and 2D dielectric inhomogeneous media. This section is mostly based on lecture notes [1, 2]. First, we recall the microscopic description of the electromagnetic field provided by Maxwell's equations. Then, we derive the Maxwell's equations for matter at a macroscopic scale. Finally, the Lorentz's oscillator model is used to define the susceptibility of dielectric material and derive the equation of propagation in 1D and 2D dielectric media, namely Helmholtz equation.

1.1.1 Light at microscopic scale

Maxwell's equations in vacuum

Light propagation is described by the electromagnetic field $(\mathbf{E}(r,t), \mathbf{B}(r,t))$, where r and t stand for spatial and temporal coordinates (see Fig. 1.1). Vector electric field and magnetic field, $\mathbf{E}$ and $\mathbf{B}$ fulfil two constitutive equations

$$\operatorname{div} \mathbf{B}(r,t) = 0 \tag{1.1}$$

$$\mathbf{rot}\, \mathbf{E}(r,t) = -\frac{\partial \mathbf{B}}{\partial t}(r,t) \tag{1.2}$$

known as Maxwell-Thomson's and Maxwell-Faraday's equations [3]. For propagation in vacuum, the electric field obeys to Maxwell-Gauss's equation

$$\operatorname{div} \mathbf{E}(r,t) = 0 \tag{1.3}$$

and the magnetic field Maxwell-Ampère equation

$$\mathbf{rot}\, \mathbf{B}(r,t) = \mu_0 \epsilon_0 \frac{\partial \mathbf{E}}{\partial t}(r,t) \tag{1.4}$$

The universal constants μ_0 and ϵ_0 are respectively the permeability and permittivity of vacuum.

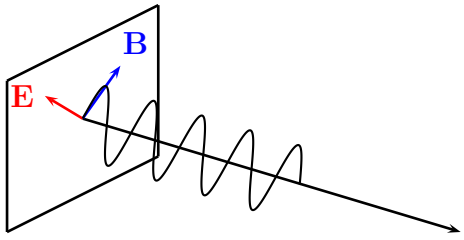

Figure 1.1: Schematic representation of light propagating in vacuum: Light is described by the oscillations of the electromagnetic field $(\mathbf{E}(r,t), \mathbf{B}(r,t))$

Maxwell's equations in matter at microscopic scale

At microscopic scale, the matter is assumed to be composed of point charges q_i at position $r_i(t)$ (as sketched in Fig.1.2). The corresponding density $\rho_m(r,t)$ reads

$$\rho_m(r,t) = \sum q_i \delta(r - r_i(t)) \tag{1.5}$$

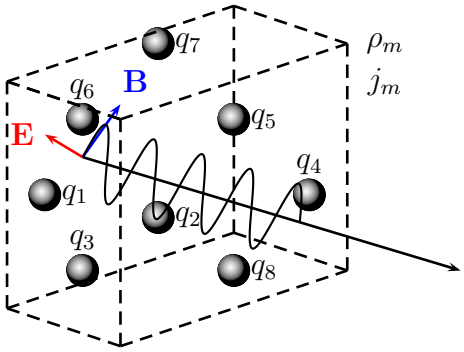

Figure 1.2: Electromagnetic in matter at microscopic scale: Here we consider point charges q_i located at r_i.

The motion of the charges induces a current density $\mathbf{j}_m(r,t)$

$$\mathbf{j}_m(r,t) = \sum q_i \frac{d\mathbf{r}_i}{dt}(t)\delta(r - r_i(t)) = \sum q_i \mathbf{v}_i(t)\delta(r - r_i(t)) \tag{1.6}$$

This charges and currents influence the evolution of the electromagnetic field by giving rise to discrete source terms in Maxwell's eq. (1.1-1.4)

$$\operatorname{div} \mathbf{B}(r,t) = 0 \tag{1.7}$$

$$\mathbf{rot}\, \mathbf{E}(r,t) = -\frac{\partial \mathbf{B}}{\partial t}(r,t) \tag{1.8}$$

$$\operatorname{div} \mathbf{E}(r,t) = \frac{\rho_m(r,t)}{\epsilon_0} \tag{1.9}$$

$$\mathbf{rot}\, \mathbf{B}(r,t) = \mu_0 \mathbf{j}_m(r,t) + \mu_0 \epsilon_0 \frac{\partial \mathbf{E}}{\partial t}(r,t) \tag{1.10}$$

1.1.2 Light at macroscopic scale

From micro to macroscopic scale

At macroscopic scale, we can no longer consider point charges (as sketched in Fig. 1.3). The gap between microscopic and macroscopic scales can be bridged by performing a spatial average [1, 2, 4]. For a function, $F(r,t)$, the macroscopic average reads

$$\langle F(r,t) \rangle = \int w(r - r') F(r',t) dr' \tag{1.11}$$

where $w(r)$ the regularization function is

- normalized : $\int w = 1$
- real and positive
- bounded, in such way that $\frac{\partial}{\partial r}\langle F(r,t)\rangle = \langle \frac{\partial}{\partial r} F(r,t)\rangle$ [1]

Macroscopic Maxwell's equations

Maxwell's eq. (1.7) and (1.8) are easily derived at macroscale:

$$\text{div}\,\langle \mathbf{B}\rangle(r,t) = 0 \tag{1.12}$$

$$\mathbf{rot}\,\langle \mathbf{E}\rangle(r,t) = -\frac{\partial \langle \mathbf{B}\rangle}{\partial t}(r,t) \tag{1.13}$$

For eq. (1.9) and (1.10), macroscopic expressions are complicated by the presence of

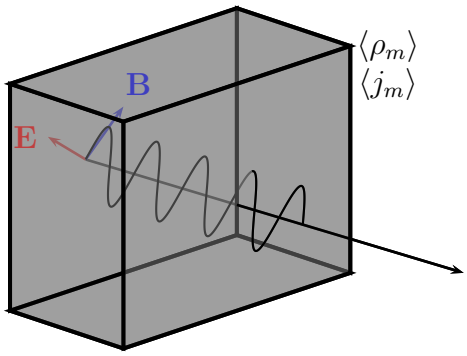

Figure 1.3: Schematic representation of light propagation in matter at macroscopic scale: The charges and currents are continuous functions.

averaged source written as $\langle \rho_m \rangle$ and $\langle \mathbf{j}_m \rangle$

$$\text{div}\,\langle \mathbf{E}\rangle(r,t) = \frac{\langle \rho_m \rangle}{\epsilon_0} \tag{1.14}$$

$$\mathbf{rot}\,\langle \mathbf{B}\rangle(r,t) = \mu_0 \langle \mathbf{j}_m \rangle + \mu_0 \epsilon_0 \frac{\partial \langle \mathbf{E}\rangle}{\partial t}(r,t) \tag{1.15}$$

Let us first consider the macroscopic charge density $\langle \rho_m \rangle$. We assume that the medium is made of atoms and we focus on an atom (at) at position r_{at} (see Fig. 1.4**(a)**). For sake of simplicity, position of the charges are expressed in the atomic frame and temporal dependency is removed. The charge density of this atom reads

$$\rho_{at\,m}(r) = \sum q_i \delta(r - r_{at} - r_i) \tag{1.16}$$

leading to a macroscopic average

$$\langle \rho_{at\,m} \rangle(r) = \sum q_i \int w(r - r')\delta(r' - r_{at} - r_i)dr' = \sum q_i w(r - r_{at} - r_i) \tag{1.17}$$

[1] The derivative of the spatial average reads $\frac{\partial \langle F\rangle}{\partial r} = \int \frac{\partial w(r-r',t)}{\partial r} F(r',t)dr' = -\int \frac{\partial w(r-r',t)}{\partial r'} F(r',t)dr'$. Using an integration by parts, $\frac{\partial \langle F\rangle}{\partial r} = \langle \frac{\partial F}{\partial r}\rangle$. Because the function is bounded $w(\pm\infty, t) = 0$. As a result $\frac{\partial \langle F\rangle}{\partial r} = \langle \frac{\partial F}{\partial r}\rangle$.

The regularization function w is extremely smooth at atom scale. Eq. (1.17) can be expanded at first order around the position $r - r_{at}$ and reads

$$\langle \rho_{at\,m} \rangle(r) \approx \sum q_i w(r - r_{at}) - \sum q_i \mathbf{r}_i . \mathbf{grad}\, f(r - r_a) \tag{1.18}$$

Defining $\sum q_i = q_{at}$ the atomic charge and $\sum q_i \mathbf{r}_i = \mathbf{p}_{at}$ the atomic dipole moment

$$\langle \rho_{at\,m} \rangle(r) \approx q_{at} w(r - r_{at}) - \mathbf{p}_{at} . \mathbf{grad}\, f(r - r_a) \tag{1.19}$$

Consequently, even for a neutral atomic charge ($q_{at} = 0$), if the atomic dipole moment $\mathbf{p}_{at} \neq 0$, a macroscopic charge $\langle \rho_{at\,m} \rangle$ exists. For instance, some neutral molecules (e.g. H_2O, CO) have permanent dipole moment or atoms can polarized when coupled to the electric field (see example in Fig. 1.4**(b)**).

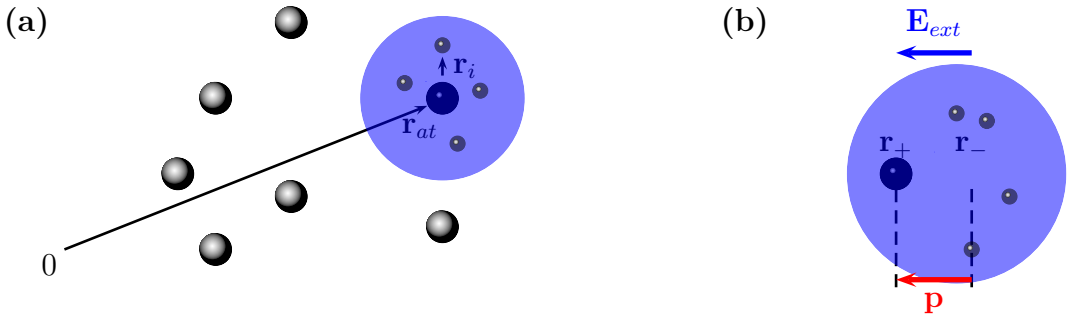

Figure 1.4: **(a)** The atomic frame (position r_{at}): In this example a positive nucleus at position r_{at} is surrounded by electrons at position r_i. **(b)** Example of neutral particle exhibiting a dipole moment $\mathbf{p}$: An atom is placed in a external electric field $\mathbf{E}_{ext}$. Barycentre of positive (q at r_+) and negative ($-q$ at r_-) charges are spatially separated, leading to the appearance of a dipole moment $||\mathbf{p}|| = q(r_+ - r_-) \neq 0$.

Now, since we perform similar operation on all atoms, the total macroscopic density reads

$$\begin{aligned} \langle \rho_m \rangle(r) &\approx \sum q_{at} w(r - r_{at}) - \sum \mathbf{p}_{at} . \mathbf{grad}\, f(r - r_a) \\ &= \sum q_{at} w(r - r_{at}) - \mathrm{div} \sum p_{at}\, f(r - r_a) \end{aligned} \tag{1.20}$$

Defining $\mathbf{P} = \sum \mathbf{p}_{at} f(r - r_a)$ as the polarization density of the medium, the averaged charge density reads

$$\langle \rho_m \rangle(r,t) = \rho_{free}(r) - \mathrm{div}\, \mathbf{P}(r,t) \tag{1.21}$$

As a result, at macroscopic scale, the charge density is the sum of two terms

- $\rho_{free}(r) = \sum q_{at} w(r - r_{at})$, referred to as the free charge density
- $-\mathrm{div}\, \mathbf{P}(r) = -\sum \mathbf{p}_{at} . \mathbf{grad}\, f(r - r_a)$, referred to as the polarization charge density

Hence, Maxwell-Gauss's eq. (1.14) reads

$$\mathrm{div}\, \langle \mathbf{E} \rangle(r) = \frac{\rho_{free}(r) - \mathrm{div}\, \mathbf{P}(r,t)}{\epsilon_0} \tag{1.22}$$

In the scope of this manuscript we will consider material with zero macroscopic charge *i.e.* $\rho_{free} = 0$. Maxwell-Ampere's eq. (1.15) can be derived by a similar approach and be written

$$\mathbf{rot}\, \langle \mathbf{B} \rangle(r) = \mu_0 \left(\mathbf{j}_{free} + \frac{\partial \mathbf{P}}{\partial t} + \mathbf{rot}\, \mathbf{M} \right) + \mu_0 \epsilon_0 \frac{\partial \langle \mathbf{E} \rangle}{\partial t} \tag{1.23}$$

where $\mathbf{M}$ is the magnetization of the medium.

From now on, we will only consider the macroscopic quantities and remove the average notation: $\langle F \rangle = F$.

1.1.3 Propagation in dielectric media

Lorentz's oscillator model

In Fig. 1.4**(b)** we presented an example of polarization mechanism when an atom is placed in the electric field. This example stresses that the polarization $\mathbf{P}$ in eq. (1.22) is imposed by the nature of the material. In this manuscript, we will consider dielectric media composed of atoms modelled as Lorentz's oscillators.

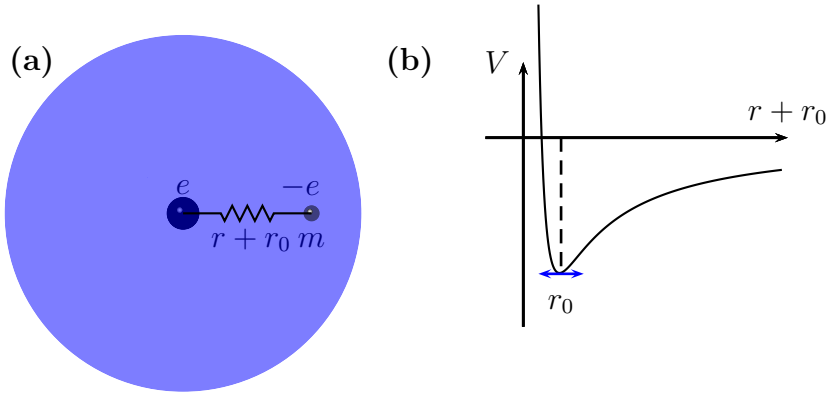

Figure 1.5: **(a)** Lorentz oscillator model: An electron $(-e, m)$ is connected to a fixed nucleus (e) by a spring. **(b)** Interaction potential between electron and nucleus. The system evolves in the vicinity of the equilibrium position r_0.

An electron of mass m and charge $-e$ is elastically linked to the nucleus of an atom (see Fig. 1.5**(a)**). This nucleus is heavy and assumed fixed. The interaction potential $V(r+r_0)$ versus the distance nucleus/electron $(r_0 + r)$ is sketched in Fig. 1.5**(b)**. The motion of the electron is achieved in the vicinity of the equilibrium position (r_0). As a result, the force deriving from the potential in the vicinity of r_0 acts like a spring

$$\mathbf{F}_{n\to e} = -\mathbf{grad}\, V \approx -m\omega_0^2 \mathbf{r} \tag{1.24}$$

We assume non-relativistic electrons and therefore we neglect the magnetic force. Moreover, a damping force is opposed to electron motion (coefficient Γ). Finally, because the wavelength is much larger than atom size, the electric field is assumed uniform.

As a result, the dynamic relation reads

$$m\frac{d^2\mathbf{r}}{dt^2} = -e\mathbf{E}(r=0) - m\omega_0^2\mathbf{r} - m\Gamma\frac{d\mathbf{r}}{dt} \tag{1.25}$$

For a monochromatic problem (single frequency ω), solution of the form $r(t) = r(\omega)e^{-i\omega t}$ can be used as an ansatz. The solution of eq. (1.25) reads

$$\mathbf{r}(\omega) = \frac{-e\mathbf{E}(\omega)/m}{\omega_0^2 - \omega^2 - i\Gamma\omega} \tag{1.26}$$

As a result, the dipole moment reads

$$\mathbf{p}(\omega) = -e\mathbf{r}(\omega) = \frac{e^2\mathbf{E}(r=0)/m}{\omega_0^2 - \omega^2 - i\Gamma\omega} = \epsilon_0\alpha_0(\omega)\mathbf{E}(\omega) \tag{1.27}$$

where $\alpha_0(\omega)$ is the polarizability of the particle[2]. At macroscopic scale, for n identical particles, the polarization density reads[3]

$$\mathbf{P}(\omega) = n\langle\mathbf{p}\rangle(\omega) = \epsilon_0\chi(\omega)\mathbf{E}(\omega) \tag{1.28}$$

where $\chi(\omega)$ is the material susceptibility.

Helmholtz equation in a uniform dielectric media

In this manuscript, we will consider propagation of light in dielectric media, without magnetic moment or current. First, we consider a uniform medium. In the spectral domain, the Maxwell's equations read

$$\operatorname{div}\mathbf{B}(r,\omega) = 0 \tag{1.29}$$

$$\mathbf{rot}\,\mathbf{E}(r,\omega) = i\omega\mathbf{B}(r,\omega) \tag{1.30}$$

$$\operatorname{div}\mathbf{E}(r,\omega) = \frac{-\operatorname{div}\mathbf{P}(r,\omega)}{\epsilon_0} \tag{1.31}$$

$$\mathbf{rot}\,\mathbf{B}(r,\omega) = -\mu_0 i\omega\mathbf{P}(r,\omega) - \mu_0\epsilon_0 i\omega\mathbf{E}(r,\omega) \tag{1.32}$$

For a susceptibility $\chi(\omega)$, eq. (1.31) reads

$$\operatorname{div}(\epsilon_0\mathbf{E}(r,\omega) + \mathbf{P}(r,\omega)) = \operatorname{div}(\epsilon_0\mathbf{E}(r,\omega) + \epsilon_0\chi(\omega)\mathbf{E}(r,\omega)) = 0 \Rightarrow \operatorname{div}\mathbf{E}(r,\omega) = 0 \tag{1.33}$$

Combining eq. (1.29-1.33)

$$\begin{aligned}\mathbf{rot}\,\mathbf{rot}\,\mathbf{E}(r,\omega) &= \mathbf{grad}\operatorname{div}\mathbf{E}(r,\omega) - \Delta\mathbf{E}(r,\omega) = i\omega\mathbf{rot}\,\mathbf{B}(r,\omega)\\ &= i\omega(-\mu_0 i\omega\mathbf{P}(r,\omega) - \mu_0\epsilon_0 i\omega\mathbf{E}(r,\omega))\end{aligned} \tag{1.34}$$

Hence, the electric field fulfils

$$\Delta\mathbf{E}(r,\omega) + \mu_0\epsilon_0\omega^2(1+\chi(\omega))\mathbf{E}(r,\omega) = 0 \tag{1.35}$$

If we define the index of refraction $n(\omega) = \sqrt{1+\chi(\omega)}$, the field is driven by an equation known as the uniform Helmhotz's equation

$$\Delta\mathbf{E}(r,\omega) + \mu_0\epsilon_0\omega^2 n(\omega)^2\mathbf{E}(r,\omega) = 0 \tag{1.36}$$

[2]The sign "$_0$" on the notation of the polarizability α_0 means we consider the static limit $\omega \to 0$ (see Appendix A).

[3]This relation is only true in the quasi-static limit ($\omega \to 0$). Otherwise, the polarizability of a single atom and the susceptibility of the material are not proportional. A complete description requires a correction factor we will recall in Appendix A.

Helmholtz equation in a non-uniform dielectric media

Now, we consider the propagation of light in 1D or 2D dielectric inhomogeneous media characterized by non uniform susceptibilities $\chi(r=(x,y),\omega)$ (composed of different dielectric materials, see Fig. 1.6 as example). In such systems, the zero divergence of the electric field ($\text{div}\,\mathbf{E}=0$) in eq. (1.33) is not fulfilled

$$\begin{aligned}\text{div}\,(\epsilon_0\mathbf{E}(r,\omega))+\text{div}\,(\epsilon_0\chi(r,\omega)\mathbf{E}(r,\omega)) =&\epsilon_0(1+\chi(r,\omega))\text{div}\,\mathbf{E}(r,\omega)\\ &+\epsilon_0\mathbf{grad}\,\chi(r,\omega).\mathbf{E}(r,\omega)=0\end{aligned} \tag{1.37}$$

We decompose the electric field into a Transverse Electric (TE) and a Transverse Magnetic (TM) components (see Fig.1.6). If we consider the TE component of the electric field $\mathbf{E}_{TE}=E_{TE}(x,y)\mathbf{z}$, where $\mathbf{z}$ is the direction orthogonal to the 2D system, eq. (1.37) reads

$$\epsilon_0\,(1+\chi(r,\omega))\text{div}\,\mathbf{E}_{TE}(r,\omega)+\epsilon_0\mathbf{grad}\,\chi(r,\omega).\mathbf{E}_{TE}(r,\omega)=\epsilon_0(1+\chi(r,\omega))\text{div}\,\mathbf{E}_{TE}(r,\omega)=0 \tag{1.38}$$

Inserting eq. (1.38), into Maxwell's eq. (1.29-1.32) and projecting along $\mathbf{z}$ leads to Helmholtz equation in non-uniform media

$$\Delta E_{TE}(r,\omega)+\mu_0\epsilon_0\omega^2 n(r,\omega)^2E_{TE}(r,\omega)=0 \tag{1.39}$$

where $n(r,\omega)^2=1+\chi(r,\omega)$.

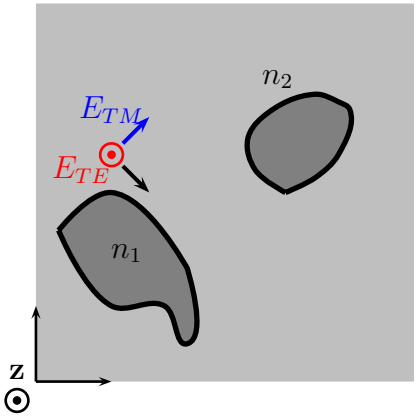

Figure 1.6: Electric field $\mathbf{E}$ in an inhomogeneous medium composed of material of index of refraction n_1 and n_2: The electric field can be expanded in a TE and a TM component.

In the case of piecewise constant refractive index distribution (for instance see Fig. 1.6), a similar equation can be derived for $\mathbf{B}_{TM}$ and the TM part of the electric field $\mathbf{E}_{TM}$ can be obtained thanks to Maxwell-Faraday's eq. (1.30) [5]. As a result, the total electromagnetic field is derived from a single scalar equation

$$\Delta U(r,\omega)+\mu_0\epsilon_0\omega^2 n(r,\omega)^2U(r,\omega)=0 \tag{1.40}$$

where U is the electric or magnetic field in transverse configuration.

In the scope of this manuscript, we will consider 1D or 2D dielectric media, where either the electric field is TE or the refractive index is piecewise. Noting $\mu_0\epsilon_0=c^{-2}$, the electromagnetic field in our media will be derived from the scalar Helmholtz equation

$$\Delta E(r,\omega)+\frac{\omega^2}{c^2}n(r,\omega)^2E(r,\omega)=0 \tag{1.41}$$

1.2 Light scattering by a particle

We derived in section 1.1.3 the evolution of the electric field in inhomogeneous media. Eq. (1.41) emphasizes the influence on light propagation of a modification in the index of refraction. In particular, when light encounters a rapid variation in the index of refraction, its propagation is affected: The wave is scattered. In this section, we introduce briefly the scattering. First we consider scattering by single particle and its effect on the electromagnetic field. Then we focus on scattering with a large number of particles and introduce averaged descriptions. More details can be found in [1, 6, 7].

1.2.1 Introduction

We consider the case of a plane wave (characterized by an electric field $\mathbf{E}_0 = E_0\mathbf{x}$ at wavelength λ) incident on a particle (length scale L, see Fig. 1.7**(a)**). When crossing the particle, the electric field spreads in many directions: The particle scatters the incident field. The resulting field $\mathbf{E}_s$ is referred to as the scattered field. Far away from this scatterer, in the far field approximation (distance $\gg L^2/\lambda$), this field reads

$$\mathbf{E}_s(\mathbf{u}) = \mathbf{S}(\mathbf{u})\mathbf{E}_0\frac{e^{i\frac{2\pi}{\lambda}r}}{r} \tag{1.42}$$

where $\mathbf{u}$ is the scattering direction and $\mathbf{S}(\mathbf{u})$ the scattering matrix. The scattering matrix stands for the modification of the incident polarization ($\mathbf{x}$ in Fig. 1.7**(a)**). From an electromagnetic point of view, the particle acts as a passive emitting source. When the medium is stricken by light (see Fig. 1.7**(b)**), the electric field induces motion of charges (free or polarization). This displacements lead to the build-up of a current density $\langle\mathbf{j}_m\rangle$ (see section 1.1.2) and these currents will radiate an electromagnetic field, referred to as the scattering field. As a result, the scattered wave and the scattering matrix are set by the geometrical shape and the material of the particle. As sketched in Fig. 1.7**(c)**, the directional scattering pattern can be rather complex and non-isotropic.

In the Helmholtz equation we derived in eq. (1.41), a scatterer is represented by a rapid change in the index of refraction. For instance, in the example provided in Fig. 1.7, the electric field satisfies

$$\Delta E(r,\omega) + \frac{\omega^2}{c^2}n(r)^2E(r,\omega) = 0 \tag{1.43}$$

where $n = 1$ outside the particle and $n = n_{mat}$ inside (n_{mat} is the index of refraction of the material).

Now, we consider the total intensity scattered on the whole space. Using eq. (1.42), this intensity reads

$$I_s = \int_{r\to+\infty}|\mathbf{E}_s|^2dS = \int_{r\to+\infty}|\mathbf{S}(\mathbf{u})|^2\frac{|\mathbf{E}_0|^2}{r^2}r^2\sin\theta d\theta d\phi \tag{1.44}$$

where θ and ϕ stand for angular coordinates. Noting $d\Omega = \sin\theta d\theta d\phi$ the solid angle, eq. (1.44) reads

$$I_s = I_0\int_{4\pi}|\mathbf{S}(\mathbf{u})|^2d\Omega \tag{1.45}$$

where $I_0 = |\mathbf{E}_0|^2$ stands for the incident plane wave intensity per unit surface area. Therefore, we can define from eq. (1.45) a surface called the scattering cross section

$$\sigma_s = \frac{I_s}{I_0} = \int_{4\pi} |\mathbf{S}(\mathbf{u})|^2 d\Omega \tag{1.46}$$

This scattering cross section gives an averaged quantity measuring the scattering strength of the particle.

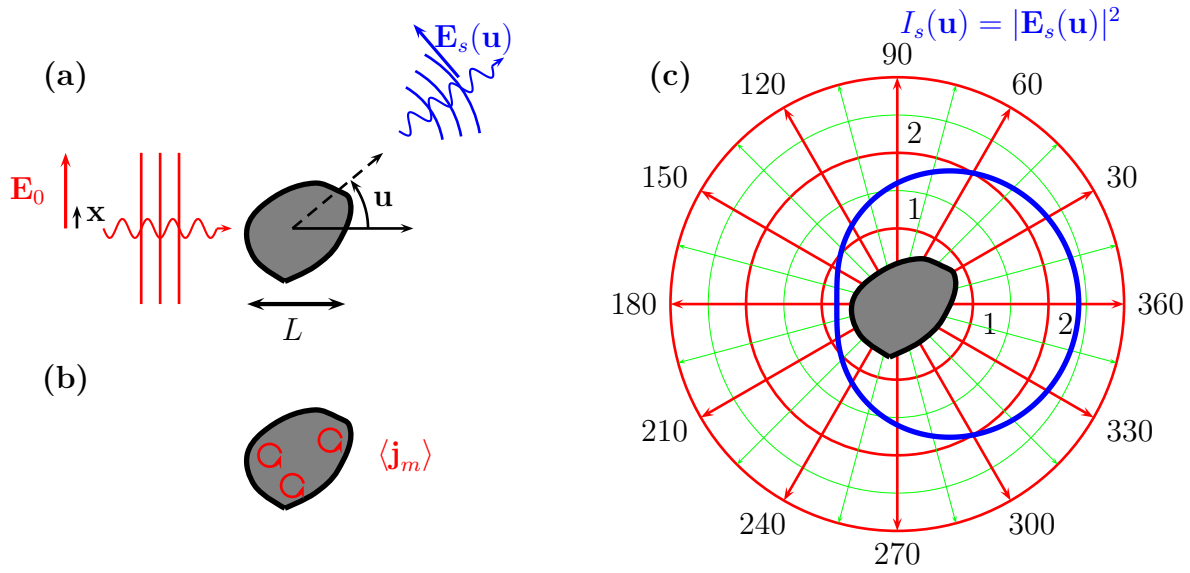

Figure 1.7: **(a)** The incident electric field $\mathbf{E}_0$ is scattered by a particle. The resulting field $\mathbf{E}_s$ is spread in all directions. **(b)** The scattered field results from the appearance of local currents in the particle induced by $\mathbf{E}_0$. **(c)** Scattering diagram: The scattered field is non-isotropic.

1.2.2 Scattering media

In section 1.2.1, we treated the scattering by a single particle. In scattering media, the propagation of the electric field is still described by Helmholtz equation (see for instance eq. (1.43)). Nevertheless, in media where the density of scattering is important, many scattering events occur, which makes the scattering of the incident electric field difficult to handle. In this section, we aim at introducing different approaches we use in Chapter 5 instead of the Helmholtz equation.

For instance, we will consider the case of a plane wave incident on a plane interface (see schematic drawing of Fig. 1.8). In this problem, each time the light is scattered, the intensity in the incident direction decays.

The decay is exponential and satisfies the Beer's law

$$I_s = I_0 e^{-\frac{x}{l_s}} \tag{1.47}$$

where l_s defines the scattering length or mean free path. l_s stands for the typical scattering length-scale of the incident intensity. From l_s we can define the transport length or mean free path l_t.

$$l_t = \frac{l_s}{1-g} \tag{1.48}$$

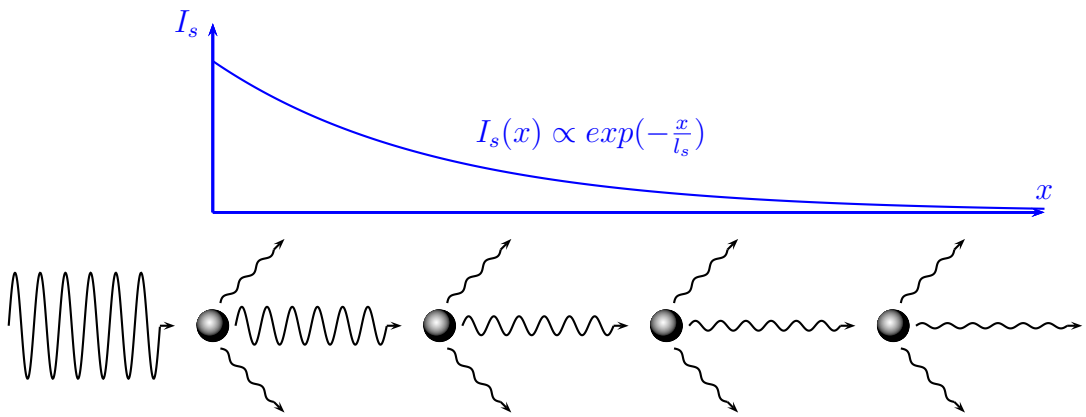

Figure 1.8: Schematic representation of light scattering: The intensity decays according to the Beer's law.

This relation between both lengths includes the asymmetry coefficient $g = \langle cos(\theta) \rangle$ standing for the averaged angular scattering of particles constituting the medium (see for instance Fig. 1.7**(c)**). l_t stands for the length after which the direction of propagation of the photon is randomized or the incident direction is lost. For an isotropic scattering $g = 0$ and for a directional scattering $g \to 1$. In diluted systems, these lengths can be related to the notion of cross section introduced in section 1.2.1. For instance the scattering cross section σ_s reads

$$\sigma_s = \frac{1}{\rho l_s} \tag{1.49}$$

where ρ is the scatterer density. As a result, in this specific configuration, the multiple scattering is easily related to single scattering quantity.

More generally, for 3D problems with a typical length-scale L much longer than the scattering length l_s ($L \gg l_s$), the light propagation will be described by a diffusion equation. If we assume no absorption, the diffusion of the intensity $I(r,t)$ will read

$$\frac{\partial I}{\partial t}(r,t) - D\Delta I(r,t) + \frac{1}{l_s} cI(r,t) = 0 \tag{1.50}$$

where c is the speed of light in the medium and $D = \frac{1}{3} c l_t$ the diffusion constant (expression only valid in 3D).

1.3 Light-Matter interaction: Matter excitation

In the first two sections, we investigated electric field evolution when interacting with matter. In this section, we rather focus on the medium itself. First, we introduce the discrete Bohr's description of energy of particle [8] and the different transition mechanisms between levels [9, 10]. Then, we investigate the static and the dynamic regimes of a two-level atom in the electric field (see [9, 10]). Finally, we consider a four-level atom and demonstrate how it can provide stimulated amplification (see [9, 10, 11]).

1.3.1 Energy conversion transfer

Bohr's hypothesis states [8] that the total energy of a particle (an atom for instance) can only exhibit a discrete set of values. Hence, energy can only be modified by "quantum jumps" described by Einstein's electromagnetic/matter interaction [12]. To introduce the different scenarii of conversion, we consider an atom with two levels of energy (see Fig. 1.9).

First, as sketched in Fig. 1.9**(a)**, the atom can be excited from state 1 to state 2 via an external input of energy. This is the pumping or external excitation. External energy can be brought in various forms (e.g. chemical, optics, electrical).

The atom can decay from energy state 2 to 1 by spontaneous emission (see Fig. 1.9**(b)**). The decay of energy is subsequently converted into a photon of similar energy $h\nu_0 = E_2 - E_1$ called the resonance transition. This emission is usually isotropic and happens randomly. However, for an initially excited system, the probability of spontaneous emission decays exponentially versus time (see section 1.3.2).

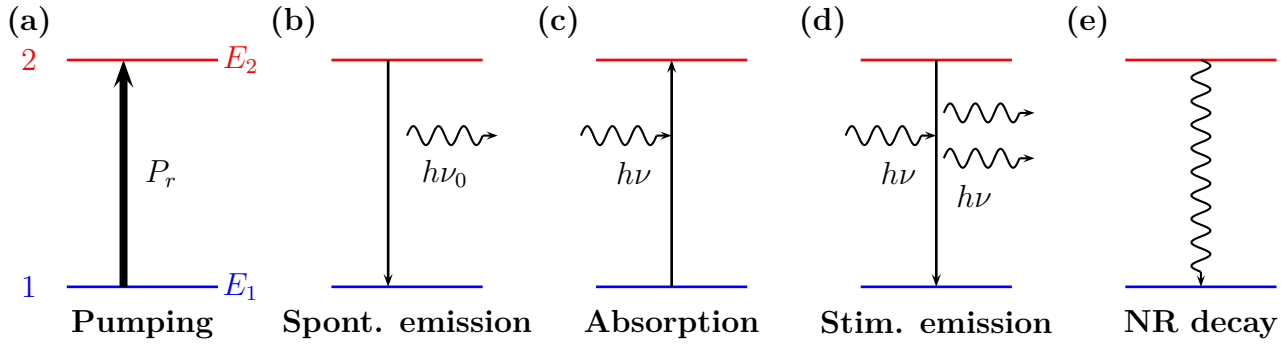

Figure 1.9: Energy transfers: **(a)** Pumping/Excitation by an external source. **(b)** Spontaneous emission of a photon. **(c)** Absorption of an incident photon. **(d)** Stimulated emission driven by an incident photon. **(e)** Non radiative (NR) decay.

The atom, initially in state 1, can also be excited into state 2 by absorption of an incident photon at energy $h\nu \approx E_2 - E_1$ (see Fig. 1.9**(c)**). The incident light beam is thus depleted and looses a photon each time an absorption event occurs.

The atom initially in state 2, can also decay into level 1 by stimulated emission [13](see Fig. 1.9**(d)**). The incident photon energy $h\nu \approx E_2 - E_1$ being close to resonance transition, the atom emits a photon identical to the incident one. The photons are duplicated by stimulated emission.

Last, the atom initially in state 2 decays to level 1 by non radiative transition (see Fig. 1.9**(e)**). No photon is emitted and energy can be transferred via different non radiative effects (e.g. vibration, collision, phonon).

1.3.2 A two-level atom in an electromagnetic field

Population equations

Here we consider the textbook case (e.g. [9, 10]) of a total population of N two-level atoms placed in the electromagnetic field. With the development of quantum dots acting like artificial two-level atoms, this model is currently used in many fields of research (e.g. in quantum information). In particular, it will be considered in Chapter 4.

The two levels are assumed non-degenerated *i.e.* there is one quantum state for each energy level. This set of atoms acts like a single emitter with two energetic levels 1 and 2. No pumping is considered and we assume that all the conversion are radiative. Thus, populations of different levels N_1 and N_2 read

$$\frac{dN_1}{dt} = A_{21}N_2 - B_{12}N_1u(\nu) + B_{21}N_2u(\nu) \tag{1.51}$$

$$\frac{dN_2}{dt} = -\frac{dN_1}{dt} = -A_{21}N_2 + B_{12}N_1u(\nu) - B_{21}N_2u(\nu) \tag{1.52}$$

where $u(\nu)$ is the photonic density at frequency ν. In eq. (1.51) and (1.52), A_{21} stands for spontaneous decay from 2 to 1, $B_{12}N_1u(\nu)$ for absorption from 1 to 2 and $B_{21}u(\nu)$ for stimulated emission from 2 to 1. Moreover, the particle conservation reads

$$N = N_1 + N_2 \tag{1.53}$$

In this specific case of non-degenerated atoms, absorption and stimulated coefficients fulfil

$$B_{12} = B_{21} \tag{1.54}$$

Leading to population equations

$$\frac{dN_1}{dt} = A_{21}N_2 + B_{21}(N_2 - N_1)u(\nu) \tag{1.55}$$

$$\frac{dN_2}{dt} = -\frac{dN_1}{dt} = -A_{21}N_2 - B_{21}(N_2 - N_1)u(\nu) \tag{1.56}$$

Steady state regime

In the steady state regime, eq. (1.55) and (1.56) read

$$0 = A_{21}N_2 - B_{12}N_1u(\nu) + B_{21}N_2u(\nu) \tag{1.57}$$

$$0 = -\frac{dN_1}{dt} = -A_{21}N_2 + B_{12}N_1u(\nu) - B_{21}N_2u(\nu) \tag{1.58}$$

As a result, for a non-degenerated problem

$$A_{21}N_2 + B_{21}u(\nu)(N_2 - N_1) = 0 \tag{1.59}$$

With conservation relation of eq. (1.53), eq. (1.59) reads

$$A_{21}N_2 + B_{21}u(\nu)(2N_2 - N) = 0 \tag{1.60}$$

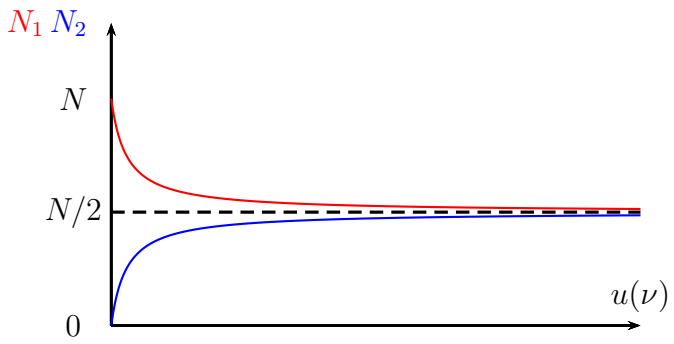

Figure 1.10: Steady state population $N_{i,ss}$: They evolve linearly for low energy. Both populations converge to $N/2$ for high energy.

Leading to steady state expressions of the populations

$$N_{1,ss} = N\frac{A_{21} + B_{21}u(\nu)}{A_{21} + 2B_{21}u(\nu)} \tag{1.61}$$

$$N_{2,ss} = N\frac{B_{21}u(\nu)}{A_{21} + 2B_{21}u(\nu)} \tag{1.62}$$

In Fig. 1.10, we plot the evolution of the population in the steady state versus the photonic density.

Fig. 1.10 highlights that, for a two-level atom, high energy population (N_2) is smaller than lower energy population (N_1). The inversion population is negative: $\Delta N = N_2 - N_1 < 0$. Moreover, we know from eq. (1.55) that stimulated emission and absorption coexist. This is emphasized by the right-hand side term $B_{21}u(\nu)(N_2 - N_1)$ in eq. (1.55). Hence, to achieve a photonic amplification with stimulated emission, we need to impose a positive inversion population ΔN to compensate for the absorption. As a result, the two-level atom cannot be used as an amplifying medium.

If at low $u(\nu)$ the populations evolve linearly with the energy, Fig. 1.10 also stresses the convergence of populations at high energy. This phenomenon is called the saturation of the emitter (see Chapter 6) and is related to the finite energy that the emitter can provide.

Dynamic regime

In Chapter 4, we will investigate the evolution of a two-level emitter in a electromagnetic field in the time domain. To give an overview of two-level atom temporal dynamic, we consider the situation of atoms excited in the steady state regime for $t < 0$. At $t = 0$, the field excitation is turned-off ($u(\nu) = 0$).

At initial time ($t = 0$), the high energy population reads $N_2(0) = N_{2,ss}$. After the excitation has been switched-off, the temporal evolution of N_2 is given by

$$\frac{dN_2}{dt} = A_{21}N_2 \Rightarrow N_2(t) = N_{2,ss}e^{-A_{21}t} \tag{1.63}$$

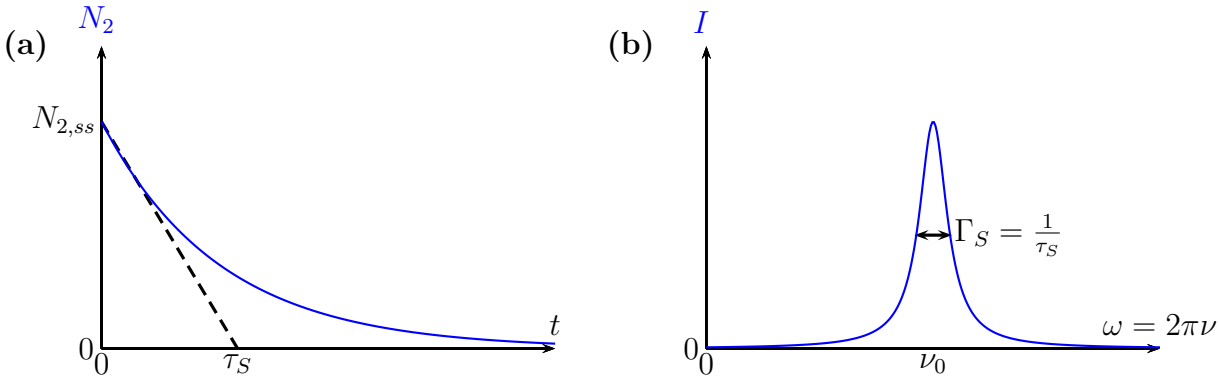

Figure 1.11: **(a)** High energy population N_2 versus time: The population decreases exponentially with a characteristic time τ_S. **(b)** Atoms are emitting photons by spontaneous emission: The resulting emission spectrum is centred in the transition frequency ν_0 and the linewidth is fixed by the time τ_S.

As a result, the population of excited atoms will be progressively depleted by spontaneous emission of photons. This decay is characterized by a time $\tau_S = 1/A_{21}$ (see Fig. 1.11**(a)**). As shown in Fig. 1.11**(b)**, the resulting spectrum has a Lorentzian shape centred at ν_0 (ν_0 is the resonant frequency between the two states). The temporal decay τ_S of excited atoms population (N_2) fixes the linewidth of emission in the spectral domain ($\Gamma_S = 1/\tau_S$). In this particular case, we have omitted non-radiative transition. In presence of non-radiative transitions, some atoms in population N_2 decay without emitting photons. Hence, the resulting spontaneous emission will be modified. Both radiative and non-radiative transitions affect the spectral linewidth $\Gamma_S = 1/\tau_S$, which reads

$$\Gamma_S = \Gamma_S^R + \Gamma_S^{NR} \tag{1.64}$$

where Γ_S^R stands for radiative decay and Γ_S^{NR} for non-radiative.

1.3.3 Four-level atomic system

Achievement of laser sources relies on the duplication of photons via stimulated emission (see Chapters 5-8). We demonstrated in section 1.3.2 that a two-level atom cannot be used to perform stimulated amplification. A more complex medium is required.

In the scope of this manuscript, we will consider media composed of four-level atoms (see for instance [9, 10, 14]). The four-level description is widely used for modelling amplifying media (e.g. Rhodamine or Ti:Sapphire). As sketched in Fig. 1.12, the atom is described by four levels of energy, namely levels 0, 1, 2 and 3. The system is pumped (W_p) by an external source of energy, which brings atoms from level 0 to 3. Transition from level 2 to 1 provides the stimulated emission. Transitions from 3 to 2 and 1 to 0 are assumed non-radiative and extremely fast. Hence, levels 3 and 1 are empty. As a result, the population of different levels read

$$\frac{dN_3}{dt} \approx 0 = W_p N_0 - A_{32} N_3 \tag{1.65}$$

$$\frac{dN_2}{dt} = A_{32} N_3 - A_{21} N_2 - B_{21}(N_2 - N_1)u(\nu) \tag{1.66}$$

$$\frac{dN_1}{dt} \approx 0 = -A_{10} N_1 + A_{21} N_2 + B_{21}(N_2 - N_1)u(\nu) \tag{1.67}$$

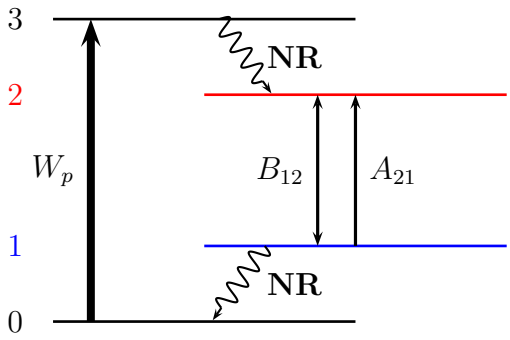

Figure 1.12: Four-level atom: Level 0 is pumped to level 3. Transitions between 3 and 2 and 1 and 0 are non-radiative. Transitions between levels 1 and 2 are radiative.

$$\frac{dN_0}{dt} = -W_p N_0 + A_{10} N_1 \tag{1.68}$$

From eq. (1.65) and $N_1 \approx 0$ we deduce

$$\frac{dN_2}{dt} = W_p N_0 - A_{21} N_2 - B_{21} N_2 u(\nu) \tag{1.69}$$

and

$$\frac{dN_0}{dt} = -W_p N_0 + A_{21} N_2 + B_{21} N_2 u(\nu) \tag{1.70}$$

Using the conservation relation $N_0 + N_2 = N$, eq. (1.69) reads

$$\frac{dN_2}{dt} = W_p (N - N_2) - A_{21} N_2 - B_{21} N_2 u(\nu) \tag{1.71}$$

Therefore, the inversion population $\Delta N = N_2 - N_1 \approx N_2$ fulfils

$$\frac{d\Delta N}{dt} = \frac{1}{\tau}\left(\Delta N_0 - \Delta N - \frac{u(\nu)}{u_{sat}}\Delta N\right) \tag{1.72}$$

where

$$\tau = (W_P + A_{21})^{-1} \tag{1.73}$$

$$\Delta N_0 = N\frac{W_p}{W_p + A_{21}} \tag{1.74}$$

$$u_{sat} = \frac{W_p + A_{21}}{B_{21}} \tag{1.75}$$

Solution of eq. (1.72) in steady state regime reads

$$\Delta N = \frac{\Delta N_0}{1 + \frac{u(\nu)}{u_{sat}}} = N\frac{W_p}{(W_p + A_{21})\left(1 + \frac{u(\nu)}{u_{sat}}\right)} \tag{1.76}$$

As a result, the inversion population is positive and its amplitude is triggered by the pump intensity. Hence, in four-level media, stimulated amplification can be achieved. Eq. (1.76) also highlights the inversion population saturates for high energy $u(\nu)$. We will investigate in Chapter 6 the role played by saturation on amplification process. In the rest of this manuscript we will consider the gain media as four-level atomic systems.

1.4 Summary

In the present chapter, we have introduced basic notions required to study light-matter interaction in a semiclassical approach. In 1D and 2D dielectric media, the electromagnetic field is studied in a classical way and is described by a scalar linear equation, namely the Helmholtz equation. This equation conveniently describes electromagnetic field propagation in media with homogeneous and inhomogeneous refractive index. We have also briefly introduced the scattering of electromagnetic field by a discontinuity embedded in the medium. We have stressed the manifestations of the scattering at particle scale and macro-scale. Finally, we have stated that the matter is described with quantized levels of energy and the "jumps" between levels are achieved with various mechanisms that we introduced. Starting from this description, we have investigated the static and the dynamic evolution of two-level and four-level systems. We have demonstrated that a photonic amplification cannot be performed on two-level atom and requires a more complex system such as four-level atoms.

Chapter 2

Modes in non-hermitian systems: The specific case of open random media

Table of Contents

In physics, a wave is described as a propagation of energy through time and space. Its study is complicated by the intrinsic dependency of time and space. The aim of the modal description is to simplify the description of wave by carrying out its expansion along specific vibrational states of the problem. These vibrational states define the modes of the system. The notion of mode has been widely used in quantum as well as in classical physics [15, 9]. However, the nature of modes differs when the system is energy-conservative (hermitian) or non-conservative (because of absorption or openness). For non-hermitian problems, the modes are associated with the resonances. Because the resonances represent specific signatures of the system, their study is of fundamental interest in various domains of application such as biophotonics [16, 17] for single molecule fluorescence detection, antennas [18, 19] and photonic crystals [20, 21]. Hence, finding the vibrational states of open structures with non-trivial geometries is thus of great theoretical and practical interest.

In this chapter, we investigate the description of modes in open problem and consider the specific case of disordered systems. First, we introduce the concept of modal expansion in hermitian and non-hermitian systems. Because, vibrational states are of different nature, the characteristics of the modes differ from hermitian to non-hermitian. Then, we describe the modes in the specific case of open systems. The openness requires to define a different mathematical formalism, which differs from hermitian physics. Finally, we consider the specific case of disordered open systems. The study of resonances provides an interesting tool to investigate the mechanism of wave localization by disorder, namely the Anderson localization.

2.1 Introduction to Modes in hermitian/non-hermitian systems

The aim of this section is to introduce the concept of modes in hermitian and non-hermitian systems using the guideline example of the Melde's string. For an energy-conservative (hermitian) system, the modes are defined as the stationary solutions of the problem. When losses are introduced, the problem becomes non-hermitian. In other words, stationary solutions no longer exist and the modes correspond to the resonances of the problem. Because, hermitian and non-hermitian modes are of distinct nature, they exhibit different properties. Among them, the mode degeneracy is a specific signature of each case.

2.1.1 Stationary solutions of hermitian systems

The Melde's string

To introduce the concept of mode, we consider the example of the Melde's string (see Fig. 2.1). A string of length L is excited by an electromagnet (frequency ν and a small amplitude a) at one edge and maintained static by a mass at the other. The height, $h(x,t)$, varies in time and space, defining a wave (see Fig. 2.1). In this academic example, losses are neglected and energy is conserved through time: The system is said hermitian. The corresponding relation of motion, with a wave celerity v, is given by the Alembert's

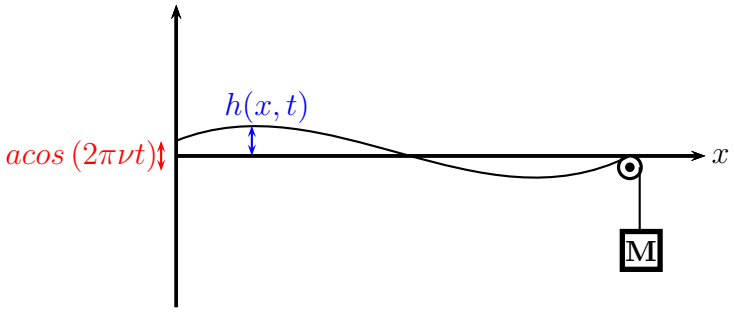

Figure 2.1: Melde's string loss free: A string of length L is excited by an electromagnet at the one edge ($x = 0$). The amplitude and frequency of the excitation are respectively a and ν. A wave described by the height of the string $h(x,t)$ propagates. The presence of a heavy mass forces the wave to be zero at the edge $x = L$.

equation

$$\frac{\partial^2 h}{\partial x^2}(x,t) - \frac{1}{v^2}\frac{\partial^2 h}{\partial t^2}(x,t) = 0 \tag{2.1}$$

This equation is a second order derivative, thus requires two boundary conditions. Because the system is excited at one edge and clamped at the other one, these boundary conditions read

$$h(0,t) = a\cos(2\pi\nu t) \quad \& \quad h(L,t) = 0 \tag{2.2}$$

The system is loss free, thus eq. (2.1) can be solved using stationary solutions. From a mathematical point of view, solving a problem by adopting stationary waves consists in adopting a trial solution of the form $h(x,t) = f(x)g(t)$, where $f, g \in \mathbb{R}^2$. Physically

speaking, this is equivalent to considering time and space separately: The spatial distribution of the wave remains identical whatever the time and *vice versa*. Adopting this approach, eq. (2.1) can be solved in the stationary regime and any solution reads

$$h(x,t) = a\,\frac{\sin(k(L-x))}{\sin(kL)}\cos(2\pi\nu t) = |h(x)|_\nu \cos(2\pi\nu t) \tag{2.3}$$

where $|h(x)|_\nu$ is the wave amplitude, k stands for spatial frequency related to spectral excitation frequency by the simple dispersion relation $k = \frac{2\pi\nu}{v}$. Now, we assume that the excitation frequency ν spans the frequency space. In Fig. 2.2**(a)**, we record the response of the Melde's string with respect to the excitation frequency. For a discrete set of frequency

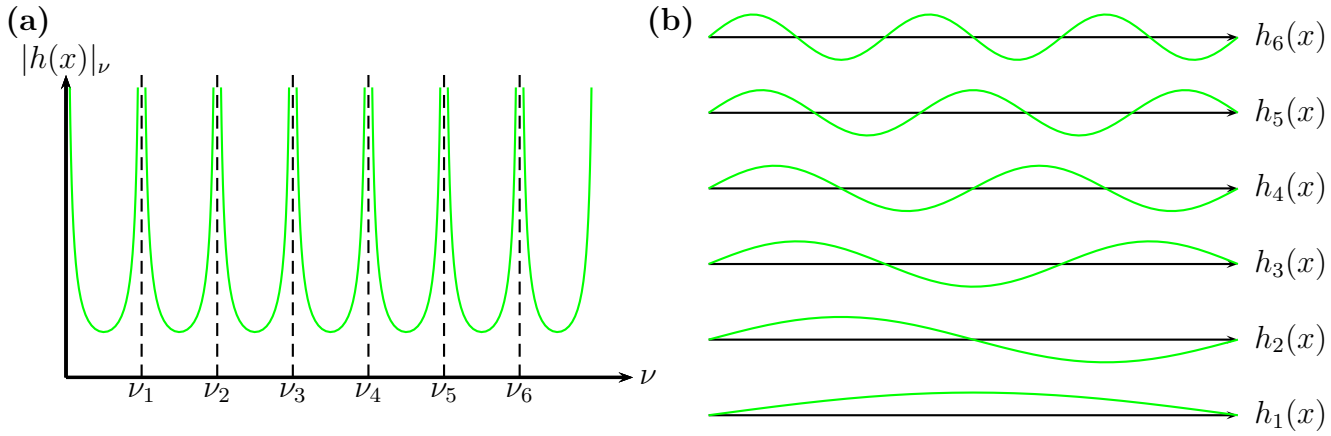

Figure 2.2: **(a)** Amplitude of wave $|h(x)|_\nu$ with respect to the excitation frequency ν: When approaching frequencies ν_p amplitude diverges. **(b)** Spatial distributions $h_p(x)$ of the wave at specific frequencies ν_p.

(ν_p), the amplitude of the wave diverges

$$|h(x)|_{\nu=\nu_p} \to +\infty \quad \Big| \quad \nu_p = \frac{vp}{2L} \tag{2.4}$$

At these particular frequencies, an infinitesimal excitation of the system ($a \to 0$) will make the string oscillate for ever. In the spatial domain, the wave will simultaneously describes oscillations

$$h_p(x) = \sin\left(\frac{2\pi\nu_p(L-x)}{v}\right) \tag{2.5}$$

Hence, each couple of frequency and spatial distribution $((\nu_p, h_p(x))$, see Fig. 2.2) represents an eigensolution or eigenstates of eq. (2.1). In wave physics, these sets of stationary solutions defined by couples of eigenvalue/eigenvector are referred to as the (hermitian) modes of the system. These modes define privileged vibrations in time and space of the string.

Modal expansion in hermitian problem

Now, the electromagnet responsible for the excitation is switched off. The system is turned into a string clamped at both extremities. When a wave propagates through the

string, it can be expanded into a sum of stationary waves solution of eq. (2.1). Hence, any wave $h(x,t)$ is a linear combination of the modes $(\nu_p, h_p(x))$ described in section 5.1.1

$$h(x,t) = \sum_p a_p h_p(x) \cos(2\pi\nu_p t) \tag{2.6}$$

where a_p are expansion coefficients. In the Fourier's domain, eq. (2.6) leads to a discrete spectrum

$$H(x,\nu) = \sum_p a_p h_p(x) \delta(\nu - \nu_p) \tag{2.7}$$

Because the spectral components are infinitely thin, there is no spectral overlap between the modes (see Fig. 2.3). In the space domain, defining the scalar product

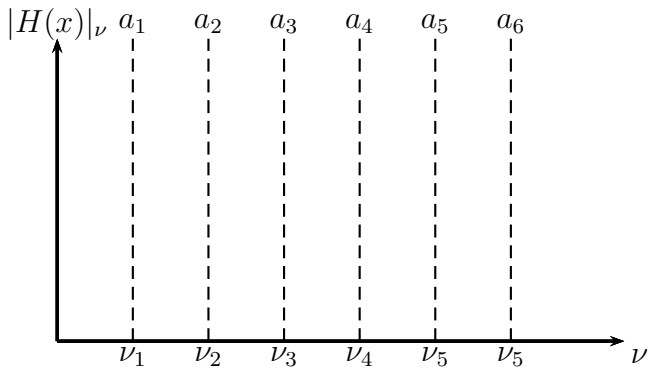

Figure 2.3: Example of a hermitian wave spectrum: The spectrum is discreet and composed of an infinite number of modes at frequencies ν_p.

$$\langle u|v\rangle = \int_L u(x)^* v(x) dx \tag{2.8}$$

it turns out that all the spatial distribution of the modes $h_p(x)$ (see Fig. 2.2) are orthogonal

$$\langle h_p|h_q\rangle = \delta_{pq} \tag{2.9}$$

Hence, there is neither spatial nor temporal overlap between the modes. From a physical point of view, a wave propagating in a hermitian system can be described by a linear superposition of independent vibrations. There is no exchange of energy between hermitian modes.

2.1.2 Resonances of non-hermitian systems

The Melde's string... with losses

When the total energy of the system is not conserved over time, the system is said non-hermitian. For non-hermitian problems, because energy escapes from the system through time, defining the modes as stationary vibrations (time independent) is not possible. In this manuscript, we consider losses of two kinds

- The presence of a complex potential: energy (wave) is absorbed or amplified.
- The openness of the system: energy (wave) leaks at the edges of the system.

To carry on with the Melde's string experiment, we introduce absorption with a damping coefficient α affecting the first order in eq. (2.1):

$$\frac{\partial^2 h}{\partial x^2}(x,t) - \alpha \frac{\partial h}{\partial t}(x,t) - \frac{1}{v^2}\frac{\partial^2 h}{\partial t^2}(x,t) = 0 \tag{2.10}$$

Because of the absorption, waves described by eq. (2.10) can no longer be considered as stationary solutions. We measure the amplitude of the wave versus excitation frequency ν in a similar manner to the hermitian case (see Fig. 2.4**(a)**). The amplitude of the spectral response no longer diverges. Because of absorption, each excitation will be attenuated in time until it disappears: The system no longer exhibits divergences resulting from stationary solutions. However, even if the amplitude does not diverge, some maxima remain at specific frequencies. These frequencies also correspond to privileged oscillations called the resonances of the system. Compared with stationary solutions, resonances are attenuated in time. This attenuation is directly related to the broadening of resonances in the spectral domain (see Fig. 2.4**(b)**). As a result, the definition of resonances differs from stationary solutions: A resonance is defined by a spatial distribution ($h_p(x)$), a central frequency (ν_p) and a spectral linewidth ($\Delta\nu_p$). Similar to the hermitian case and the stationary solutions, it is possible to define frequency for resonances, but these frequencies are now complex ($\Omega_p = 2\pi\nu_p - i2\pi\frac{\Delta\nu_p}{2}$) as initially suggested by Gamov [22]. In wave physics, the sets of complex frequency Ω_p and spatial distribution $h_p(x)$, are referred to as the quasi-modes or non-hermitian modes of the system. Hence, in hermitian systems,

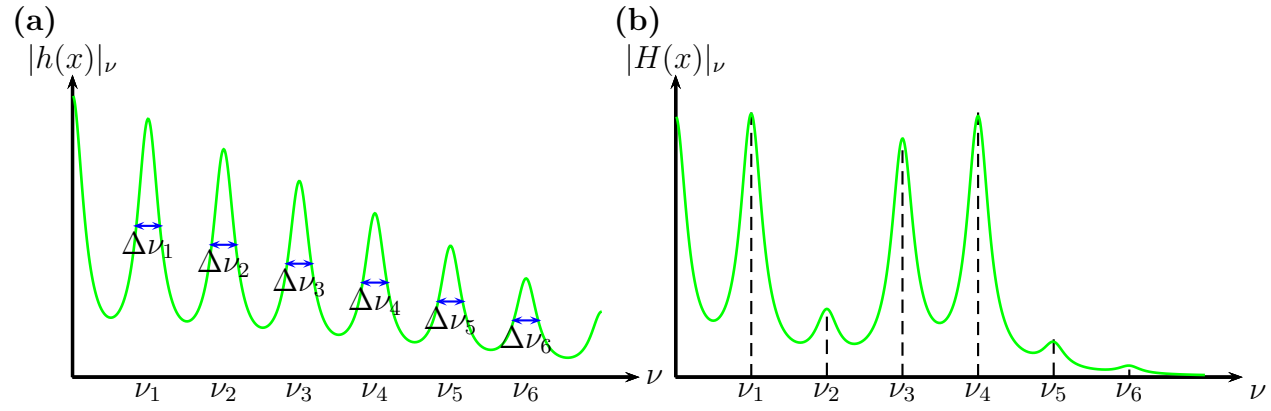

Figure 2.4: **(a)** Amplitude of the wave $|h(x)|_\nu$ according to the frequency excitation ν: The response exhibits specific maxima referred to the resonances. Each resonance is characterized by a central frequency ν_p and a linedwith $\Delta\nu_p$. **(b)** Example of wave decomposition in the spectral domain: The spectrum is continuous. Each maximum is related to a resonance of the system.

modes are derived from stationary solutions, while in non-hermitian systems, modes are related to resonances. However, in both cases, the modes are related to a privileged vibrational frequencies and thus stand for eigenstates of the problem.

Modal expansion in non-hermitian system

Similar to the hermitian case, the wave in non-hermitian systems can be expanded along the modes of the system. But unlike the hermitian case, the modes are not independent

and influence each other. By way of illustration, if we perform the modal expansion in the case of the Melde's string, any wave solution of eq. (2.10) reads

$$h(x,t) = \sum_p a_p h_p(x) \cos(2\pi\nu_p t)\, e^{-\frac{\Delta\nu_p}{2}t} \tag{2.11}$$

where a_p are simple coefficients. Each component is now damped. Eq. (2.11) leads to a continuous spectrum in the spectral domain (see Fig. 2.4**(b)**)

$$H(x,\nu) = \sum_p a_p h_p(x) \frac{1}{i\omega - i\Omega_p} \tag{2.12}$$

Moreover, this damping also affects the spatial distribution of the modes and breaks there orthogonality

$$\langle h_p | h_q \rangle \neq \delta_{pq} \tag{2.13}$$

Hence, non-hermitian modes have spatial and spectral overlap.

From a physical point of view, this basic example highlights that non-hermitian modes are not independent vibrations. Energy can be exchanged between modes, which makes them different from hermitian modes. The field is described by a superposition of non independent vibrations. Hence, the properties of non-hermitian modes will differ from the hermitian case. Mathematically speaking, the non-orthogonality of modes affects the completeness of the set of spatial distribution $(h_p(x))_p$ in infinite dimension problem. In others words, the uniqueness of the coefficients in eq. (2.11) is no longer guaranteed and is problem-dependent.

2.1.3 Fingerprint of hermitian/non-hermitian systems

As stated in sections 2.1.1 and 2.1.2, modes in hermitian or non-hermitian systems have different properties. To highlight their differences, we propose to investigate a simple example of Quantum Mechanics problem: The electron in a double quantum well.

Two-mode interaction in a hermitian system

First, we consider two independent quantum wells L and R far away from each other. In hermitian quantum mechanics, the stationary solutions of this problem are given by the eigenstates (eigenvalues/eigenvectors) of the energy operator called the Hamiltonian. The two quantum wells are considered distant and independent (see Fig. 2.5**(a)**). Each quantum well is characterized by a spatial distribution $|\Phi_{L/R}\rangle$ and a real energy $E_{L/R}$. Hence, the problem can be reduced in the form of a Hamiltonian H_0:

$$H_0 = \begin{pmatrix} E_L & 0 \\ 0 & E_R \end{pmatrix} \tag{2.14}$$

In this simple case, the eigenstates of the full problem correspond to the eigenstates of each individual well $\left(E_{L/R}, |\Phi_{L/R}\rangle\right)$.

Now, the two wells are brought closer to each other (see Fig. 2.5**(b)**). The interaction between the two wells is introduced by adding a hermitian perturbation described by an

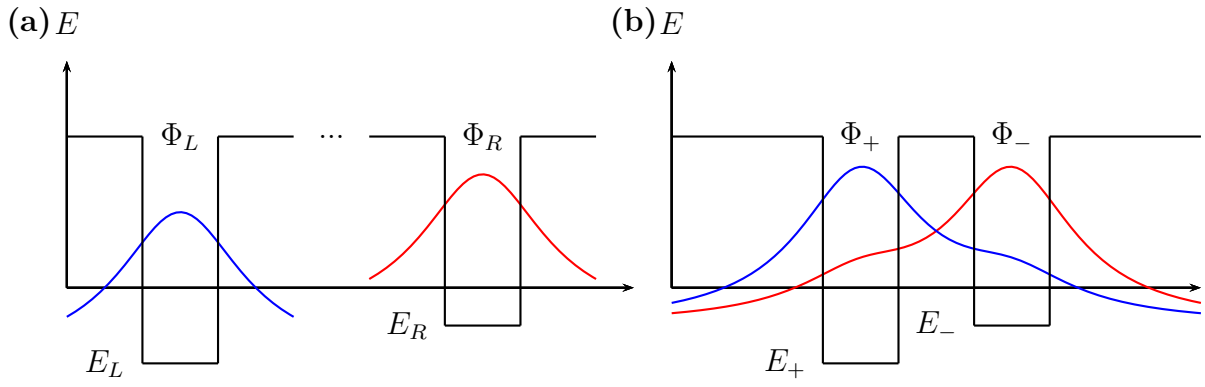

Figure 2.5: **(a)** Two quantum wells R/L are considered independently: They define eigenstates equivalent to stationary solutions $(E_{R/L}, \Phi_{R/L})$. **(b)** When the two eigenstates interact, they create new eigenstates $(E_\pm, \Phi_\pm)$.

operator T responsible for tunnelling from one well to the other. The new Hamiltonian H writes

$$H = H_0 + T = \begin{pmatrix} E_L & 0 \\ 0 & E_R \end{pmatrix} + \begin{pmatrix} 0 & T_{LR} \\ T_{RL} & 0 \end{pmatrix}$$

$$H = \begin{pmatrix} E_L & T_{LR} \\ T_{RL} & E_R \end{pmatrix} \tag{2.15}$$

where $T_{LR} = \langle \Phi_L | T | \Phi_R \rangle \in \mathbb{R}$, $T_{RL} = \langle \Phi_R | T | \Phi_L \rangle = T_{LR}$. In this case, the Hamiltonian describing the electron evolution is hermitian: By extension the problem is said hermitian. Because H is hermitian, its eigenstates are described by real energy $E_\pm$

$$E_\pm = \frac{E_L + E_R}{2} \pm \sqrt{\frac{(E_L - E_R)^2}{4} + |T_{RL}|^2} \in R \tag{2.16}$$

And defining the inner product

$$\langle a | b \rangle = [a_1^* a_2^*] \, [b_1 b_2]^T \tag{2.17}$$

the eigenvectors $\Phi_\pm$ are orthogonal

$$\Phi_\pm = \begin{bmatrix} T_{LR} \\ \pm\sqrt{\frac{(E_L - E_R)^2}{4} + |T_{RL}|^2} - \frac{E_L - E_R}{2} \end{bmatrix} \quad \& \quad \langle \Phi_+ | \Phi_- \rangle = 0 \tag{2.18}$$

Similar to the case of the Melde's string, the wave function of the electron will infinitely "oscillate" at real frequencies $E_\pm$ along non interacting spatial distributions $\Phi_\pm$. Thus, the total energy of the system will be conserved over time. These eigenstates $(E_\pm, \Phi_\pm)$ (see Fig. 2.5**(b)**) are analogue to eigenmodes introduced in section 5.1.1 for the hermitian problem.

Hermitian degeneracy: Diabolic Point

Carrying on the previous example of the double hermitian quantum well, we assume that the different parameters (E_L, E_R and T_{RL}) can be modified by playing with the depths

of wells and the gap between them. We assume that these parameters are independent, which means that they can be varied without influencing each other. We consider a configuration where eigenvalues become degenerated

$$E_+ = E_- = (E_L + E_R)/2 \tag{2.19}$$

In the present case, the problem is non-dissipative with time-reversal symmetry, thus H is real and symmetric [23]. We need to fix the two real parameters (e.g. for a given E_L we will modify E_R and T_{RL}) to achieve the degeneracy suggested in eq. (2.19)

$$E_R = E_L \quad \& \quad T_{RL} = 0 \Rightarrow E_+ = E_- \tag{2.20}$$

The problem is said of co-dimension 2 [23]. For hermitian but complex hamiltonian (non-dissipative without time-reversal symmetry), three parameters are needed (co-dimension 3 [24]).

If eigenvalues can become identical at a specific point in the parameter space (E_R, T_{RL}), the spatial distribution of the modes remain orthogonal at degeneracy because the system is hermitian. This specific configuration introduced by Berry and Wilkinson [25], where eigenvalues are identical and eigenvectors are orthogonal, is called a Diabolic Point. The origin of the appellation comes from geometry of the Riemann's sheets of eigenvalues $E_\pm$ in the parameter space. They describe a double cone (diabolo) connected at the degeneracy [25]. As a matter of illustration, we plot in Fig. 2.6 the evolution of the real eigenvalues ($E_\pm$) of the double-quantum well in the parameter space (E_R, T_{RL}). Diabolic Point can also appear in non-hermitian systems but its observation is hindered by the required number of independent parameters (at least a co-dimension of 4). Hence, with 2 independent parameters, the observation of a Diabolic Point is specific to hermitian problems.

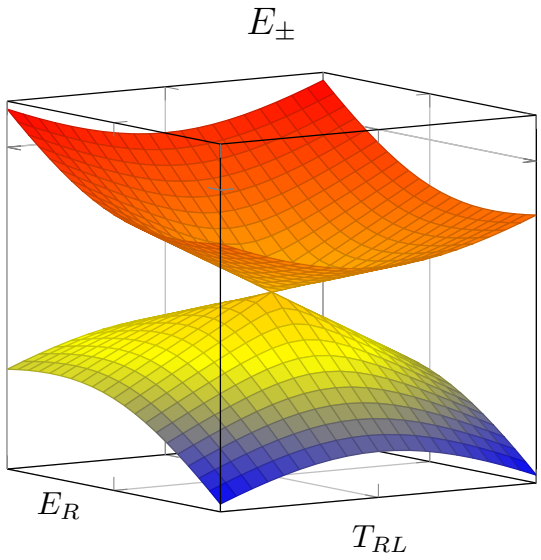

Figure 2.6: Evolution of the real eigenvalue $E_\pm$ in the parameter space (E_R, T_{RL}). The eigenvalues evolve along Riemann's sheet intersecting at a single point: The Diabolic Point. The two sheets describe cones connected like a diabolo.

One of the major manifestation of the Diabolic Point is its influence on the Berry's phase [26]. The Berry's phase is of geometrical origin. When a system (indifferently quantum

or classical) undergoes an adiabatic transformation, it acquires a residual phase due to its evolution within the parameter space. The Berry's phase has been observed in quantum optics [27], classical optics [28] and even microwave cavity [29]. When a Diabolic Point is encircled within the parameter space, the Berry's phase accumulates a π phase [30].

Two-mode interaction in a non-hermitian system

The hermiticity is related to the conservation of the energy and breaks down when losses are introduced. Here, we consider the double quantum well with complex energies $E_{L/R} - i\Gamma_{L/R}$, where $\Gamma_{L/R}$ are due to absorption introduced within each well. The problem being non-hermitian, its Hamiltonian is non-hermitian and $T_{RL} = T_{LR} \in \mathbb{C}$:

$$H = \begin{pmatrix} E_L - i\Gamma_L & T_{LR} \\ T_{RL} & E_R - i\Gamma_R \end{pmatrix} \tag{2.21}$$

The eigenstates are now defined by eigenvalues:

$$E_\pm = \frac{(E_L + E_R) - i(\Gamma_L + \Gamma_R)}{2} \pm \sqrt{\frac{((E_L - E_R) + i(\Gamma_L - \Gamma_R))^2}{4} + T_{RL}^2} \in R \tag{2.22}$$

The eigenvectors $\Phi_\pm$:

$$\begin{aligned} \Phi_+ &= \begin{bmatrix} T_{LR} \\ \sqrt{\frac{((E_L-E_R)+i(\Gamma_L-\Gamma_R))^2}{4} + T_{RL}^2} - \frac{(E_L-E_R)+i(\Gamma_L-\Gamma_R)}{2} \end{bmatrix} \\ \Phi_- &= \begin{bmatrix} T_{RL} \\ -\sqrt{\frac{((E_L-E_R)+i(\Gamma_L-\Gamma_R))^2}{4} + T_{RL}^2} - \frac{(E_L-E_R)+i(\Gamma_L-\Gamma_R)}{2} \end{bmatrix} \end{aligned} \tag{2.23}$$

And the scalar product between $\Phi_\pm$ is no longer zero

$$\langle \Phi_+ | \Phi_- \rangle \neq 0 \tag{2.24}$$

Similar to the example of the Melde's string developed in sections 2.1.1 and 2.1.2, the introduction of losses makes the eigenvalues complex and the spatial distribution non-orthogonal. The complex eigenvalues and the spatial non-orthogonality of modes remain valid if openness is responsible for the losses instead of absorption.

Non-hermitian degeneracy: Exceptional Point

In non-hermitian systems, varying different parameters can also bring to a degeneracy of energies $E_\pm = E$. However, unlike hermitian case, in non-hermitian systems the eigenvectors are *a priori* non-orthogonal. Hence, within the parameter space, both the eigenvalues and the eigenvectors of the Hamiltonian can become identical at a specific position. For instance, in the eigenstates derived in eq. (2.22) and (2.23)

$$\frac{((E_L - E_R) + i(\Gamma_L - \Gamma_R))^2}{4} + T_{RL}^2 = 0 \Rightarrow E_+ = E_- \quad \& \quad \Phi_+ = \Phi_- \tag{2.25}$$

Introduced by Kato in 1966 [31], this "non-hermitian degeneracy" is called an **Exceptional Point**. At Exceptional Point, rather than leading to a simple degeneracy, the two

eigenstates coalesce and become indistinguishable. For complex non-hermitian Hamiltonian, only 2 independent parameters are required to reach this non-hermitian degeneracy. Eq. (2.25) is fulfilled by imposing both the real and the imaginary parts of T_{RL}: The problem is of co-dimension 2.

From a mathematical point of view, at Exceptional Point, the space formed by eigenstates is incomplete. At this specific position, both eigenstates merge to form a Jordan's Matrix:

$$H_{@EP} \sim \begin{bmatrix} E & 1 \\ 0 & E \end{bmatrix} \tag{2.26}$$

The paradox of this matrix is to be diagonalizable and thus to be equivalent to the identity

$$H_{@EP} \sim E \begin{bmatrix} 1 & 0 \\ 0 & 1 \end{bmatrix} \tag{2.27}$$

Because no matrix is equivalent to the identity (except the identity itself), the Jordan's matrix cannot be diagonalizable. Hence, the 2 dimensional space described by the matrix is incomplete and equivalent to a single point. For that reason, an Exceptional Point can be understood like a topological default. To emphasize this statement, we plot the real and imaginary parts of eigenvalues $E_\pm$ in Fig. 2.7**(a)** and **(b)**. In the vicinity of an Exceptional Point, the eigenvalues (or complex frequencies) exhibit an intricate topology. The real and imaginary parts of the eigenvalues define intersecting Riemann's sheets. Thus Exceptional Point is of a totally different nature from Diabolic Point.

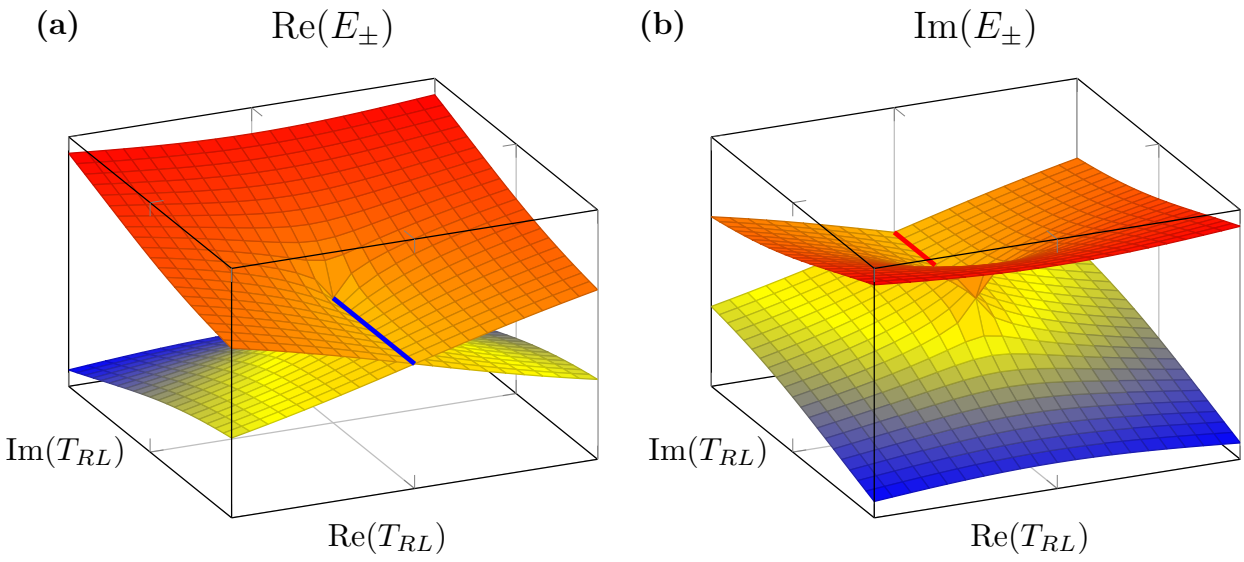

Figure 2.7: Riemann's sheets described by eigenvalues $E_\pm$ in the vicinity of the Exceptional Point in the parameter space $(\mathrm{Re}(T_{RL}), \mathrm{Im}(T_{RL}))$: **(a)** Real parts of $E_\pm$ are identical along a blue stripe. **(b)** Imaginary parts are similar along the red stripe. At Exceptional Point, both complex eigenvalues are identical and eigenvectors are collinear.

We stressed in section 2.1.3 that Diabolic Point could be observed in non-hermitian problems, but for a co-dimension 4 at least. Hence, we explained that in co-dimension 2 it stands for a signature of hermitian problems. Here the situation is unambiguous: Exceptional Point cannot be observed in hermitian systems. The Exceptional Point is the

fingerprint of non-hermitian systems. The non-trivial evolution of eigenvalues close to the Exceptional Point (see Fig. 2.7) also involves a geometrical phase when encircling the Exceptional Point in the parameter space [32, 33]. However, unlike the Diabolic Point, four round trips are needed to restore the eigenstates. Moreover, because both eigenvalues and eigenvectors coalesce, discerning one mode from the other becomes impossible, which leads to problem with mode labelling [34, 35, 36].

Exceptional Points have a certain robustness, which makes them rather easy to investigate than Diabolic Point. Remarkably enough, they appeared to be involved directly or indirectly in a several physical effects. For instance, they are related to level repulsion [37], mode hybridization [38], quantum phase transition [39] or even strong coupling [35]. In fact, Exceptional Point appears to be a convenient tool to give a new insight to many effects.

2.2 Modes in open system

In section 2.1.2, we have introduced the concept of modes in non-hermitian problems, where absorption was responsible for losses. In open systems, the derivation of the modes is different because the wave is not necessarily bounded and can propagate outside the system. This propagation inducing striking difficulties, different approaches have been proposed to overcome them. In this section we derive the modes of an open cavity using the Siegert's approach, also known as quasi-bound states, quasi-normal modes or Siegert states. Then, we emphasize the limitation of the Siegert's description of resonances. Finally, we introduce the biorthogonal formalism required to develop linear algebra with Siegert states.

2.2.1 Deriving modes in open media

The Siegert states

In many physical applications, the electrical field, like many other waves, cannot be confined spatially and propagates outside the system. In this kind of problem, the non-conservation of the energy is due to system openness. Therefore, the standard approaches for the introduction of modes and quantization based on eigenvectors of Hermitian operators are not applicable in this situation [40]. To overcome this difficulty, different approaches have been proposed: The Fox-Li modes [41], the Siegert states [42], the modes of the universe, the natural modes [43] or more recently the Constant Flux modes [44]. All those sets of modes have benefits and drawbacks and their use is often case-dependent. In the study of highly open systems, the modes are commonly derived thanks to the Siegert states or the Constant Flux modes. In the present work, we choose the Siegert states approach[1].

In his seminal paper [42], Siegert investigated the resonances in atomic and molecular systems and proposed to describe the resonances in a way similar to field quantization in

[1]For Constant Flux modes, the outside propagation is characterised by a real frequency ω and a constant flux of energy. Unfortunately the frequency of oscillation ω is driven by a numerical parameter. The introduction of this parameter highly complicates the formalism we aim at developing here.

quantum optics. To derive them, he solved the Schrödinger's equation with a boundary condition at infinity containing only outgoing waves and no incoming incident waves. This outgoing condition is referred today as the Siegert's condition or Gamov-Siegert's condition [22]. Noting $(\Omega_p, \Phi_p(r))$ the mode corresponding to this resonance, $k_p = \Omega_p/c$ the wave vector and r the spatial coordinate, the Siegert's condition reads

$$\Phi(r \to \infty) \propto e^{ik_p r} \quad \Leftrightarrow \quad \frac{\partial \Phi}{\partial r}(r \to \infty) = ik_p \Phi(r \to \infty) \tag{2.28}$$

Modes of a 1D slab

As a guideline example, we consider the case of a 1D slab of index n and length L. A perfect mirror is placed at its left edge $x = 0$ whereas its right edge $x = L$ is open in vacuum (see Fig. 2.8**(a)**). For such dielectric problem in dimension 1 or 2, the electrical field $E(r,t)$ fulfils Helmholtz equation:

$$\Delta E(r,t) - n(r)^2 \frac{\partial^2 E}{\partial t^2}(r,t) = 0 \tag{2.29}$$

where r stands for spatial coordinates, $n(r)$ the refractive index distribution and the speed of light of vacuum is fixed to 1 for sake of notation compactness. Eq. (2.29) reads in the frequency domain

$$\Delta E(r,\omega) + n(r)^2 k^2 E(r,\omega) = 0 \tag{2.30}$$

where the dispersion relation imposes $\Omega = kc = k$. Hence, in this one dimension problem, each mode $(\Omega_p, \Phi_p(x))$ fulfils:

$$\frac{d^2 \Phi_p}{dx^2}(x) + n(x)^2 \Omega_p^2 \Phi_p(x) = 0 \tag{2.31}$$

With the boundary conditions enforced by the mirror and the Siegert's condition for each mode

$$\Phi_p(0) = 0 \quad \& \quad \left(\frac{d}{dx} - i\Omega_p \right) \Phi_p \Big|_{x \to \infty} = 0 \tag{2.32}$$

Eq. (2.31) gives the motion of modes inside the cavity $\Phi_{p,in}$:

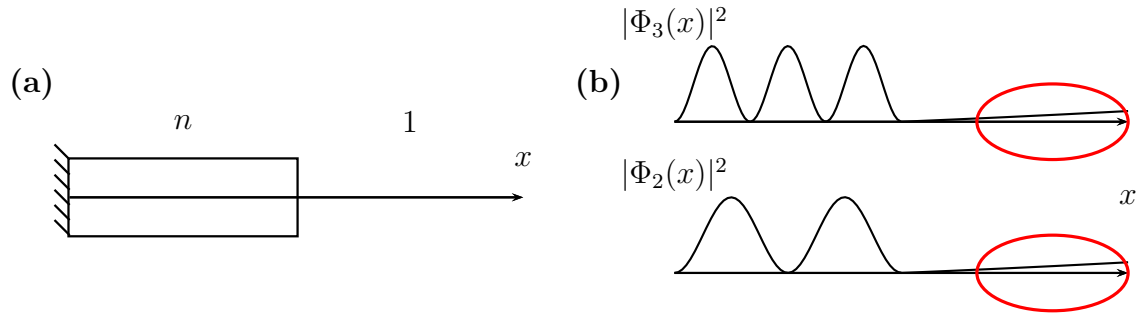

Figure 2.8: **(a)** 1D slab open medium of length L with a uniform index of refraction n. **(b)** Intensity of different modes derived with the Siegert's approch. The red ellipses point out the divergence of intensity outside the medium.

$$\Phi_{p,in}(x) = A_{in} e^{in\Omega_p x} + B_{in} e^{-in\Omega_p x} \tag{2.33}$$

where A_{in} and B_{in} correspond respectively forward and backward propagation coefficients. From eq. (2.32), we can easily deduce that $B_{in} = -A_{in}$ and

$$\Phi_{p,in}(x) = 2iA_{in}\sin(n\Omega_p x) \tag{2.34}$$

In this particular case, the outgoing condition is fulfilled as soon as the mode escapes from the cavity *i.e.* when $x \geq L$. Hence, the mode outside the cavity $\Phi_{p,out}$ reads

$$\Phi_{p,out}(x) = A_{out}e^{i\Omega_p x} \tag{2.35}$$

To link inside and outside expressions, we use the energy continuity:

$$\Phi_{p,in}(L) = \Phi_{p,out}(L) \quad \& \quad \frac{d\Phi_{p,in}}{dx}(L) = \frac{d\Phi_{p,out}}{dx}(L) \tag{2.36}$$

Using expressions of mode inside and outside (eq. (2.34) and (2.35)):

$$2iA_{in}\sin(n\Omega_p L) = A_{out}e^{i\Omega_p L} \quad \& \quad 2in\Omega_p A_{in}\cos(n\Omega_p L) = i\Omega_p A_{out}e^{i\Omega_p L} \tag{2.37}$$

leading to

$$\tan(n\Omega_p L) = -in \Leftrightarrow -e^{i2\Omega_p L} = \frac{n+1}{n-1} \tag{2.38}$$

Hence, we find an infinite set of mode frequencies referred to as Ω_p:

$$\Omega_p = \frac{(2p+1)\pi}{2nL} - i\frac{1}{2nL}\ln\left(\frac{n+1}{n-1}\right) \quad \forall p \tag{2.39}$$

and the corresponding spatial distributions $\Phi_p(x)$:

$$\begin{array}{lll} \Phi_{p,in} & \propto & e^{i\frac{(2p+1)\pi x}{2L}}e^{\frac{x}{2L}ln(\frac{n+1}{n-1})} - e^{-i\frac{(2p+1)\pi x}{2L}}e^{-\frac{x}{2L}ln(\frac{n+1}{n-1})} \\ \Phi_{p,out} & \propto & e^{i\frac{(2p+1)\pi x}{2nL}}e^{\frac{x}{2nL}ln(\frac{n+1}{n-1})} \end{array} \tag{2.40}$$

The Siegert's approach solve the eigenvalue problem defined by eq. (2.29) using a specific boundary condition. The complex frequency $\Omega_p = k_p c$ and related spatial distribution $\Phi_p(x)$ are derived for each mode.

2.2.2 Limits of Siegert's modes

Infinite spatial energy

Carrying on the example of the 1D slab, we plot the spatial evolution of the modes inside and outside the cavity in Fig. 2.8**(b)**. Unlike hermitian modes, the non-hermitian modes have a complex frequency as shown in eq. (2.39). The imaginary part of the complex frequency, standing for the linewidth of the resonance, has to be negative to ensure temporal decay of the field intensity. The spatial amplitude of the modes is bounded inside the slab (see Fig. 2.8**(b)**). However, because of negative imaginary part of the complex frequency, the amplitude of all modes exponentially diverges outside the system (see Fig. 2.8**(b)**). Physically, this exponential divergence corresponds to a wavefront excited at past times and propagating away from the system. The infinite energy can be understood as the accumulation of the energy radiated from the open system to the rest of the universe. This point stresses that space and time cannot be separately considered like in hermitian stationary cases: The spatial divergence is compensated by a temporal "damping". This spatial divergence of Siegert's modes stands for the main limitation of Siegert states and requires specific mathematical investigations.

Inner product

One of the major limitation of a diverging spatial energy is the impossibility of using the conventional inner product

$$\langle u|v\rangle = \int u^*(x)v(x)dx \tag{2.41}$$

Because of this divergence, the integral of eq. (2.41) between two modes requires a special investigation: The modes are not square integrable. To overcome that difficulty, several solutions have been proposed. A possible solution consists in correcting the spatial distribution of the modes, by imposing for instance the outgoing condition at a well-defined finite distance [45, 46], or considering separately the mode behaviour inside and outside the cavity [43]. Another approach relies on carrying out a suitable mathematical transform (as initially suggested by Zeldovich [47]). Zeldovich's idea consisted in compensating for the divergence by defining a regularized inner product. He historically proposed the function $F(x) = e^{-\epsilon x^2}$ to define a new inner product:

$$\langle u|v\rangle \rightarrow \langle u|F|v\rangle = \int u^*(x)F(x)v(x)dx \tag{2.42}$$

The negative exponent in x^2 overcomes the divergence of the modes at infinity. To avoid any loss of physical information, Zeldovich proposed to take the limit case where $\epsilon \rightarrow 0$. Many other transforms have been proposed, which recast the space coordinates and perform what is called complex scaling (see [48] for a complete description). The basic idea of these transforms is to use complex coordinates to compensate for the exponential divergence of the mode and make the inner product integrable. In the rest of this manuscript, we will assume that the inner products are regularized using Zeldovich's approach

$$\langle u|v\rangle \Leftrightarrow lim_{\epsilon\rightarrow 0} \int u^*(x)e^{-\epsilon x^2}v(x)dx \tag{2.43}$$

Completeness of modal expansion

In some cases, the divergence of the mode also implies the non-completeness of the Siegert states basis. When the modal expansion requires an infinite set of modes, its coefficients may not be unique. In such cases, the set of modes must be completed to allow a correct modal description [49]. The study of completeness of the modes in open systems is still an active field of research for both mathematicians and physicists and turns out to be case dependent. In particular, Leung *et al.* [50, 51, 52, 53] demonstrated that the completeness of the modal expansion in dielectric open systems is ensured if

- the index distribution has a discontinuity (L in the present case), which provides a natural demarcation of the system
- the index is constant ($n = 1$) outside the system ($x > L$), so that outgoing waves are not scattered back into the system

In the example of the 1D slab experiment, these conditions (known as the discontinuity and no tail conditions, respectively) are fulfilled and the modal expansion can be performed. In this document, all the systems under study will respect these two conditions and allow a complete modal expansion of the field.

2.2.3 Biorthogonal formalism

Introduction to the biorthogonal formalism

In non-hermitian problems, the modes Φ_p are not orthogonal

$$\langle \Phi_p | \Phi_q \rangle \neq \delta_{pq} \tag{2.44}$$

However, a projection operator is needed to develop linear algebra with non-hermitian modes. In non-hermitian problems it is possible to introduce a different product known as the biorthogonal product [54, 55]. The biorthogonal product relies on a very simple idea: The orthogonality of left and right eigenvectors of a linear operator.

If we consider a non-hermitian matrix A, with eigenstates $(\lambda_i, |X_i\rangle)$:

$$\forall i \quad A|X_i\rangle = \lambda_i |X_i\rangle \tag{2.45}$$

Eigenvectors $|X_i\rangle$ are referred to "right eigenvectors". Corresponding "left eigenvectors" $\langle Y_i|$ are associated with similar eigenvalues and fulfil:

$$\forall i \quad \langle Y_i | A = \lambda_i \langle Y_i | \tag{2.46}$$

Now we can write

$$\langle Y_i | A | X_j \rangle = \lambda_i \langle Y_i | X_j \rangle = \lambda_j \langle Y_i | X_j \rangle \tag{2.47}$$

Hence, in the case of non degenerated eigenstates

$$\langle Y_i | X_j \rangle = \delta_{ij} \tag{2.48}$$

And if A is symmetric (but non-hermitian), eq. (2.48) becomes

$$\langle X_i^* | X_j \rangle = \delta_{ij} \tag{2.49}$$

This biorthogonal product can replace the conventional inner product of hermitian physics, assuming that no modes are degenerated. In particular, assuming the completeness of the eigenstates, a closure relation can be defined

$$\sum_p |X_q\rangle \langle X_q^*| = I \tag{2.50}$$

where I stands for matrix identity. Any vector Φ can be written down as a unique superposition of the eigenvectors

$$\Phi = \sum_p \frac{\langle X_p^* | \Phi \rangle}{\langle X_p^* | X_p \rangle} |X_p\rangle \tag{2.51}$$

A complete mathematical formalism is derived from the biorthogonal product. This product leads to the definition of linear algebra tools for non-hermitian modes.

The biorthogonal product in a 1D slab

We carry on the example of the 1D slab developed in section 2.2.1. In this problem, the field fulfils the Helmholtz eq. (2.29) and each mode $(\Omega_p, \Phi_p(x))$ reads

$$\frac{d^2\Phi_p}{dx^2}(x) + n(x)^2\Omega_p^2\Phi_p(x) = 0 \tag{2.52}$$

The weak formulation[2] of eq. (2.52) along another spatial distribution Φ_q $(p \neq q)$ reads

$$\int_0^L \frac{d^2\Phi_p}{dx^2}(x)\Phi_q(x)dx + \int_0^L n(x)^2\Omega_p^2\Phi_p(x)\Phi_q(x)dx = 0 \tag{2.53}$$

Using an integration by parts

$$-\left[\frac{d\Phi_p}{dx}(x)\Phi_q(x)\right]_0^L + \int_0^L \frac{d\Phi_p}{dx}(x)\frac{d\Phi_q}{dx}(x)dx = \Omega_p^2\int_0^L n(x)^2\Phi_p(x)\Phi_q(x)dx \tag{2.54}$$

Using a second integration by parts

$$-\frac{d\Phi_p}{dx}(L)\Phi_q(L) + \left[\Phi_p(x)\frac{d\Phi_q}{dx}(x)\right]_0^L - \int_0^L \Phi_p(x)\frac{d^2\Phi_q}{dx^2}(x)dx = \Omega_p^2\int_0^L n(x)^2\Phi_p(x)\Phi_q(x)dx \tag{2.55}$$

Using eq. (2.52) for mode $(\Omega_q, \Phi_q(x))$, eq. (2.55) reads

$$\Phi_p(L)\frac{d\Phi_q}{dx}(L) - \frac{d\Phi_p}{dx}(L)\Phi_q(L) = (\Omega_p^2 - \Omega_q^2)\int_0^L n(x)^2\Phi_p(x)\Phi_q(x)dx \tag{2.56}$$

Using the Siegert's condition $\frac{d\Phi_{q,q}}{dx}(L) = i\Omega_{p,q}\Phi_{p,q}(L)$, eq. (2.56) reads

$$-i(\Omega_p + \Omega_q)\int_0^L n(x)^2\Phi_p(x)\Phi_q(x)dx + \Phi_p(L)\Phi_q(L) = 0 \tag{2.57}$$

Now, we apply to modes $(\Omega_q, \Phi_q(x))$ and $(\Omega_p, \Phi_p(x))$ the biorthogonal product, with the Zeldovich's regularization introduced in section 2.2.2

$$\langle\Phi_q^*|\Phi_p\rangle = lim_{\epsilon\to 0}\int_0^{+\infty} n(x)^2 e^{-\epsilon x^2}\Phi_p(x)\Phi_q(x)dx \tag{2.58}$$

Eq. (2.57) can be split into an inside and an outside integral terms

$$\langle\Phi_q^*|\Phi_p\rangle = \int_0^L n(x)^2\Phi_p(x)\Phi_q(x)dx + lim_{\epsilon\to 0}\int_L^{+\infty} e^{-\epsilon x^2}\Phi_p(x)\Phi_q(x)dx \tag{2.59}$$

Outside the system $(x \leq L)$, we know that modes read $\Phi_p(x) \propto e^{i\Omega_p x}$. Using an integration by part, the outside integral term reads

$$lim_{\epsilon\to 0}\int_L^{+\infty} e^{-\epsilon x^2}\Phi_p(x)\Phi_q(x)dx \propto lim_{\epsilon\to 0}\int_L^{+\infty} e^{-\epsilon x^2}e^{i(\Omega_p+\Omega_q)x}dx$$

$$= lim_{\epsilon\to 0}\left[\frac{e^{-\epsilon x^2}e^{i(\Omega_p+\Omega_q)x}}{i(\Omega_p+\Omega_q)}\right]_L^{+\infty} + \epsilon\int_L^{+\infty} 2x\frac{e^{-\epsilon x^2}e^{i(\Omega_p+\Omega_q)x}}{i(\Omega_p+\Omega_q)}dx = -\frac{e^{i(\Omega_p+\Omega_q)L}}{i(\Omega_p+\Omega_q)} \tag{2.60}$$

[2]For a function $f(x) = 0$, whatever the function g included in a Banach space, we can write $\int f(x)g(x)dx = 0$.

Leading to

$$\langle \Phi_q^* | \Phi_p \rangle = \int_0^L n(x)^2 \Phi_p(x) \Phi_q(x) dx - \frac{\Phi_p(L)\Phi_q(L)}{i(\Omega_p + \Omega_q)} \tag{2.61}$$

Using the relation derived in eq. (2.57), the modes $(\Omega_q, \Phi_q(x))$ and $(\Omega_p, \Phi_p(x))$ fulfil the biorthogonal relation:

$$\langle \Phi_q^* | \Phi_p \rangle = \delta_{pq} \tag{2.62}$$

Application of the biorthogonal formalism

We demonstrated in section 2.2.3 the existence of a biorthogonal relation between modes derived from the Siegert's condition in a 1D uniform slab. This biorthogonal relation can be easily generalized to non-uniform refractive index distribution and 2D problems. The general definition of the biorthogonal product reads

$$\langle \Phi_p^* | \Phi_q \rangle = \int n(r)^2 \Phi_p \Phi_q = \delta_{pq} \tag{2.63}$$

Hence, for 1D and 2D systems fulfilling the no-tail and discontinuity condition ensuring the completeness of the modal expansion (see section 2.2.2), the biorthogonal formalism developed in section 2.2.3 can be applied. The closure relation can be defined between modes and reads

$$\sum_p |\Phi_q\rangle\langle\Phi_q^*| = I \tag{2.64}$$

Any spatial distribution $\Phi(x)$ reads

$$\Phi(x) = \sum_p \frac{\langle \Phi_p^* | \Phi \rangle}{\langle \Phi_p^* | \Phi_p \rangle} |\Phi_p\rangle = \sum_p \frac{\int n(r)^2 \Phi_p(x) \Phi(x) dx}{\int n(r)^2 \Phi_p^2(x) dx} \Phi_p(x) \tag{2.65}$$

The modal expansion of the electric field

$$E(x,t) = \sum_p a_p \Phi_p(x) e^{-i\Omega_p t} \tag{2.66}$$

is complete and coefficients a_p are unique. In the rest of the document, we will consider open systems where the biorthogonal formalism can be applied.

2.3 Anderson-localized modes

We shown in section 2.2.1 how modes can be derived in any open system using the Siegert's condition. In this section, we consider an open system with a disordered refractive index distribution, where the random scattering may lead to the spatial confinement of light. First, we briefly review the history of this physical effect known as Anderson localization. Then, using a 1D example, we show that modes can be extended or spatially localized, depending on the strength of the disorder. Finally, we summarize the different numerical methods that we have developed to compute these modes in disordered media.

2.3.1 A brief introduction to Anderson localization

In his seminal paper [56], Anderson was inspired by experiments performed by George Feher [57], where anomalous relaxation times of electron were observed in semiconductors. Using a quantum tight binding model of a lattice with a random potential in each site, he demonstrated that diffusion of electrons can go to a zero when disorder becomes important enough. In particular, this model has been used to explain why a metal can turn into an insulator when the density of impurities increases. In the eighties, the gap was bridged between quantum and classical waves. After an early prediction of existence of localized waves in classical systems [58], Anderson localization was demonstrated for classical waves in several experiments [59, 60, 61]. It is now recognized that Anderson localization originates from the interference between multiple scattering paths and plays also an essential role in classical wave physics.

A naive picture of localization mechanism is proposed in Fig. 2.9**(a)**. We consider an incoming wave propagating in a 1D random potential. The wave is scattered each time it encounters a step in the random potential (see explanation in Chapter 1). The wave is spilt into a transmitted (forward-scattering) and a reflected wave (backscattering). The amplitude of the backscattering is triggered by the height of the step in the random potential. The backscattered wave interferes with the incoming wave. If the wave encounters many steps of various amplitudes, the backscattering leads to a localization of the wave by constructive interference (see Fig. 2.9**(a)**). This spatial localization, known as Anderson localization, differs from trapping where light is confined because of presence of walls (see Fig. 2.9**(b)**). Localization is rather understood as the result of many reflections of moderate amplitude.

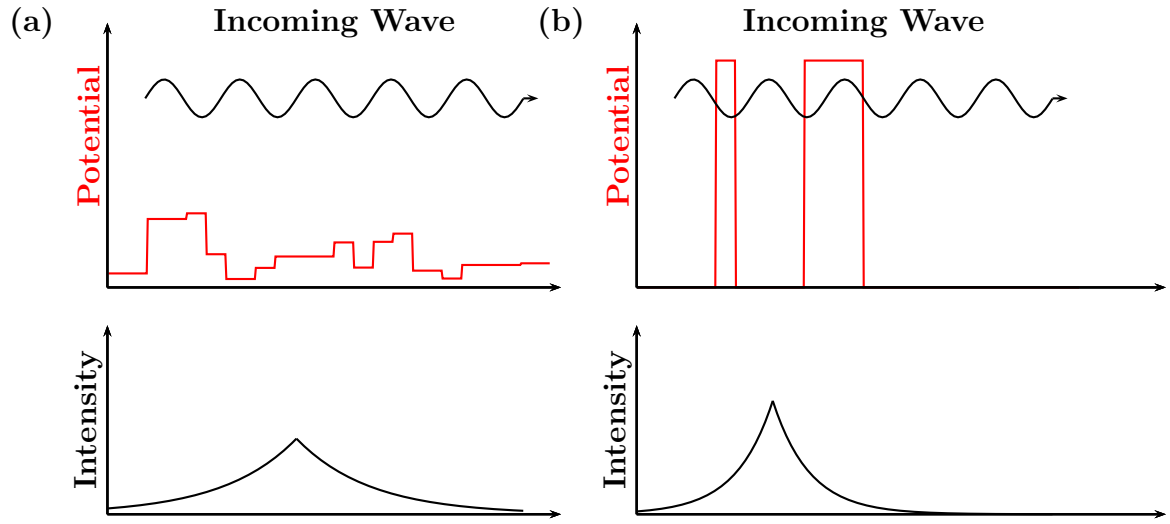

Figure 2.9: **(a)** An incoming wave propagates through a random potential: Each step in the potential scatters the incoming wave. The backscattering interferes with the incoming wave and the resulting field spatially localizes into the system. **(b)** Incoming wave trapped within a well: The wave is localized because of the presence of high potentials.

Anderson localization has been observed in different areas of classical waves physics (acoustics [62]) or quantum wave physics (e.g. Wave matter [63]). For optical waves, if localization has been observed for 1D and 2D systems, the 3D localization of light is

still an open issue [64]. In this manuscript we will restrict ourself to optical systems of dimension 1 or 2.

2.3.2 Modes in localized/weakly scattering regimes

As stated in section 2.3.1, the Anderson localization is triggered by the disorder. To emphasize this influence, we introduce disorder into an uniform 1D system and progressively increase its "strength". In this 1D example, we differentiate between two different kinds of modes resulting from Anderson localization.

A uniform 1D problem

We consider a 1D uniform medium of index of refraction n and length L open at both edges (see Fig. 2.10**(a)**). In this problem, the field's evolution is driven by the uniform Helmholtz equation

$$\frac{d^2E}{dx^2}(x,\omega) + n^2\Omega^2 E(x,\omega) = 0 \tag{2.67}$$

Using the Siegert's approach (see section 2.2.1), we can derive the amplitude of the mode

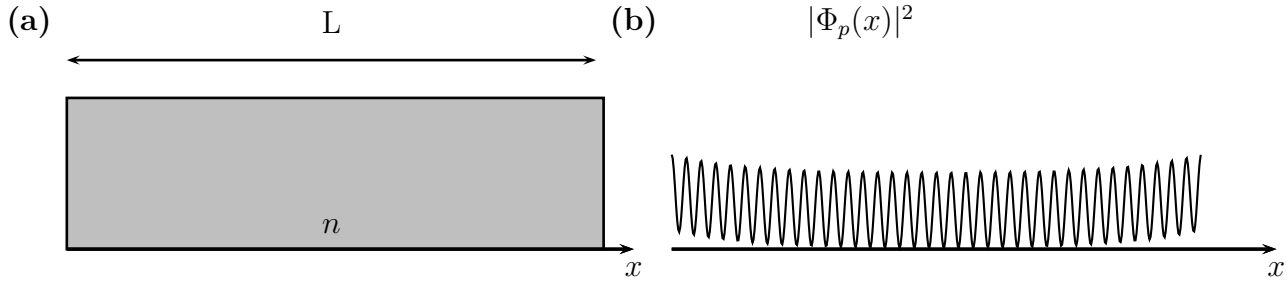

Figure 2.10: **(a)** A uniform 1D slab of length L and with an index of refraction n. **(b)** The spatial distribution intensity of one mode $|\Phi_p(x)|^2$ inside the system: The mode has been derived using the Siegert's approach.

inside this cavity. The frequency of mode p reads

$$\Omega_p = p\frac{\pi}{nL} - \frac{i}{nL} ln\left(\frac{n+1}{n-1}\right) \tag{2.68}$$

And the corresponding spatial distribution

$$|\Phi_{p,in}(x)|^2 \propto \left(\frac{n-1}{n}\right)^2 exp\left(\frac{2x}{L} ln\left(\frac{n+1}{n-1}\right)\right) + \left(\frac{n+1}{n}\right)^2 exp\left(-\frac{2x}{L} ln\left(\frac{n+1}{n-1}\right)\right) + 2\left(\frac{n^2-1}{n^2}\right)\cos\left(p\pi\frac{x}{L}\right) \tag{2.69}$$

As shown in Fig. 2.10**(b)**, the modes are extended all over the system.

Introduction of disorder

To introduce disorder in the 1D slab, we randomly introduce slices of a different material (see Fig. 2.11**(a)**). The system is now composed of slabs of refractive index n and $n+\Delta n$. The index of refraction becomes random and given by $n^2(x) = \bar{n}^2 + \Delta n^2 p(x)$, where Δn is the index difference, $p(x)$ the location of the new material and $\bar{n}$ the average refractive index. The evolution of the field is now driven by the non-uniform Helmholtz equation

$$\frac{d^2E}{dx^2}(x,\omega) + (\bar{n}^2 + \Delta n^2 p(x))\Omega^2 E(x,\omega) = 0 \tag{2.70}$$

To understand the influence of the disorder, we can write eq. (2.70) in a form similar to the Schrödinger equation

$$-\frac{d^2E}{dx^2}(x,\omega) - \Delta n^2 p(x)\Omega^2 E(x,\omega) = \bar{n}^2\Omega^2 E(x,\omega) \tag{2.71}$$

It turns out that the disorder term $\Delta n^2 p(x)\Omega^2$ plays a role similar to the interaction potential in the Schrödinger equation. Like a well, this "random potential" scatterers the wave. Remarkably, the "strength" of this "random potential" is triggered by the variance of $\Delta n^2 p(x)$ [65]. Hence, the random scattering strength will be important for high index contrast and strong fluctuations of the position $p(x)$.

Extended and localized modes

As an illustration, we consider a given realization of disorder of 39 slabs of index of refraction n and 39 slabs of index $n + \Delta n$. The mean thickness of the slabs is 150 nm, and the thickness of each slab follows a uniform distribution of amplitude 50 nm (see Fig. 2.11**(a)** for a schematic description). As explained by eq. (2.71), the strength of the randomness is triggered by the index contrast between the two media. The modes resulting from this non-uniform distribution of refractive index are numerically computed using the Transfer Matrix approach (introduced in section 2.3.3). This numerical method rigorously derives the modes fulfilling the Siegert's condition. In Fig. 2.11, we compute a particular mode Φ_n for a low and a high index contrast (respectively $\Delta n = 0.1$ and 1.0).

In Fig. 2.11**(b)**, the disorder is weak and the modes are extended over the system. Nevertheless, the spatial distribution is already strongly modified as compared to the case of a system with a uniform index (see Fig. 2.10**(b)**). In Fig. 2.11**(c)**, the disorder is strong and the mode is confined within the system. The envelope of the mode is exponentially confined around a central position

$$|\Phi_n|^2 \propto exp\left(-\frac{|x|}{\xi}\right) \tag{2.72}$$

where ξ defines the localization length. The modes plotted in Fig. 2.11**(b)** and 2.11**(c)**, represent the two different regimes of disordered modes. For low disorder, the system is in the weakly localized regime: The mode is extended over the medium but the disorder influences its spatial distribution. For high disorder, the system is in the strongly scattering regime: The mode is trapped/localized by disorder inside the medium. In 1D and 2D, a mode will be localized if the size of the system is smaller than the localization length of the mode (here $\xi < L$). In 3D, a mobility edge is predicted. Nevertheless, if its existence for scalar waves was confirmed, in polarized waves however, its observation is still an open issue [64].

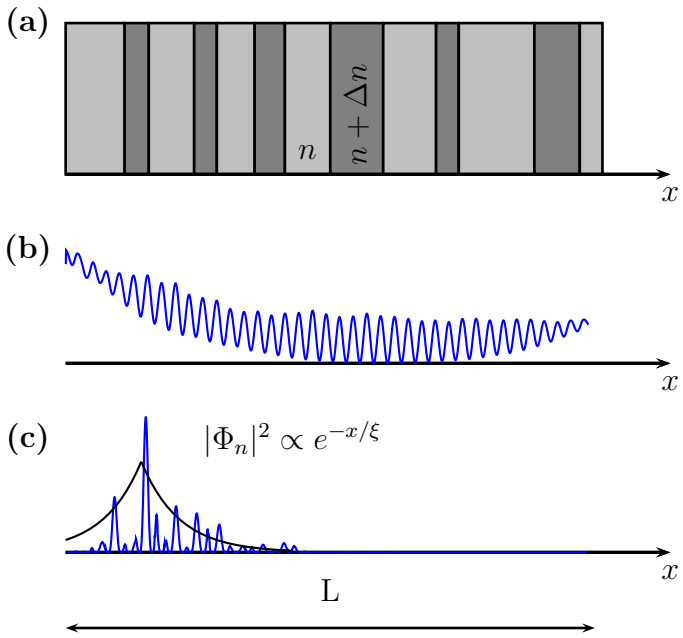

Figure 2.11: **(a)** Schematic description of the 1D random system: Superposition of slabs of indexes n and $n + \Delta n$. **(b)** Spatial mode distribution in the weakly scattering regime ($\Delta n = 0.1$): The mode is extended all over the device but differs from the uniform case. **(c)** Mode in the strong scattering regime ($\Delta n = 1.0$): The mode is spatially localized inside the system.

2.3.3 Numerical computation of modes

In disordered systems, the derivation of modes cannot be analytic but requires numerical computations. In this subsection, we briefly summarize the different numerical methods that we developed.

The Transfer Matrix approach

The Transfer Matrix approach has been widely used to study Anderson localization problems in 1D systems [66]. This technique solves Helmholtz equation in the frequency domain in 1D system with the Siegert's condition. Within numerical accuracy, the Transfer Matrix provides the exact Siegert states (Φ_p, Ω_p) fulfilling

$$\frac{d^2\Phi_p}{dx^2}(x) + n(x)^2\Omega_p^2\Phi_p(x) = 0 \quad \& \quad \left(\frac{d}{dx} - i\Omega_p\right)\Phi_p\Big|_{r\to\infty} = 0 \tag{2.73}$$

The modes shown in Fig. 2.11**(b)** and **(c)** were computed with this method.

The principle of the method can be exposed using, for instance, a system made of two materials (as in Fig. 2.11**(a)**). In a 1D system, the field can be expanded into a forward P and a backward Q part:

$$E(x,\omega) = \begin{bmatrix} P(x,\omega) \\ Q(x,\omega) \end{bmatrix} \tag{2.74}$$

When propagating through the system the field can:

- Propagate through medium of index n
- Cross the interface from n to $n + \Delta n$
- Propagate through medium of index $n + \Delta n$
- Cross the interface from $n + \Delta n$ to n

Combining these four operations, we can derive a matrix M connecting the electric field on the left edge $E(0, \omega)$ and the right edge $E(L, \omega)$:

$$\begin{bmatrix} P(L,\omega) \\ Q(L,\omega) \end{bmatrix} = M(\omega) \begin{bmatrix} P(0,\omega) \\ Q(0,\omega) \end{bmatrix} \tag{2.75}$$

This matrix represents the Helmholtz equation in the 1D system. The Siegert's condition enforces:

$$E(0,\omega) = \begin{bmatrix} P(0,\omega) \\ 0 \end{bmatrix} \quad \& \quad E(L,\omega) = \begin{bmatrix} 0 \\ Q(L,\omega) \end{bmatrix} \tag{2.76}$$

Imposing eq. (2.76) onto eq. (2.75) can only be satisfied for a discrete set of Ω_n. These Ω_n and the corresponding spatial distribution Φ_n define the modes of the problem fulfilling the Siegert's condition.

Finite Elements Method

A Finite Element Method can be used to solve Helmholtz's. In the scope on this study, a Finite Element Method code has been developed to solve Helmholtz equation in 2D

$$\Delta E(r) + n(r)^2 \Omega^2 E(r) = 0 \tag{2.77}$$

The 2D systems are composed of circular pillars in a host medium (see Fig. 2.12). The

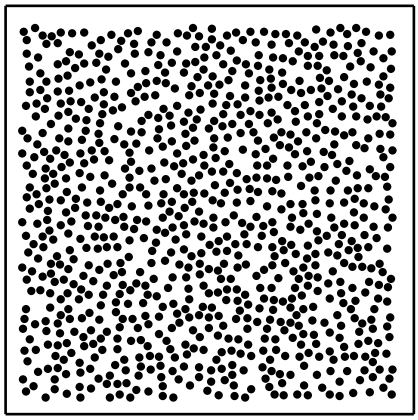

Figure 2.12: 2D random system composed of pillars randomly distributed. The system is surrounded by a numerical boundary condition.

physical system (see Fig. 2.12) is enclosed by numerical boundary conditions (Absorbing Boundary Conditions or Perfectly Matched Layer [67]) to ensure the decay of electric

field outside the system. The system is spatially discretized and test functions are used to build a matrix from eq. (2.77)

$$A + \Omega^2 B = 0 \tag{2.78}$$

Then, a generalized eigenvalue solver is used to find the eigensolutions (Ω^2, Φ) of eq. (2.78) corresponding to the modes of the 2D open system (see Fig. 2.13 as example). Unlike the

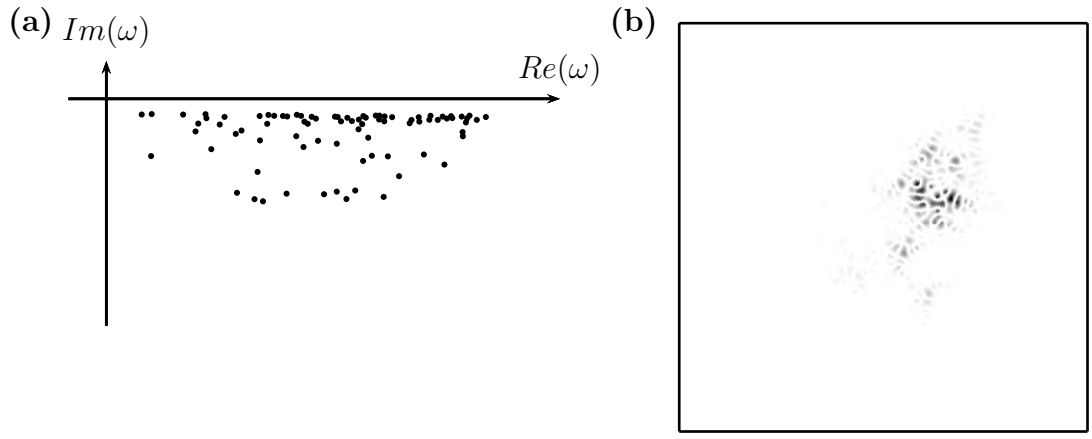

Figure 2.13: **(a)** Complex frequency Ω_p of modes computed by Finite Element Method on system described in Fig. 2.12. **(b)** A spatial distribution of the intensity of a mode $|\Phi_p|^2$ computed by Finite Element Method.

Transfer Matrix method, a numerical boundary condition is imposed outside the medium instead of the Siegert's condition. Hence, the modes computed with the Finite Element Method correspond to an approximation of the modes fulfilling the Siegert's condition. The Siegert states and the modes will be similar inside the system but will differ outside.

Finite Difference Time Domain

In this manuscript, we will also present computation of 2D systems (see Fig. 2.12) in the temporal domain. For that matter, we use a Finite Difference Time Domain technique allowing the resolution of Maxwell's equation

$$\begin{aligned} \nabla \times E(r,t) &= -\mu_0 \tfrac{\partial H}{\partial t}(r,t) \\ \nabla \times H(r,t) &= \epsilon_0 n(r)^2 \tfrac{\partial E}{\partial t}(r,t) \end{aligned} \tag{2.79}$$

Using the intricate spatial and temporal sampling, the evolution of electric and magnetic field (namely E and H) can be computed in time and space. The spatial distribution of the modes and their complex frequency can be obtained from $E(r,t)$. A complete description of the method can be find in [68].

2.4 Summary

Here, we have introduced the concept of mode and developed this notion for non energy-conservative systems, also called non-hermitian systems.

Generally speaking, modes are associated with privileged vibrational states of the system. For hermitian problem, the modes correspond to the stationary solutions, where time and space are separable. In non-hermitian problems, no stationary solution exists and the modes are defined by resonances. In particular, we have introduced the modes of open systems and presented an approach to derive them, using the Siegert's radiative condition. The resulting modes are physically relevant inside the cavity and diverge in amplitude outside. Nevertheless, we have demonstrated the existence of a rigorous formalism to describe the electric field using these modes. In the scope of this manuscript, we will focus on open systems with constitutive disorder encoded in the index of refraction distribution. We have explained in such systems the mechanism of Anderson localization, in which the disordered leads to a spatial localization of the modes. For strong disorder, the system is in the localized regime and the modes are confined within the system, while for low disorder the system is in the weakly scattering regime and the modes are spatially extended. We have briefly presented different numerical methods used to compute them.

In the rest of this manuscript, we will investigate light-matter interaction in random systems. The electric field will be expressed in term of modes (Anderson-localized or extended) computed with numerical techniques and the biorthogonal formalism will be applied.

Part II

Managing light-matter interaction in passive random media

Chapter 3

Coalescence of Anderson-localized modes at exceptional point in random media

Table of Contents

Losses are inherent to most physical systems, either because of dissipation and/or as a result of openness. We explained in Chapter 2 that these systems are described mathematically by a non-hermitian Hamiltonian, where eigenvalues are complex and eigenstates form a nonorthogonal set. In such systems, interaction between pairs of eigenstates, when a set of external parameters is varied, is essentially driven by the existence of Exceptional Points (EP)(see Chapter 2). At an EP, complex eigenvalues degenerate and eigenstates coalesce. In its vicinity, eigenvalues display a singular topology. The eigenstates become indistinguishable [69] and encircling the EP in the parameter space leads to a residual geometrical phase [32, 33]. Since their introduction by Kato in 1966 [31], EPs have appeared to be involved in a rich variety of physical effects (e.g. level repulsion [37], mode hybridization [38], quantum phase transition [39], lasing mode switching [70], Parity Time (PT) symmetry breaking [71, 72] or even strong coupling [35]). They have been observed experimentally in different systems such as microwave billiards [34], chaotic optical microcavities [73] or two-level atoms in high-Q cavities [35]. We explained in Chapter 2 that open random media are a particular class of non-hermitian systems. Their modal confinement may be solely driven by the degree of scattering. For sufficiently strong scattering, the spatial extension of the modes becomes smaller than the system size, resulting in transport inhibition and Anderson localization [56]. Disordered-induced localized states or localized modes have raised much interest. They provide with natural optical cavities in random lasers [74, 75] and recently appeared to be good candidates for quantum electrodynamics cavity [76, 77], with the main advantage of being inherently disorder-robust. These modes can also be manipulated by a local change of the disorder and can coupled to form necklace states [78, 79, 80], which open channels in a nominally localized system [81, 82] and are foreseen as a key mechanism in the transition from localization to diffusion regime. PT symmetry has been studied in the context of disordered media and Anderson localization [83, 84, 85], but so far, EPs between localized modes have not been investigated.

In this chapter, coalescence at an EP between two Anderson-localized optical modes is demonstrated in a two dimensional dielectric random system. To bring the system in the vicinity of an EP, the dielectric permittivity is varied at two different locations in the random system. First, we propose a general theory to follow the spectral and spatial evolution of modes in 2D dielectric media. Then, this theory is applied in the specific case of Anderson-localized modes. We find excellent agreement between theoretical prediction and Finite Element Method (FEM) simulations. Finally, we demonstrate that such a theory requires to go beyond the standard two interacting states model and to consider N-mode interaction. This problem can be easily implemented in an actual experiment [86, 75]. We believe that the design of an EP between modes could pave the way to a control of Anderson localization properties and could offer a new insight to its understanding.

3.1 Manipulation of modes via the dielectric permittivity

In this section we propose a general theory, which describes the evolution of modes in an open system in which scattering is modified. This approach relies on the biorthogonal formalism introduced in Chapter 2 and applied to modes of 2D dielectric open systems. We stress that this approach is not limited to disordered media but can be used for any open inhomogeneous dielectric system. First, we define modes of a non-hermitian system and recall the condition of the use of the biorthogonal formalism. Finally, we consider a modification of the system and investigate the evolution of modes by deriving a linear system.

3.1.1 A 2D open dielectric medium

We first consider the general case of a finite-size dielectric medium in 2D space, with inhomogeneous dielectric constant distribution $\epsilon(r)$. In this chapter, for sake of notation compactness, we will consider the dielectric permittivity $\epsilon(r)$ rather than the index of refraction $n(r)$ ($\epsilon(r) = n^2(r)$). The distribution of $\epsilon(r)$ is indifferently ordered or disordered. In the frequency domain, the electromagnetic field follows the Helmholtz equation:

$$\Delta E(r,\omega) + \epsilon(r)\omega^2 E(r,\omega) = 0 \tag{3.1}$$

where $E(r,\omega)$ stands for the electrical field and the speed of light, c=1. Eigensolutions of eq. (3.1) define the modes or eigenstates of the problem:

$$(\Omega_i, |\Psi_i\rangle)_{i\in\mathbb{N}} \quad | \quad \Delta|\Psi_i\rangle + \epsilon(r)\Omega_i^2|\Psi_i\rangle = 0 \tag{3.2}$$

Because of its openness, the system has inherent losses and is therefore described by a non-hermitian Hamiltonian (see Chapter 2). For non-hermitian systems, modes are *a priori* non-orthogonal, complex and the completeness of the expansion along the eigenvectors is not ensured. Here, we will consider modes derived with the Siegert's approach in open systems with finite range potential, in which a discontinuity in the permittivity provides a natural demarcation of the problem. We know from Chapter 2 that the completeness of the modal expansion [51, 50, 50, 52] is ensured in such a system. Hence, the electrical field can be expanded along the modes:

$$E(r,\omega) = \sum_i a_i(\omega)|\Psi_i\rangle \tag{3.3}$$

where $a_i(\omega)$ stand for unique coefficients of the expansion along the basis. Moreover, the biorthogonal formalism can be used provided that the eigenstates are not degenerated. This formalism relies on a biorthogonal product between modes, which reads [87, 55]:

$$\langle\Psi_p^*|\epsilon(r)|\Psi_q\rangle = \delta_{pq} \tag{3.4}$$

Nevertheless, the theory derived here can be extended to different set of modes (e.g Constant Flux [44], Fox-Li modes [41]), assuming that the biorthogonal formalism can be used.

3.1.2 Modification of the permittivity

Now, we consider two locations R_1 and R_2, where the permittivity is varied

$$\tilde{\epsilon}(r) = \epsilon(r) + \Delta\epsilon_1(r)p_1(r) + \Delta\epsilon_2(r)p_2(r) \tag{3.5}$$

where $\{p_i(r \in R_i) = 1 | p_i(r \notin R_i) = 0\}_{i\in[1,2]}$ is the location and $\{\Delta\epsilon_i(r)\}_{i\in[1,2]}$ the shape of the variation of permittivity. Eq. (3.1) becomes:

$$\Delta E(r,\omega) + \omega^2 \left(\epsilon(r) + \Delta\epsilon_1(r)p_1(r) + \Delta\epsilon_2(r)p_2(r)\right) E(r,\omega) = 0 \tag{3.6}$$

The permittivity distribution $\tilde{\epsilon}(r)$ describes a new distribution of permittivity with new modes $(\tilde{\Omega}_i, |\tilde{\Psi}_i\rangle)_{i\in\mathbb{N}}$. Nevertheless, we can still consider the basis of the original random system, $(\Omega_i, |\Psi_i\rangle)_{i\in\mathbb{N}}$, to expand the electric field as follows:

$$E(r,\omega) = \sum_i b_i(\omega)|\Psi_i\rangle \tag{3.7}$$

where $b_i(\omega)$ are the new expansion coefficients. Inserting eq. (3.7) into eq. (3.6):

$$\sum_i b_i(\omega) \left[\Delta + \omega^2 \left(\epsilon(r) + \Delta\epsilon_1(r)p_1(r) + \Delta\epsilon_2(r)p_2(r)\right)\right] |\Psi_i\rangle = 0 \tag{3.8}$$

Using eq. (3.2)

$$\sum_i b_i(\omega) \left[-\Omega_i^2\epsilon(r) + \omega^2 \left(\epsilon(r) + \Delta\epsilon_1(r)p_1(r) + \Delta\epsilon_2(r)p_2(r)\right)\right] |\Psi_i\rangle = 0 \tag{3.9}$$

Projecting eq. (3.9) along $\langle\Psi_j^*|$

$$\langle\Psi_j^*| \sum_i b_i(\omega) \left[(\omega^2 - \Omega_i^2)\epsilon(r) + \omega^2 \left(\Delta\epsilon_1(r)p_1(r) + \Delta\epsilon_2(r)p_2(r)\right)\right] |\Psi_i\rangle = 0 \tag{3.10}$$

$$\sum_i b_i(\omega) \left[(\omega^2 - \Omega_i^2)\langle\Psi_j^*|\epsilon(r)|\Psi_i\rangle + \langle\Psi_j^*|\Delta\epsilon_1(r)p_1(r) + \Delta\epsilon_2(r)p_2(r)|\Psi_i\rangle\right] = 0 \tag{3.11}$$

Using the biorthogonal product of eq. (3.4) leads to

$$\forall\ i \quad b_i(\omega)\left(\Omega_i^2 - \omega^2\right) = \omega^2 \sum_j b_j(\omega) C_{ij} \tag{3.12}$$

where

$$C_{ij} = \langle\Psi_j^*|\Delta\epsilon_1(r)p_1(r)|\Psi_i\rangle + \langle\Psi_j^*|\Delta\epsilon_2(r)p_2(r)|\Psi_i\rangle \tag{3.13}$$

If we consider a finite set of N modes, the generalized eigenvalue problem of eq. (3.12) can be written conveniently in a matrix form:

$$\left[\begin{pmatrix} \Omega_1^2 & \dots & 0 \\ \vdots & \ddots & \vdots \\ 0 & \dots & \Omega_N^2 \end{pmatrix} - \omega^2 \begin{pmatrix} 1 + C_{11} & \dots & C_{1N} \\ \vdots & \ddots & \vdots \\ C_{N1} & \dots & 1 + C_{NN} \end{pmatrix}\right] = 0 \tag{3.14}$$

The eigensolutions of eq. (3.14), $(\tilde{\Omega}_i, |\tilde{\Psi}_i\rangle)_{i\in[1,N]}$, are the eigensolutions of eq. (3.1) for the permittivity distribution $\tilde{\epsilon}(r)$. In eq. (3.14), the coupling coefficients, C_{ij}, between original modes i and j depend on the variation of the permittivity and the spatial overlap

of the modes at the location of the permittivity modification. Noteworthily, the coupling integral not only depends on the spatial overlap of the mode intensity profiles but also on the overlap of their phase profile.

Remarkably, when reducing the problem to two modes, we recover a system equivalent to 2 inductance/capacitor circuits coupled via an inductance L_c (see Fig .3.1). L_c induces the coupling of the two independent oscillators and the charges of each capacitor (namely Q_1 and Q_2) fulfil

$$\ddot{Q}_1 + \frac{Q_1}{L_1 C_1} = \frac{L_C}{L_1}(\ddot{Q}_1 + \ddot{Q}_2) \tag{3.15}$$

$$\ddot{Q}_2 + \frac{Q_2}{L_2 C_2} = \frac{L_C}{L_2}(\ddot{Q}_1 + \ddot{Q}_2) \tag{3.16}$$

which can be recast in a matrix form

$$\left[\begin{pmatrix} \left(\frac{1}{\sqrt{L_1 C_1}}\right)^2 & 0 \\ 0 & \left(\frac{1}{\sqrt{L_2 C_2}}\right)^2 \end{pmatrix} - \omega^2 \begin{pmatrix} 1 + \frac{L_C}{L_1} & \frac{L_c}{L_1} \\ \frac{L_c}{L_2} & 1 + \frac{L_c}{L_2} \end{pmatrix}\right] \begin{bmatrix} Q_1 \\ Q_2 \end{bmatrix} = 0 \tag{3.17}$$

Eq. (3.14) extends this result to a number of interacting modes $N > 2$ and can be understood as a basic linear coupling between modes playing the role of simple L/C oscillators.

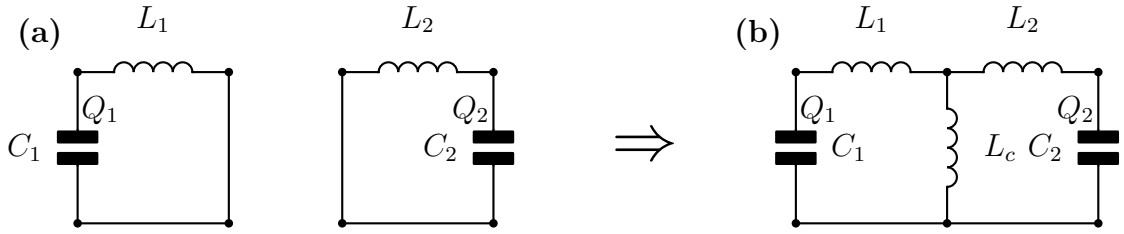

Figure 3.1: **(a)** Two independent inductance/capacitor (L_i/C_i) oscillators uncoupled. **(b)** The two systems are coupled via an inductance L_c.

3.2 Application to Anderson-localized modes: Prediction of Exceptional Points

Our theory is now applied to the particular case of a disordered system in the localized regime (see Chapter 2). First, we present the numerical 2D system that we consider to apply our theory, in which two local modifications of the permittivity distribution are introduced. Then, we discuss the nature of the modes of the initial system, which are computed via Finite Elements Method (FEM) and we investigate the computation of the biorthogonal product of eq. (3.4). Finally, we study the evolution of modes when the permittivity is modulated at two distinct locations. When the parameter space is scanned, we predict an EP between two specific modes and confirm its existence numerically.

3.2.1 The 2D open disorder dielectric medium

We consider a 2D random collection of 896 circular dielectric scatterers (radius 60 nm) with dielectric permittivity, $\epsilon = 4.0$, embedded in a host material of index $\epsilon_{mat} = 1.0$, with

a filling fraction of 40% (Fig. 3.2**(a)**). The system dimensions are $L \times L = 5.3\ \mu\text{m} \times 5.3\ \mu\text{m}$. The two circular regions of diameter 340 nm, R_1 and R_2, are shown in Fig. 3.2**(a)**. The dielectric permittivity of the scatterers within these regions is varied from ϵ to $\epsilon+\Delta\epsilon_1$ and $\epsilon+\Delta\epsilon_2$, respectively. This can be achieved experimentally by shining 2 laser beams on the surface of the sample and take advantage of optical nonlinearity to change locally the refractive index.

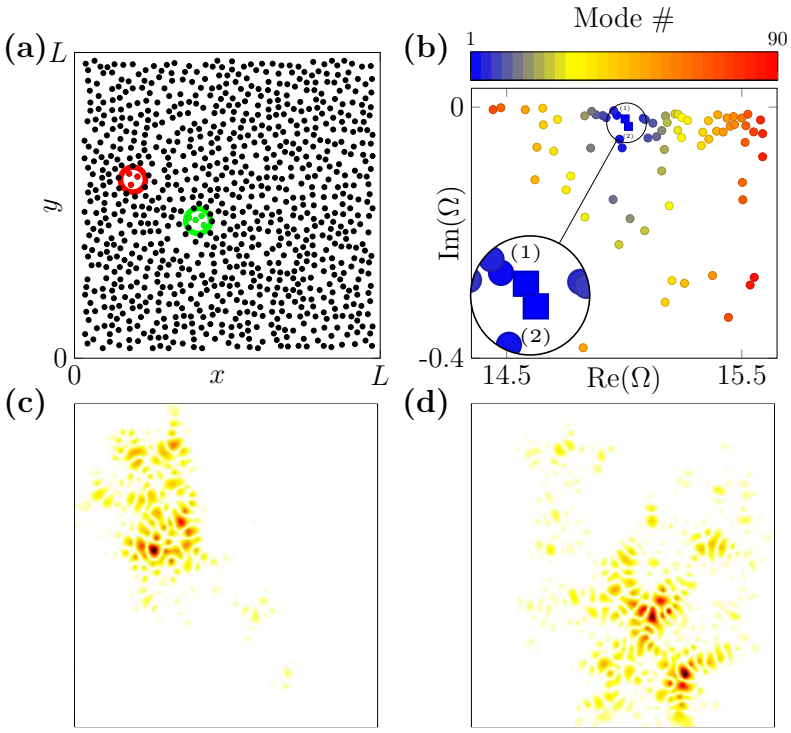

Figure 3.2: **(a)** 2D random medium: 896 scatterers of dielectric permittivity $\epsilon = 4$ are embedded in vacuum $\epsilon_{mat} = 1.0$, system is open at edges. The permittivity of the scatterers is modified in two circular domains of diameter $340\,nm$ (respectively $R_1 =$ red circle and $R_2 =$ green circle). **(b)** Original eigenvalues $(\Omega_i)_{i\in[1,90]}$: Computed by FEM in absence of dielectric permittivity modulation and sorted in the complex plane according the distance $d(1,i)$. An inset focuses on eigenvalues of interest (namely Ω_1 and Ω_2). **(c)**,**(d)** Original eigenvectors intensities of $|\Psi_1\rangle$ and $|\Psi_2\rangle$ respectively.

3.2.2 Original modes and biorthogonal product

The original modes $(\Omega_i, |\Psi_i\rangle)_{i\in[1,N]}$, which are the only input requested by eq. (3.14), cannot be obtained analytically in such a complex random system. Here, we have developed a FEM routine [88, 89] to compute these modes (see Chapter 2). Boundary conditions are placed $0.4\,\mu m$ away from each edge of the system. We consider a frequency range in which the localization length is estimated around $\xi \approx 1\,\mu m \ll L$[1]. As a result, the modes are strongly confined within the system.

A large number of modes ($N = 90$) are computed for the original system (Fig. 3.2**(b)**) in this spectral range. We checked that modes are not degenerated (see Fig. 3.2**(b)**),

[1]In 2D problems, the localization length satisfies $\xi \approx l_t exp\,(\omega l_t/c)$[65]. Different methods can be used to estimate ξ like the spatial correlation of modes or transmission measurement, see for instance [90]

which is one of the conditions for the application of the biorthogonal formalism. Among these modes, we consider two localized states $|\Psi_1\rangle$ and $|\Psi_2\rangle$ respectively at Ω_1 and Ω_2, spectrally close (Fig. 3.2**(b)**) but spatially distinct (Fig. 3.2**(c)** and **(d)**). We define in the complex plane the spectral distance of mode i to mode 1 as $d(1,i) = |\Omega_1 - \Omega_i|$. This distance, color-coded in Fig. 3.2**(b)**, is a measure of the spectral overlap between mode i and mode 1. Here, mode 2 is most likely to couple to mode 1 but we will see later in this chapter that the influence of other nearby modes cannot be neglected in the modal interaction.

The biorthogonal product defined in eq. (3.4) corresponds to an integration over the whole space, $\mathbb{R}^2$

$$\langle \Phi_q^* | \epsilon(r) | \Phi_p \rangle = \int_{\mathbb{R}^2} \epsilon(r) \Phi_q(r) \Phi_p(r) dr \tag{3.18}$$

However, the computed modes are only defined over a finite spectral domain $V = [-0.1\,\mu m, 5.7\,\mu m]^2$. To understand the relation between integral over $\mathbb{R}^2$ and integral over V, let us consider the weak formulation[2] of eq. (3.2) along another mode $(\Omega_q, |\Psi_q\rangle)$

$$\int_V \Delta\Phi_p \Phi_q + \int_V \Omega_p^2 \epsilon(r) \Phi_p \Phi_q = 0 \tag{3.19}$$

Using an integration by parts, eq. (3.19) reads

$$\int_{\partial V} \mathbf{grad}\, \Phi_p . \Phi_q - \int_V \mathbf{grad}\, \Phi_p . \mathbf{grad}\, \Phi_q + \int_V \Omega_p^2 \epsilon(r) \Phi_p \Phi_q = 0 \tag{3.20}$$

where ∂V stands for the boundary of V. With a second integration by parts, eq. (3.20) reads

$$\int_{\partial V} \mathbf{grad}\, \Phi_p . \Phi_q - \int_{\partial V} \mathbf{grad}\, \Phi_q . \Phi_p + \int_V \Delta\Phi_q \Phi_q + \int_V \Omega_p^2 \epsilon(r) \Phi_p \Phi_q = 0 \tag{3.21}$$

Eq. (3.21) leads to

$$\int_{\partial V} \mathbf{grad}\, \Phi_p . \Phi_q - \int_{\partial V} \mathbf{grad}\, \Phi_q . \Phi_p + \left(\Omega_p^2 - \Omega_q^2\right) \int_V \epsilon(r) \Phi_q \Phi_q = 0 \tag{3.22}$$

As a result the biorthogonal relation of eq. (3.18) reads

$$\langle \Phi_q^* | \epsilon(r) | \Phi_p \rangle = \int_V \epsilon(r) \Phi_q(r) \Phi_p(r) dr + \frac{1}{\Omega_q^2 - \Omega_p^2} \left(\int_{\partial V} \mathbf{grad}\, \Phi_p . \Phi_q - \mathbf{grad}\, \Phi_q . \Phi_p \right) = \delta_{pq} \tag{3.23}$$

Anderson-localized modes are non-degenerated ($\Omega_p \neq \Omega_q$) and have a small spatial overlap in our case. As a result, the biorthogonal relation can be approximated by

$$\langle \Phi_q^* | \epsilon(r) | \Phi_p \rangle \approx \int_V \epsilon(r) \Phi_q(r) \Phi_p(r) dr = \delta_{pq} \tag{3.24}$$

The edge term (integral along ∂V) in the biorthogonal product can be easily neglected. It leads to an inaccuracy of 0.8% in the position of EP[3].

[2]For a function $f(x) = 0$, whatever the function $g(x)$, performing the weak formulation of f along g means we consider the integral $\int f(x)g(x) = 0$.

[3]This edge term can be inserted in the eigenvalue problem provided in eq. (3.14). It results in the addition of extra on and off-diagonal terms in both matrices.

3.2.3 Exceptional Point between two Anderson-localized modes

Coalescence of eigenvalues

The parameter space, $(\Delta\epsilon_1, \Delta\epsilon_2)$, is sampled and eq. (3.14) is solved with $N = 60$ interacting modes inorder to compute the new eigenstates $(\tilde{\Omega}_i, |\tilde{\Psi}_i\rangle)_{i\in[1,N]}$. The difference between the two eigenvalues of interest, $|\tilde{\Omega}_1 - \tilde{\Omega}_2|$, in the small range of parameter space is shown in Fig. 3.3**(a)**. This difference sharply drops to zero at $(\Delta\epsilon_1, \Delta\epsilon_2)_{@EP} = (0.939, 0.90)$. The existence of an EP at this position is confirmed by plotting the real and imaginary parts of the eigenvalues, $\tilde{\Omega}_{i\in[1,2]}$ (Fig. 3.4**(a)** and **(b)**). The intricate topology of intersecting Riemann's sheets around the singular point $(\Delta\epsilon_1, \Delta\epsilon_2)_{@EP}$, is the hallmark of an exceptional point (see explanations in Chapter 2).

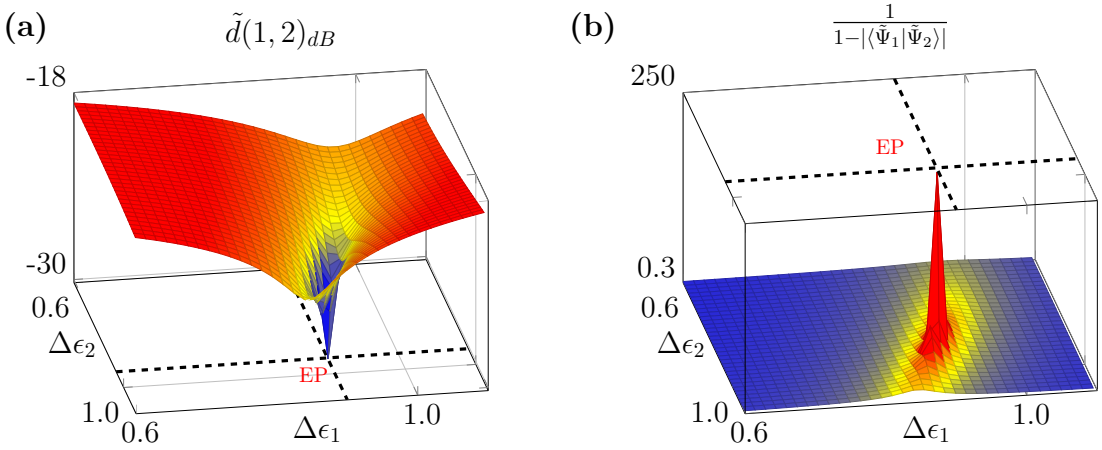

Figure 3.3: **(a)** The difference of eigenvalues 1 and 2 $\tilde{d}(1,2)_{dB} = |\tilde{\Omega}_1 - \tilde{\Omega}_2|_{dB}$ (arbitrary units), canceling out close to $(\Delta\epsilon_1, \Delta\epsilon_2)_{@EP}$. **(b)** Measure of the collinearity in the parameter space. At $(\Delta\epsilon_1, \Delta\epsilon_2)_{@EP}$, both eigenvectors are collinear.

Coalescence of eigenfunctions

We now focus on the eigenfunctions (or spatial distribution) of modes. We compute the inner product of the two eigenstates, $\langle\tilde{\Psi}_1^*|\tilde{\Psi}_2\rangle$ and plot $1/(1 - |\langle\tilde{\Psi}_1^*|\tilde{\Psi}_2\rangle|)$, as shown in Fig. 3.3**(b)**. At the exact position where $|\tilde{\Omega}_1 - \tilde{\Omega}_2|$ becomes zero, the two eigenvectors become collinear, confirming the coalescence of the two eigenstates. The amplitude of spatial distribution at EP is shown in Fig. 3.6**(a)**. As a result, we have a strict coalescence of the two eigenstates: Both eigenvalues and eigenvectors merge.

3.2.4 FEM validation

Finally, the theory is further confirmed by FEM simulation. We compute the modes of interest $|\tilde{\Psi}_{i\in[1,2]}\rangle$ in a discretized parameter space range enclosing prediction $(\Delta\epsilon_1, \Delta\epsilon_2)_{@EP}$. The resolution of the sampling is set to 0.04 along $\Delta\epsilon_1$ and $\Delta\epsilon_2$. The eigenvalues merge at position $(\Delta\epsilon_1, \Delta\epsilon_2) = (0.92, 0.88) \pm (0.04, 0.04)$ and exhibit characteristic intersecting

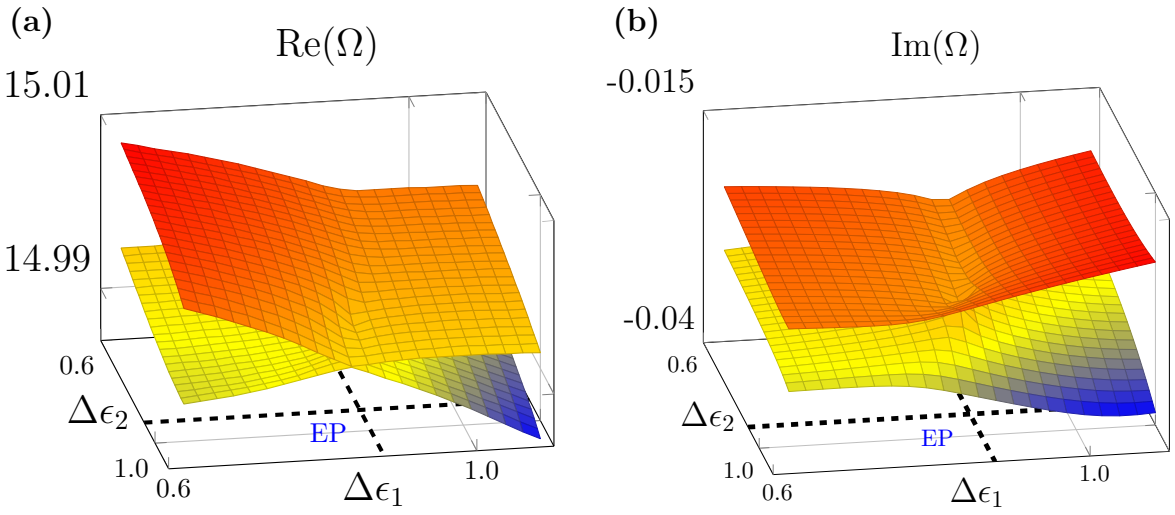

Figure 3.4: **(a)** and **(b)** Respectively real and imaginary parts of eigenvalues $\tilde{\Omega}_1$ and $\tilde{\Omega}_2$. Both real and imaginary parts are identical at $(\Delta\epsilon_1, \Delta\epsilon_2)_{@EP}$.

Riemann's sheets. The collinearity of the eigenvectors ensures the existence of an EP at this specific position. The theoretical prediction falls within the errorbar of the numerical value of the EP. Despite the assumption made on biorthogonal product in eq. (3.24) and inherent numerical inaccuracy, the prediction is confirmed by FEM simulation.

3.3 A complex N-mode process

The capability of our theoretical approach to predict EP between two Anderson-localized modes has been demonstrated in the section 3.2. In this section, we investigate the properties of the modes in the vicinity of EPs. First, we demonstrate that this problem cannot be reduced to a two-mode interaction and appears to be a N-mode process. Then, we show the evolution of spatial distribution of modes in the vicinity of EP. Finally, we demonstrate the presence of multiple EPs in the parameter space and propose some applications.

3.3.1 Mulimode process

Many observations of EP are based on weak perturbation of hermitian problems. In such problems, the study of EP can be reduced to a two-mode interaction. Here, we consider a strongly non-hermitian system. The influence of distant modes is tested by reproducing the computation of $(\Delta\epsilon_1, \Delta\epsilon_2)_{@EP}$ for a number of modes, N,ranging from 2 to 60 (see Fig. 3.5). Fig. 3.5 shows that the position of the EP is not accurately predicted if only a small number of interacting modes are considered. Actually, more than 30 modes are required to correctly pinpoint the exact position of the coalescence of mode 1 and mode 2. However, this figure shows that the method converges for N larger than 55, which confirms that spectrally distant modes have a vanishing influence on the interaction of the two modes. The amplitude spatial distribution of the coalescing modes is shown in Fig. 3.6**(a)**, namely $|\tilde{\Psi}_{1,2@EP}\rangle$. Fig. 3.6**(b)** shows the biorthogonal projection of $|\tilde{\Psi}_{1,2@EP}\rangle$

along the original modes $|\Psi_i\rangle$. It demonstrates the vanishing, though non negligible, contribution of nearby modes. These results confirm the degree of complexity of modal interaction in a disordered open system and the ability of our theoretical approach to provide with a control of the disorder landscape to manipulate the N-mode interaction.

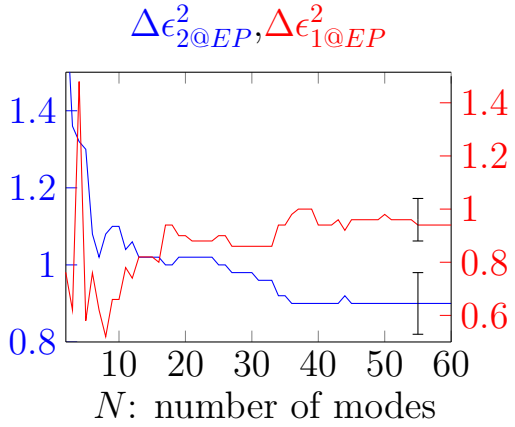

Figure 3.5: Predicted EP position $(\Delta\epsilon_1, \Delta\epsilon_2)_{@EP}$ versus number N of original modes. Black errors bars correspond to location of EP computed by FEM.

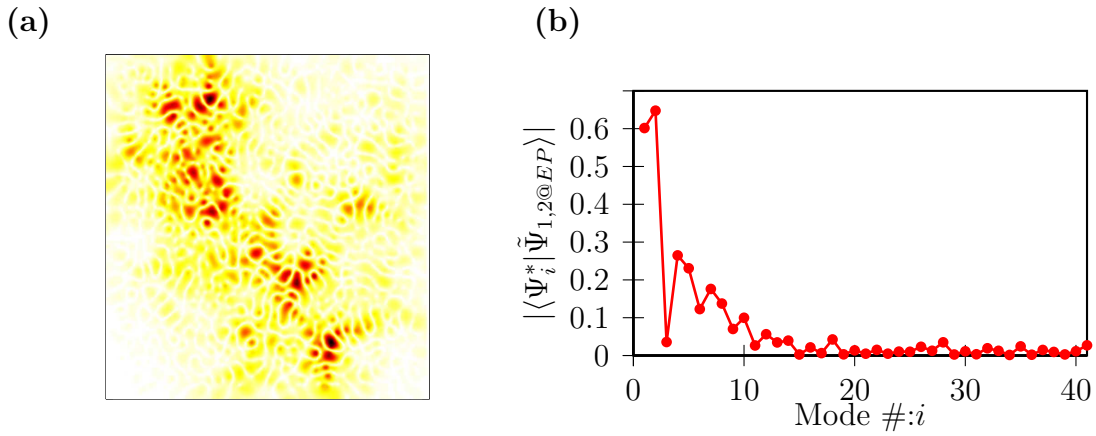

Figure 3.6: **(a)** Amplitude of modes $|\tilde{\Psi}_{1@EP}\rangle$ and $|\tilde{\Psi}_{2@EP}\rangle$, which are identical at EP $((\Delta\epsilon_1, \Delta\epsilon_2)_{@EP})$. **(b)** Absolute value of biorthogonal projection of $|\tilde{\Psi}_{1,2@EP}\rangle$ along the original modes $|\Psi_i\rangle$.

3.3.2 Modes in the vicinity of an EP

The previous section 3.3.1 highlighted the complexity of the mode mixing. Modes can hybridize (see Fig. 3.6**(a)**) and form a beaded chain, which connects both ends of the system. Hence, as already observed in [78], the presence of EP can be used to create necklace states [79, 80] resulting from mode hybridization.

Our calculations allows us to go further and check that $|\tilde{\Psi}_1\rangle = \pm i|\tilde{\Psi}_2\rangle$ on both sides of the EP. In Fig. 3.7, when the EP is crossed in the parameter space, the real part of $|\tilde{\Psi}_1\rangle$ becomes the imaginary part of $|\tilde{\Psi}_2\rangle$ and *vice versa*. This exchange is responsible for the phase shift measured when the EP is encircled within the parameter space (see Chapter 2).

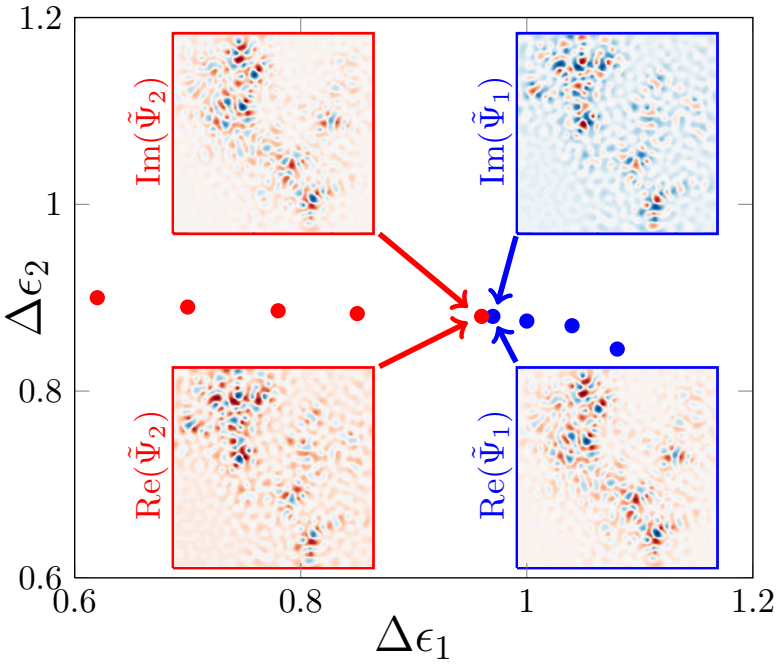

Figure 3.7: Pinch-line: The blue points correspond to identical real parts $\mathrm{Re}(\tilde{\Omega}_1) = \mathrm{Re}(\tilde{\Omega}_2)$ and red points to identical imaginary parts $\mathrm{Im}(\tilde{\Omega}_1) = \mathrm{Im}(\tilde{\Omega}_2)$.

3.3.3 Multiple EP and potential applications

The investigation of EP can be done for different couples of modes. In Fig. 3.8, we plot the position in the parameter space of the different EPs that we obtain for different couples of modes. We find, for instance, that the original mode 1, $|\Psi_1\rangle$, can coalesce with

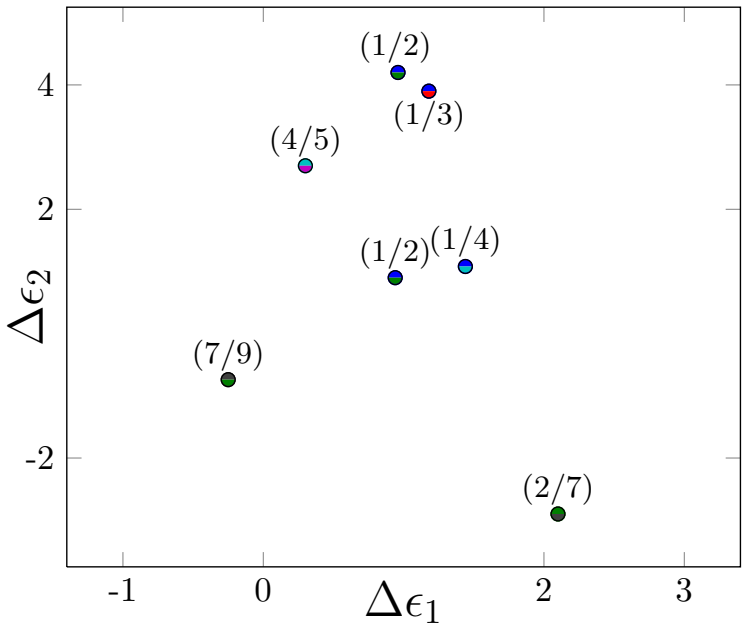

Figure 3.8: Position of different EPs in the parameter space $(\Delta\epsilon_1, \Delta\epsilon_2)$. Each EP is identified by the labels of the two coalescing modes.

modes 2, 3 and 4 in the parameter range we scanned. Interestingly, we find two EPs for the couple of original modes 1 and 2 (1/2). The two different spatial distributions $|\tilde{\Psi}_{1,2@EP}\rangle$ and complex frequencies $\tilde{\Omega}_{1,2@EP}$ are different. Each EP results from a different combination of original modes $|\Psi_i\rangle$. In others words, they correspond to different mixings of modes.

Based on this first exploration of EPs between interacting localized modes, the presence of multiple EP paves the road to various applications. As already stated, EP could be used to hybridize modes. The presence of multiple EPs could force a multi-hybridization of modes and open channels via necklace states in random media. By adding multiple local modifications in this numerical experiment, we could drive the system to EP in which three or more modes are coalescing. Moreover, we could use the high sensitivity of eigenvalues in the vicinity of EP. We should be able to drive the frequency of modes or achieve quality factor improvement. This could be particularly helpful in strong coupling experiment between an emitter and a mode, in which the frequency of the mode must be as close as possible to the resonance of the emitter (see Chapter 4). We demonstrated in section 3.2 that this system forms a N-mode interaction platform. Hence, in a more prospective view, it could provide a naturally disorder-robust network of interacting cavities, in which we could perform quantum simulation [91, 92].

3.4 Summary

Here, we have developed a general theory to study the evolution of modes in a 2D open dielectric media, while the permittivity distribution is modified. In the specific case of Anderson-localized modes, this theory could be used to force the coalescence of modes at a position called an Exceptional Point (EP).

Starting from modes of a 2D open system, we have developed the biorthogonal formalism to derive a linear eigenvalue problem. This provides the modes resulting from a modification of the permittivity. Using an analogy based on L/C oscillators coupled via an inductance, this linear system behaves like an infinite set of oscillators coupled via the modification of the permittivity. We have stressed the nature of this coupling, which relies on spatial and spectral overlap of the modes. We have applied this theory to the specific case of Anderson-localized modes, in which two local spots modulate the permittivity. Starting from a given disorder and corresponding FEM computed modes, we have gone beyond the simple evolution of localized modes and predicted the coalescence of two states. For a specific position in the modulation parameter space, namely the EP, simultaneous merging of eigenvalues and eigenvectors have been observed. EP prediction has been confirmed by FEM computations. Then, we have investigated the physical mechanism involved in the build-up of EP and demonstrated that the nearby modes play an important role. The merging of two states cannot be naively described by a two-mode model. It has been also pointed out that this system provides multiple EPs. From this EP density, we have proposed different applications relative to current active fields of research.

Finally, we would like to emphasize that this numerical experiment could be easily implemented in actual experiments. For instance, it could be achieved in 2D samples exhibiting optical localized states with the simple use of two laser spots [86, 93].

Chapter 4

Linear and non-linear Rabi oscillations of two-level systems resonantly coupled to an Anderson-localized mode

Table of Contents

The development of optical devices at the micro and nanoscales allows to address fundamental quantum phenomena in practical experiments. One of the most striking examples is probably quantum electrodynamics cavity (cavity QED), where an emitter is coupled to a resonant cavity mode. When an emitter interacts with a resonant cavity mode, two different regimes can occur. If the coupling is weak, the spontaneous decay of the emitter is modified. The energy is irreversibly transferred from the emitter to the cavity and immediately radiates to the far field. This alteration of spontaneous emission, is known as the Purcell effect [94] and was observed in optics for the first time by Drexhage [95]. The strong coupling regime is characterized in the time domain by Rabi oscillations of the electric field, or equivalently by a splitting in the frequency spectrum. The energy is reversibly exchanged between the emitter and the cavity mode leading to quantum effects [96]. Cavity QED is a major challenge of quantum optics in general and quantum information technology in particular. Achievement of cavity QED is of a fundamental interest e.g. for all-optical [97] and electro-optical [98] switching, many body quantum simulation [99, 100], single photon sources [101] as well as photon blockade [102]. Nevertheless, their development is currently hindered by the sensitivity of cavities to fabrication imperfections. To address this issue, an innovative approach was suggested by Lodahl's group [76, 103]. They proposed to use Anderson-localized modes as a cavity to perform "inherently disorder-robust quantum information devices". In a 1D disordered photonic waveguide, with embedded semiconductor quantum dots, they observed a strong enhancement of the spontaneous decay (the very signature of weak coupling). Their work was completed by Gao *et al.* [77], who demonstrated the strong coupling regime with similar samples. Recently, the strong coupling between a two-level system and localized modes was numerically observed by Cazé *et al.* [104] in 2D.

In this chapter, we explore the dynamical response of an emitter (a two-level atom as introduced in Chapter 1) interacting with an Anderson-localized mode. We demonstrate that Rabi regimes of two kinds may occur and co-exist, namely the linear and non-linear Rabi regimes. First, we consider a two-level atom in vacuum excited by a monochromatic electric field. At low intensity, the atomic response is linear and characterized by a monochromatic polarization. At high intensity, Stark shifts induced by the electric field profoundly modify the energy-level structure of the atom, leading to new resonances in the susceptibility. The polarization is composed of three frequencies forming a triplet as predicted by [105]. Second, we investigate the linear regime of a two-level atom in the steady state interacting with a 2D Anderson-localized mode. Linear Rabi oscillations/frequency splitting can occur when the strong coupling regime between the atom and the mode is reached. We express the strong coupling condition and the corresponding linear Rabi splitting amplitude, which are consistent with the work of Cazé [104]. Then, a mode with a high intensity is considered. The atom polarization is non-linear and exhibits non-linear Rabi oscillation/frequency splitting. A condition as well as an expression for the amplitude of the non-linear Rabi splitting are derived. Finally, we demonstrate that the two regimes can co-exist and can be observed simultaneously in a temporal experiment. Numerical computation run by Christian Vanneste with a Finite Difference Time Domain method confirms our prediction.

4.1 A two-level system coupled to the electric field

Here, we consider the academic case of a two-level atom excited by a monochromatic electric field [106]. For low excitation intensity, the polarization of the atom is linear. For high intensity, Stark shifts induce new transitions in the atomic wave function and the polarization is non-linear.

4.1.1 Coupled levels

In this section, we consider a quantum treatment of a two-level system (as in Chapter 1). An atom is modelled as a two-level system and characterized by a Hamiltonian H_0 in free space. Eigenstates of H_0 are $A = \{|u_a(r)\rangle, \hbar\omega_a\}$ and $B = \{|u_b(r)\rangle, \hbar\omega_b\}$ respectively lower and upper levels. The state of an electron is a linear combination of those eigenstates

$$\Psi(r,t) = C_a e^{-i\omega_a t}|u_a(r)\rangle + C_b e^{-i\omega_b t}|u_b(r)\rangle \tag{4.1}$$

where $|C_a|^2$ and $|C_b|^2$ represent the probability for the particle to be respectively in state A or B. When an electron decays from B to A a photon can be emitted at the specific frequency $\omega_{ba} = \omega_b - \omega_a$. The polarization $P(\omega)$ resulting from the transition of the atom from B to A is monochromatic and oscillates at ω_{ba}. The polarization is said to be linear.

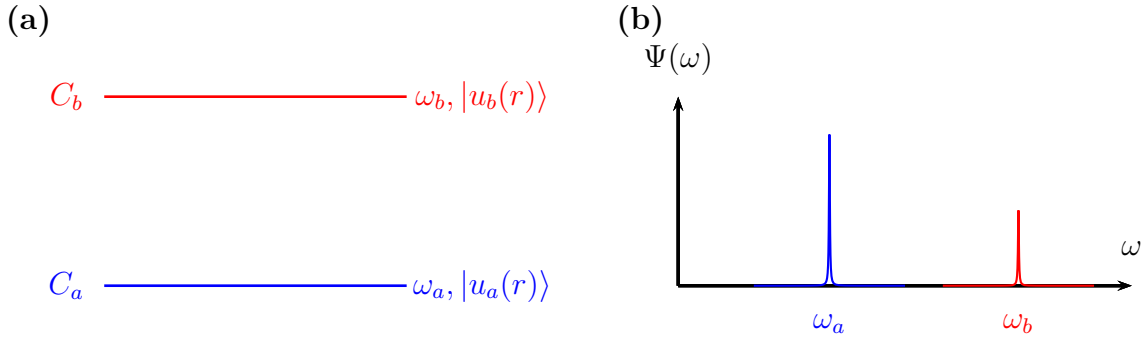

Figure 4.1: **(a)** A two-level system with eigenstates $A = \{|u_a(r)\rangle, \hbar\omega_a\}$ and $B = \{|u_b(r)\rangle, \hbar\omega_b\}$. **(b)** Example of the realization of an electron wave function composed of eigenstate A and B. Components at ω_a and ω_b are monochromatic and thus have a zero linewidth.

In free space, H_0 is hermitian and thus has orthogonal eigenstates:

$$\langle u_a(r)|u_b(r)\rangle = \int u_a^*(r)u_b(r) = \delta_{ab} \tag{4.2}$$

The system is excited by an electric field $\tilde{E}(t) = Ee^{-i\omega t} + cc$, where cc denotes the complex conjugate. This field is real and oscillates at frequency ω. The wavelength of the field is much larger than the dimensions of the atom. The electric field $\tilde{E}(t)$ is thus uniform at the scale of the atom. Hence, the interaction of the laser light with the atomic system can be approximated in the long-wavelength or the dipole approximation by the potential $V(t) = \mu\tilde{E}(t)$, where μ is the transition dipole operator of the system [106]

$$\mu = \begin{bmatrix} 0 & -\mu_{ab} \\ -\mu_{ba} & 0 \end{bmatrix} \tag{4.3}$$

The Hamiltonian of the system $H(t)$ reads

$$H(t) = H_0 + V(t) = \begin{bmatrix} \hbar\omega_a & 0 \\ 0 & \hbar\omega_b \end{bmatrix} + \begin{bmatrix} 0 & -\mu_{ab}\tilde{E}(t) \\ -\mu_{ba}\tilde{E}(t) & 0 \end{bmatrix} \tag{4.4}$$

Therefore the expansion coefficients of the wave function along the states A and B is also time-dependent

$$\Psi(r,t) = C_a(t)e^{-i\omega_a t}|u_a(r)\rangle + C_b(t)e^{-i\omega_b t}|u_b(r)\rangle \tag{4.5}$$

This wave function satisfies the Schrödinger equation

$$i\hbar\frac{\partial\Psi}{\partial t}(r,t) = H\Psi(r,t) \tag{4.6}$$

Inserting eq. (4.5) into eq. (4.6):

$$\begin{aligned} &i\hbar\left(\dot{C}_a(t)e^{-i\omega_a t}|u_a(r)\rangle - i\omega_a C_a(t)e^{-i\omega_a t}|u_a(r)\rangle + \dot{C}_b(t)e^{-i\omega_b t}|u_b(r)\rangle - i\omega_b C_b(t)e^{-i\omega_b t}|u_b(r)\rangle\right) \\ &= C_a(t)\hbar\omega_a e^{-i\omega_a t}|u_a(r)\rangle + C_b(t)\hbar\omega_b e^{-i\omega_b t}|u_b(r)\rangle - \mu_{ab}C_b(t)\tilde{E}(t)|u_a(r)\rangle - \mu_{ba}\tilde{E}(t)C_a(t)|u_b(r)\rangle \end{aligned} \tag{4.7}$$

Using the orthogonality relation of eq. (4.2) and $\omega_{ba} = \omega_b - \omega_a$ yields

$$\begin{cases} \dot{C}_a(t) &= -\frac{\mu_{ab}}{i\hbar}C_b(t)\tilde{E}(t)e^{-i\omega_{ba}t} \\ \dot{C}_b(t) &= -\frac{\mu_{ba}}{i\hbar}C_a(t)\tilde{E}(t)e^{i\omega_{ba}t} \end{cases} \tag{4.8}$$

Inserting the expression of the electric field, eq. (4.8) transforms into

$$\begin{cases} \dot{C}_a(t) &= -\frac{\mu_{ab}}{i\hbar}C_b(t)(Ee^{-i(\omega_{ba}+\omega)t} + E^*e^{-i(\omega_{ba}-\omega)t}) \\ \dot{C}_b(t) &= -\frac{\mu_{ba}}{i\hbar}C_a(t)(Ee^{i(\omega_{ba}-\omega)t} + E^*e^{i(\omega_{ba}+\omega)t}) \end{cases} \tag{4.9}$$

Using the Rotating Wave Approximation, we neglect the fast oscillations. Introducing the detuning $\Delta = \omega - \omega_{ba}$

$$\begin{cases} \dot{C}_a(t) &= -\frac{\mu_{ab}}{i\hbar}C_b(t)E^*e^{i\Delta t} \\ \dot{C}_b(t) &= -\frac{\mu_{ba}}{i\hbar}C_a(t)Ee^{-i\Delta t} \end{cases} \tag{4.10}$$

Eigenstate distributions $C_i(t)_{i\in[1,2]}$ are now coupled and time-dependent. The probability density of the electron $|C_i|^2_{i\in[a,b]}$, which was constant in free space, now fluctuates with time.

4.1.2 Oscillation of populations

Eq. (4.10) can be readily solved by adopting a trial solution of the form $C_a(t) = Ke^{-iXt}$.

$$\begin{cases} C_a(t) &= Ke^{-iXt} \\ C_b(t) &= -\frac{\hbar\lambda K}{\mu_{ab}E^*}e^{-i(\Delta+X)t} \\ \dot{C}_b(t) &= -\frac{\mu_{ba}}{i\hbar}C_a(t)Ee^{-i\Delta t} \end{cases} \tag{4.11}$$

Eq. (4.11) leads to the polynomial expression

$$X(X+\Delta) = \frac{|\mu_{ab}|^2|E|^2}{\hbar^2} \tag{4.12}$$

With solutions

$$X_{\pm} = -\frac{1}{2}\Delta \pm \frac{1}{2}\sqrt{\left|2\frac{\mu_{ab}E}{\hbar}\right|^2 + \Delta^2} \tag{4.13}$$

Using

$$\Omega = \left|2\frac{\mu_{ab}E}{\hbar}\right| \tag{4.14}$$

We can derive the expressions

$$\begin{cases} C_a(t) &= e^{i\frac{1}{2}\Delta t}(A_+e^{-i\frac{1}{2}\sqrt{\Omega^2+\Delta^2}t} + A_-e^{i\frac{1}{2}\sqrt{\Omega^2+\Delta^2}t}) \\ C_b(t) &= e^{-i\frac{1}{2}\Delta t}(B_+e^{-i\frac{1}{2}\sqrt{\Omega^2+\Delta^2}t} + B_-e^{i\frac{1}{2}\sqrt{\Omega^2+\Delta^2}t}) \end{cases} \tag{4.15}$$

where $A_{\pm}$ and $B_{\pm}$ are fixed by the initial conditions. Hence, the wave function of the electron is now made up of four components (see Fig. 4.2) [105, 107]. The atom can be treated as a four-level system. These "virtual" electronic levels are equally spaced around the eigenstates of the free space Hamiltonian H_0 (see Fig. 4.2). From a physical point of view, the electronic populations of states A and B read

$$\begin{cases} |C_a(t)|^2 &= |A_+e^{-i\frac{1}{2}\sqrt{\Omega^2+\Delta^2}t} + A_-e^{i\frac{1}{2}\sqrt{\Omega^2+\Delta^2}t}|^2 \\ |C_b(t)|^2 &= |B_+e^{-i\frac{1}{2}\sqrt{\Omega^2+\Delta^2}t} + B_-e^{i\frac{1}{2}\sqrt{\Omega^2+\Delta^2}t}|^2 \end{cases} \tag{4.16}$$

Populations oscillate over time and create "virtual" states on the electronic wave function. Hence, as sketched in Fig. 4.2, three resonance transitions are now allowed:

- (1): $\omega_{ba} - 2\sqrt{\Omega^2 + \Delta^2}$
- (2): ω_{ba}
- (3): $\omega_{ba} + 2\sqrt{\Omega^2 + \Delta^2}$

These three transitions correspond to three different frequencies within the polarization of the atom. They form a triplet [105]. Nevertheless, this triplet should not be mistaken for the Mollow triplet of resonance fluorescence [108] which requires a quantization of the electric field. As explained in Chapter 1, these transitions have a linewidth, which is driven by the spontaneous decay between the different levels.

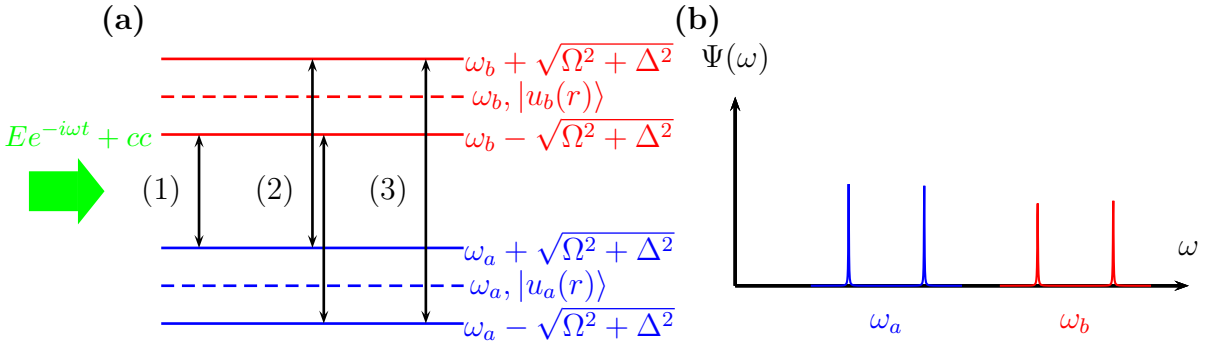

Figure 4.2: **(a)** Two-level system under an external field excitation $Ee^{-i\omega t} + cc$. Two "virtual states" appear around the eigenstates of the free space Hamiltonian H_0. **(b)** Example of the wave function $\Psi(\omega)$ of an electron composed of 4 different states.

4.1.3 Linear vs nonlinear polarization

Virtual states condition

If eq. (4.15) demonstrates the appearance of several components in the atomic polarization, it is of common knowledge that the observation of a triplet is an exception rather than the rule. In practice, to discern the appearance of the triplet, the spectral distance between the "side frequencies" must be larger than the linewidth of the central frequency (see Fig. 4.3). The central linewidth is given by the linewidth of the emitter embed-

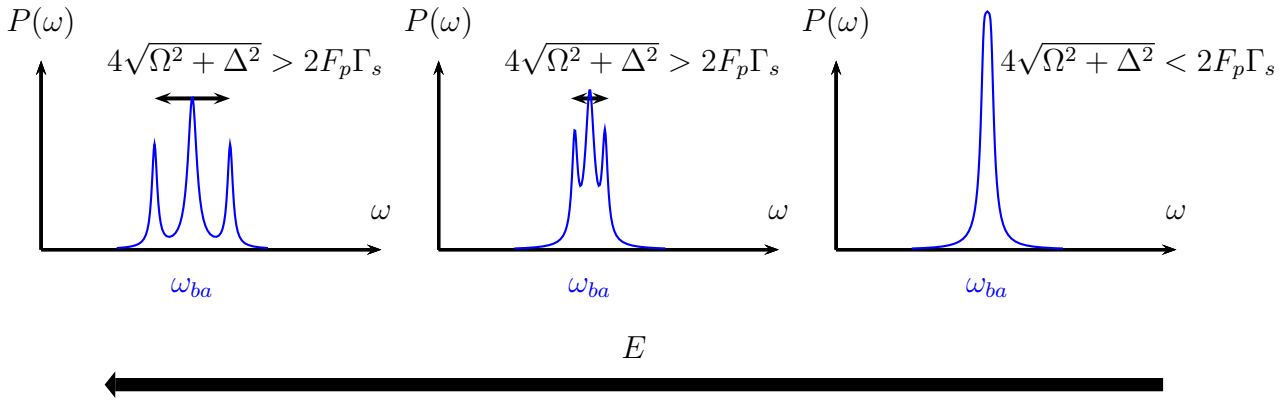

Figure 4.3: Frequency spectrum of the polarization of the atom: Excitation field amplitude increases from right to left. When the spectral distance between the two "side frequencies" is smaller than the central linewidth, the triplet can no longer be observed.

ded within the medium (see Chapter 1 for explanation). Compared to free space, the spontaneous decay of the emitter reads

$$2F_p\Gamma_s \tag{4.17}$$

where $\Gamma_s = \Gamma_s^R + \Gamma_s^{NR}$ is the spontaneous decay rate in vacuum of the emitter, which can be separated into a radiative (R) and a non-radiative (NR) component. F_p is the Purcell factor standing for modification of the decay rate due to the medium [94]. The system has no loss. Hence, for a single atom, the decay rate is purely radiative and is driven by the transition time T_1 between the two levels of the atom

$$\Gamma_s = \frac{1}{T_1} = \Gamma_s^R$$

For a collection of atoms, the decoherence time T_{2p} resulting from atom interactions must be taken into account as a non-radiative component

$$\Gamma_s = \frac{1}{T_1} + \frac{2}{T_{2p}} = \Gamma_s^R + \Gamma_s^{NR}$$

The triplet is observable if the electric field is strong enough to satisfy

$$F_p\Gamma_s < 2\sqrt{\Omega^2+\Delta^2} = 2\sqrt{\left|2\frac{\mu_{ab}E}{\hbar}\right|^2 + \Delta^2} \tag{4.18}$$

Linear and non-linear polarization regimes

As sketched in Fig. 4.3, the polarization of the atom has two different regimes depending on eq. (4.18).

If eq. (4.18) is not fulfilled, the electric field amplitude is relatively small, and only one frequency remains in the polarization. Both the polarization and the electric field are monochromatic. The emitter is in the linear regime and its polarization reads

$$P(\omega) = \chi_s(\omega)E(\omega) \tag{4.19}$$

where $\chi_s(\omega)$ is the two-level susceptibility (see Appendix A).

In the non-linear regime, the polarization is made up of three components: ω, $\omega - 2\sqrt{\Omega^2 + \Delta^2}$, $\omega + 2\sqrt{\Omega^2 + \Delta^2}$. This polarization can be expressed in terms of a non-linear susceptibility [106]. However, in this chapter, we will not need the complete expression of the polarization and therefore simply use the notation

$$P(\omega) = P_{NL}(\omega) \tag{4.20}$$

4.2 Linear Rabi regime: Strong coupling

Here we consider a two-level atom interacting with a 2D Anderson-localized mode (see Chapter 2). The two-level atom evolves in the linear regime and no external excitation is considered. Using modal expansion and the corresponding biorthogonal formalism (see Chapter 2), we derive the strong coupling condition of [104] and the linear Rabi splitting. This approach offers a new insight into the strong coupling condition and serves as a benchmark for our approach.

4.2.1 A two-level system coupled to a 2D Anderson-localized mode

We consider a 2D open disordered system of finite dimensions, with a position-dependent index of refraction $n(r)$ (see Fig. 4.4). In the absence of a source, the electric field fulfils the source-free Helmholtz equation (see Chapter 1)

$$\Delta E(\vec{r}, \omega) - \omega^2 n^2(\vec{r}) E(\vec{r}, \omega) = 0 \tag{4.21}$$

Modes are defined as the eigensolutions of Helmholtz eq. (4.21):

$$\Omega_i = \omega_i - i\frac{\Gamma_i}{2} \quad | \quad \Delta|\Psi_i\rangle - n^2(\vec{r})\Omega_i^2|\Psi_i\rangle = 0 \tag{4.22}$$

If the scattering is strong enough, these modes are spatially localized within the system limits, as in Fig. 4.4**(b)**.

Let us now consider a two-level system of polarization $P(\omega)$ embedded at the position r_a (see Fig. 4.4**(a)**). No external excitation is considered. The electric field is thus driven by Helmholtz equation with a right-hand side term

$$\Delta E(\vec{r}, \omega) - \omega^2 n^2(\vec{r}) E(\vec{r}, \omega) = \omega^2 P(\omega)\delta(r - r_a) \tag{4.23}$$

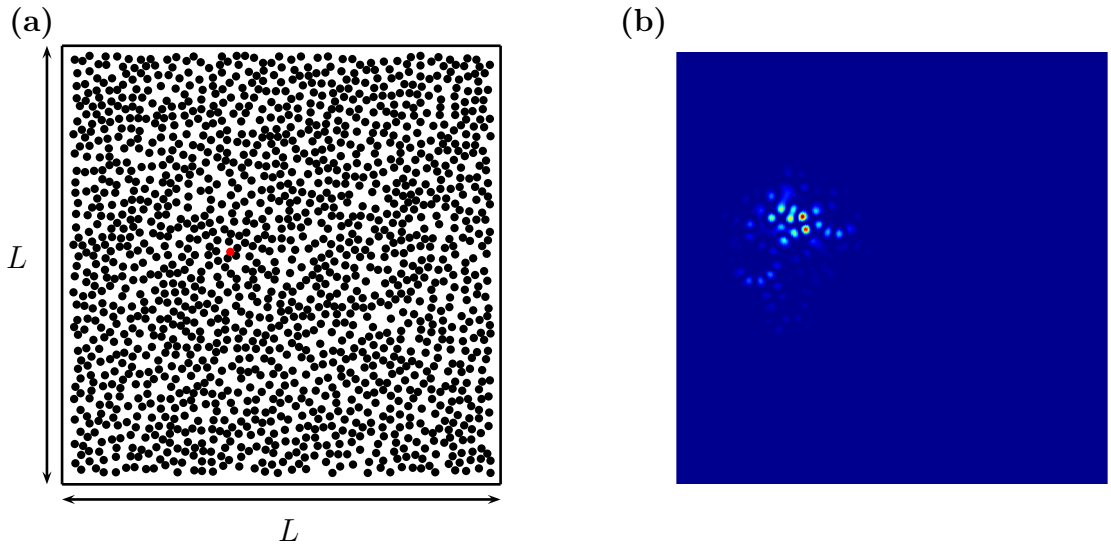

Figure 4.4: **(a)** A 2D scattering medium of refractive index distribution $n(r)$. The system is open at the edges. The red dot is the location of the atom r_a. **(b)** The spatial distribution of mode M, $|\Phi_M(r)\rangle$.

The susceptibility of the emitter is given by (see Appendix A)

$$\chi_s(\omega) = \frac{2}{\omega^2}\frac{\Gamma_s^R}{\omega_s - \omega - i\Gamma_s^{NR}/2} \tag{4.24}$$

where Γ_s^R/Γ_s^{NR} stand for radiative/non-radiative decays of the emitter respectively and ω_s is the central frequency of the mode. Hence the polarization $P(\omega)$ of the emitter reads

$$P(\omega) = \frac{2}{\omega^2}\frac{\Gamma_s^R}{\omega_s - \omega - i\Gamma_s^{NR}/2}E(\omega) \tag{4.25}$$

For the rest of the chapter we consider a specific localized mode ($\Omega_M = \omega_M - i\frac{\Gamma_M}{2}, |\Psi_M\rangle$) (presented in Fig. 4.4), and assume its central frequency is equal to the transition of the emitter:

$$\omega_M = \omega_s \tag{4.26}$$

4.2.2 Strong coupling and Rabi oscillations

Expansion of the field along the modes

As stated in Chapter 2, the electric field can be expanded along the modes of the system. Thus, the electric field reads

$$E(\vec{r},\omega) = \sum_i \frac{a_i(\omega)}{-i\omega + i\Omega_i}|\Psi_i\rangle \tag{4.27}$$

Using this expansion in eq. (4.23) and (4.24), we write

$$\sum_i \Delta\frac{a_i(\omega)}{-i\omega + i\Omega_i}|\Psi_i\rangle - \omega^2 n^2(r)\sum_i \frac{a_i(\omega)}{-i\omega + i\Omega_i}|\Psi_i\rangle = \frac{2\Gamma_s^R}{\omega_s - \omega - i\Gamma_s^{NR}/2}\sum_i \frac{a_i(\omega)}{-i\omega + i\Omega_i}|\Psi_i\rangle\delta(r - r_a) \tag{4.28}$$

Inserting the definition of mode given by eq. (4.22), eq. (4.28) reads

$$\sum_i \frac{a_i(\omega)}{-i\omega + i\Omega_i}(\Omega_i^2 - \omega^2)n^2(r)|\Psi_i\rangle = \frac{2\Gamma_s^R}{\omega_s - \omega - i\Gamma_s^{NR}/2}\sum_i \frac{a_i(\omega)}{-i\omega + i\Omega_i}|\Psi_i\rangle\delta(r - r_a) \quad (4.29)$$

As in Chapter 2, we define a biorthogonal product:

$$\langle\Psi_j^*|n(r)^2|\Psi_i\rangle = \int_{R^2} \Psi_j(r)\Psi_i(r)n(r)^2 = \delta_{ji} \quad (4.30)$$

Using the biorthogonal product of eq. (4.30) along the mode $\langle\Phi_M^*|$ leads to

$$\frac{a_M(\omega)}{-i\omega + i\Omega_M}(\Omega_M^2 - \omega^2) = \frac{2\Gamma_s^R}{\omega_s - \omega - i\Gamma_s^{NR}/2}\sum_i \frac{a_i(\omega)}{-i\omega + i\Omega_i}\Psi_i(r_a)\Psi_M(r_a) \quad (4.31)$$

Some reasonable assumptions

The modes used for the field expansion are Anderson-localized and thus have a very weak spectral overlap. Moreover, we assume that the spectral distance between two modes is larger than the linewidth of the susceptibility. The susceptibility of the emitter can be considered very narrow and centred on the central frequency of mode M. Hence, on the right-hand side of eq. (4.31) only the contribution of mode M remains

$$\frac{a_M(\omega)}{-i\omega + i\Omega_M}(\Omega_M^2 - \omega^2) = \frac{2\Gamma_s^R}{\omega_M - \omega - i\Gamma_s^{NR}/2}\frac{a_M(\omega)}{-i\omega + i\Omega_M}\Psi_M^2(r_a) \quad (4.32)$$

And if $j \neq M$

$$\frac{a_j(\omega)}{-i\omega + i\Omega_j} = 0 \quad (4.33)$$

Then, eq. (4.32) is now equivalent to a polynomial

$$(\Omega_M^2 - \omega^2)(\omega_M - \omega - i\Gamma_s^{NR}/2) = 2\Psi_M^2(r_a)\Gamma_s^R \quad (4.34)$$

Eq. (4.34) is simplified using the Rotating Wave Approximation

$$\Omega_M^2 - \omega^2 \approx 2\Omega_M(\Omega_M - \omega) \quad (4.35)$$

Leading to

$$(\Omega_M - \omega)(\omega_M - \omega - i\Gamma_s^{NR}/2) = \Psi_M^2(r_a)\frac{\Gamma_s^R}{\Omega_M} \quad (4.36)$$

Since the modes are localized, they have high Q-factor Q_M

$$Q_M = \frac{\omega_M}{\Gamma_M} \gg 1 \quad \Rightarrow \quad \frac{\Gamma_s^R}{\Omega_M} = \frac{\Gamma_s^R}{\omega_M}\frac{1}{1 - i\frac{1}{2Q_M}} \approx \frac{\Gamma_s^R}{\omega_M} \quad (4.37)$$

As a result

$$(\Omega_M - \omega)(\omega_M - \omega - i\Gamma_s^{NR}/2) = \Psi_M^2(r_a)\frac{\Gamma_s^R}{\omega_M} \quad (4.38)$$

Linear Rabi oscillations and splitting

Eq. (4.38) is now a simple polynomial of degree 2

$$\omega^2 - \omega\left(2\omega_M - \frac{i}{2}(\Gamma_M + \Gamma_s^{NR})\right) + \omega_M^2 - \omega_M\frac{i}{2}(\Gamma_M + \Gamma_s^{NR}) - \frac{\Gamma_M\Gamma_s^{NR}}{4} - \Psi_M^2(r_a)\frac{\Gamma_s^R}{\omega_M} = 0 \quad (4.39)$$

Defining the discriminant Δ of eq. (4.39):

$$\Delta = (2\omega_M - \frac{i}{2}(\Gamma_M + \Gamma_s^{NR}))^2 - 4\left(\omega_M^2 - \omega_M\frac{i}{2}(\Gamma_M + \Gamma_s^{NR}) - \frac{\Gamma_M\Gamma_s^{NR}}{4} - \Psi_M^2(r_a)\frac{\Gamma_s^R}{\omega_M}\right)$$

$$= -\frac{1}{4}\left(\Gamma_M + \Gamma_s^{NR}\right)^2 + \Gamma_M\Gamma_s^{NR} + 4\Psi_M^2(r_a)\frac{\Gamma_s^R}{\omega_M}$$

$$= -\left(\frac{\Gamma_s^{NR}}{2} - \frac{\Gamma_M}{2}\right)^2 + 4\Psi_M^2(r_a)\frac{\Gamma_s^R}{\omega_M} \quad (4.40)$$

The two frequencies fulfilling eq. (4.39) are:

$$\omega_\pm = \omega_M \pm \left[\Psi_M^2(r_a)\frac{\Gamma_s^R}{\omega_M} - \frac{(\Gamma_s^{NR} - \Gamma_M)^2}{16}\right]^{1/2} - \frac{i}{2}\left(\frac{\Gamma_s^{NR}}{2} + \frac{\Gamma_M}{2}\right) \quad (4.41)$$

And defining

$$g_c^2 = \Psi_M^2(r_a)\frac{\Gamma_s^R}{\omega_M} \quad (4.42)$$

leads to

$$\omega_\pm = \omega_M \pm \left[g_c^2 - \frac{(\Gamma_s^{NR} - \Gamma_M)^2}{16}\right]^{1/2} - \frac{i}{2}\left(\frac{\Gamma_s^{NR}}{2} + \frac{\Gamma_M}{2}\right) \quad (4.43)$$

Hence, the electric field can be expressed in the temporal domain (with constants $E_\pm$) as the superposition of two components

$$E(r,t) = \left(E_+e^{-i\omega_+ t} + E_-e^{-i\omega_- t}\right)|\Psi_M(r)\rangle \quad (4.44)$$

We must emphasize that mode M has a high Q-factor (small leakage at the edges, see Fig. 4.4). For that reason, $\Psi_M^2(r_a)$ is almost a real value and so is g_c^2. Assuming g_c^2 satisfies

$$g_c^2 > \frac{(\Gamma_s^{NR} - \Gamma_M)^2}{16} \quad (4.45)$$

thus, we can define a real value called the "linear Rabi splitting"

$$\Omega_R^L = \frac{\omega_+ - \omega_-}{2} = \left[g_c^2 - \frac{(\Gamma_s^{NR} - \Gamma_M)^2}{16}\right]^{1/2} \in \mathbb{R} \quad (4.46)$$

The envelope of the electric field oscillates over time and simultaneously the field in the spectral domain is split into two peaks (see Fig. 4.5). This phenomenon is called Rabi oscillation (in time), or Rabi splitting (in frequency) and is the footprint of strong coupling between an emitter and a cavity, a mode in the present case. Before going any further, we must emphasize that eq. (4.43,4.45,4.46) are consistent with the approach based on Local Density of States (LDOS) developed in [104]. There, a similar splitting is predicted with a different definition of g_c, derived from a LDOS formalism, $g_c^2 = \frac{\Gamma_R^S\Gamma_M F_p}{4}$, where F_p is the Purcell factor. In order to differentiate between linear and non-linear cases, we will refer to this Rabi oscillation/splitting as the linear Rabi regime.

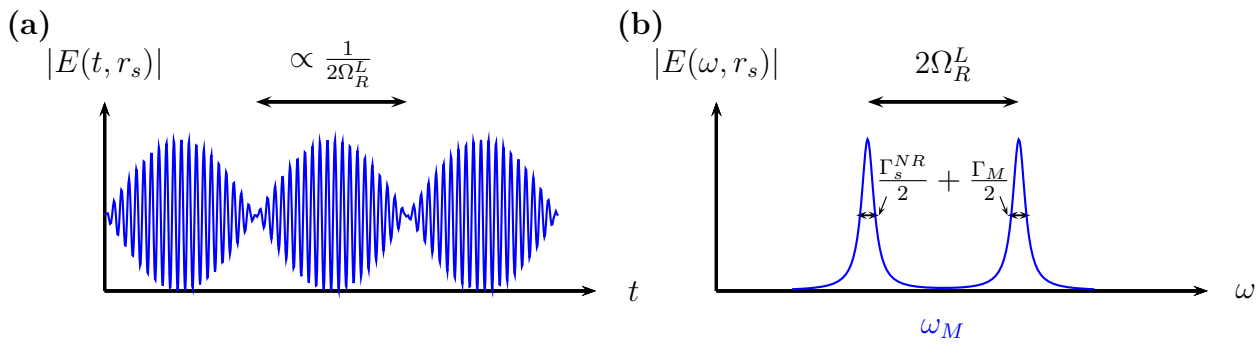

Figure 4.5: **(a)** Field amplitude at r_s exhibiting linear Rabi oscillations in time: The fast oscillation at optical frequency ω_M is modulated by the oscillation of the envelope at Ω_R^L. **(b)** Spectral field amplitude exhibiting linear Rabi splitting: The spectrum is split into two components.

4.2.3 Linear Rabi regime condition

As already stated, the linear Rabi regime corresponds to the very signature of strong coupling between the emitter and the cavity. The term g_c^2, defined in eq. (4.42), directly triggers the linear Rabi splitting, thus stands for the strength of the spatio/temporal coupling between the emitter and the mode. Spatial coupling is efficient if the emitter is placed at a position where the field intensity $\Psi_M^2(r_a)$ is large. Spectrally, the radiative rate of the emitter, Γ_s^R, needs to be sufficiently high to inject energy into the mode.

However, the condition driven by eq. (4.45) is not sufficient to observe a linear Rabi regime. For Rabi oscillations to be discernible, we must ensure the Rabi splitting is larger than the linewidth of each peak (see Fig. 4.5). The linewidth is directly given by the imaginary part of eq. (4.43). Leading to

$$2\Omega_R^L \geq \frac{\Gamma_s^{NR} + \Gamma_M}{2} \tag{4.47}$$

Hence, the necessary condition for linear Rabi regime is

$$g_c^2 \geq \frac{{\Gamma_s^{NR}}^2 + {\Gamma_M}^2}{8} \tag{4.48}$$

If eq. (4.48) is fulfilled linear Rabi regime is reached.

4.3 Non-linear Rabi regime

Unlike the linear Rabi regime, the two-level atom is here submitted to an intense electric field. In this section, we derive the condition for the observation of the triplet and predict the amplitude of the non-linear Rabi splitting. We refer to this situation as the non-linear Rabi regime. Rather than considering a non-linear susceptibility for the atom as in Ref. [106], we propose a different approach. Here we use an external source to neglect the influence of the non-linear polarization of the atom, and thus make the problem linear.

4.3.1 A two-level atom in an Anderson-localized mode ... with external excitation

First, we consider a two-level atom embedded in the same random medium as in section 4.2 (see Fig. 4.4). We know from section 4.1 that if the electric field is intense, the polarization of the two-level atom exhibits new resonances. Consequently this polarization is non-linear and noted P_{NL}. The electric field is driven by a non-linear version of the Helmholtz equation

$$\Delta E(\vec{r},\omega) - \omega^2 n^2(\vec{r}) E(\vec{r},\omega) = \omega^2 P_{NL}(\omega)\delta(r - r_a) \tag{4.49}$$

Nevertheless, the study of this problem is made more complex by the need for a non-linear susceptibility to link the electric field and the non-linear polarization. Moreover, we know from section 4.1 that the amplitude of the non-linear Rabi splitting is directly triggered by the amplitude of the field at the position of the atom (eq. (4.14)). Taking into account these two observations, we propose an alternative approach to eq. (4.49).

In this section, we will insert an external monochromatic source with amplitude P_{ext} at frequency ω_{ext} and positioned at r_{ext} (see Fig. 4.6**(a)**). Unlike the linear problem of section 4.2, here we consider an emitter providing for the external excitation at r_{ext} and the two-level atom at r_a. Eq. (4.49) is now transformed into

$$\Delta E(\vec{r},\omega) - \omega^2 n^2(\vec{r}) E(\vec{r},\omega) = \omega^2 P_{NL}(\omega)\delta(r - r_a) + \omega^2 P_{ext}\delta(r - r_{ext})\delta(\omega - \omega_{ext}) \tag{4.50}$$

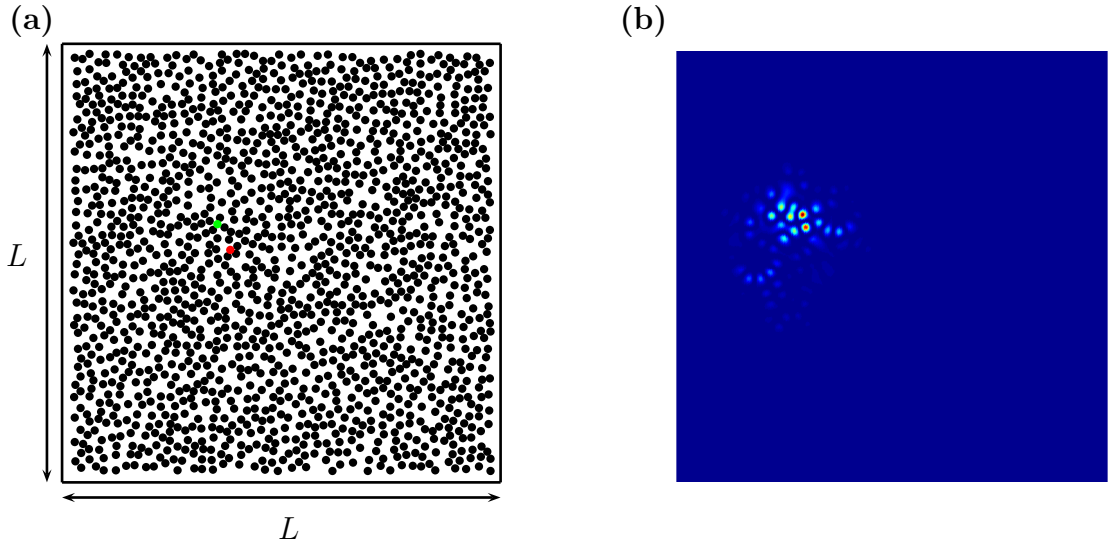

Figure 4.6: **(a)** 2D scattering medium with dielectric refractive index distribution $n(r)$. The system is open at the edges, the red dot is the location of the atom r_a and the green dot the location of the excitation r_{ext}. **(b)** Spatial distribution of Anderson-localized mode M, $|\Phi_M(r)\rangle$.

The amplitude of the electric field is the superposition of a first component due to the non-linear polarization of the atom at r_a and a second one due to the excitation source at r_{ext}

$$E(r,\omega) = E_{NL}(r,\omega) + E_{ext}(r,\omega) \tag{4.51}$$

where E_{NL} is driven by the non-linear polarization of the atom and E_{ext} by the external excitation.

Here we consider the case where the external excitation is much stronger than the non-linear polarization of the atom and the amplitude of the non-linear Rabi oscillations is mostly forced by $E_{ext}(r,\omega)$.

4.3.2 Non-linear Rabi regime

Expansion along the modes

When the non-linear polarization is neglected in eq. (4.50), it reads

$$\Delta E_{ext}(\vec{r},\omega) - \omega^2 n^2(\vec{r}) E_{ext}(\vec{r},\omega) \approx \omega_{ext}^2 P_{ext}\delta(r - r_{ext}) \tag{4.52}$$

Starting from eq. (4.52), it is possible to perform modal expansion of E_{ext} along the Anderson-localized modes:

$$\sum_i \frac{a_{i,ext}(\omega)}{-i\omega + i\Omega_i}(\Delta|\Psi_i\rangle - \omega^2 n^2(r)|\Psi_i\rangle) = \omega_{ext}^2 P_{ext}\delta(r - r_{ext})\delta(\omega - \omega_{ext}) \tag{4.53}$$

As in the previous section, we consider here the localized mode M (see Fig. 4.6**(b)**). Using the mode definition and the biorthogonal relation along $\langle\Psi_M^*|$:

$$\frac{a_{M,ext}(\omega)}{-i\omega + i\Omega_M}(\Omega_M^2 - \omega^2) = \omega_{ext}^2 \Psi_M(r_{ext}) P_{ext}\delta(\omega - \omega_{ext}) \tag{4.54}$$

Some reasonable assumptions

The modes are Anderson-localized and thus their spectral overlap is weak. The external excitation is tuned to match the central frequency of mode M

$$\omega_{ext} = \omega_M$$

As a result, only mode M is excited. The electric field reads

$$E_{ext}(\omega, r) = \frac{a_{M,ext}(\omega)}{-i\omega + i\Omega_M}|\Psi_M\rangle \tag{4.55}$$

Using eq. (4.54)

$$E_{ext}(\omega, r) = P_{ext}\frac{\Psi_M(r_{ext})\omega_M^2}{\Omega_M^2 - \omega^2}\delta(\omega - \omega_M)|\Psi_M(r)\rangle = P_{ext}\frac{\Psi_M(r_{ext})\omega_M^2}{\Omega_M^2 - \omega_M^2}|\Psi_M(r)\rangle \tag{4.56}$$

Now, we perform the Rotating Wave Approximation

$$\Omega_M^2 - \omega_M^2 \approx 2\omega_M(\Omega_M - \omega_M) = -i\omega_M\Gamma_M$$

We obtain the electric field driven by the external excitation

$$E_{ext}(\omega, r) = iP_{ext}\Psi_M(r_{ext})\frac{\omega_M}{\Gamma_M}|\Psi_M(r)\rangle \tag{4.57}$$

Non-linear Rabi splitting/oscillations

According to eq. (4.13), the amplitude of the non-linear Rabi splitting Ω_R^{NL} is triggered by the amplitude of the electric field at the position of the atom

$$\Omega_R^{NL} = 2\sqrt{\Omega^2 + \Delta^2} = 2\sqrt{\left|2\frac{\mu_{ab}E(r_a,\omega)}{\hbar}\right|^2 + \Delta^2} \tag{4.58}$$

With the expression of the electric field derived in eq. (4.57)

$$|E(r_a,\omega)| \approx |E_{ext}(r_a,\omega)| = P_{ext}Q_M\Psi_M(r_{ext})\Psi_M(r_a) \tag{4.59}$$

where $Q_M = \frac{\omega_M}{\Gamma_M}$ is the quality factor of mode M. Hence, the non-linear Rabi splitting reads in our case:

$$\Omega_R^{NL} = 2\sqrt{\left|2\frac{\mu_{ab}}{\hbar}P_{ext}Q_M\Psi_M(r_{ext})\Psi_M(r_a)\right|^2 + \Delta^2} \tag{4.60}$$

If we assume there is no detuning (*i.e.*) $\Delta = \omega_s - \omega_M = 0$:

$$\Omega_R^{NL} = 4\frac{\mu_{ab}}{\hbar}P_{ext}Q_M\Psi_M(r_{ext})\Psi_M(r_a) \tag{4.61}$$

The spectrum of the field is split (see Fig. 4.7). This splitting in the frequency domain is equivalent to oscillations in the temporal domain (with constants A_i)

$$|E(r,\omega)| \approx A_{-1}e^{-i(\omega_M-\Omega_R^{NL})t} + A_0e^{-i\omega_M t} + A_1e^{-i(\omega_M+\Omega_R^{NL})t} \tag{4.62}$$

As shown in Fig. 4.7**(a)**, the envelope of the electric field has a non-sinusoidal shape. These oscillations differ from the linear Rabi oscillations and will be referred to as the non-linear Rabi oscillation. In the frequency domain (Fig. 4.7**(b)**), the splitting of the field in three components will be referred to as the non-linear Rabi splitting. Both effects characterize the non-linear Rabi regime.

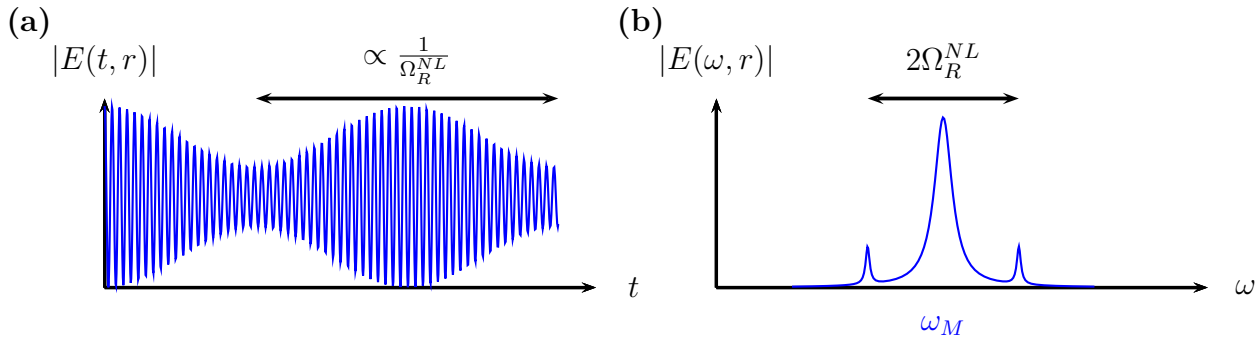

Figure 4.7: **(a)** Field amplitude time evolution exhibits non-linear Rabi oscillations: A fast oscillation at optical frequency ω_M is modulated by a non-sinusoidal oscillation of the envelope at Ω_R^{NL}. **(b)** Spectral field amplitude exhibits non-linear Rabi splitting: The spectrum splits into three components.

4.3.3 Non-linear Rabi regime condition

Existence condition

As stated in section 4.1, the non-linear Rabi regime is effective when

$$F_p\Gamma_s < \Omega_R^{NL} \tag{4.63}$$

In the case of no detuning, referring to eq. (4.61)

$$F_p\Gamma_s < 4\frac{\mu_{ab}}{\hbar}P_{ext}Q_M\Psi_M(r_{ext})\Psi_M(r_a) \tag{4.64}$$

Using [104], the Purcell factor is given by the ratio of the local density of state at the atom's position and the local density of state in vacuum

$$F_p = \frac{\rho(r_a,\omega_M)}{\rho_0} = \frac{4}{c^2}\,\mathrm{Im}(G(r_a,r_a,\omega_M)) \tag{4.65}$$

Noting that $c^2 = 1$ and

$$\mathrm{Im}(G(r_a,r_a,\omega_M)) = \mathrm{Im}\left(\frac{\Psi_M(r_a)^2}{\Omega_M^2-\omega_M^2}\right) \approx \frac{\Psi_M(r_a)^2}{\omega_M\Gamma_M} \tag{4.66}$$

where G is the Green function of the system. Hence, the non-linear Rabi regime condition reads

$$\Psi_M(r_a)\Gamma_s < \omega_{ext}^2\frac{\mu_{ab}}{\hbar}P_{ext}\Psi_M(r_{ext}) \tag{4.67}$$

As predicted in section 4.1, the non-linear Rabi regime is enforced by an external excitation (*i.e.* $P_{ext}\Psi_M(r_{ext})$).

Linear vs non-linear conditions

Remarkably enough, existence conditions for linear and non-linear Rabi oscillations may oppose each other. Indeed, using eq. (4.42,4.45) the linear and non-linear conditions read

$$\begin{cases} \Psi_M^2(r_a)\frac{\Gamma_s^R}{\omega_{ext}} & > & \frac{{\Gamma_s^{NR}}^2+{\Gamma_M}^2}{8} & \text{linear} \\ \Psi_M(r_a)\Gamma_s & < & \omega_{ext}^2\frac{\mu_{ab}}{\hbar}P_{ext}\Psi_M(r_{ext}) & \text{non-linear} \end{cases} \tag{4.68}$$

Unlike the non-linear case, the linear regime requires a large amplitude of the mode at the position of the atom $\Psi_M(r_a)$. The non-linear case needs a small decay rate $\Gamma_s = \Gamma_s^R+\Gamma_s^{NR}$, while in the other regime the non-radiative must be low and the radiative part must be important. Hence, these remarks emphasize the fact that the two regimes of oscillation are related to different mechanisms.

In the linear regime (strong coupling), energy is reversibly exchanged between the mode and the emitter. This exchange is possible if the radiative transfer from the emitter (namely Γ_S^R) is well coupled to the mode intensity (namely $\Psi_M(r_a)^2$). This coupling condition is exemplified by the left-hand-side term of eq. (4.68). To be effective, this reversible exchange must be stronger than the losses provided by the right-hand side of eq. (4.68) (namely ${\Gamma_s^{NR}}^2+{\Gamma_M}^2$).

In the non-linear regime the amplitude of the splitting is driven by the amplitude of atom population oscillations. This is triggered by the interaction potential between the atom and the field present in the right-hand side of non-linear eq. (4.68)(namely $\mu_{ab}\Psi_M(r_{ext})$). The non-linear Rabi splitting must be larger than the linewidth of the emitter encoded in $\Psi_M(r_a)\Gamma_s$.

4.4 Coexistence of both regimes in a realistic experiment in the temporal domain

In this section, we consider a realistic experiment in the temporal domain. A two-level atom is placed in a localized mode. The system is excited by a point source. When the excitation is turned-off, the amplitude of the electric field at the position of the atom decays. During this decay, the atom can successively exhibit non-linear and linear Rabi regimes.

4.4.1 Setup

We consider a 2D dielectric random medium similar to the one considered in sections 4.2 and 4.3. The modes are Anderson-localized and among them the mode M is excited by a source placed at position r_{ext} (see Fig. 4.8**(a)**). The point source emits a polarization pulse $P_{ext}(r_{ext}, t)$ of duration T_{ext} oscillating at frequency ω_{ext} matching mode M: $\omega_{ext} = \omega_M$. The source is located inside mode M and its duration T_{ext} is assumed to be long enough so that only mode M is excited (see Fig. 4.8**(b)**). Numerically, instead of a single atom, we insert a collection of N_{tot} two-level atoms in mode M at location r_a (see Fig. 4.8**(a)**). The linewidth of the emitters is thus given by $\Gamma_s = \Gamma_s^R + \Gamma_s^{NR} = \frac{1}{T_1} + \frac{2}{T_{2p}}$ as stated in section 4.1.3. The atomic central frequency ω_s matches the mode, and thus

$$\omega_M = \omega_{ext} = \omega_s \tag{4.69}$$

4.4.2 Linear/Non-linear regimes in the transient regime

Transient regime

The linear and non-linear Rabi regimes considered in the previous sections 4.2 and 4.3 have been studied in their steady states. In the present case, we are investigating the transient response when the excitation is switched off and the electric field intensity is decaying. Intensity stored in mode M is driven by Γ_M:

$$|E(r,t)|^2_{env} \propto e^{-\Gamma_M t} \tag{4.70}$$

where $|E(r,t)|^2_{env}$ stands for the envelope of the intensity.

Regarding the linear Rabi regime, this temporal evolution of the field intensity has no influence. Indeed, as emphasized in eq. (4.32) and (4.34), the amplitude of mode M is suppressed from the derivation of the linear Rabi splitting Ω_R^L. From a physical point

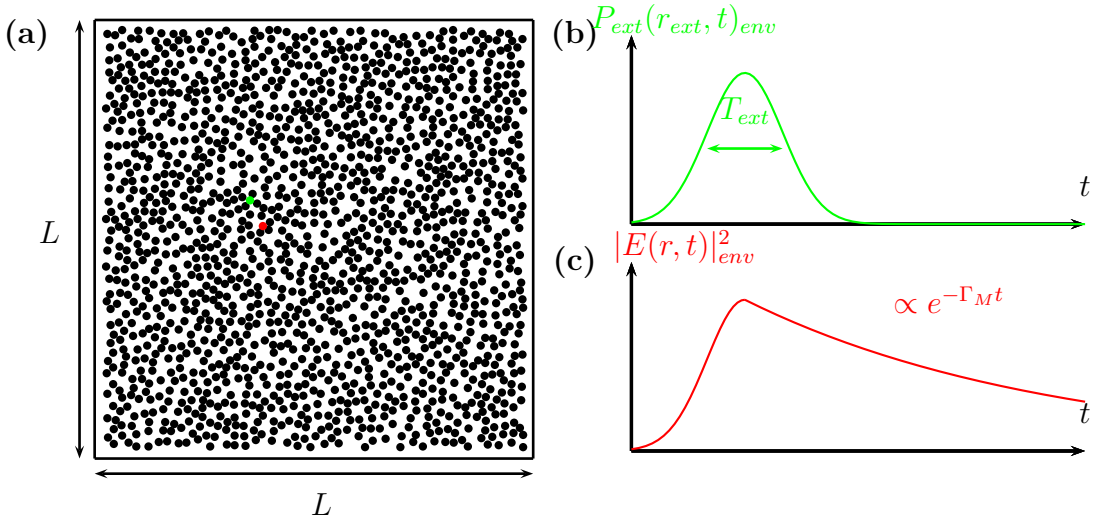

Figure 4.8: **(a)** 2D scattering medium of dielectric refractive index distribution $n(r)$. The system is open at the edges, the red dot is the location of the atom r_a and the green dot the location of the excitation r_{ext}. **(b)** Shape of the envelope of the temporal excitation of duration T_{ext} and amplitude P_{ext}, $P_{ext}(r_{ext},t)_{env}$ **(c)** Evolution of the envelope of the intensity of the electric field stored in mode M, $|E(r,t)|^2_{env}$.

of view, the strong coupling achieved between the two-level emitter and the mode is similar to two coupled springs. Therefore, this coupling mechanism is only affected by the coupling strength and the frequencies of both oscillators.

Unlike the linear regime, the non-linear Rabi splitting is directly driven by the field intensity (see eq. (4.14) in section 4.1). Hence, the amplitude of the non-linear Rabi splitting will progressively decay whit the intensity.

Linear/Non-linear splittings

The evolution of the electric field $E_{ext}(\omega,r)$ is given by eq. (4.57) in the steady state. Therefore, we can easily derive its value in the transient regime

$$E_{ext}(\omega,r_a) \rightarrow E_{ext}(t,r_a) = \underbrace{iN_{tot}P_{ext}\Psi_M(r_{ext})\Psi_M(r_a)\frac{\omega_M}{\Gamma_M}}_{E(r_a,\omega_M)} e^{-\frac{\Gamma_M}{2}t} \tag{4.71}$$

The use of a collection of atoms is responsible for the factor N_{tot}.

By inserting the field evolution in eq. (4.58), it is now possible to obtain the expression of the non-linear Rabi splitting versus time

$$\Omega_R^{NL}(t) = 2\sqrt{\Omega^2+\Delta^2} = 2\sqrt{\left|2\frac{\mu_{ab}E(r_a,\omega_M)e^{-\Gamma_M t}}{\hbar}\right|^2+\Delta^2} \tag{4.72}$$

The linear Rabi splitting remains identical to the one derived in section 4.2. Assuming there is no detuning (*i.e.* $\Delta=0$, $\omega_M=\omega_{ext}$) and if the coupling is strong ($g_c^2 \gg \Gamma_s^{NR},\Gamma_M$),

the linear and non-linear splittings read

$$\Omega_R^L = \sqrt{N_{tot}\Psi_M^2(r_a)\frac{\Gamma_s^R}{\omega_M}} \tag{4.73}$$

$$\Omega_R^{NL}(t) = 4\left|\frac{\mu_{ab}N_{tot}P_{ext}\Psi_M(r_{ext})\Psi_M(r_a)\omega_M}{\Gamma_M\hbar}\right| e^{-\frac{\Gamma_M}{2}t} \tag{4.74}$$

Hence, assuming that both regimes can be reached, the non-linear Rabi splitting decreases over time while the linear one remains identical. Therefore, we must observe successively the non-linear and the linear regime. In Fig. 4.9, we plot the schematic evolution of the spectral peaks with respect to time. When the excitation is turned-off, both regimes are present. Then, the non-linear Rabi splitting quickly decays and only the linear regime remains.

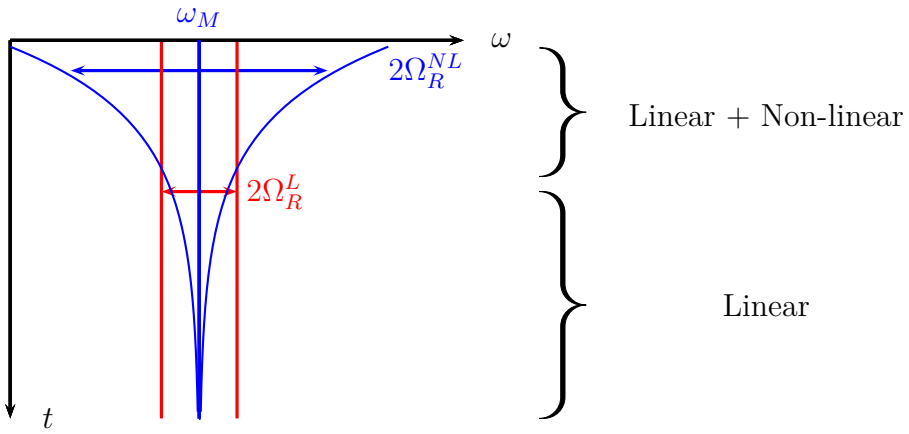

Figure 4.9: Evolution over time of linear splitting Ω_R^L and non-linear splitting Ω_R^{NL}. When the non-linear splitting vanishes, the linear splitting is observed.

4.4.3 Numerical investigation

Numerical setup

To observe the prediction of section 4.4.2 we present Finite Difference Time Domain (FDTD) simulations (see Chapter 2) performed by Christian Vanneste[1]. The 2D system is made of a collection of circular dielectric scatterers with radius $r = 60$ nm and optical index $n = 2$ embedded in a background medium of index $n = 1$. The volume fraction is 40 % and the system size is $L^2 = 6.6 \times 6.6\ \mu m^2$. We insert a source at position $r_{ext} = (2.10\,\mu m, 2.78\,\mu m)$ (see Fig. 4.10**(a)**) and atoms at $r_a = (2.04\,\mu m, 2.80\,\mu m)$. The localized mode M ($\omega_M - i\frac{\Gamma_M}{2} = 14.1548 - 1.95.10^{-4}i\ \mu m^{-1}$, with $c = 1$) is shown in Fig. 4.10**(b)**. Mode M is excited by the external source at position r_{ext} during $T_{ext} = 100\,ps$. There are $N_{tot} = 3\,10^{24}$ atoms, with a decay time $T_1 = 1$ ns and a decoherence time $T_{2p} = 1$ ns. The electric field and the population difference at the position of the atom, namely $E(r_a, t)$ and $\Delta N(t)$, are computed with the FDTD method coupled to the

[1]Laboratoire de Physique de la Matière Condensée, CNRS UMR 3776, Université de Nice-Sophia Antipolis, Parc Valrose, 06108 Nice Cedex 02, France

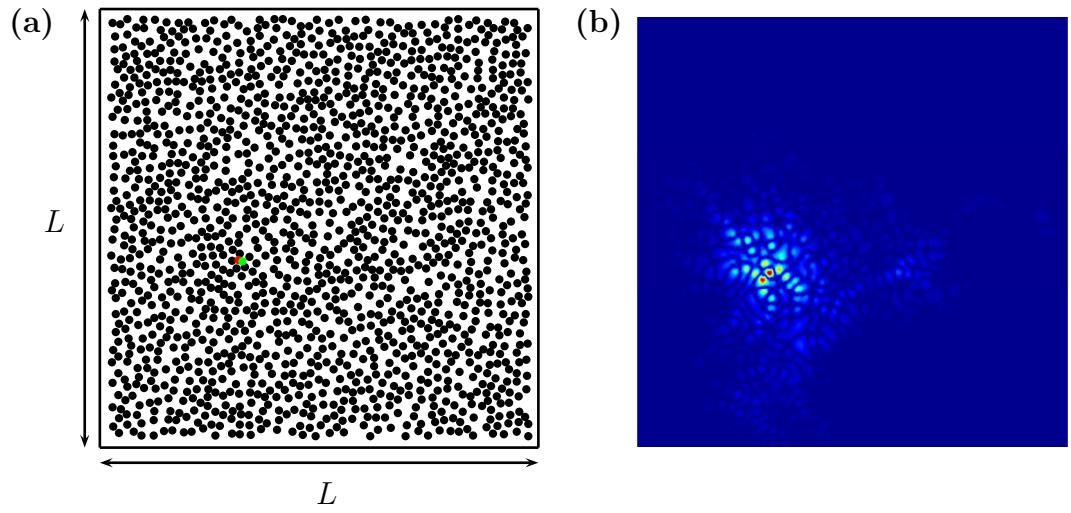

Figure 4.10: **(a)** 2D random system made of dielectric pillars of index $n = 2$ in vacuum: The excitation source r_{ext} is marked by a green dot and the atoms by a red dot. **(b)** Mode M distribution $|\Phi_M(r)\rangle$ considered for the numerical experiment (computed by Finite Element Method).

population equations of the two-level atomic structure [109, 110, 111] (see Fig.4.11). In Fig. 4.11**(a)** we plot the envelope of the excitation at r_{ext} ($P_{ext}(r_{ext}, t)_{env}$), the average population difference ($\langle \Delta N \rangle$) in Fig. 4.11**(b)** and the electric field envelope at the position of the atom ($|E(r_a, t)|_{env}$) in Fig. 4.11**(c)**. When the excitation is turned-off, the transient

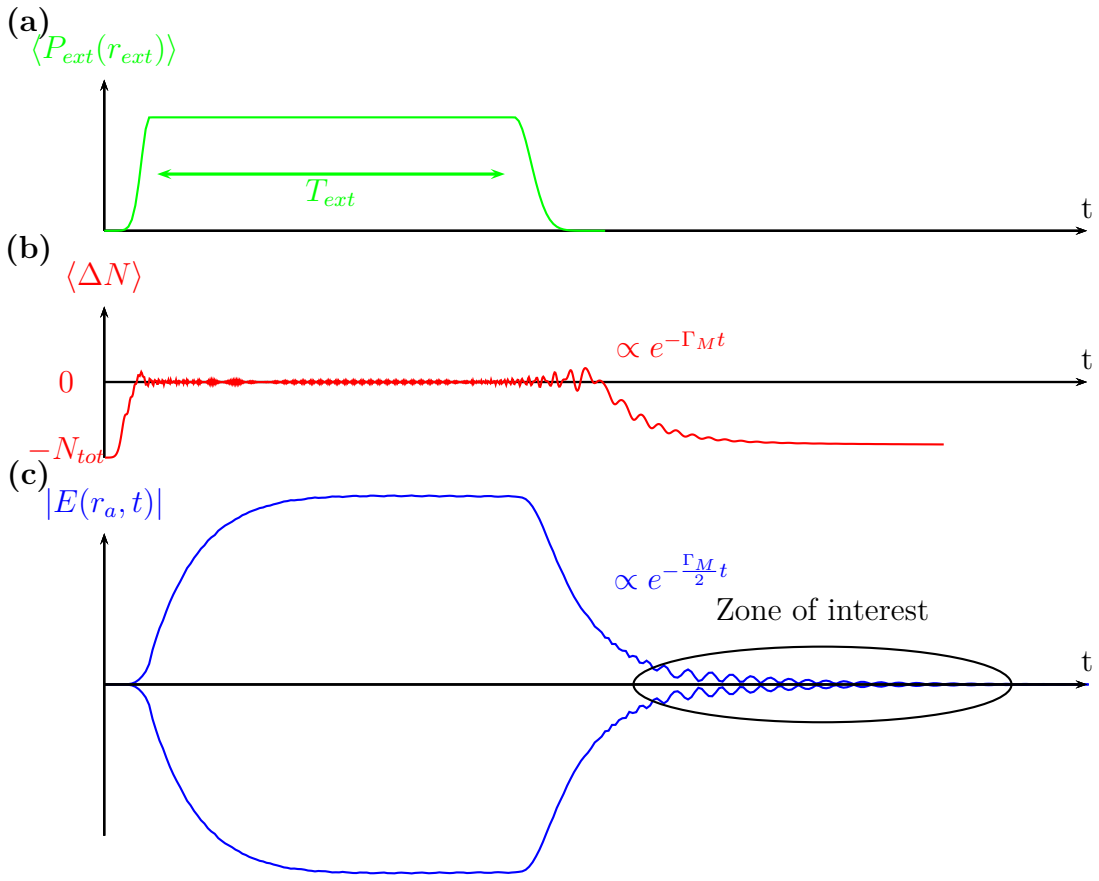

Figure 4.11: **(a)** The envelope of the excitation $P_{ext}(r_{ext})$. **(b)** Averaged population difference $\langle \Delta N \rangle$. **(c)** Envelope of the electric field at the atoms' position $|E(r_a, t)|$.

regime starts and the average population difference decays like the intensity of mode M (see Fig. 4.11**(b)**). The electric field decreases and we observe oscillations of its envelope in a temporal range (referred to as the Zone of interest in Fig. 4.11**(c)**).

Successive observation of non-linear and linear Rabi splittings

We now plot in Fig. 4.12**(a)** the electric field envelope in the final stage of its decay (the Zone of interest in Fig. 4.11**(c)**). As explained in sections 4.2 and 4.3 we can distinguish between two different regimes of oscillations corresponding to non-linear and linear Rabi oscillations. To identify these two regimes, we compute the Fourier transform of

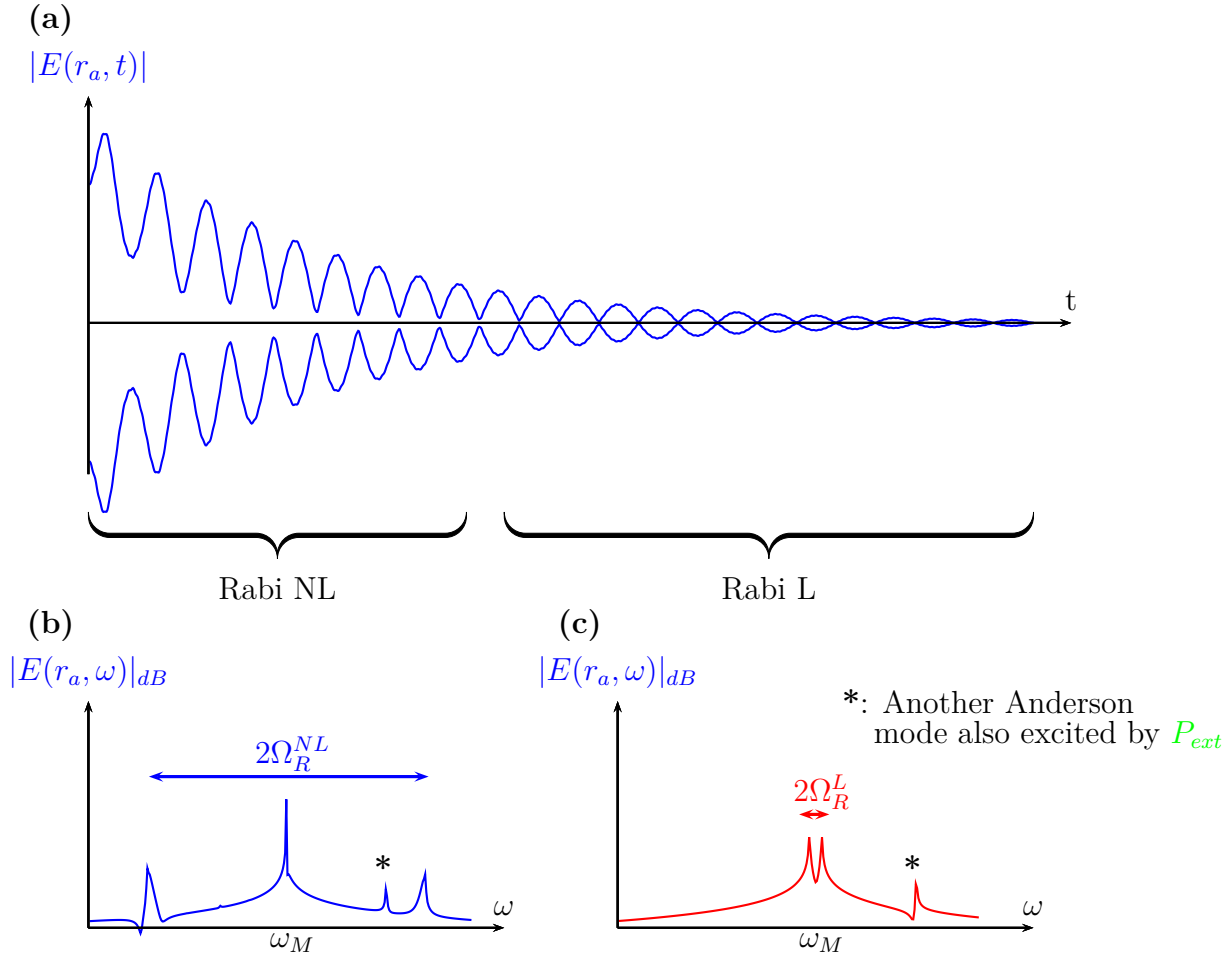

Figure 4.12: **(a)** Electric field envelope at r_a in the transient regime, exhibiting successively non-linear and linear oscillations. **(b)** Spectrum of the electric field in the non-linear regime: Observation of the triplet. **(c)** Spectrum of the electric field in the linear regime: Observation of linear Rabi splitting. The * in both spectra points out the presence of another Anderson-localized mode excited by the external excitation. This mode has no influence on the different Rabi regimes.

the electric field within each temporal domain (see Fig. 4.12**(b)** and **(c)**). At early time, the spectrum is made of three components in the electric spectrum forming the triplet. Afterwards, only two components are present and characterize the strong coupling regime

between the emitter and the mode. An extra peak is present in both spectra and corresponds to another Anderson-localized mode of the system, which was also excited by the source (its amplitude is very low and only appears because a log-scale is used in Fig. 4.12).

Spectra presented in Fig. 4.12**(b)** and **(c)** validate the prediction derived in section 4.4.2. When the field intensity decreases, successively non-linear and linear Rabi regimes occur. This observation of both regimes is made possible by exponential decay over time of the non-linear Rabi splitting and the time independence of the linear Rabi splitting.

4.5 Summary

Here, we have investigated the interaction between a two-level emitter and an Anderson-localized mode.

First, we have recalled the two different regimes of interaction between a two-level atom and the electric field, namely the linear and the non-linear regimes. At low intensity of the electric field, the polarization of the atom is linear: A monochromatic electric field induces a monochromatic polarization of the atom. At high intensity the polarization becomes non-linear: A monochromatic electric field induces a non-monochromatic polarization characterized by three frequency components. This triplet is observable under conditions we have recalled. Then we have considered the linear regime of interaction in the specific case of an electric field supported by a single Anderson-localized mode. Using the biorthogonal formalism of Chapter 2, a condition for strong coupling between the emitter and the mode as well as the resulting linear Rabi splitting have been obtained. Afterwards, we have investigated the non-linear regime of interaction for a similar system, but in presence of an external excitation. In this specific configuration, the condition for the observation of the triplet and the amplitude of the non-linear Rabi splitting have been derived. Finally, the co-existence of both regimes in a temporal experiment has been predicted. Different decay time-scales lead to the consecutive observation of non-linear and linear regimes. This prediction was confirmed numerically by a FDTD computation.

If the strong coupling regime between an Anderson-localized mode and a two-level emitter was to be expected from early works [76, 103, 104, 77], the observation of three components originating from Stark shifts can be seen as the major output of this work. We demonstrate here the possibility of achieving strong light matter interaction using Anderson-localized modes. Therefore, we can think of reaching different strong light matter interaction effects. For instance, Anderson-localized could be used to force the resonance fluorescence of two-level atoms [108]. The sidebands of the generated Mollow triplet are known to emit photons with a particular statistic and specific correlation, and could be used as single-photon sources [112, 113, 114, 115, 116]. Moreover their brightness combined with the easy frequency-tuning of the non-linear Rabi splitting make them good candidates for quantum light spectroscopy.

Part III

Active random media: Random lasers

Chapter 5

Introduction to random laser: Basic concepts and experimental achievements

Table of Contents

A laser is composed of two parts: A gain medium and an optical cavity. The role of the gain medium is to achieve a photonic amplification using stimulated emission (see Chapter 1). In order to illustrate this photonic amplification mechanism, let's consider a flask in which was inserted a four-level system (e.g. Rhodamine diluted in ethanol). When pumped by an external laser, photons are generated by spontaneous emission inside the flask and are amplified before exiting the medium (the term "Amplified Spontaneous Emission" (ASE) is used to describe that phenomenon). The emitted intensity is isotropic and defined by a spectrally broadband emission, which narrows with the pump excitation. Now, let us assume that the medium is embedded in the following optical cavity: Two parallel mirrors, one totally reflecting and the other just partially. This cavity provides a feedback mechanism: The photons make several round trips in the amplifying medium before exiting. The presence of the cavity deeply affects the emission properties. The light amplification is spatially confined to the cavity (e.g. the two mirrors) and the emission direction is fixed (e.g. by the partially reflecting mirror). We know from Chapter 2 that a cavity defines privileged vibrations called modes. These modes "select" photons at specific frequencies, which are duplicated by stimulated emission: Resulting photons are similar or coherent. Hence, only several frequencies could oscillate and the emission intensity is characterized by sharps peaks narrowing with the pump excitation. These peaks are observed when the stimulated emission of coherent photons is predominant, when it compensates for the losses of the cavity (e.g. the partially reflecting mirror). As a result, the lasing intensity exhibits a threshold according to the pump excitation. In the late 1960s, Lethokov [117] proposed to replace the optical cavity by a scattering medium. Instead of creating this feedback mechanism using mirrors, he suggested to embed scatterers within the active medium. Because of multiple scattering, the lifetime of photons inside the gain medium is enhanced and the amplification can compensate for optical cavity losses. He suggested that an amplification similar to "conventional laser" could be achieved in this "random laser". Nevertheless his approach relied on an ASE description. In 1999, Professor Hui Cao [118, 119] observed for the first time characteristics similar to conventional laser (see Fig. 5.5) in a random laser device.

In this chapter, we first introduce the model proposed by Letokhov [117] to give a description of the random laser in the framework of the diffusion approximation. Then, we present the optofluidic random laser, a random laser we have developed [120] and intensively used in the studies presented in this document. Experimental observations will illustrate the limitations of the diffusive model and the requirement of a modal expansion approach as described in Chapter 2.

5.1 The "photonic bomb" model

In this section, we introduce a simple model based on the diffusion approximation to describe the random laser. First we compare the features of a random laser with those of a conventional laser and emphasize their characteristics. Then, we derive the diffusion of photons in a gain medium.

5.1.1 From conventional to random laser

Conventional laser

The standard laser is composed of an externally pumped medium and an optical cavity. In the schematic of Fig. 5.1, the optical cavity is formed by two parallel mirrors. One mirror is totally reflecting while the other is only partially reflecting. A simple description

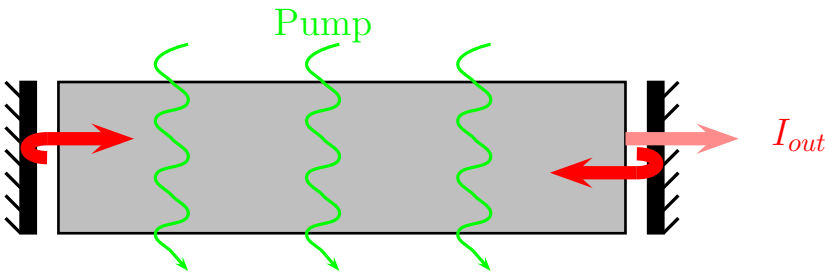

Figure 5.1: Schematic description of an ordinary laser: A gain medium (in gray) is excited by an external pump. The cavity of length L is made of two mirrors, one perfectly reflecting and another partially. This cavity forces the light to experience an amplification several time before escaping. Finally, when amplification reaches the losses, the laser intensity I_{out} is emitted.

of the amplification in the steady state reads

$$\frac{dI}{dz}(z) = I(z)(\alpha - g) \Rightarrow I(z) = I_0 e^{(g-\alpha)z} \tag{5.1}$$

where I is the lasing intensity inside the medium, α the losses and g the gain. The gain g is directly related to the pump intensity while the losses depend on the openness of the cavity. From eq. (5.1), it is clear that if the gain becomes larger than the losses ($g > \alpha$), the lasing emission occurs. Let us assume that the photons make N round trips on average on the cavity of length (L) before exiting. Thus, the average intensity of the laser output reads

$$I_{out} = I(z = 2NL) = I_0 e^{(g-\alpha)2NL} \tag{5.2}$$

Eq. (5.2) carries two main messages. First, the emitted intensity versus pump energy exhibits a threshold (see Fig. 5.2**(a)**). Second, the amplification increases exponentially with the time spent by photons inside the gain medium.

The stimulated emission responsible for the lasing emission is a coherent process: Photons are duplicated. As sketched in Fig. 5.2**(b)**, because of light coherence, narrow peaks appear in the emission spectrum. These peaks are regularly spaced in the spectrum and

the mode spacing is fixed by the cavity length, L. These peaks also become spectrally narrower when pumping is increased. To summarize, a lasing emission is characterized

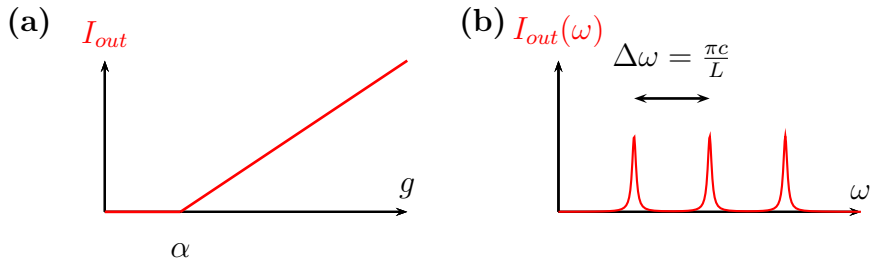

Figure 5.2: **(a)** Lasing output intensity I_{out} versus gain. **(b)** Spectrum of emitted laser intensity I_{out}: It is composed of peaks regularly spaced.

by three main properties:

- A threshold of the emission intensity
- The presence of peaks within the emission spectrum
- A narrowing of peak spectral linewidth

Random laser

In his seminal paper, Letokhov [117] suggested to fill the gain medium with scatterers (see Fig. 5.3) to provide with feedback. In conventional lasers, the time spend by photons in the amplification medium is critical to achieve lasing. In a similar way, in random lasers,

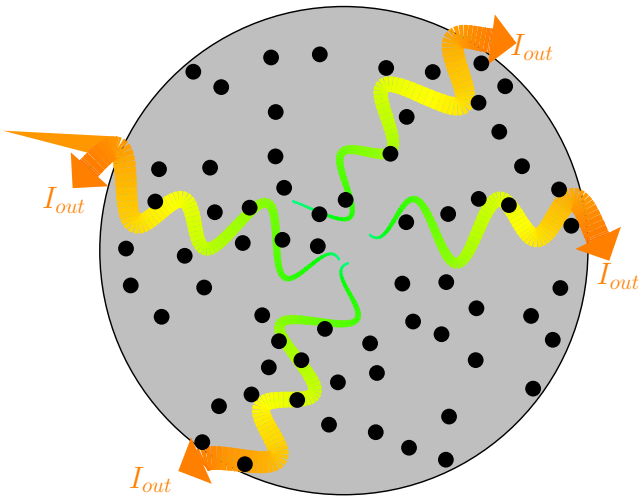

Figure 5.3: Schematic view of random lasing process: A gain medium (in gray) is filled with scatterers (black dots). Photons generated (e.g. in the center of the system) are scattered several times before exiting the medium and thus are amplified, which results in amplification.

the presence of scatterers increases that time. Here the feedback is provided by scattering instead of mirror reflection.

To give a naive picture of the gain mechanism in this system (see Fig. 5.3), we consider a photon emitted by spontaneous emission at the centre of the gain medium. In absence of scatterers, this photon will directly exit from the medium and be hardly amplified. In the presence of scatterers, it will be scattered and therefore spend a very long time before leaving the system [121]. As sketched in Fig. 5.3, if the gain overcomes the losses lasing emission occurs.

As a result, in a similar way to ordinary lasers, if the emission is coherent, this emission should be characterized by a threshold and peaks narrowing with the pump excitation. Unlike ordinary lasers, because the system is disordered, its peaks would be randomly distributed.

Early achievements: Incoherent/coherent random lasers

The first experimental observation of random lasing was made by Gouedard *et al.* [122] in 1993, using a neodymium powder. In this system, gain and scattering were provided by the powder. One year later, Lawandy *et al.* [123], in a controversial experiment [124, 125], observed random lasing emission in a colloidal suspension (see Fig. 5.4). Similarly to a

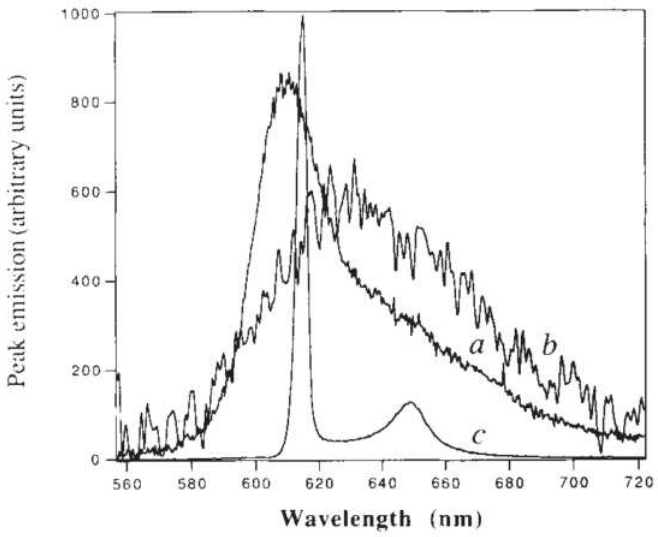

Figure 5.4: First observations of incoherent random lasing in a colloidal suspension by Lawandy *et al.* [123]: **a** Rhodamine fluoresence emission in methanol. **b** and **c** Rhodamine in methanol filled with TiO_2 particles below and above threshold of emission.

classical laser, they observed a threshold for the emission and a narrowing of the spectral linewidth. But unlike standard cavity lasers, they observed a single broadband peak in the spectrum. This type of lasing has been identified as incoherent random lasing, which is similar to ASE.

In 1998-1999, Hui Cao *et al.* demonstrated coherent random lasing in disordered semiconductor powder and polycrystalline films [126, 118] (see Fig. 5.5). In this sample where the disorder was frozen, they observed multiple narrow peaks in the emission. These experiments show that coherent lasing emission can be achieved. In other words, disordered media can emit lasing light with properties similar to conventional lasers.

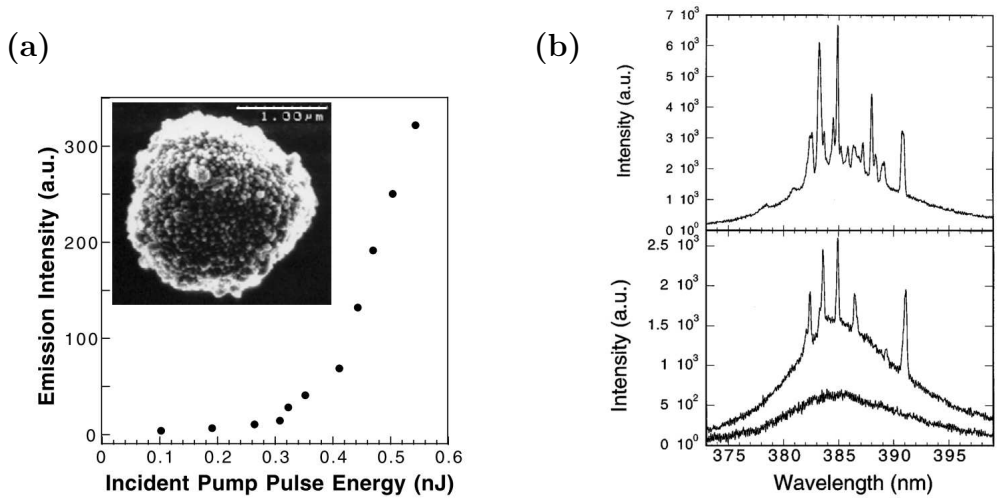

Figure 5.5: First observation of coherent random lasing in ZnO based disordered media by Cao *et al.* [118]. **(a)** They measured a threshold in the emission characteristic. **(b)** Above the threshold, they observed multiple randomly distributed peaks in the emission spectrum narrower than the linewidth of the ASE.

5.1.2 A scattering process ... with gain

Different scattering regimes

The simple description of section 5.1.1, points out that the random lasing process is based on multiple scattering. One can expect that depending on the scattering strength, different scattering regimes can occur as well as different random lasing regimes.

Here we consider the general case of a light beam of intensity I_0 impinging on a scattering sample (see Fig. 5.6). When the light penetrates through the sample, photons are scattered in many different directions. A convenient approach to investigate this problem consists in averaging the scattering over all directions. The average scattered energy can be described by a 1D quantity

$$\langle I(x,y,z)\rangle_R = I(z) \tag{5.3}$$

where R is the radius of the sphere used to average the scattered intensity (see Fig. 5.6).

This scattering problem can now be treated like a 1D slab problem (similar to Chapter 1). The intensity of the incident beam decreases as a function of depth inside the sample according to the Beer's law, which reads

$$I(z) = I_0 e^{-\frac{z}{l_s}} \tag{5.4}$$

where l_s is the scattering mean free path. In a dilute system, it reads

$$l_s = \frac{1}{\rho\sigma_s} \tag{5.5}$$

where σ_s is the scattering cross section of the scattering particles and ρ their density. We saw in Chapter 1, that the transport mean free path can be defined from the scattering

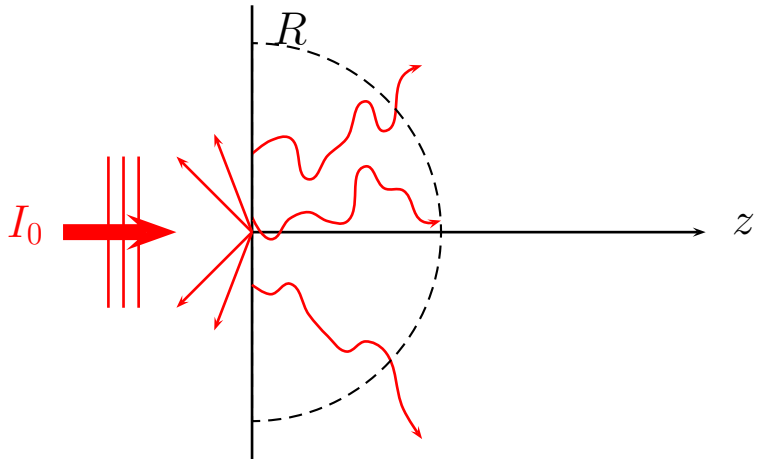

Figure 5.6: A medium is enlightened by an incoming beam of intensity I_0: Part of the photons are scattered back at the interface while others are scattered inside the medium within all directions.

mean free path

$$l_t = \frac{l_s}{1 - \langle cos\ \theta \rangle} \tag{5.6}$$

where $\langle cos\ \theta \rangle$ is the average angle describing the anisotropy of the scattering.

Comparing the transport mean free path with the length of the system allows to classify different regimes of propagation. If the characteristic size of the system L is smaller than the transport mean free path ($L < l_t$), the system is in the ballistic regime. Part of the photons are scattered, while some manage to travel through the system without being scattered. The light keeps memory of the incident direction. When $\lambda < l_t < L$, the light is in the diffusive regime (λ is the light wavelength). Photons follow a random walk inside the system before exiting. A third regime exists, in which the light is spatially localized in the medium. As stated in Chapter 2, in 1D and 2D this regime occurs as soon as the size of the system is larger than the localization length. In 3D, because light is a polarized wave, the possibility of achieving Anderson's localization is still debated [64]. Assuming localization can be performed in 3D, it occurs if the Ioffe-Regel criterion [127, 58, 128] is satisfied

$$l_t \sim \frac{\lambda}{2\pi} \tag{5.7}$$

The "photonic bomb" model

In his seminal work, Letokhov [117] considered a scattering system with a photon mean free path much smaller than the size of the system, therefore placing his theory in the diffusive regime. Similar to a thermal problem, the photons are driven by a diffusion equation (see Chapter 1)

$$\frac{\partial W}{\partial t}(r,t) = D\nabla^2 W(r,t) + \frac{vW(r,t)}{l_g} \tag{5.8}$$

where $W(r,t)$ is the photonic energy density, v the light celerity, D the diffusion constant and l_g the amplification length-scale within the medium. The gain is provided by the term

$\frac{vW(r,t)}{l_g}$ standing for the medium amplification. This gain must compensate the leakage of energy due to diffusion to the outside.

The diffusion constant D fulfills in 3D

$$D = \frac{1}{3} v l_t \tag{5.9}$$

and the diffusion length l_{diff} is defined as

$$l_{diff} = \frac{vL^2}{D} \tag{5.10}$$

It describes the averaged length spent by a photon in the system. Eq. (5.10) leads to the time scale

$$\tau_{diff} = \frac{l_{diff}}{v} \tag{5.11}$$

The gain time scale τ_g is driven by the length scale l_g

$$\tau_g = \frac{l_g}{v} \tag{5.12}$$

To achieve photonic amplification, the time spent by the photon inside the system (τ_{diff}) must be important enough to allow for the generation of a least one extra photon (τ_g), which reads

$$\tau_{diff} > \tau_g \tag{5.13}$$

The amplification condition of eq. (5.13) reads

$$\frac{L^2}{\frac{1}{3} v l_t} > \frac{l_g}{v} \Rightarrow 3L^2 > l_t l_g \tag{5.14}$$

Therefore, when the excited system reaches a critical value, the photonic energy density explodes. This "photonic bomb" effect, occurs at a threshold limit

$$L_c = \sqrt{\frac{l_t l_g}{3}} \tag{5.15}$$

This simple model similar to Letokhov's approach [117] defines a critical value for the lasing to happen. It can be understood like the threshold of the random laser emission. This resulting threshold is required in neutron scattering to observe nuclear fission [129], hence is sometimes named "photon bomb".

5.2 The optofluidic random laser

Various random laser devices have been proposed in the literature based on a large variety of technical processes [130, 131]. In this section, we present microfluidic-based random lasers developed in collaboration with Shivakiran Bhaktha and Xavier Noblin [120]. Using routine techniques in microfluidic engineering, we achieve on-demand 1D and 2D random lasers with controlled disorder strength. First, we recall the advantages of optofluidic devices and introduce the fabrication process of microfluidic random lasers. Then we present the characterization of a 1D optofluidic random laser. Finally, we perform similar study on 2D optofluidic random lasers.

5.2.1 Advantages of optofluidic devices

Optofluidic devices are an innovative and emerging field. Indeed, manipulating light at micro-scale is particularly attractive for all set of lab-on-chip applications and opens avenues for sensing applications [132, 133]. In particular, developing optofluidic lasers is of major interest for micro-scale optical systems.

An optofluidic laser source is composed of a micro-channel filled with dye (in many applications optically pumped). Unlike solid states lasers, optofluidic lasers have great fabrication flexibility, which makes them experimentally convenient. For instance, because they are produced from a mold, the bulk material can be easily changed and they can be reproduced with a good accuracy. The circulating dye can be removed and its concentration can be adjusted by enhancing the pressure. As a result, they can be re-configured on-demand. Moreover, their fabrication can lead to almost any 1D or 2D patterns and such devices can be arranged to create optofluidic networks. Because a flow circulation is enforced inside the microchannel, the dye is continuously replaced, which precludes the bleaching of dye molecules. Finally, in the specific case of optofluidic random laser devices, disordered is naturally achieved as a result of the limited accuracy of the photolithographic process. The scattering is fixed by the pattern and the index contrast between the bulk material and the dye solvent. Consequently, the disorder strength can be precisely adjusted.

5.2.2 Fabrication process

Different microfluidic channels have been fabricated following the soft lithography protocol described by Xia and Whitesides [134]. For instance, Fig. 5.7 shows a 1D serpentine-like channel and a 2D random device. Two types of bulk material have been used for their different optical properties.

First, for each pattern, a structured mask is used to form the corresponding thick negative photoresist SU-8 mold. The mask is unlighted by a UV lamp at 365 nm. Its resolution is of 25,400 dpi. The diffraction at 365nm and imperfect adhesion of the mask on the resin limit the resolution of the photolithography process leading to fluctuations in the mold vertical walls position. At the optical scale, the structures are therefore not periodic as it may appear to the naked eye in Fig. 5.7 but totally random. The mold is used to replicate the microstructures.

Polydimethylsiloxane (PDMS) or resin (OE-7620, from Dow Corning) is poured into the mold and then degassed before being cured. After perforating holes in the device for the inlets, the microchannel is bonded on glass slides by plasma treatment. Rhodamine 6G dye solution in ethanol circulates into the microchannel through the tubes connected to the inlets. Index of refraction of the dye is $n_{dye} = 1.36$ and refractive index of the polymer and the resin are respectively $n_{PDMS} = 1.42$ and $n_{OE} = 1.60$.

5.2.3 1D optofluidic random laser

One dimensional random lasing is achieved using the serpentine pattern of Fig. 5.7**(a)** in polymer PDMS filled with Rhodamine dye of concentration 2.5 mM in ethanol. The re-

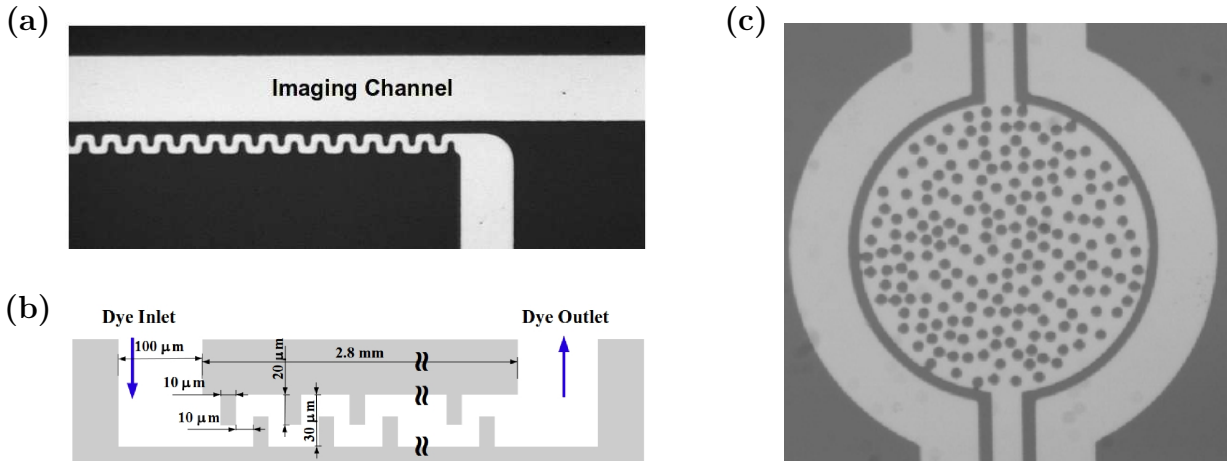

Figure 5.7: **(a)** and **(b)** A 1D serpentine pattern: The dye flows in a channel designed into resin or PDMS bulk. An auxiliary channel (Imaginary channel) is present to collect light emitted from the laser. **(c)** A 2D optofluidic random laser: The dye flows in the central part between the pillars made in resin or PDMS. Two auxiliary channels surround the central structure to collect light.

sulting refractive index contrast is $\Delta n = n_{PDMS} - n_{dye} = 0.06$. As sketched in Fig. 5.7**(b)**, the period of the pattern is 40 μm, the polymer pegs are 10 μm thick and 20 μm-long. The microchannel is 28 μm-deep and the fluctuation on pegs thickness is $\pm$ 0.65 μm. The total length of the structure is 2.8 mm long and is much smaller than the transport mean free path (of several cm)[1]. The system is in the ballistic regime of scattering. The second harmonic (@532 nm) of a Q-switched Nd:YAG laser (6 ns pulsewidth, 20Hz repetition rate) is used to excite the system. A cylindrical lens turns the pump beam into a 3 mm-long and 4 μm-thick stripe (see Fig. 5.8**(a)**). Only one part of the serpentine is pumped. The narrow stripe pump provides uniform illumination and forces the dye emission along the length of the channel. The emission spectrum is recorded with the fiber probe of a HR4000 (Ocean Optics) spectrometer having a spectral resolution of 0.11 nm. During the experiments, the random optofluidic channel is imaged with the help of a Zeiss Axioexaminer microscope and a Hamamatsu Orca-R2 silicon CCD camera, to ensure perfect alignment of the pump stripe with the channel (see Fig. 5.8**(a)**).

Due to the inherent disorder of the structure, the stimulated photons, channelized by the pump stripe, are multiply scattered at each PDMS-dye interface and eventually exhibit random laser action when the losses are overcome. In Fig. 5.8**(b)**, the emission intensity of the optofluidic random laser is plotted against the input fluence. Inset to the left is a photograph of the emission of the dye-filled optofluidic channel when pumped by a green laser. In Fig. 5.8**(c)**, the emission spectrum is recorded at a pump fluence of 233 μJ/mm^2. The pulse to pulse variations of the spectrum and the average spectrum are plotted. Fig. 5.8 exhibits clear signatures of coherent random lasing emission. We observe a threshold of lasing emission, which is determined to be about 80 μJ/mm^2. We point out that this threshold value is comparable with values found in the literature for precisely designed optofluidic lasers. Single shot spectra are shown in Fig. 5.8**(c)**,

[1]We use a Transfer Matrix approach (introduced in Chapter 6) to estimate numerically the mean free path.

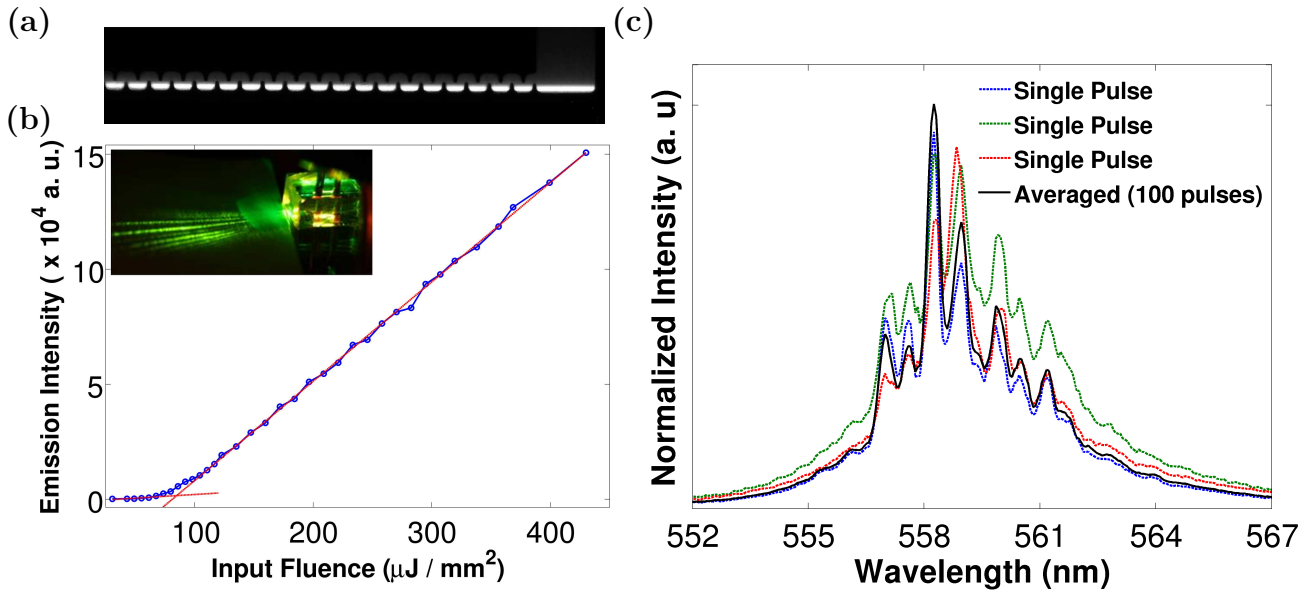

Figure 5.8: **(a)** A part of a 1D serpentine channel PDMS made and filled with Rhodamine diluted in ethanol is pumped by a stripe laser line (white line). **(b)** Emission occurs in the direction of the stripe line and is collected by a fiber. The integrated intensity exhibits a clear threshold characteristic of lasing emission. **(c)** Shot-to-shot spectra and average spectrum: All acquisitions exhibit peaks at the same positions in the spectrum.

together with the 100-pulse averaged spectrum. The emission spectrum is composed of randomly distributed peaks with a linewidth of about 0.3 nm. Since this corresponds to the instrument resolution limit, the actual emission spectrum is expected to be denser and the laser peaks to be sharper. Fig. 5.8**(c)** shows that the spectral position of the peaks does not vary from shot to shot. As a result, we can claim that the random lasing emission is coherent.

5.2.4 2D optofluidic random laser

Random laser are cavity free sources, thus their emission is not spatially constrained. To investigate the directional properties of the emission, we developed a 2D sample as shown in Fig. 5.7**(c)**.

In this 2D device, the losses occur in all the directions and are not restricted to a line (as in 1D device). To compensate for this increase of losses, we use a resin (OE-7620, Dow Corning) instead of the PDMS to achieve higher scattering. The resulting refractive index contrast is $\Delta n = n_{OE} - n_{dye} = 0.18$ and the system is in the ballistic regime of scattering.

The 2D design of Fig. 5.7**(c)**, is composed of a central part and two auxiliary channels. The central part of diameter 500 μm contains 201 pillars of radius 10 μm, leading to a filling fraction of $\phi = 0.32$. A flow of Rhodamine dye (emitting around 565 nm) of concentration 2.5 mM in ethanol provides for the gain. The excitation is achieved by the second harmonic (@532 nm) of an EKSPLA diode-pumped high energy mode-locked Nd:YAG laser (30 ps pulsewidth, 50 Hz repetition rate). The two auxiliary channels, filled with a Nile Blue dye of concentration 2.5 mM in ethanol remain non pumped. Nile blue

absorption bandwidth is centred around 625 nm (with a Full Width at Half Maximum of 80 nm) in ethanol solution. Thus the scattering of the pump (532 nm) is not absorbed within the channels, while the emission from the random laser ($\approx$ 565 nm) is. Hence, light emitted in the channels is a direct signature of the random lasing emission.

The system is imaged using a Hamamatsu Orca-R2 silicon CCD camera microscope. The emission is collected via an optical fibre connected to a Horiba iHR550 imaging spectrometer equipped with a 2,400 l.mm^{-1} grating and a liquid nitrogen-cooled Symphony II camera (sampling rate 1 MHz, 1,024 $\times$ 56 pixels, 26 μm pixel pitch). The entrance slit is 50 μm. The resulting spectral resolution is 20 pm. The integrating time is 1 s. In Fig. 5.9**(a)**, the emission intensity is integrated over the spectrum plotted for different input pump fluences. We also plot in Fig. 5.9**(b)**, the emitted spectra for different pump fluences.

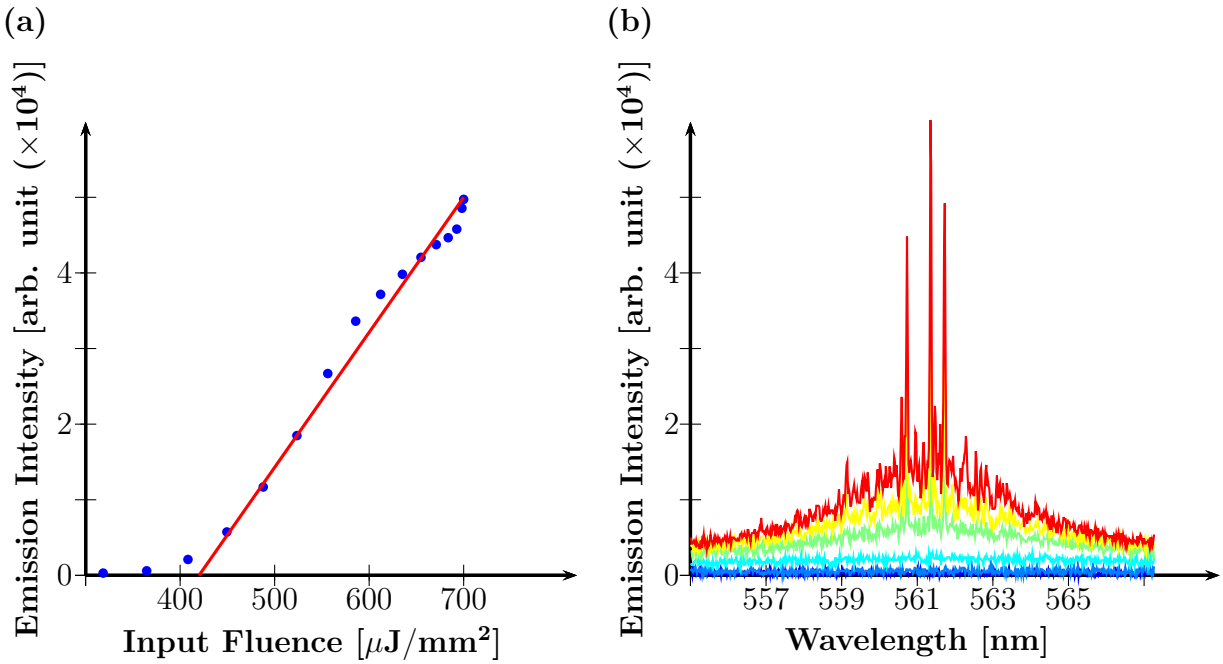

Figure 5.9: **(a)** Emission intensity integrated over the whole spectrum. **(b)** Random laser spectrum for different pump intensities.

Emission properties of the device are similar to the 1D system and characteristics of a coherent random laser. The emission intensity exhibits a clear threshold at 420 μJ/mm^2 (see Fig. 5.9**(a)**). The spectrum is composed of randomly positioned peaks (see Fig. 5.9**(b)**). Using the auxiliary channels, images of the random lasing emission are taken below and above threshold in Fig. 5.10**(a)** and 5.10**(b)**. Below threshold, the emission within the channel is only spontaneous emission: The emission pattern is smooth and isotropic. Above threshold, the pattern becomes structured and exhibits rays.

Therefore, this 2D device also provides the characteristics of a lasing emission. Moreover, it represents an interesting platform to investigate spatial properties of random lasing emission.

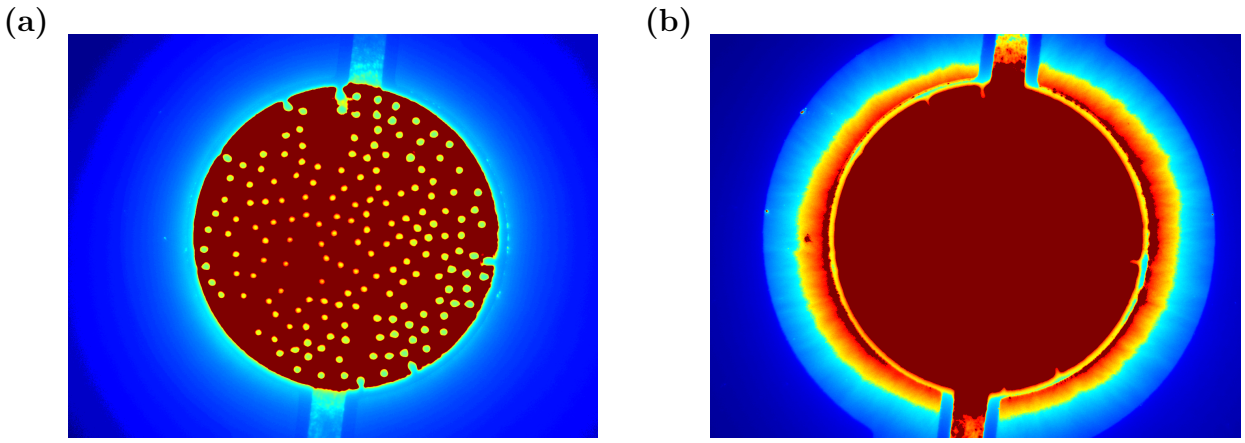

Figure 5.10: **(a)** Image of the random lasing system below threshold: The light absorbed and re-emitted from the imaginary channels is isotropic. **(b)** Random lasing above threshold: Light in the imaginary channels is non-isotropic and exhibits some stripes.

5.3 An energetic model for random laser ... an incomplete description

Experimental observations presented in section 5.2 cannot be described in the framework of the Letokhov model of random lasing. In this section, we complete this approach by introducing gain medium population equations (see the four-level medium description in Chapter 1). This energetic model gives an intuitive overview of the light-matter interaction involved in random lasing emission. Nevertheless, a complete understanding of random lasing requires to go beyond this basic energetic approach. The wave nature of the field and its modal expansion must be considered for an accurate description.

5.3.1 An energetic model

The "photonic bomb" model is not valid above threshold. As we observed experimentally, the lasing intensity increases progressively with the pump intensity. Indeed, because the gain medium only provides a finite amplification, the gain length-scale (l_t) decreases above the threshold. The gain saturates until a balance is found. Moreover, this model does not explain the narrowing of emission peaks. To give a more complete description of the random lasing mechanism, the gain medium saturation must be considered. Several approaches have been proposed in the past [135, 136, 14, 137, 138, 139] in order to model experimental observations. Here, we consider early descriptions suggested by Wiersma *et al.* [14].

In this approach, they considered a gain medium similar to a four-level system optically pumped in the diffusive regime, able to give a simplified description of gain media (e.g. Rhodamine, Ti/Sapphire) (see Chapter 1 and Fig. 5.11). Populations for each level are referred to as $\{N_i(r,t)\}_{i\in[1,4]}$. In this medium, the transitions from (3) to (2) and (1) to (0) are extremely fast compared to the radiative transition (2) to (1). This radiative transition is characterized by an emitting cross section σ_{em}, an absorbing cross section σ_{abs} and a spontaneous decay τ_e (see Chapter 1 for explanation). Noting N_{tot} the total

density of carrier

$$N_{tot} \approx N_2(t) - N_0(t) \tag{5.16}$$

and thus the population can simply be derived from the evolution of $N_2(t)$. They suggested

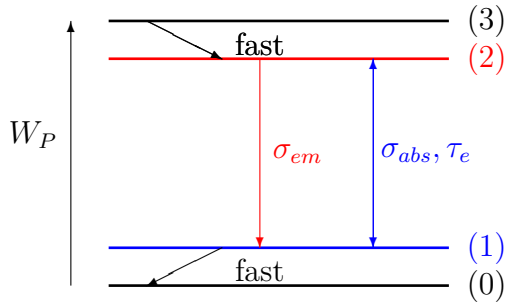

Figure 5.11: The gain medium described by a four-level system: The pump W_P excites carriers from state (0) to the upper level (3). Non-radiative decays from (3)/(2) and (1)/(0) are much faster than the radiative transition (2)/(1).

to consider two different energy densities, respectively W_P for the pump and W_F for the random lasing emitted energy. To mimic the incoming energy due to the optical pump, they used an incident beam I_{coll}. The complete set of equations reads

$$\frac{\partial N_2}{\partial t}(z,t) = \sigma_{abs} v (N_{tot} - N_2) W_p - \sigma_{em} v N_2 W_F - \frac{1}{\tau_e} N_2 \tag{5.17}$$

$$\frac{\partial W_P}{\partial t}(z,t) = D\nabla^2 W_P - \sigma_{abs} v (N_{tot} - N_2) W_P + \frac{1}{l_s(1-g)} I_{coll}(z,t) \tag{5.18}$$

$$\frac{\partial W_F}{\partial t}(z,t) = D\nabla^2 W_F + \sigma_{em} v N_2 W_F + \frac{1}{\tau_e} N_2 \tag{5.19}$$

The model proposed in eq. (5.17-5.19) completes the Letokhov's description. The "photonic bomb" gain length l_g introduced in eq. (5.8) reads

$$l_g = \frac{1}{\sigma_{em} N_2} \tag{5.20}$$

The gain is directly triggered by the density of excited atoms N_2, which is linked to the pump excitation by eq. (5.17-5.18). When the lasing intensity increases, the excited population N_2 decreases, leading to a longer amplification length l_t. Photons need to spend more time in the medium to be duplicated: The amplification saturates.

5.3.2 Incoherent random laser

Steady state description

In the steady state regime, the incident beam is scattered in the sample according to the Beer's law given in eq. (5.4)

$$I_{coll}(z,t) = I_0 e^{-\frac{z}{l_s}} \tag{5.21}$$

The incident beam I_{coll} is converted into pump photons via eq. (5.18). The pump photons density W_P is absorbed by the gain medium $\sigma_{abs} v (N_{tot} - N_2) W_p$ and excites population

N_2. These excited carriers give rise to random laser photons W_F, by either stimulated $\sigma_{em} v N_2 W_F$ or spontaneous emission $\frac{1}{\tau_e} N_2$. This leads to an increase in the lasing energy density W_F. The amplitude of the incident beam I_0 triggers N_2, which is responsible for the gain length. Hence, using a reasoning similar to the one developed in section 5.1, we can derive a excitation threshold $I_{0,th}$ for I_0.

The spectral narrowing observed by Lawandy *et al.* [123] (see section 5.1.1), can also be described by introducing a frequency-dependent emission cross section. More amplification will be provided at light frequencies closest to the atomic resonance frequency, the gain at these frequencies will be first to match the loss as the pumping rate is increased. Outside this frequency region, amplification is still lower than the loss rate. With a maximum amplification close to the maximum of the gain curve, the spectral width of the emission peak will narrow.

Dynamic description

This model allows to go beyond the steady state regime and to describe temporal oscillations of the emission density W_F (see Fig. 5.12). For that matter, we model the incoming pump by a pulse

$$I_{coll}(z,t) = I_0 e^{-\frac{z}{l_s}} e^{-\frac{(t-z/v)^2}{2c^2}} \tag{5.22}$$

where $I_0 \gg I_{th}$.

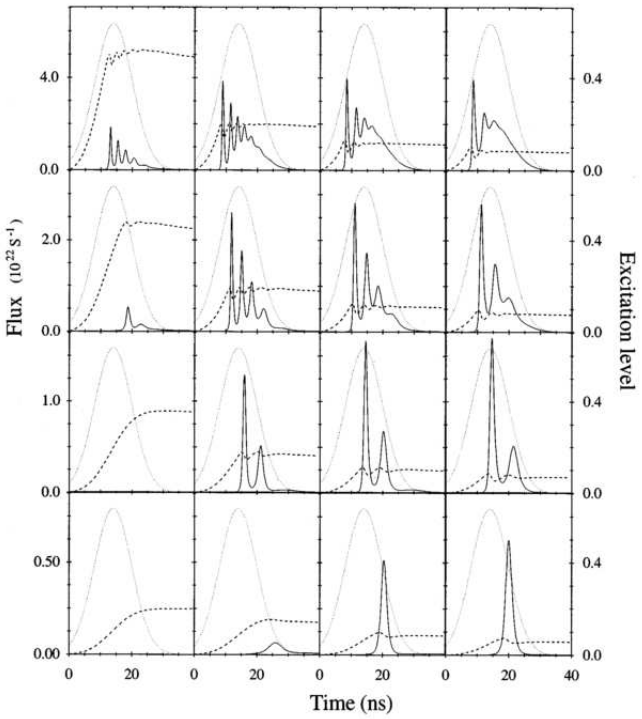

Figure 5.12: Evolution of W_F over time for different input pulse intensities I_0 [14]: Dashed curves $N_2(t)$ and solid curves $W_F(t)$. For high pump intensity the emission fluence oscillates over time.

For large input pulse, because the laser density W_F needs some time to build-up, the population N_2 overshoots above its steady state value, inducing a sharp increase in lasing

emission W_F. Because W_F is multiply scattered, it needs some time to exit the system, which induces a new overshoot of N_2, leading to a new temporal lasing peak *etc.* Hence, the lasing intensity oscillates.

5.3.3 Coherent random laser: Need of a modal description

In conventional lasers the feedback is provided by the mirrors, which reflect the electric field. The cavity responsible for the feedback defines privileged oscillations of the electric field called modes. The amplification of these modes by the gain medium leads to peaks in the lasing spectrum and the emitted light is coherent.

In section 5.2, we shown that random lasers can exhibit similar peaks randomly distributed. Hence, the gain amplifies the modes of the underlying disordered system. Like in conventional lasers, the modes of the random laser result from a feedback on the electric field provided by the scattering. Such lasers are called lasers with coherent feedback in contrast to random lasers with incoherent feedback (see section 5.1.1).

The energetic model derived from eq. (5.17-5.18) considers the total lasing energy. More specifically, the photonic density is described by a diffusion process. It assumes that the scattering performs an incoherent or intensity feedback. As a result, the presence of peaks in the microfluidic spectra observed in section 5.2 cannot be described with an energetic approach which ignores the phase. A description of coherent feedback amplification requires to consider the modes of the disordered system.

5.4 Summary

In the present chapter, we have introduced the concept of random laser and presented microfluidic devices we have developed.

We have explained that in random lasers, the necessary feedback for lasing to occur is provided by the presence of scatterers. The scattering increases the photons dwell time inside the system leading to their amplification. A diffusion model describes the explosion of the photon density above a certain amplification and introduces a threshold. Early experimental achievements of random lasers have been reminded, where two distinct kinds of random lasers emerged, namely the coherent and incoherent random lasers. Then we have presented an innovative technique to process on-demand microfluidic random lasers. 1D and 2D structures with precisely controlled scattering have been fabricated and allow to investigate random lasing properties (e.g. randomly distributed spectral modes, non-directive emission). Finally, we have completed the diffusion model by studying the saturation of the gain medium we have considered as a four-level atomic system. This model emphasizes the necessity of a modal expansion of the electric field is required to describe the coherent random laser emission.

Chapter 6

Modes in random lasers: Below and Above threshold

Table of Contents

Lasing requires the combination of amplification and feedback. In random lasers, the feedback is provided by scattering instead of optical cavity for ordinary lasers. We stated in Chapter 5 that the description of coherent random laser requires to go beyond the simple energy diffusion process and to consider the modes of the electric field. In a similar way to ordinary laser, the gain medium "feeds" the modes of the random passive system. After the first historical achievement of maser and laser in the late 50's and early 60's [140, 141, 142, 143, 144, 145], theoretical description was developed independently by Haken and Sauermann on one hand [146] and Lamb and coworkers on the other hand [147, 148]. In this so-called semiclassical approach, the electric field is derived from classical electromagnetism with Maxwell's equation, while the medium is described by quantum equations of motion (see Chapter 1). The amplification of modes is achieved via a non-linear polarization of the gain medium. The semiclassical description was consistently used to describe both numerically and analytically many non-linear effects of standard lasers [9]. After the pioneer work of Hui Cao and coworkers [118], this model was applied numerically to random lasers [149, 109, 66, 110]. Effects observed in conventional laser, such as mode competition, gain saturation and temporal oscillations, were predicted in coherent random lasers [150, 151]. Nevertheless, the physics of regular and random lasers modes is not necessarily the same. Indeed, in conventional lasers, the passive modes of the cavity have large quality factors. Hence, these modes are "almost hermitian", which means that they are "almost orthogonal" vibrations (see Chapter 2). Precluding any pulling effect due to the gain medium, one can say that they are hardly affected by the gain medium. By contrast, passive modes in random lasers are provided by the disordered system, which is open and therefore non-hermitian. Consequently random lasers naturally experiment coupling (see Chapter 3 for an illustration) and they are highly affected by the pumping. The study of conventional lasers can be understood as an "almost hermitian" problem in term of modes, whereas random lasers must be investigated within the scope of non-hermitian physics. In the theoretical understanding of random laser, the works of Deych [152, 153, 40] stands for a major step forward. Using the biorthogonal formalism, he derived the semiclassical model in the scope of the cubic approximation used by Haken and Sauermann in their seminal paper [146]. Turecï *et al.* [44] developed a numerical/analytical description based on a set of modes, named the constant flux states. This allowed them to go beyond the cubic approximation.

In this chapter, we carry on the original approach of Deych [152] and analytically investigate the modes of random lasers. In the scope of this manuscript, we apply this approach in the specific case where modal expansion is achieved with the Siegert states and the corresponding biorthogonal formalism introduced in Chapter 2. Furthermore, a perturbation expansion is performed to derive the complex frequencies and the spatial distributions of the modes. The results proposed in this chapter are preliminary. The purpose of that study is to bring a theoretical insight to Chapters 7 and 8. First, we stress the necessity of considering two distinct regimes of random lasing, requiring two distinct descriptions. When no mode is lasing, the laser is below threshold and the evolution of the electric field resulting from light-matter interaction is described by linear coupling of passive modes. Above threshold, the evolution of the electric field is non-linear because of hole-burning

effect and modes couple non-linearly. Then, using the biorthogonal formalism, we investigate the evolution of mode below threshold and describe the mode mixing. Finally, we consider the evolution above threshold in the cubic approximation. The modes couple both linearly and non-linearly and a balance between gain and loss stabilizes the lasing emission.

6.1 Below and Above threshold description of random lasers

The lasing emission is a non-linear process characterized by the presence of a threshold in emission intensity versus pump excitation. In this manuscript, we make a distinction between the non-lasing and the lasing modes: Modes below and above threshold are referred to as active and lasing, respectively. In the present chapter we aim at expressing these modes in term of passive modes *i.e.* modes of the unpumped/passive system. In this section, we first introduce the descriptions of random laser below and above threshold. Then, we model the random laser in both regimes using the semiclassical theory as proposed in [152, 44].

6.1.1 Introduction

Active modes, below threshold

In the "photonic bomb" model (see Chapter 2) introduced by Letokhov [117], the random laser was understood as a gain medium filled with scatterers. In the modal description, the random laser is rather the superposition of a passive system amplified by a gain medium.

As a guideline example, we consider the case of a 1D random system (see Fig. 6.1). This passive system is composed of slabs of random size, made of dielectric components with refractive indicee n and $n + \Delta n$. The electromagnetic modes of the passive system are

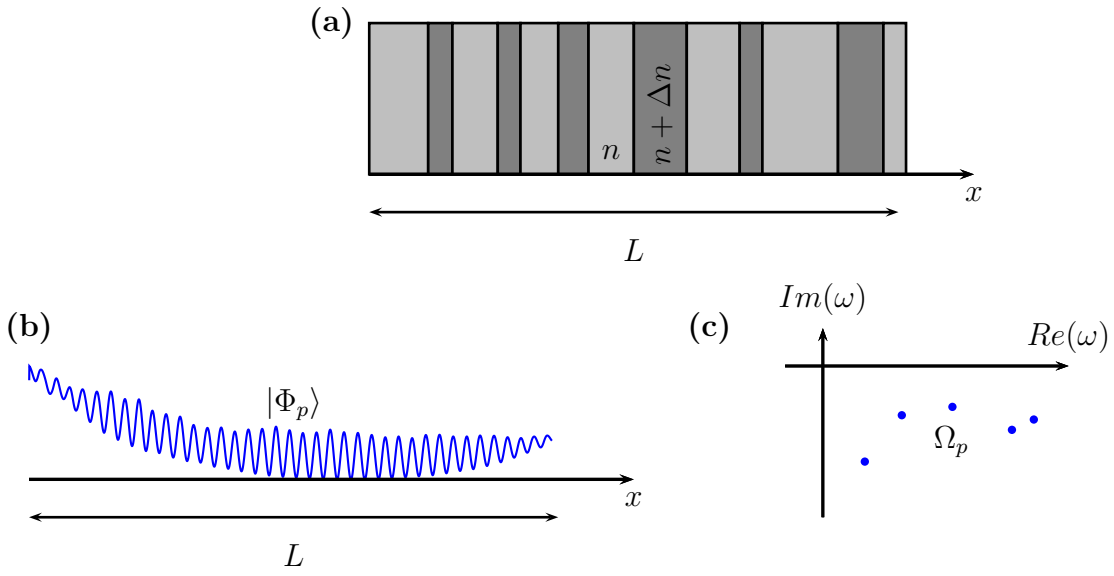

Figure 6.1: **(a)** Schematic representation of a 1D random medium of length L: Superposition of slabs of indices n and $n + \Delta n$. **(b)** Spatial distribution of one specific passive mode $|\Phi_p\rangle$. This mode has been computed with a Transfer Matrix Approach we present later on in section 6.2.4. **(c)** The position of the passive complex frequencies within the complex plane.

determined by the random structure. In the example of spatial distribution and complex

frequency proposed of Fig. 6.1**(b)** and **(c)**, the mode is extended as the disordered system is weakly scattering (see Chapter 2).

Now, within the system, we introduce some gain described by a linear susceptibility $\chi_g(\omega)$. This linear susceptibility affects the refractive index of the system. The refractive indices $\tilde{n}$ and $\tilde{n} + \Delta\tilde{n}$ are now complex and frequency dependent. This new distribution gives rise to new modes referred to as active modes (see Fig. 6.2). The complex frequency $\tilde{\Omega}_p$ and spatial distribution $|\tilde{\Phi}_p\rangle$ of active modes differ from the passive ones (see Fig. 6.2). As sketched in Fig. 6.2**(a)**, active modes are determined by the superposition of passive system and gain.

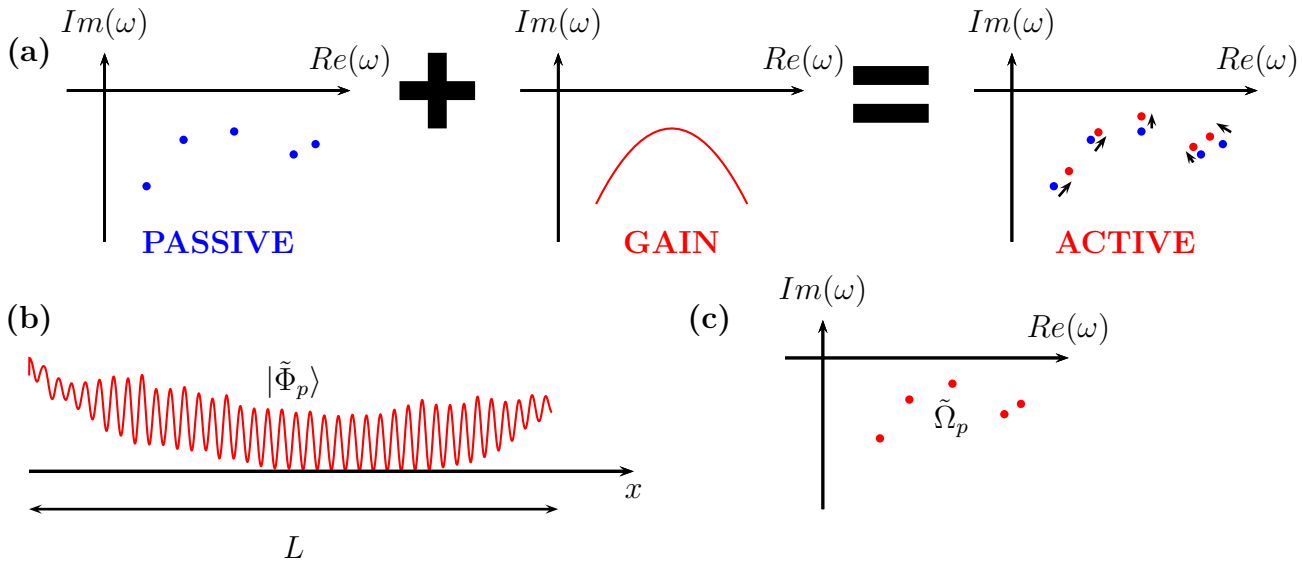

Figure 6.2: **(a)** Schematic description of the active modes: Gain is added to the passive system and resulting modes are called actives modes when below threshold. **(b)** Spatial distribution of one specific active mode $|\tilde{\Phi}_p\rangle$. **(c)** The position of active complex frequencies within the complex plane.

The susceptibility of the gain medium depends on the pump excitation. When the pump excitation is increased, complex frequency of the active modes are brought closer to the real axis. If the complex frequency crosses the real axis, its amplitude diverges in time. This divergence, similar to the Letokhov's "photonic bomb" (see Chapter 5), mimics the lasing emission for each mode. For each individual active mode, the corresponding excitation necessary to bring the mode to the real axis defines its threshold. Below threshold, all the modes are non-lasing and called active: The modes are free of non-linear amplification and mode competition.

Lasing modes above threshold

Above threshold, the divergence of mode amplitude (see section 6.1.1) is impeded by the saturation of the gain. Mathematically, in the complex plane, the imaginary part of the eigenvalue remains strictly zero when the threshold is reached. Physically, the carrier density providing the amplification saturates and a balance between losses and gain sets the amplitude of the mode. As a result, the gain medium can no longer be described

by a linear susceptibility and the evolution of the mode is non-linear. In Fig. 6.3, we draw the schematic evolution of the mode in the complex plane for an increasing pump excitation. The modes start lasing successively and their complex frequencies remain purely real. Therefore, the random laser will be in the above threshold regime as soon as the first mode starts lasing. Thus, the gain is non-linear above threshold and decreases.

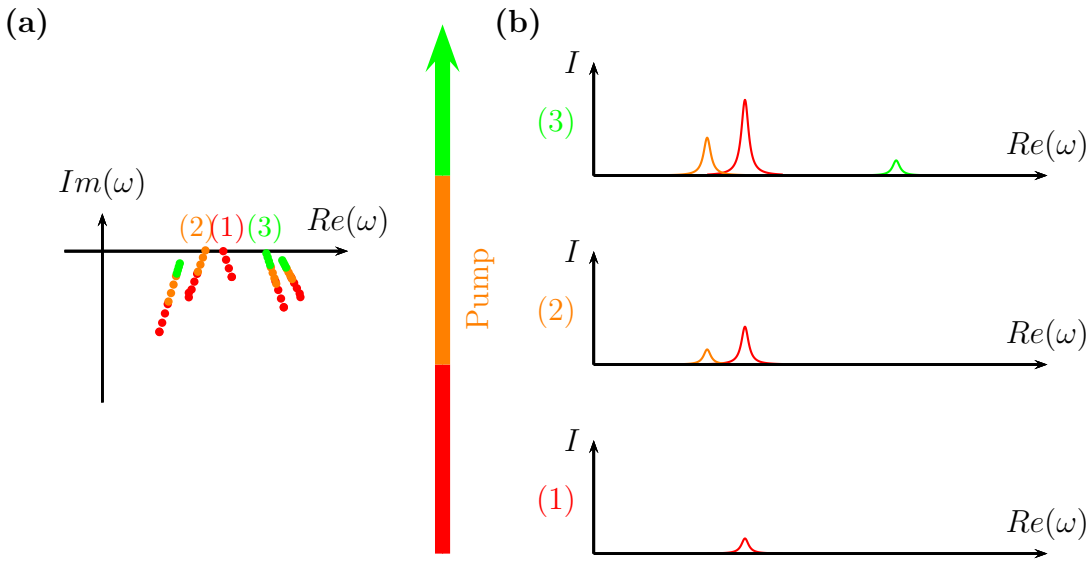

Figure 6.3: **(a)** Schematic example of complex frequencies of modes for an increasing excitation: When below real axis modes are not emitting and referred to as active. When modes reach the real axis they start lasing and referred to as lasing modes. Their imaginary parts remain zero. **(b)** Schematic evolution of the emission spectrum for different excitations.

This is the so-called saturation of the gain, due to spatial hole burning. The physical origin of hole-burning is related to the finite density of carrier, in other words the finite amplification that the medium can provide. The saturation affecting the thresholds of other modes, it may either forbid modes to lase or lead to complex transient regimes [154]. Nevertheless, the saturation is required to stabilise the lasing emission as we will see below.

6.1.2 Modelling the random laser

The passive system

The passive system is modelled by a dielectric medium characterized by a non-uniform distribution of the refractive index $n(r)$ (see Fig. 6.1**(a)**). In the semiclassical approach, the electric field is considered classic and requires no quantization. As demonstrated in Chapter 1, its evolution in 1D or 2D passive systems satisfies the Helmholtz equation

$$\Delta E(r,\omega) + n^2(r)\omega^2 E(r,\omega) = 0 \tag{6.1}$$

The modes of the passive system are derived using Siegert's approach developed in Chapter 2

$$\left(\Phi_p, \Omega_p = \omega_p - i\frac{\Gamma_p}{2}\right) \quad | \quad \Delta|\Phi_p\rangle + n^2(r)\Omega_p^2|\Phi_p\rangle = 0 \quad \& \quad \frac{d}{dr}|\Phi_p\rangle - i\Omega_p|\Phi_p\rangle\Big|_{r\to\infty} = 0 \tag{6.2}$$

Furthermore, the refractive index distribution is assumed to fulfil the no-tail and discontinuity conditions required to apply the biorthogonal description introduced in Chapter 2. Hence the set of passive modes defines a complete basis and the biorthogonal product can be used to derive the expansion coefficients along them (see Chapter 2)

$$E(r,t) = \sum a_p e^{-i\Omega_p t}|\Phi_p\rangle \quad \Leftrightarrow E(r,\omega) = \sum a_p \frac{1}{i\Omega_p - i\omega}|\Phi_p\rangle \tag{6.3}$$

The gain

In the semiclassical model, the gain is assumed to be provided by four-level quantum emitters (see description in Chapter 1). The introduction of gain into the system leads to a polarization term in Helmholtz equation (6.1), which translates the light-matter interaction

$$\Delta E(r,\omega) + n^2(r)\omega^2 E(r,\omega) = -\omega^2 P(r,\omega) \tag{6.4}$$

The different population of the four levels N_i are given by the population equations

$$\frac{dN_3}{dt} = P_r N_0 - \frac{N_3}{\tau_{32}} \tag{6.5}$$

$$\frac{dN_2}{dt} = \frac{N_3}{\tau_{32}} - \frac{\mathrm{Im}(EP^*)}{\hbar} - \frac{N_2}{\tau_{21}} \tag{6.6}$$

$$\frac{dN_1}{dt} = \frac{N_2}{\tau_{21}} + \frac{\mathrm{Im}(EP^*)}{\hbar} - \frac{N_1}{\tau_{10}} \tag{6.7}$$

$$\frac{dN_0}{dt} = \frac{N_1}{\tau_{10}} - P_r N_0 \tag{6.8}$$

where P_r is the pump rate, τ_{21} is the spontaneous emission decay, τ_{10} and τ_{32} are the non-radiative decays and $\frac{\mathrm{Im}(EP^*)}{\hbar}$ stands for the stimulated emission. The stimulated term is both proportional to the electric field at the atom position and the polarization. Assuming that the electric field is not too intense, the polarization is linearly derived from the electric field using the Lorentz's oscillator model introduced in Chapter 1

$$\frac{\partial^2 P}{\partial t^2} + \Delta\omega_a \frac{\partial P}{\partial t} + \omega_a^2 P = -\frac{2\omega_a}{\hbar} d^2 \Delta N E \tag{6.9}$$

where, ω_a is the atomic frequency, d the dipole moment, $\Delta\omega_a$ the linewidth of the atomic response and $\Delta N = N_2 - N_1$ the population difference of the radiative transition. The evolution of the polarization can be simplified using the Rotating Wave Approximation. In this assumption, the oscillations of the polarization are assumed close to the atomic frequency ω_a. Hence, eq. (6.9) reads in the frequency domain

$$P(r,\omega) = -\frac{2\omega_a}{\hbar(-\omega^2 - i\omega\Delta\omega_a + \omega_a^2)} d^2(\Delta N \star E)(r,\omega) \approx \frac{\omega_a}{\hbar(\omega - \omega_a + i\frac{\Delta\omega_a}{2})} d^2(\Delta N \star E)(r,\omega) \tag{6.10}$$

where the symbol $\star$ is the convolution product defined by

$$(A \star B)(t) = \int A(t-u)B(u)du \tag{6.11}$$

As a result, the polarization can be expressed in term of a susceptibility $\chi_g(\omega)$

$$P(r,\omega) = \chi_g(\omega).(\Delta N \star E)(r,\omega) \Leftrightarrow P(r,t) = (\chi_g \star (\Delta N.E))(t) \tag{6.12}$$

Because of the ΔN dependency, the polarization expression in eq. (6.12) is *a priori* non-linear in the frequency domain. This population difference can be derived assuming that the non-radiative transitions are extremely fast compared to the radiative transition. Populations N_3 and N_1 are instantaneously depleted (see Chapter 1), leading to

$$\frac{d\Delta N(r,t)}{dt} = \frac{1}{\tau}\left(\Delta N_0(r,t) - \Delta N(r,t) - 2\frac{\mathrm{Im}(EP^*)(r,t)}{\hbar}\right) \tag{6.13}$$

where $N = N_2 + N_0$ is the total density of emitters, in which ΔN_0 reads

$$\Delta N_0 = \frac{NP_r}{P_r + \frac{1}{\tau_{21}}} \tag{6.14}$$

and τ the time decay of the population difference reads

$$\tau = \frac{1}{P_r + \frac{1}{\tau_{21}}} \tag{6.15}$$

For pump excitation fulfilling $\tau_{21}P_r \ll 1$, ΔN_0 is proportional to the pump excitation

$$\Delta N_0 \approx N\tau_{21}P_r \tag{6.16}$$

Hence, the electromagnetic problem is reduced to three physical quantities E, P and ΔN, fulfilling eq. (6.4, 6.12, 6.13), respectively.

Stationary Inversion Approximation and steady state

We consider the case of a Continuous Wave (CW) pump regime (P_r is constant in time): The system is in steady state. In a similar way to the problem studied in Chapter 4, the time-scale of population difference ΔN is much longer than the time scale of E and P. As a result, the temporal fluctuations of the population difference can be neglected, and thus eq. (6.13) reads

$$\frac{d\Delta N(r,t)}{dt} \approx 0 = \frac{1}{\tau}\left(\Delta N_0(r,t) - \Delta N(r,t) - 2\frac{\mathrm{Im}(EP^*)(r,t)}{\hbar}\right) \tag{6.17}$$

The approximation of a time-independent inversion population, originally introduced by Haken [146] and referred to as the Stationary Inversion Approximation (SIA), is only valid in the steady state regime: $\Delta N \approx cst$. We also assume the pump to be uniform in time and space, leading to a constant ΔN_0. Hence, the population difference reads

$$\Delta N(r,t) = \frac{\Delta N_0}{1 + 2\frac{\mathrm{Im}(E(\chi_g \star E)^*)(r,t)}{\hbar}} \tag{6.18}$$

If $\Delta N(r,t)$ is assumed constant in time, we can replace it by its averaged value

$$\langle \Delta N(r,t) \rangle_T = \left\langle \frac{\Delta N_0}{1 + 2\frac{\mathrm{Im}(E(\chi_g \star E)^*)(r,t)}{\hbar}} \right\rangle_T \tag{6.19}$$

The population difference is responsible for the lasing amplification. If some modes are lasing, the denominator of eq. (6.18) and (6.19) increases with the amplitude of the intensity of the field. This leads to a reduced amplification, also referred to as gain saturation (see section 6.1.1). This mechanism is responsible for the non-linearity arising above threshold. Below threshold (BT), no mode is lasing and thus the population difference reads

$$\Delta N_{BT} = \langle \Delta N(r,t) \rangle_T = \Delta N_0 \tag{6.20}$$

Above threshold (AT), it reads

$$\Delta N_{AT} = \langle \Delta N(r,t) \rangle_T = \left\langle \frac{\Delta N_0}{1 + 2\frac{\mathrm{Im}(E(\chi_g \star E)^*)(r,t)}{\hbar}} \right\rangle_T \tag{6.21}$$

Eq. (6.20) and (6.21) point out that the amplification is triggered by the population difference between the two states of the radiative transition (see Chapter 1). As expected from Chapter 1, the population difference must be positive to achieve the stimulated amplification. Below threshold, the population difference is considered as static: The gain is said linear. Above threshold, it is assumed triggered by the amplitude of the lasing modes: The gain is non-linear and saturates.

6.2 Active mode, below threshold

Below threshold, the absence of gain saturation leads to a linear amplification of the modes. Here, we expand the electric field along the passive modes of the system via the biorthogonal formalism of Chapter 2. Using a perturbation expansion, we analytically derive the complex frequency and spatial distribution of each active mode.

6.2.1 Modal expansion

Expansion along the passive modes

Because the passive system fulfils the no-tail and the discontinuity conditions, the passive modes derived from the Siegert's approach in eq. (6.2) form a complete set (see Chapter 2). The electric field reads

$$E(r,\omega) = \sum_p a_p \frac{1}{-i\omega + i\Omega_p} \Phi_p(r) = \sum_p a_p(\omega) \Phi_p(r) \tag{6.22}$$

where coefficients $a_p(\omega)$ are introduced for sake of notation compactness. Inserting the electric field expansion into eq. (6.4)

$$\Delta \sum_p a_p(\omega) \Phi_p(r) + \epsilon(r)\omega^2 \sum_p a_p(\omega) \Phi_p(r) = -\omega^2 P(r,\omega) \tag{6.23}$$

Using the definition of the passive modes of eq. (6.2) and the expression of ΔN_{BT}

$$\sum_p a_p(\omega)\epsilon(r)\Omega_p^2\Phi_p(r) - \epsilon(r)\omega^2\sum_p a_p(\omega)\Phi_p(r) = -\omega^2\Delta N_0\sum_p a_p(\omega)\Phi_p(r) \tag{6.24}$$

The biorthogonal product between passive modes reads (see Chapter 2)

$$\langle\Phi_q^*|\Phi_p\rangle = \int \epsilon(r)\Phi_q(r)\Phi_p(r) = \delta_{pq} \tag{6.25}$$

The biorthogonal product of eq. (6.24) applied along $\langle\Phi_p^*|$ reads

$$a_p(\omega)(\Omega_p^2 - \omega^2) = \omega^2\chi_g(\omega)\Delta N_0\sum_q a_q(\omega)\int \Phi_p(r)\Phi_q(r) \tag{6.26}$$

Eq. (6.26) defines an eigenvalue problem, considering a finite number of passive modes N, we can recast the system in a matrix form

$$\begin{bmatrix}\Omega_1^2 & \dots & 0\\ \vdots & \ddots & \vdots\\ 0 & \dots & \Omega_N^2\end{bmatrix} = \omega^2\begin{bmatrix}1+\Delta N_0\chi_g(\omega)V_{11} & \dots & \Delta N_0\chi_g(\omega)V_{1N}\\ \vdots & \ddots & \vdots\\ \Delta N_0\chi_g(\omega)V_{N1} & \dots & 1+\Delta N_0\chi_g(\omega)V_{NN}\end{bmatrix} \tag{6.27}$$

where

$$V_{ij}(\omega) = \int \Phi_p(r)\Phi_q(r) \tag{6.28}$$

are the spatial overlap coefficients introduced by Deych [152, 40] standing for linear coupling of the modes. Now, using definition of $\chi_g(\omega)$ of eq. (6.12), eq. (6.27) reads

$$\begin{bmatrix}\Omega_1^2 & \dots & 0\\ \vdots & \ddots & \vdots\\ 0 & \dots & \Omega_N^2\end{bmatrix} = \omega^2\begin{bmatrix}1+\frac{\Delta N_0\omega_a d^2}{\hbar\left(\omega-\omega_a+i\frac{\Delta\omega_a}{2}\right)}V_{11} & \dots & \frac{\Delta N_0\omega_a d^2}{\hbar\left(\omega-\omega_a+i\frac{\Delta\omega_a}{2}\right)}V_{1N}\\ \vdots & \ddots & \vdots\\ \frac{\Delta N_0\omega_a d^2}{\hbar\left(\omega-\omega_a+i\frac{\Delta\omega_a}{2}\right)}V_{N1} & \dots & 1+\frac{\Delta N_0\omega_a d^2}{\hbar\left(\omega-\omega_a+i\frac{\Delta\omega_a}{2}\right)}V_{NN}\end{bmatrix} \tag{6.29}$$

Therefore, the active modes of random lasers are the eigensolutions of a non-linear eigenvalue problem derived in eq. (6.29). Each active mode will be associated with a complex frequency $\tilde{\Omega}_p = \tilde{\omega}_p - i\frac{\tilde{\Gamma}_p}{2}$ and a spatial distribution $\tilde{\Phi}_p$.

Mode mixing

Eq. (6.27) and (6.29) emphasize that the active modes of a random laser differ from the modes of the passive system. Passive modes mix to yield a new set of active modes: Active modes read like a linear combination of the passive modes. This mixing is directly triggered either by the spatial overlap or coupling encoded in coefficients V_{ij}.

When the passive modes are Anderson-localized, the terms $V_{i\neq j}$ are weak because the modes have a small spatial overlap. Hence, in the localized regime, the active modes correspond as expected [109, 110, 155] to the passive modes of the system. As a matter of illustration, we can consider the example of localized modes in Fig. 6.4**(a)**, in which we plot the passive mode and the corresponding active mode. As expected, both modes are identical because no mode mixing is performed. However, in the weakly scattering regime, because the modes are extended and strongly overlap, the coupling is important. For a weakly scattering system (see Fig. 6.4**(b)**), the coupling between passive modes is important. Thus, the active mode spatial distribution is very different from the passive one.

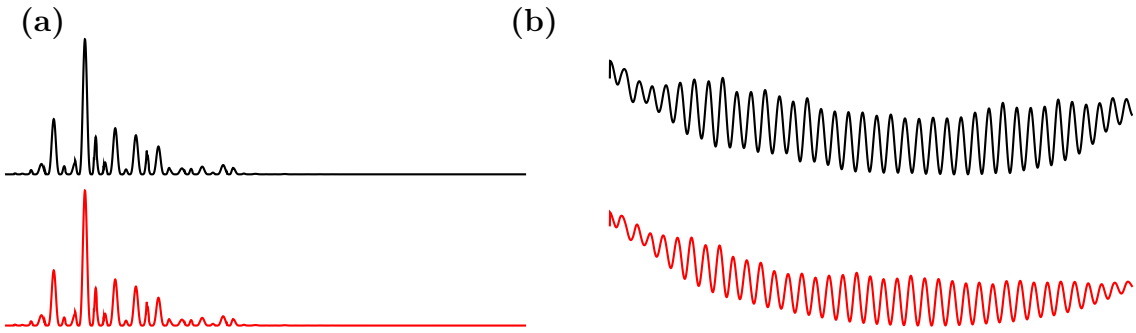

Figure 6.4: **(a)** Spatial distribution of a passive mode Φ_p and the corresponding active mode $\tilde{\Phi}_p$ in a localized system: The coupling between passive modes is very low and no mode-mixing is performed. **(b)** Similar case for a weakly scattering system: Φ_p and $\tilde{\Phi}_p$ differ because the coupling of passive modes induces a linear mixing.

6.2.2 Broadband gain medium

A linear eigenvalue problem

As explained in section 6.2.1, the active modes are solutions of the non-linear eigenvalue problem of eq. (6.29). The non-linearity of the problem results from the frequency dependence of the susceptibility of the gain medium $\chi_g(\omega)$. Many amplifying media, such as Rhodamine (see Chapter 5) or Ti:Sapphire, are broadband (large $\Delta\omega_a$). Thus, considering active modes with frequency close to the central frequency ω_a, we can assume an almost constant susceptibility

$$\omega - \omega_a \ll \Delta\omega_a \Rightarrow \chi_g(\omega) = \chi_g(\omega_a) \tag{6.30}$$

Consequently, the non-linear eigenvalue problem of eq. (6.29) can be assumed linear

$$\begin{bmatrix} \Omega_1^2 & \dots & 0 \\ \vdots & \ddots & \vdots \\ 0 & \dots & \Omega_N^2 \end{bmatrix} = \omega^2 \begin{bmatrix} 1+\Delta N_0\chi_g(\omega_a)V_{11} & \dots & \Delta N_0\chi_g(\omega_a)V_{1N} \\ \vdots & \ddots & \vdots \\ \Delta N_0\chi_g(\omega_a)V_{N1} & \dots & 1+\Delta N_0\chi_g(\omega_a)V_{NN} \end{bmatrix} \tag{6.31}$$

where

$$\chi_g(\omega) \approx \chi_g(\omega_a) = -i\frac{2d^2\omega_a}{\hbar\Delta\omega_a} \tag{6.32}$$

Noting $\lambda = 1/\Omega$ and $\Delta\tilde{N}_0 = \Delta N_0\chi_g(\omega_a)$, eq. (6.31) reads

$$\lambda^2 = \begin{bmatrix} \lambda_1^2(1+\Delta\tilde{N}_0V_{11}) & \dots & \lambda_1^2\Delta\tilde{N}_0V_{1N} \\ \vdots & \ddots & \vdots \\ \lambda_N^2\Delta\tilde{N}_0V_{N1} & \dots & \lambda_N^2(1+\Delta\tilde{N}_0V_{NN}) \end{bmatrix} \tag{6.33}$$

Perturbation expansion

The linear eigenvalue problem defined by eq. (6.33) has no analytical solution. Since modes are normalised, $|V_{ij}| < 1$. If we preclude high energy pumping, we can assume

that $\Delta\tilde{N}_0|V_{ij}| \ll 1$. This excludes the case of weakly diffusive random lasers, where high excitation is required to reach lasing [156]. Thus, we can perform a perturbation expansion of the linear system in eq. (6.33), which reads

$$\lambda^2 = \begin{bmatrix} \lambda_1^2 & \dots & 0 \\ \vdots & \ddots & \vdots \\ 0 & \dots & \lambda_N^2 \end{bmatrix} + \begin{bmatrix} \lambda_1^2 V_{11}\Delta\tilde{N}_0 & \dots & \lambda_1^2 V_{1N}\Delta\tilde{N}_0 \\ \vdots & \ddots & \vdots \\ \lambda_N^2 V_{N1}\Delta\tilde{N}_0 & \dots & \lambda_N^2 V_{NN}\Delta\tilde{N}_0 \end{bmatrix} \tag{6.34}$$

Eq. (6.34) can be understood as a passive system perturbed by a matrix resulting from the coupling between the passive modes and proportional to the pump. Hence, we can derive the perturbation expansion of the active modes (see Appendix C)

$$\tilde{\lambda}_p^2 = \lambda_p^2 + \lambda_p^2 V_{pp}\Delta\tilde{N}_0 + \sum_{q\neq p} \frac{\lambda_p^2\lambda_q^2}{\lambda_p^2 - \lambda_q^2} V_{pq}^2 \Delta\tilde{N}_0^2 \tag{6.35}$$

Leading to:

$$\tilde{\Omega}_p = \frac{\Omega_p}{\sqrt{1 + V_{pp}\Delta\tilde{N}_0 + \sum_{q\neq p} \frac{\lambda_q^2}{\lambda_p^2 - \lambda_q^2} V_{pq}^2 \Delta\tilde{N}_0^2}} \tag{6.36}$$

Approximated by:

$$\tilde{\Omega}_p \approx \Omega_p \left(1 - \frac{V_{pp}}{2}\Delta\tilde{N}_0 - \frac{1}{2}\sum_{q\neq p} \frac{\lambda_q^2}{\lambda_p^2 - \lambda_q^2} V_{pq}^2 \Delta\tilde{N}_0^2 + \frac{3}{8} V_{pp}^2 \Delta\tilde{N}_0^2\right) \tag{6.37}$$

Equivalent to:

$$\tilde{\Omega}_p \approx \Omega_p \left(1 - \frac{V_{pp}}{2}\Delta\tilde{N}_0 + \sum_{m\neq n} \frac{\Omega_p^2}{\Omega_q^2 - \Omega_p^2} V_{pq}^2 \Delta\tilde{N}_0^2 + \frac{3}{8} V_{pp}^2 \Delta\tilde{N}_0^2\right) \tag{6.38}$$

And the corresponding spatial distribution

$$\tilde{\Phi}_p = \Phi_p + \sum_{q\neq p} \frac{\Omega_q^2}{\Omega_q^2 - \Omega_p^2} V_{pq}\Delta\tilde{N}_0\Phi_q \tag{6.39}$$

Eq. (6.38) and (6.39) show the active modes corresponding to the mode of the passive system plus a perturbation. This perturbation, which is a linear combination of the passive modes, stands for the mixing of passive modes. They also emphasize that the mixing of passive modes to build active modes not only depends on a spatial overlap or coupling (V_{ij}) but also results from a spectral overlap, namely $1/(\Omega_i^2 - \Omega_j^2)$. Moreover, this amplitude of the mixing is directly triggered by the excitation (ΔN_0): The stronger the pump fluence, the stronger the perturbation and thus the mixing.

In this approach of small excitation, the active and passive modes are in one-to-one correspondence. The active mode is understood like a perturbation of the passive mode. When higher pumping is required [156], the coupling is more important (V_{ij}) and the correspondence no longer holds.

The lasing threshold

Eq. (6.38) gives the evolution of the modes in the complex plane when the excitation of the gain medium varies. When the excitation increases, the saturation of population inversion $\Delta\tilde{N}_0$ increases too (see eq. (6.14)). This leads to a diminution of the imaginary part of the active mode in the complex plane as it gets closer to the real axis. For a given active mode p, the threshold is reached when the pump excitation cancels the imaginary part of its complex frequency. This threshold $\Delta\tilde{N}_{0p,th}$ reads

$$\Delta\tilde{N}_{0p,th} \quad | \quad Im(\tilde{\Omega}_p) = 0 \tag{6.40}$$

Considering only first order of eq. (6.38) and $\Omega_p = \omega_p - i\frac{\Gamma_p}{2}$, we can derive the lasing threshold of mode p

$$0 = -\frac{\Gamma_p}{2} + Im\left(\Omega_p \Delta\tilde{N}_{0,th}\frac{V_{pp}}{2}\right) \tag{6.41}$$

Inserting the complete expression of V_{pp} and the relation $\Delta\tilde{N}_0 = \Delta N_0 \frac{2d^2\omega_a}{\hbar\Delta\omega_a}$, equation (6.41) reads

$$0 = -\frac{\Gamma_p}{2} + \Delta N_{0,th}\frac{2d^2\omega_a}{\hbar\Delta\omega_a} Re(\Omega_p \int \Phi_p^2) \tag{6.42}$$

Leading to

$$\Delta N_{0p,th} = \frac{\hbar\Delta\omega_a\Gamma_p}{4d^2\omega_a Re(\Omega_p \int \Phi_p^2)} \tag{6.43}$$

Assuming the quality factor of mode p fulfils $Q_p = \frac{\omega_p}{\Gamma_p} \gg 1$

$$\Delta N_{0p,th} \approx \frac{\hbar\Delta\omega_a}{4d^2\omega_a Q_p Re(\int \Phi_p^2)} \tag{6.44}$$

Eq. (6.44) simply shows that a high-Q passive mode will give rise to a low threshold active mode. Moreover, the threshold of the mode is also triggered by its spatial extent $Re(\int \Phi_p^2)$.

6.2.3 Narrow gain medium

When the susceptibility cannot be assumed constant in frequency anymore, the eigenvalue problem of eq. (6.29) becomes non-linear. Assuming the excitation is limited, we can perform a perturbation expansion on eq. (6.29).

If we consider the non matrix form of eq. (6.29)

$$a_p(\omega)(\Omega_p^2 - \omega^2) = \omega^2\Delta N_0 \sum_q a_q(\omega)\chi_g(\omega) \int \Phi_p(r)\Phi_q(r) \tag{6.45}$$

where we assume ΔN_0 to be small. Under this assumption, frequencies $\tilde{\omega}_n$ of the active modes will remain close to the frequencies of the passive ones ω_n. Thus, we can perform a Taylor expansion of $\chi_g(\omega)$ close to the passive frequency, and eq. (6.45) reads

$$a_p(\omega)(\Omega_p^2 - \omega^2) \approx \omega^2\Delta N_0 \sum_q a_q(\omega)\left(\chi_g(\omega_p) + \Delta N_0 \frac{\partial\chi_g}{\partial\Delta N_0}(\omega_p)\right) V_{pq} \tag{6.46}$$

As a result, eq. (6.46) is recast in the form

$$\begin{bmatrix} \Omega_1^2 & \dots & 0 \\ \vdots & \ddots & \vdots \\ 0 & \dots & \Omega_N^2 \end{bmatrix} = \omega^2 \begin{bmatrix} 1+\Delta N_0\chi_g(\omega_1)V_{11} & \dots & \Delta N_0\chi_g(\omega_N)V_{1N} \\ \vdots & \ddots & \vdots \\ \Delta N_0\chi_g(\omega_1)V_{N1} & \dots & 1+\Delta N_0\chi_g(\omega_N)V_{NN} \end{bmatrix}$$
$$+\omega^2\Delta N_0^2 \begin{bmatrix} \frac{\partial\chi_g}{\partial\Delta N_0}(\omega_1)V_{11} & \dots & \frac{\partial\chi_g}{\partial\Delta N_0}(\omega_N)V_{1N} \\ \vdots & \ddots & \vdots \\ \frac{\partial\chi_g}{\partial\Delta N_0}(\omega_1)V_{N1} & \dots & \frac{\partial\chi_g}{\partial\Delta N_0}(\omega_N)V_{NN} \end{bmatrix} \tag{6.47}$$

The perturbation to first order of eq. (6.47) reads for complex frequency

$$\tilde{\Omega}_p \approx \Omega_p \left(1 - \frac{V_{pp}}{2}\Delta N_0\chi_g(\omega_p)\right) \tag{6.48}$$

And the corresponding spatial distribution

$$\tilde{\Phi}_p \approx \Phi_p + \sum_{q\neq p} \frac{\Omega_q^2}{\Omega_q^2-\Omega_p^2} V_{pq}\chi_g(\omega_p)\Delta N_0\Phi_q \tag{6.49}$$

It is thus possible to derive the threshold of modes

$$\Delta N_{0,th} = -\frac{\Gamma_p}{\mathrm{Im}(\Omega_p V_{pp}\chi_g(\omega_p)} \approx -\frac{1}{Q_p \mathrm{Im}(V_{pp}\chi_g(\omega_p))} \tag{6.50}$$

The threshold in eq. (6.50) differs from the one derived for a broadband gain medium (eq. 6.37). The susceptibility in the denominator $\chi_g(\omega_p)$ being not purely imaginary, this will affect the threshold value and induce some shift in the real part of the complex frequency.

6.2.4 Numerical computation

As stated in eq. (6.33), the derivation of active modes (below threshold) relies on a non-linear eigenvalue problem. To solve it numerically, we have developed a numerical code based on the Transfer Matrix Approach (see Chapter 2). In passive system, this method numerically derives the modes using the Siegert's condition in 1D structure (see Chapter 2). For instance, if we carry on the example of section 6.1.1, the passive modes (Φ_p, Ω_p) fulfil

$$\frac{d^2\Phi_p}{dx^2}(x) + n(x)^2\Omega_p^2\Phi_p(x) = 0 \quad \& \quad \left(\frac{d}{dx} - i\Omega_p\right)\Phi_p\Big|_{x\to\infty} = 0 \tag{6.51}$$

Below threshold, the gain is modelled by a linear susceptibility, which reads

$$\chi_g(\omega) = \frac{d^2\omega_a}{\hbar\left(\omega - \omega_a + i\frac{\Delta\omega_a}{2}\right)} \tag{6.52}$$

As a result, the active modes $(\tilde{\Phi}_p, \tilde{\Omega}_p)$ are numerically derived from

$$\frac{d^2\tilde{\Phi}_p}{dx^2}(x) + \left(n(x)^2 + \Delta N_0\chi_g(\omega)\right)\tilde{\Omega}_p^2\tilde{\Phi}_p(x) = 0 \quad \& \quad \left(\frac{d}{dx} - i\tilde{\Omega}_p\right)\tilde{\Phi}_p\Big|_{x\to\infty} = 0 \tag{6.53}$$

where, ΔN_0 mimics the pump excitation. Eventually, the active modes can be either defined by a complex frequency $\tilde{\Omega}_p = \tilde{\omega}_p + i\frac{\tilde{\Gamma}_p}{2}$ or by $(\tilde{\omega}_p, \Delta N_{0p,th})$, where $\Delta N_{0p,th}$ is the threshold fulfilling

$$\Delta N_{0p,th} \quad | \quad \mathrm{Im}(\tilde{\Omega}_p) = 0 \tag{6.54}$$

The spatial distributions of Fig. 6.1 and 6.2 have been computed with a Transfer Matrix approach.

6.3 Lasing modes, above threshold

In this section, we derive the evolution of modes above threshold by performing the modal expansion of the field. Using a perturbation approach, we derive complex frequency and spatial distribution of the active modes. Then, assuming that the number of lasing modes is known, we write the expressions of the lasing modes. Finally the single-mode and two-mode regimes are investigated.

6.3.1 Modal expansion

The expansion along the passive mode

Above threshold, the electric field evolution is driven by eq. (6.4) and reads

$$\Delta E(r,\omega) + \epsilon(r)\omega^2 E(r,\omega) = -\omega^2 \chi_g(\omega)\Delta N_{AT} E(r,\omega) \tag{6.55}$$

where ΔN_{AT} reads

$$\Delta N_{AT} = \left\langle \frac{\Delta N_0}{1 + \frac{2}{\hbar}\mathrm{Im}(E.(\chi_g \star E)^*(r,t))} \right\rangle_T \tag{6.56}$$

In a similar way to section 6.2, the electric field is expanded along the passive modes of the system

$$E(r,\omega) = \sum_p a_p \frac{1}{-i\omega + i\Omega_p}\Phi_p(r) = \sum_p a_p(\omega)\Phi_p(r) \quad \Leftrightarrow \quad E(r,t) = \sum_p a_p e^{-i\Omega_p t}\Phi_p(r) \tag{6.57}$$

Inserting expansion of eq. (6.57) into eq. (6.56) reads

$$\Delta N_{AT} = \left\langle \frac{\Delta N_0}{1 + \frac{2}{\hbar}\mathrm{Im}(\sum_{p,q} a_p a_q^* \Phi_p(r)\Phi_q(r)^* e^{-i\Omega_p t}(e^{i\Omega_q t} \star \chi_g(t)^*))} \right\rangle_T \tag{6.58}$$

Eq. (6.58) can be simplified assuming

$$e^{-i\Omega_p t}(e^{i\Omega_q t} \star \chi_g(t)^*)) = \mathrm{TF}^{-1}\left(\mathrm{TF}\left(e^{-i\Omega_p t}(e^{i\Omega_q t} \star \chi_g(t)^*)\right)\right)$$

$$\approx \mathrm{TF}^{-1}\left(\delta(\omega-\omega_p) \star (\delta(\omega-\omega_q)\chi_g(\omega)^*)\right) = \mathrm{TF}^{-1}\left(\delta(\omega_p-\omega_q)\chi_g(\omega_q)^*\right) = \delta_{pq}\,\chi_g(\omega_q)^* \tag{6.59}$$

As a result, eq. (6.58) reads

$$\Delta N_{AT} \approx \frac{\Delta N_0}{1 + \frac{2}{\hbar}\sum_p |a_p \Phi_p(r)|^2 \mathrm{Im}(\chi_g(\omega_p)^*)} \tag{6.60}$$

Using the electric field expansion of eq. (6.57) in (6.55)

$$\Delta \sum_p a_p(\omega)\Phi_p(r) + \epsilon(r)\omega^2 \sum_p a_p(\omega)\Phi_p(r) = -\omega^2\chi_g(\omega)\Delta N_0 \frac{\sum_p a_p(\omega)\Phi_p(r)}{1+\frac{2}{\hbar}\sum_p |a_p\Phi_p(r)|^2 \mathrm{Im}(\chi_g(\omega_p)^*)} \tag{6.61}$$

Inserting passive mode definition of eq. (6.2), eq. (6.61) reads

$$\sum_p a_p(\omega)\epsilon(r)(\Omega_p^2-\omega^2)\Phi_p(r) = \omega^2\chi_g(\omega)\Delta N_0 \frac{\sum_p a_p(\omega)\Phi_p(r)}{1+\frac{2}{\hbar}\sum_p |a_p\Phi_p(r)|^2 Im(\chi_g(\omega_p)^*)} \tag{6.62}$$

The passive modes conserve the biorthogonal relation of eq. (6.25). Using the biorthogonal projection along $\langle\Phi_p^*|$, eq. (6.62) reads

$$\sum_p a_p(\omega)(\Omega_p^2-\omega^2) = \omega^2\chi_g(\omega)\Delta N_0 \sum_q \int \frac{a_q(\omega)\Phi_p(r)\Phi_q(r)}{1+\frac{2}{\hbar}\sum_l |a_l\Phi_l(r)|^2 Im(\chi_g(\omega_l)^*)} \tag{6.63}$$

In a similar way to the regime below threshold, the electric field is described by a non-linear eigenvalue problem. However, the non-linearity arises here via non-linear wave mixing function of the intensity of each mode ($|a_p|^2$). This system is similar to a Non-Linear Schrödinger equation.

Linear versus non-linear mode mixing

Eq. (6.63) emphasizes the complexity of the modal description above threshold. The appearance of hole burning and the resulting saturation of the gain is responsible for non-linear mixing of passive modes. To simplify eq. (6.63), we choose to carry on the idea of Haken and Sauermann [146] and perform a Taylor expansion of the saturation term at third order: The so called cubic approximation. For small intensity of the lasing intensity we can assume

$$\begin{aligned}\sum_p a_p(\omega)(\Omega_p^2-\omega^2) &\approx \omega^2\chi_g(\omega)\Delta N_0 \sum_q \int a_q(\omega)\Phi_p(r)\Phi_q(r) \\ &- \omega^2\chi_g(\omega)\Delta N_0 \sum_q \int a_q(\omega)\Phi_p(r)\Phi_q(r)\frac{2}{\hbar}\sum_l |a_l\Phi_l(r)|^2 \mathrm{Im}(\chi_g(\omega_l)^*)\end{aligned} \tag{6.64}$$

Under this assumption, eq. (6.64) shows that we can separate the linear and non-linear wave mixings. The linear contribution results from the expression below threshold. Thus, the gain saturation and the regime above threshold can be understood like a non-linear correction. Moreover, eq. (6.64) can be recast in a matricial form

$$\begin{aligned}\begin{bmatrix}\Omega_1^2 & \dots & 0\\ \vdots & \ddots & \vdots \\ 0 & \dots & \Omega_N^2\end{bmatrix} &= \omega^2 \begin{bmatrix}1+\Delta N_0\chi_g(\omega)V_{11} & \dots & \Delta N_0\chi_g(\omega)V_{1N}\\ \vdots & \ddots & \vdots \\ \Delta N_0\chi_g(\omega)V_{N1} & \dots & 1+\Delta N_0\chi_g(\omega)V_{NN}\end{bmatrix} \\ &- \omega^2\Delta N_0\frac{2\chi_g(\omega)}{\hbar}\begin{bmatrix}\sum_p |a_p|^2 A_{11pp} & \dots & \sum_p |a_p|^2 A_{1Npp}\\ \vdots & \ddots & \vdots \\ \sum_p |a_p|^2 A_{N1pp} & \dots & \sum_p |a_p|^2 A_{NNpp}\end{bmatrix}\end{aligned} \tag{6.65}$$

where non-linear coupling coefficients A_{pqrs} [152] reads

$$A_{pqrs} = \int \Phi_p(r)\Phi_q(r)\Phi_r(r)\Phi_s(r)^* Im(\chi_g(\omega_s)^*) \tag{6.66}$$

Therefore, the saturation induces the apparition of non-linear coupling, characterized in eq. (6.66). The combination of passive modes resulting from these coefficients will be called non-linear mixing.

6.3.2 Perturbation expansion

As for below threshold, we perform a perturbation expansion of eq. (6.65) to derive the modes of the random laser. Noting $\lambda = 1/\omega$ eq. (6.65) reads

$$\lambda^2 = \begin{bmatrix} \lambda_1^2 & \dots & 0 \\ \vdots & \ddots & \vdots \\ 0 & \dots & \lambda_N^2 \end{bmatrix} + \Delta N_0 \begin{bmatrix} \lambda_1^2 \chi_g(\omega) V_{11} & \dots & \lambda_1^2 \chi_g(\omega) V_{1N} \\ \vdots & \ddots & \vdots \\ \lambda_N^2 \chi_g(\omega) V_{N1} & \dots & \lambda_N^2 \chi_g(\omega) V_{NN} \end{bmatrix}$$
$$- \Delta N_0 \frac{2\chi_g(\omega)}{\hbar} \begin{bmatrix} \lambda_1^2 \sum_p |a_p|^2 A_{11pp} & \dots & \lambda_1^2 \sum_p |a_p|^2 A_{1Npp} \\ \vdots & \ddots & \vdots \\ \lambda_N^2 \sum_p |a_p|^2 A_{N1pp} & \dots & \lambda_N^2 \sum_p |a_p|^2 A_{NNpp} \end{bmatrix} \tag{6.67}$$

At first order (see Appendix C), eigenvalues of eq. (6.67) read

$$\tilde{\lambda}_p^2 = \lambda_p^2 \left(1 + \Delta N_0 \chi_g(\omega_p) V_{pp} - \Delta N_0 \frac{2\chi_g(\omega_p)}{\hbar} \sum_p |a_p|^2 A_{qqpp} \right) \tag{6.68}$$

Leading to a complex frequency of mode p

$$\tilde{\Omega}_p = \Omega_p \left(1 - \frac{\Delta N_0 \chi_g(\omega_p)}{2} V_{pp} + \frac{\Delta N_0 \chi_g(\omega_p)}{\hbar} \sum_p |a_p|^2 A_{qqpp} \right) \tag{6.69}$$

where we will note

- $|a_p|^2 A_{pppp}$ the self-saturation term
- $\sum_{p \neq q} |a_p|^2 A_{qqpp}$ the cross-saturation term

and spatial distributions of the modes read

$$\tilde{\Phi}_p = \Phi_p + \Delta N_0 \chi_g(\omega_p) \sum_{q \neq p} \frac{\Omega_q^2}{\Omega_q^2 - \Omega_p^2} \left(V_{pq} - \frac{2}{\hbar} \sum_p |a_p|^2 A_{qqpp} \right) \Phi_p \tag{6.70}$$

Complex frequency derived in eq. (6.69) gives an insight into the role played by saturation in the lasing emission. Below threshold, no mode is lasing and the amplification in increased by the term $\frac{\Delta N_0 \chi_g(\omega_p)}{2} V_{pp}$. When the threshold is reached, modes start lasing and increase the saturation term $\frac{\Delta N_0 \chi_g(\omega_p)}{\hbar} \sum_p |a_p|^2 A_{qqpp}$. Physically, the saturation term compensates for the amplification and leads to an balance between the energy required by modes to lase and the energy the medium can provide. Mathematically, the saturation enforces a zero imaginary part of complex frequency. In others words, the saturation is required to stabilize the lasing emission. Moreover, the cross-saturation will also forbid some modes to reach their threshold. The spatial distribution of eq. (6.70) emphasizes the influence of the pump excitation (mimicked by ΔN_0), which triggers the mode mixing. Here, in addition to the linear mode mixing below threshold, a non-linear mixing of modes is performed.

6.3.3 Lasing modes

Method

Here, using a common method used in conventional lasers, we derive intensity of lasing modes above threshold. Expressions of the modes proposed in eq. (6.69) and (6.70) made no distinction between the modes below and above threshold, namely the active and lasing modes. Lasing modes have a real frequency and a non-zero intensity, whereas active mode have a complex frequency and zero intensity. We note $I_p = |a_p|^2$ the intensity of each mode, and we sort the modes to fulfil

$$\text{lasing modes: } p \leq N_l \Rightarrow I_p > 0 \quad \& \quad \text{Im}(\tilde{\Omega}_p) = 0$$

$$\text{active modes: } p > N_l \Rightarrow I_p = 0 \quad \& \quad \text{Im}(\tilde{\Omega}_p) < 0$$

where N_l is the number of lasing modes. Inserting the definition of the lasing modes into eq. (6.69)

$$\forall p \leq N_l \quad | \quad 0 = Im\left(\Omega_p - \Omega_p \frac{\Delta N_0 \chi_g(\omega_p)}{2} V_{pp} + \Omega_p \frac{\Delta N_0 \chi_g(\omega_p)}{\hbar} \sum_{q \leq N_l} I_q A_{ppqq}\right) \tag{6.71}$$

Using the complex frequency definition $\Omega_p = \omega_p - i\frac{\Gamma_p}{2}$, eq. (6.71) is equivalent to

$$\forall p \leq N_l \quad | \quad 0 = -\frac{\Gamma_p}{2} + \Delta N_0 Re\left(\Omega_p \frac{i\chi_g(\omega_p)}{2} V_{pp}\right) - \Delta N_0 Re\left(\Omega_p \frac{i\chi_g(\omega_p)}{\hbar} \sum_{q \leq N_l} I_q A_{ppqq}\right) \tag{6.72}$$

Noting

$$B_p = Re\left(\Omega_p \frac{i\chi_g(\omega_p)}{2} V_{pp}\right) \tag{6.73}$$

And

$$D_{pq} = Re\left(\Omega_p \frac{i\chi_g(\omega_p)}{\hbar} A_{ppqq}\right) \tag{6.74}$$

We can derive a linear system

$$\begin{bmatrix} D_{11} & \dots & D_{1N_l} \\ \vdots & \ddots & \vdots \\ D_{N_l 1} & \dots & D_{N_l N_l} \end{bmatrix} \begin{bmatrix} I_1 \\ \vdots \\ I_{N_l} \end{bmatrix} = \begin{bmatrix} B_1 - \frac{\Gamma_1}{2\Delta N_0} \\ \vdots \\ B_{N_l} - \frac{\Gamma_{N_l}}{2\Delta N_0} \end{bmatrix} \tag{6.75}$$

By solving the system of eq. (6.75), we obtain the intensity of each mode to achieve the balance required by lasing in the steady state. Then, we insert the intensities of the different lasing modes in complex frequency and spatial distribution given in eq. (6.69) and (6.70). Thus, we can fully characterize the modes above threshold: The different non-linear effects (e.g. mode competition, hole burning) are encoded in eq. (6.75).

Application to the single-mode regime

If we consider the case of one lasing mode, the linear system of eq. (6.75) reads

$$D_{11} I_1 = B_1 - \frac{\Gamma_1}{2\Delta N_0} \tag{6.76}$$

Hence the steady state intensity of the lasing mode reads

$$I_1 = \frac{1}{D_{11}}\left(B_1 - \frac{\Gamma_1}{2\Delta N_0}\right) \tag{6.77}$$

The self-saturation in eq. (6.77) is encoded in D_{11} and is necessary in this description. As already stated, the pump strength drives ΔN_0. Because the mode intensity must fulfil $I_1 > 0$, the mode intensity exhibits a threshold according to the pump strength. According to eq. (6.77) the threshold $\Delta N_{0,1th}$ can be derived

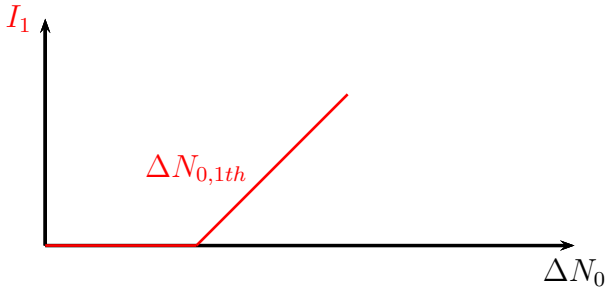

Figure 6.5: Mode$_1$ intensity I_1 versus ΔN_0 mimicking the pump excitation: The threshold corresponds to the one obtained in the below threshold regime.

$$\Delta N_{0,1th} = \frac{\Gamma_1}{2B_1} = \frac{\Gamma_1}{Re\left(\Omega_1 i\chi_g(\omega_1)V_{11}\right)} \tag{6.78}$$

In the case of a single-mode laser, the threshold is similar to the one derived below threshold (see eq. (6.50) and Fig. 6.5). It emphasizes that the approach used below threshold assumes the modes to be independent. If the quality factor of the mode is high enough $Q_1 \gg 1$, eq. (6.78) reads

$$I_1(\Delta N_0) = \frac{B_1}{D_{11}} - \frac{1}{Q_1 Re(i\chi_g(\omega_1)A_{1111})\Delta N_0} \tag{6.79}$$

Hence the slope of mode intensity versus the excitation ($\Delta N_{0,1th}$) is directly triggered by the quality factor of the passive mode and the non-linear coupling term A_{1111}.

Application to the two-mode regime

Now, we consider the case of two modes lasing simultaneously. Eq. (6.75) reads

$$\begin{bmatrix} D_{11} & D_{12} \\ D_{21} & D_{22} \end{bmatrix} \begin{bmatrix} I_1 \\ I_2 \end{bmatrix} = \begin{bmatrix} B_1 - \frac{\Gamma_1}{2\Delta N_0} \\ B_2 - \frac{\Gamma_2}{2\Delta N_0} \end{bmatrix} \tag{6.80}$$

The steady state evolutions of the two lasing modes read

$$I_1 = \frac{1}{\Delta}\left(D_{22}B_1 - D_{12}B_2 - \frac{D_{22}\Gamma_1 - D_{12}\Gamma_2}{2\Delta N_0}\right) \tag{6.81}$$

$$I_2 = \frac{1}{\Delta}\left(D_{11}B_2 - D_{21}B_1 - \frac{D_{11}\Gamma_2 - D_{21}\Gamma_1}{2\Delta N_0}\right) \tag{6.82}$$

where

$$\Delta = D_{11}D_{22} - D_{12}D_{21} \tag{6.83}$$

As expected, the thresholds are modified compared to the single mode (or below threshold) because of the cross-saturation terms encoded in D_{12} and D_{21}

$$\Delta N_{0,1th} = \frac{D_{22}\Gamma_1 - D_{12}\Gamma_2}{2(D_{22}B_1 - D_{12}B_2)} \tag{6.84}$$

$$\Delta N_{0,2th} = \frac{D_{11}\Gamma_2 - D_{21}\Gamma_1}{2(D_{11}B_2 - D_{21}B_1)} \tag{6.85}$$

As sketched in Fig. 6.6, the saturation also affects the slopes with regards to the single-mode case. The system described by eq. (6.80) gives an interesting insight on mechanisms

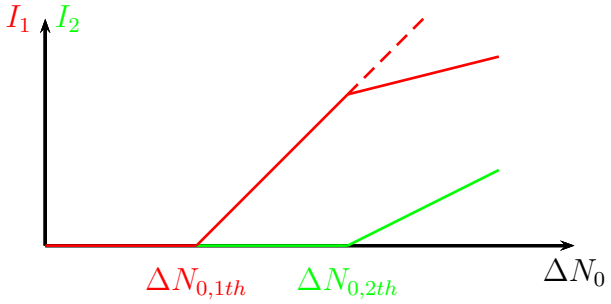

Figure 6.6: Mode$_1$ and Mode$_2$ intensities (I_1,I_2) versus ΔN_0 mimicking the pump excitation: When the second mode reaches the threshold, the slope of the first mode is modified because of cross-saturation terms.

above threshold in conventional and random lasers. The off-diagonal terms D_{12} and D_{21} (driven by the cross-saturation) couple intensities I_1 and I_2. For a system with no cross-saturation, $D_{12} = D_{21} = 0$ and the two modes evolve independently.

Moreover, these off-diagonal terms are directly triggered by the hole-burning cross-saturation A_{1122} and A_{2211}:

$$D_{pq} = \mathrm{Re}\left(\Omega_p \frac{i\chi_g(\omega_p)}{\hbar} A_{ppqq}\right) \tag{6.86}$$

In conventional lasers, because the system is "almost hermitian", the mode coupling between passive modes is weak and their spatial distribution is almost real

$$A_{ppqq} = \int \Phi_p(r)^2 |\Phi_q(r)^2| \mathrm{Im}(\chi_g(\omega_s)^*) \approx \int |\Phi_p(r)|^2 |\Phi_q(r)^2| \mathrm{Im}(\chi_g(\omega_q)^*) = \frac{\mathrm{Im}(\chi_g(\omega_q)^*)}{\mathrm{Im}(\chi_g(\omega_p)^*)} A_{qqpp} \tag{6.87}$$

The non-linear coupling between modes is thus almost symmetric. In the case of random laser, the modes in the weakly scattering regime are highly non-hermitian and thus complex

$$A_{ppqq} = \int \Phi_p(r)^2 |\Phi_q(r)^2| \mathrm{Im}(\chi_g(\omega_s)^*) \neq \int |\Phi_p(r)|^2 \Phi_q(r)^2 \mathrm{Im}(\chi_g(\omega_q)^*) = \frac{\mathrm{Im}(\chi_g(\omega_q)^*)}{\mathrm{Im}(\chi_g(\omega_p)^*)} A_{qqpp} \tag{6.88}$$

Therefore, the non-hermiticity breaks down the symmetry of the cross-saturation terms. In other words, in an hermitian system, there is a mutual competition between modes which cross-saturate each other with the same strength. By contrast, in non-hermitian systems, one mode can saturate other modes while remaining unaffected by the presence of these other modes (see Chapter 7).

6.4 Summary

Here, we have derived an analytical expression of the complex frequency and spatial distribution of random laser modes below and above threshold. This has been achieved by using the modal expansion along the Siegert states of the disordered passive system in the semiclassical approach. These results are only preliminary and will be used to offer an analytical insight to Chapters 7 and 8.

Emission threshold enforces two distinct regimes, namely below and above threshold. No mode can lase below threshold, while increasing the amplification modifies the modes of the random laser (referred to as active modes). Above threshold, at least one mode is emitting. The emitting modes are referred to as lasing modes. We have modelled the electric field evolution in the scope of the semiclassical theory (similar to [152, 44]). Below threshold, the population inversion, which triggers the amplification, is assumed static. Above threshold, the lasing modes lead to a saturation of the population difference. Then, we have carried on the approach developed in [152, 44] and expanded the electric field along the Siegert states of the passive random system. We have proposed to go beyond this description and have derived the modes by using a perturbation expansion. The passive modes linearly combine/mix to make up the active modes. This mixing is triggered by the linear coupling between the passive mode. Finally, above threshold, we have considered the cubic approximation, where four-wave mixing between passive modes may come into play. The modes have been also derived via a perturbation expansion. It turns out that the modes are the result of the linear and non-linear mixing of the passive modes. The non-linear mixing is induced by a non-linear coupling coefficients. Then, we have presented an approach common in laser physics to derive the intensity of lasing modes. It highlights that the threshold and the spatial distribution of active and lasing modes are strongly affected by the non-linear mixing. This approach stresses the existence of physical differences in non-linear mechanisms in conventional and random lasers.

Part IV

Control of random lasers

Chapter 7

Adaptive pumping for the control of random lasers: Numerical investigation

Table of Contents

Designing lasers at nano or microscale is extremely challenging, while assembling several nanometer particles makes a perfect random laser. Therefore, random lasers offer many potential applications. Random lasers can be used for medical application or as a unique and irreproducible coding key [157, 130]. Moreover, it was demonstrated recently that they could serve as speckle free lasing source [158]. They also offer surprising possibilities in bio-imaginary as a powerful and coherence-manageable source. However, since random lasers are highly multimode with unpredictable lasing frequencies and polydirectional output, their prospects are strongly hindered by the absence of emission control. Manipulation of the underlying random structure [159, 160, 161, 162, 163] and recent works constraining the range of lasing frequencies [164, 165] resulted in significant progress toward possible control. However, these different approaches do not allow the choice of a specific frequency in generic random lasing systems. In Chapter 6, we demonstrated the role played by linear and non-linear mixing of passive modes in the build-up of random lasers emission. The use of a non-uniform spatial profile for the pump is an interesting degree of freedom to modulate this mode-mixing and thus paves the road to a possible control of laser emission. In a regime of very strong scattering where the modes of the random system are spatially localized [56], local pumping allows the selection of spatially non-overlapping modes [109, 110]. In weaker scattering media (e.g. [166, 167, 168]), several hurdles appear toward achieving fine control. Selecting modes is hampered by a narrow distribution of lasing thresholds [169, 170] and spatial mode overlap. Increased pumping required in these lossy systems begins to alter the random laser itself. Moreover, modifying the shape of the pump introduces changes to both spatial and spectral properties of lasing modes [171, 172, 173]. Such difficulties are typically absent in more conventional lasers, which employ pump shaping (both electrically [174, 175] and optically [176]) to select favorable lasing modes. This raises the question whether the shaping of the incident pump field can achieve some degree of control of random lasers?

In this chapter, we exercise control over the distribution of lasing thresholds via the pump geometry to choose the random laser emission frequency. The numerical work we report here was published in [177]. First, the early achievements on partial pumping are reviewed. Then, the method is applied to 1D random lasers both in the weakly scattering and in the localized regimes to select specific mode in the emission spectrum. Optimization in the localized regime confirms that modes can be addressed by local pumping and serves as a benchmark for our method [109, 110]. In the weakly scattering regime, where modes overlap and spatial selectivity is no more possible, similar mode selection is achieved with a non-trivial pump profile. Finally, we explain this method in terms of mode-mixing. Using the analytical approach developed in Chapter 6, we give some insights to the optimization mechanism and propose some research perspectives we will aim at pursuing in future works.

7.1 Early achievements of local pumping

After Hui Cao's pioneer work [118], many numerical approaches were developed to investigate the nature of random laser modes [149, 109]. In random lasers, the pump excitation is not geometrically constrained. In the localized regime, Sebbah *et al.* [110] used this property to address the lasing modes individually via a local pumping (see Fig. 7.1). They demonstrated the weak spatial and spectral interactions between Anderson-localized modes (see Chapter 6 and [155]). In turn, random lasers are shown to be good candidates for the investigation of localized modes. Following a preliminary work of Wu *et al.* [172],

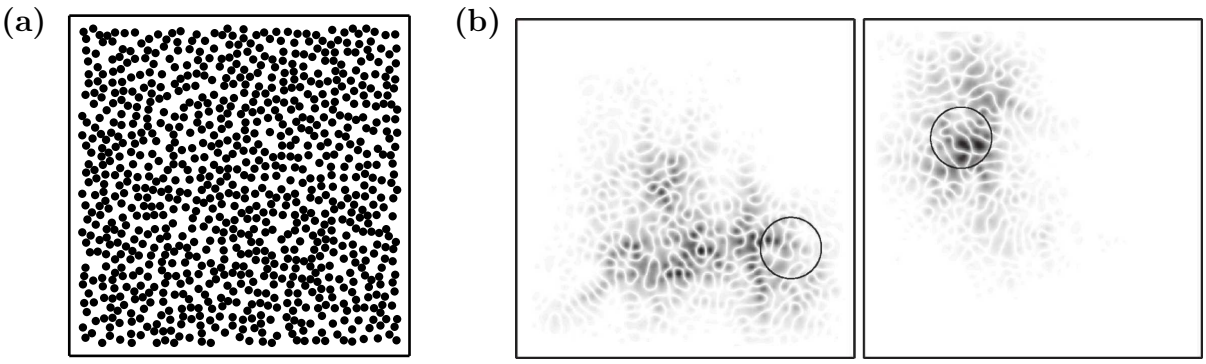

Figure 7.1: **(a)** 2D random laser in the localized regime Sebbah *et al.* [110]. **(b)** Selectively excited individual modes with local pump spots (circles).

the idea of local pumping was extended to the weakly scattering regime by Andreasen *et al.* [171]. They computed the modes of a 1D random laser using a Transfer Matrix Method (see Chapter 2 and 6) and investigated the evolution of the active modes in case of a gradual reduction of the extension of the pump (see Fig. 7.2). The authors observed modifications in the complex frequency and the spatial distribution of the active modes. Finally, they demonstrated that this partial pumping performed a linear-mixing of the

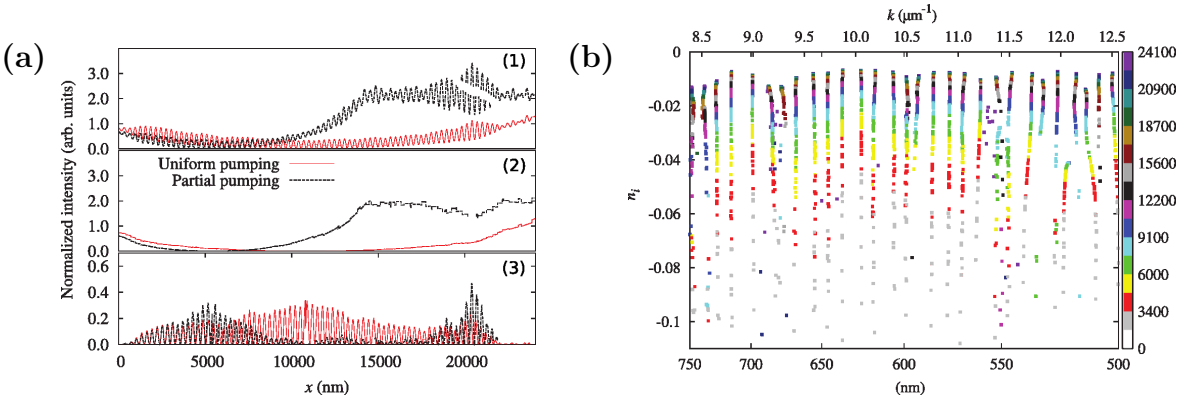

Figure 7.2: **(a)** 1D random medium (in the weakly scattering regime) used by Andreasen *et al.* [171]. Partial pumping was achieved with a uniform stripe of variable length: **(1)** red curve: A mode for a full pumping of the system and black curve: the corresponding mode for a pumping restricted to $0 \leq x \leq 14$ μm (14 μm large pump stripe) **(2)** Travelling components of previous modes (see Appendix B) **(3)** Stationary components. **(b)** Evolution of modes within the complex plane for an increasing size of the pump. The color-scale maps the pump stripe length.

passive modes. This is highlighted in Fig. 7.3 where they expanded the active modes obtained in Fig. 7.2 along the passive modes. The complete excitation of the system leads to an active mode close (but not similar) to a passive mode, while the partial pumping leads to the presence of several passive modes. In other words, the partial pumping achieves a different linear combination or mixing of the passive modes.

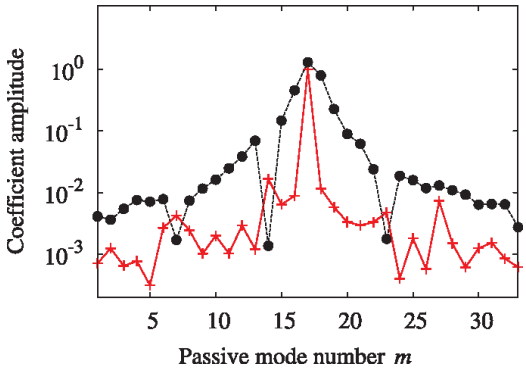

Figure 7.3: Decomposition along the passive mode of the system: Crosses stand for the decomposition of the mode obtained for a uniform pumping (Red curve on Fig. 7.2**(a)**). Dots stand for the decomposition of the mode obtained for a partial pumping (Black curve on Fig. 7.2**(a)**).

7.2 Taming random laser emission through the pump profile: Threshold optimization

In this section we extend the previous achievements on partial-pumping and present the first control of a random laser through the optimization of the pump excitation [177]. The pump profile is iteratively shaped to select one mode in the spectral emission. The threshold of this targeted mode becomes lower than others thresholds, thus achieving a single-mode emission. The modes are computed with a Transfer Matrix Approach. As this method is, strictly speaking, only valid at or below threshold, non-linearities are neglected. First, we present the numerical model and the influence of the pump profile. Then, we test our method on a random laser in the localized regime. Finally, we demonstrate emission control in the more difficult case of a random laser in the weakly scattering regime.

7.2.1 Numerical system

A 1D random random laser

We consider a one dimensional random laser represented by a stack of 161 dielectric layers (optical index n_1) separated by air gaps (n_0) (see Fig. 7.4). Randomness is introduced in the thickness of each layer $d_{0,1} = \langle d_{0,1} \rangle (1 + \eta\zeta)$, where $\langle d_{0,1} \rangle$ is the average thickness, $0 < \eta < 1$ the degree of randomness, and ζ is a uniformly distributed random number. The position along the system is $x \in [0, L]$, where L is the total length. We impose $\langle d_1 \rangle$ = 100 nm for the dielectric layers and $\langle d_0 \rangle$ = 200 nm for air, giving a total average length

$\langle L \rangle = 48.1\ \mu$m. The degree of randomness is set to $\eta = 0.9$. The scattering strength is directly triggered by the contrast index $\Delta n = n_1 - n_0$. Depending on the value of the index contrast, the studied random laser can either be in the strongly scattering regime, where light is confined within the random system, or in the weakly scattering regime (see Chapter 2), where modes are extended.

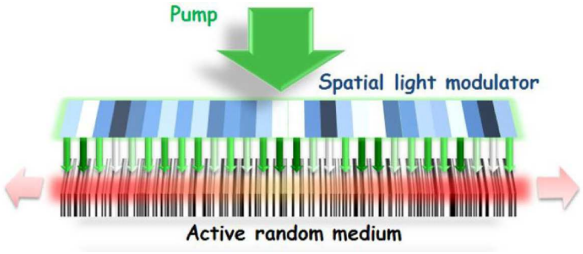

Figure 7.4: Principle of a 1D random laser pump profile optimization. The black slabs represent the dielectric material, which is also the gain medium. The optical pumping (small arrows) is transverse to the structure and amplitude modulated. In real experiment, this spatial modulation may be provided by a Spatial Light Modulator. Lasing (red arrows) occurs along the structure and will depend on the pump profile.

The gain is inserted into the dielectric medium. The dielectric medium is thus described by a frequency dependent susceptibility (see Chapter 6)

$$\chi_g(\omega)\Delta N_0 = \frac{d^2\omega_a}{\hbar(\omega - \omega_a + i\frac{\Delta\omega_a}{2})}\Delta N_0 \tag{7.1}$$

where d^2 is a material-dependent constant, ΔN_0 is the density of excited atoms when the system is uniformly pumped, ω_a is the atomic transition and $\Delta\omega_a$ is the spectral linewidth of the atomic resonance. For numerical reasons, the light celerity is fixed unitary ($c = 1$), thus $\omega = kc = k$[1]. The electric field is described by the below threshold equation

$$\Delta E(r,\omega) + n^2(r)\omega^2 E(r,\omega) \approx -\omega^2\chi_g(\omega)\Delta N_0(r)E(r,\omega) \tag{7.2}$$

As a result, eq. (7.2) satisfies a non-linear eigenvalue problem

$$\Delta E(r,\omega) + n^2(r,\omega)\omega^2 E(r,\omega) = 0 \tag{7.3}$$

where the index of refraction $n(r,\omega)$ is now frequency dependent, with value n_0 in air and $\sqrt{n_1^2 + \chi_g(\omega)\Delta N_0}$ in dielectric. We fix the transition frequency $\omega_a = 10.25\,\mu m^{-1}$ (typical of a solution of Rhodamine 590) and the spectral linewidth $\Delta\omega_a = 0.25\,\mu m^{-1}$ (598-628 nm). We use a Transfer Matrix Method (see Chapters 2 and 6) to compute the active modes. As stated in Chapter 6, rather than the complex frequency of each active mode $(\omega_r + i\omega_i)$, we equivalently consider its real frequency and threshold $(\omega_r, \Delta N_i)$.

[1]The numerical routine we propose in this section relies on an optimization algorithm. Such algorithm needs an important numerical precision on ω to converge. Fixing $c = 1$ provides more significant digits on ω and a better convergence.

Introduction of the pump profile

The pump profile $f_E(x)$ spatially modulates the density of excited atoms ΔN_0. The non-uniform density of excited atoms reads

$$f_E(x)\Delta N_0 \tag{7.4}$$

where x is the position of the layer. The function $f_E(x)$ fulfils the constraint

$$0 < f_E(x) < 1 \tag{7.5}$$

to mimic, for instance, the amplitude modulation of the pump beam by a spatial light modulator (see Fig. 7.4). In the present case, for numerical reasons, $f_E(x)$ is discretized in 161 pixels in one-to-one correspondence with the dielectric slabs. The value of each pixel stands for the amplitude of f_E within the slab. This pump profile changes the gain provided by each dielectric layer, giving possible control over the active modes of the random laser.

Optimization algorithm

Here, we aim at selecting a particular active mode by optimizing the pump profile (as proposed in section 7.3.1). Experimentally, a lasing mode Mode_i will be selectively excited if its threshold, N_i, is sufficiently low and significantly lower than that of all other modes. Hence, we introduce the rejection rate

$$RR_i = \frac{min_{j\neq i}(N_j)}{N_i} \tag{7.6}$$

which compares the threshold of Mode_i with the lowest threshold $min_{j\neq i}(N_j)$.

Selection of Mode_i is achieved when $RR_i > 1$ provided its threshold, N_i remains reasonably low. We therefore modify the pump profile f_E to minimize

$$C = \frac{1}{RR_i} + \alpha N_i \tag{7.7}$$

with α properly chosen to balance each term. This optimization of the criterion C defined in eq. (7.7) is performed using an algorithm based on a projected gradient method. At each iteration, the gradient of C is computed with respect to the pump profile $f_E(x)$. In the present case, we estimate the derivative of C with respect to the 161 pixels of the pump profile. Then, the pump profile is tuned along the direction where the previous derivative is maximum. Finally, the resulting pump profile is projected into $[0, 1]$ to fulfil the constraint of eq. (7.5). Convergence is reached if its relative variation is less than 10^{-4}.

7.2.2 Optimization in the localized regime

A random laser in the localized regime

We consider a disorder induced by an index contrast $\Delta n = 0.6$. Over the spectral range $10.0\,\mu m^{-1} < \omega < 10.5\,\mu m^{-1}$, we find a localization length[2] $\xi = 1.7\,\mu m < L$. The system

[2]In 1D systems, the localization length and the mean free path are identical [65]. As a result, the transmission T depends on the system length L and ξ. More precisely, $T \propto exp(-L/\xi)$. Since ξ only

is therefore in the localized regime and the active modes are spatially confined within the system (see Chapter 2). As explained in section 7.1, mode selection is achieved by local pumping at the location of modes of the passive system [109, 110]. The localized case serves here as a test case for our iterative algorithm, to check whether modes can be selected without any prior knowledge of their spatial location.

The pump profile is initialized with a uniform profile, which is the natural pumping scheme for broad area gain lasers. The threshold and optical frequency of the active modes are thus computed with the profile, $f_E(x) = 1$. Ten active modes are found in the spectral window of interest. They are positioned in the frequency-threshold plane and represented as crosses in Fig. 7.5**(a)**. Four active modes with reasonably low thresholds and partial spatial overlap are chosen for demonstration. Their spatial profiles are shown Fig. 7.5**(b)**, together with the profile of a higher threshold active mode at $\omega = 10.4\,\mu m^{-1}$, associated with a lossy mode confined on the left end of the sample.

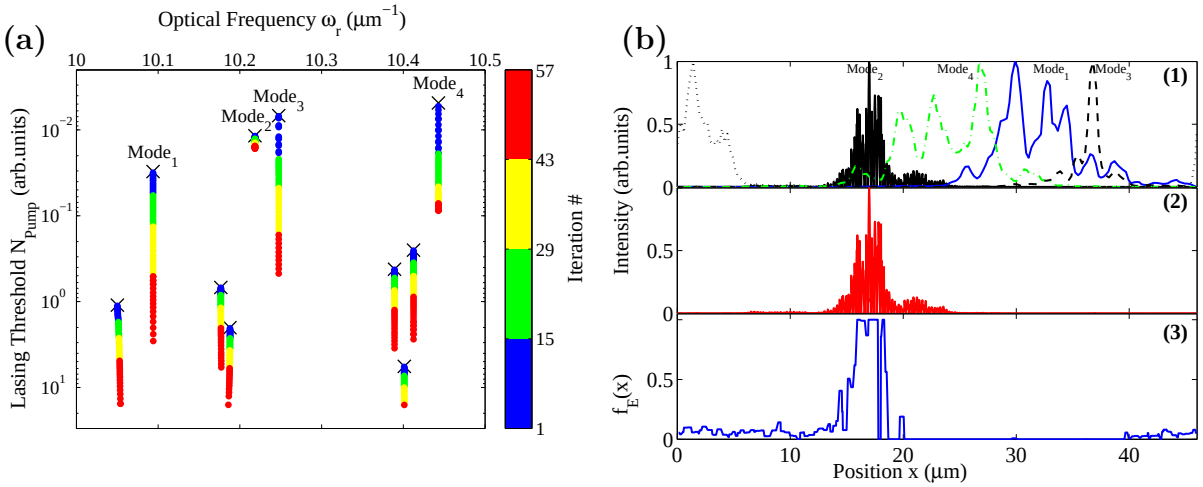

Figure 7.5: **(a)** Frequency vs threshold of the active modes at successive iterations, when the optimization routine is applied to select Mode_2. Crosses represent initial positions for uniform pumping. **(b)(1)** Spatial distributions of five modes. The mode profile on the left edge corresponds to the leaky mode with the highest threshold at $\omega = 10.4\,\mu m^{-1}$ **(2)** Spatial distribution of Mode_2 after optimization **(3)** Resulting optimized spatial pump profile $f_E(x)$.

Optimization

We consider Mode_2 ($\omega = 10.22\,\mu m^{-1}$). Its rejection rate for uniform pumping is $RR_2 = 0.45 < 1$, meaning it would not lase first at threshold. We now apply the iterative process to select this active mode, with $\alpha = 10$. Its rejection rate increases rapidly as shown in Fig. 7.7**(b)**. It is larger than unity after 10 iterations and converges to $RR_2 = 5.4$ after 57 iterations. The relative increase of threshold of Mode_2 is less than 50%. In contrast,

depends on the refractive index contrast, we vary L (by adding layers) to find T and we use it to find ξ. 1-For each L, we generate 10000 random structures. 2-For each structure, we find T as a function of frequency $T(\omega)$ for the passive system by computing the field at both edges with the Transfer Matrix Method. 3- We take the natural logarithm of each spectrum separately to get $ln(T(\omega))$. 4-We average $ln(T(\omega))$ over all structures to obtain $\langle ln(T(k))\rangle$ for each L. 5-We use a linear fit to get the slope (ξ=-1/slope). 6-In the end, we obtain $\xi(\omega)$.

for all other modes, the threshold increases by at least one order of magnitude. This is illustrated in Fig. 7.5**(a)** showing the evolution of the spectrum in the frequency-threshold plane. Mode_2 is efficiently selected and will be the first to lase above threshold. Single mode operation is robust even at relatively high pumping rate since RR_2 is large. The optimization algorithm has been successfully applied to all computed modes (respectively $\text{Mode}_{i\in[1-4]}$, see Fig. 7.6)

	Mode_1	Mode_2	Mode_3	Mode_4
RR_{i0}	0.02	0.45	0.76	1.51
$RR_{i\infty}$	2.1	5.4	50.9	30.3
N_{i0}	0.031	0.012	0.007	0.005
$N_{i\infty}$	0.057	0.017	0.013	0.01
$C_{fi\infty}$	0.67	0.82	0.77	0.76

Figure 7.6: Values of the rejection rate (respectively threshold) before optimization (uniform pumping), RR_{i0} (respectively N_{i0}), and after convergence, $RR_{i\infty}$ (respectively $N_{i\infty}$), as well as the correlation, $C_{fi\infty}$, with the final pump profile, $f_E(x)$, when the iterative process is applied successively to each mode, $\text{Mode}_{i\in[1-4]}$. Values in second column correspond to the optimized case of figure 7.5.

Interpretation of the pump profile

The optimized pump profile, $f_E(x)$, obtained for Mode_2 is shown in Fig. 7.5**(b)(3)**. As expected [109, 110], it is similar to the active mode spatial distribution (see Fig. 7.5**(b)(2)**). The degree of similarity is measured by the spatial correlation between the pump profile and the spatial distribution of $\Phi_i(x)$

$$C_{fi} = \langle (f_E - \langle f_E \rangle)(\Phi_i - \langle \Phi_i \rangle) \rangle \tag{7.8}$$

where f_E and Φ_i have been normalized by their variance. For Mode_2, the correlation is close to one since $C_{f2} = 0.82$ at the last iteration. The solution reached by the algorithm is therefore consistent with the predicted efficiency of a local pumping in the localized regime, even in the presence of moderate overlap [109, 110]. It is also worth to note that the change of pump profile barely affects the frequency (see Fig. 7.5**(a)**) and spatial profile (see Fig. 7.5**(b)(2)**) of the active modes, as expected in the localized regime [178].

To give a better insight into the optimization process, we examine the evolution of the correlations $C_{fi\in[1-4]}$ relative to the number of iterations. As the optimization routine is applied, C_{f2} consistently increases, while correlations of the other modes tend to zero, as shown in Fig. 7.7**(a)**. This results in increased thresholds for these modes. The crosses in Fig. 7.7**(a)** indicate the mode with the lowest threshold, $min_{j\neq 2}(N_j)$, entering the calculation of RR_2 at a given iteration. After having worked alternatively on Mode_3 and Mode_4, the algorithm works exclusively on the rejection of Mode_4. This mode has the largest overlap with Mode_2; a fine tuning of the pump profile is therefore required to increase its threshold without greatly increasing the threshold of Mode_2. Actually, this optimization mechanism emphasizes that the modes can be addressed individually in the localized regime. For that matter, the pump profile must correlate with the spatial distribution of the targeted mode.

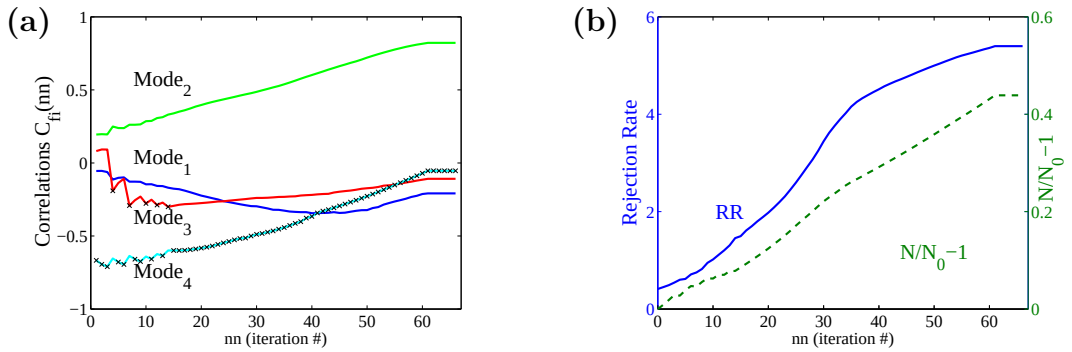

Figure 7.7: **(a)** Spatial correlations functions, C_{f_i}, between pump profile and Mode$_i$. Crosses indicate the mode with lowest threshold entering the calculation of RR_2. **(b)** Rejection rate, RR_2, and threshold N_2 for selected mode.

7.2.3 Optimization in the weakly scattering regime

A random laser in the weakly scattering regime

We now consider the more difficult case of a weakly scattering random laser. For an index contrast of $\Delta n = 0.05$, the localization length is $\xi \approx 200\,\mu m >$ L over the frequency range $10.0\,\mu m^{-1} < \omega < 10.5\,\mu m^{-1}$. The threshold and optical frequency of the active modes are thus computed with the profile, $f_E(x) = 1$. Twelve active modes are found in the spectral window of interest. They are positioned in the frequency-threshold plane

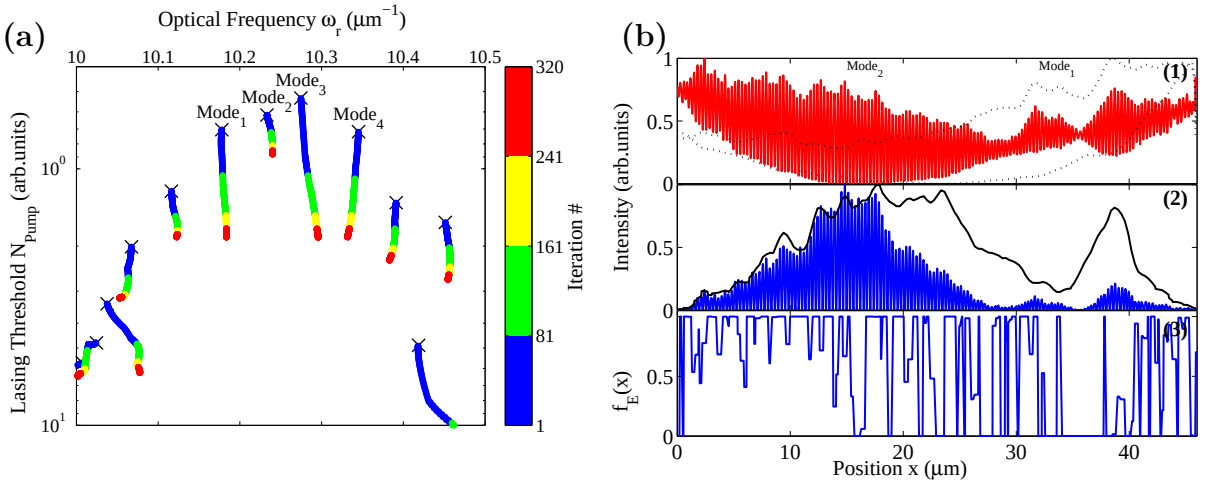

Figure 7.8: **(a)** Frequency vs threshold of the active modes at successive iterations, when the optimization routine is applied to select Mode$_2$. Crosses represent initial positions for uniform pumping. **(b)(1)** Spatial profile of Mode$_1$ (envelope) and Mode$_2$ (full) **(2)** Stationary component of Mode$_2$ before (envelope) and after optimization (full) **(3)** Resulting optimized spatial pump profile.

and represented as crosses in Fig. 7.8**(a)**. As in the localized regime, we consider four active modes with reasonably low thresholds, namely Mode$_{i\in[1-4]}$. Spatial distributions of Mode$_1$ and Mode$_2$ are shown in Fig. 7.10**(b)(1)**. Modes are now overlapping over the whole system precluding spatial selection of the mode by local pumping.

Optimization

The optimization procedure is applied to the Mode_2, with $\alpha = 0.3$. For a uniform pump profile, this mode is characterized by a rejection rate $RR_2 = 0.86$ and a frequency $\omega = 10.23\,\mu m^{-1}$.

The algorithm converges after 320 iterations with a final rejection rate $RR_2 = 2.47$. Although more modest than in the localized regime, this increase is significant enough to consider single-mode operation of the random laser at this selected frequency. Similar results are obtained for all other modes tested (see Fig. 7.9)

	Mode_1	Mode_2	Mode_3	Mode_4
RR_{i0}	0.75	0.86	1.17	0.74
$RR_{i\infty}$	1.26	2.11	2.53	1.24
N_{i0}	0.70	0.12	0.53	0.72
$N_{i\infty}$	0.81	0.28	0.74	0.81
$C_{f\,i\infty}$	0.20	0.28	0.21	0.31

Figure 7.9: Values of the rejection rate (respectively threshold) before optimization (uniform pumping), RR_{i0} (respectively N_{i0}), and after convergence, $RR_{i\infty}$ (respectively $N_{i\infty}$), as well as the correlation, $C_{f\,i\infty}$, with the final pump profile, $f_E(x)$, when the iterative process is applied successively to each mode, $\text{Mode}_{i\in[1-4]}$. Values in second column correspond to the optimized cases of Fig. 7.8.

Fig. 7.8**(a)** shows the impact of the iterative process on Mode_2. As the thresholds increase, this active modes experience a spectral shift as well as a spatial deformation (see Fig. 7.8**(b)**), in contrast to the localized regime.

Interpretation of the pump profile

Fig. 7.8**(b)(3)** shows that the optimized pump profile is rather unpredictable.

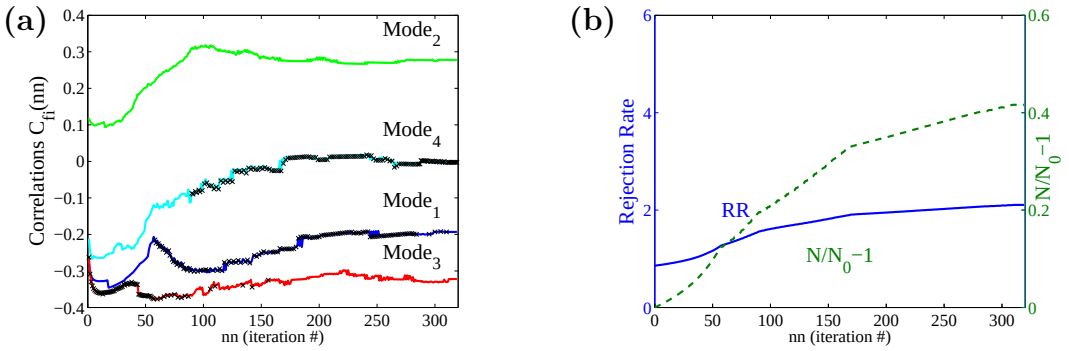

Figure 7.10: **(a)** Spatial correlation functions, C_{f_i}, between pump profile and stationary part of Mode_i. Crosses indicate the mode with the lowest threshold entering the calculation of RR_2. **(b)** Rejection rate, RR_2, and threshold N_2 for selected mode.

A small but significant correlation $C_{f2} = 0.28$ (see Fig. 7.10**(a)**) is found only when comparing the stationary component of Mode_2 (see Fig. 7.8**(b)(2)**) and the pump profile

(see Appendix B). The subtlety of the optimization process, which is successfully demonstrated for all modes, is exemplified in Fig. 7.10**(a)**. The ceaseless switching between modes $\text{Mode}_{i\in[1;3;4]}$ (crosses) forces reduced correlation, and even anticorrelation between the rejected modes and the pump profile.

7.3 Below threshold modal expansion

In section 7.2, we numerically demonstrated the optimization of random lasing emission. However, if the optimized pump profile obtained in the localized regime is well understood, its shape in the weakly scattering regime is rather unpredictable. In this section, we investigate the previous optimization in term of mixing of passive modes. First, we include the non-uniform pump profile in the below threshold modal expansion that we derived in Chapter 6. We highlight the influence of mode mixing in localized and weakly scattering regimes. The observations made in the following paragraphs will be further studied in future work. Finally, we explain that similar control can be achieved on spatial distribution of modes as recently shown numerically [179].

7.3.1 Principle of the below threshold pump profile optimization

Introduction of the non uniform pump profile

In Chapter 6, we demonstrated that the electric field for a uniform pumping reads

$$\Delta E(r,\omega) + \epsilon(r)\omega^2 E(r,\omega) \approx -\omega^2 \chi_g(\omega)\Delta N_0 E(r,\omega) \tag{7.9}$$

As stated in section 7.2, the non-uniform pump profile $f_E(r)$ modulates the density ΔN_0. Hence, eq. (7.9) reads

$$\Delta E(r,\omega) + \epsilon(r)\omega^2 E(r,\omega) \approx -\omega^2 \chi_g(\omega)\Delta N_0 f_E(r) E(r,\omega) \tag{7.10}$$

The electric field is expanded along the passive modes (Ω_i, Φ_i)

$$E(r,\omega) = \sum_p a_p(\omega)\Phi_p(r) \tag{7.11}$$

Using the biorthogonal product between the passive modes, eq. (7.10) reads

$$a_p(\omega)(\Omega_p^2 - \omega^2) = \omega^2 \chi_g(\omega)\Delta N_0 \sum_q a_q(\omega) \int f_E(r)\Phi_p(r)\Phi_q(r) \tag{7.12}$$

Eq. (7.12) defines a non-linear eigenvalue problem. Considering a finite number of passive modes N, we can recast the system in a matrix form

$$\begin{bmatrix} \Omega_1^2 & \dots & 0 \\ \vdots & \ddots & \vdots \\ 0 & \dots & \Omega_N^2 \end{bmatrix} = \omega^2 \begin{bmatrix} 1+\Delta N_0\chi_g(\omega)V_{11} & \dots & \Delta N_0\chi_g(\omega)V_{1N} \\ \vdots & \ddots & \vdots \\ \Delta N_0\chi_g(\omega)V_{N1} & \dots & 1+\Delta N_0\chi_g(\omega)V_{NN} \end{bmatrix} \tag{7.13}$$

where

$$V_{ij} = \int f_E(r)\Phi_p(r)\Phi_q(r) \tag{7.14}$$

are referred to as spatial overlap coefficients. These coefficients stand for the interaction, the coupling between the passive modes. The active modes of the random laser are the eigenmodes of the non-linear eigenvalue problem derived in eq. (7.13). Each active mode will be associated with a complex frequency $\tilde{\Omega}_p = \tilde{\omega}_p - i\frac{\tilde{\Gamma}_p}{2}$ and a spatial distribution $\tilde{\Phi}_p$.

Perturbation expansion

We perform the first order perturbation expansion of eq. (7.13). This expansion of the active modes is similar to the one performed in Chapter 6. For a non-constant susceptibility, the complex frequency at first order reads

$$\tilde{\Omega}_p \approx \Omega_p \left(1 - \Delta N_0 V_{pp} + \Delta N_0^2 \sum_{q\neq p} \frac{\Omega_p^2}{\Omega_q^2 - \Omega_p^2} V_{pq}^2 + \frac{3}{8}\Delta N_0^2 V_{pp}^2\right) \tag{7.15}$$

And the corresponding spatial distribution reads

$$\begin{aligned}\tilde{\Phi}_p &\approx \Phi_p + \Delta N_0 \sum_{q\neq p} \frac{\Omega_q^2}{\Omega_q^2 - \Omega_p^2} \chi_g(\omega_p) \left(\int f_E(u)\Phi_p(u)\Phi_q(u)du\right) \Phi_q(r) \\ &= \Phi_p + \Delta N_0 \sum_{q\neq p} \frac{\Omega_q^2}{\Omega_q^2 - \Omega_p^2} \chi_g(\omega_p) V_{pq} \Phi_q(r)\end{aligned} \tag{7.16}$$

We stated in Chapter 6 that eq. (7.15) and (7.16) emphasize that the linear mixing is responsible for the active modes. A non-uniform pump profile affects the coupling coefficients V_{pq} and in turn changes the mixing of passive modes thus giving rise to the active modes. Hence, different non-uniform pump profiles achieve different linear mode mixing.

Managing the mode mixing

Eq. (7.15) and (7.16) offer an interesting insight to the optimization process.

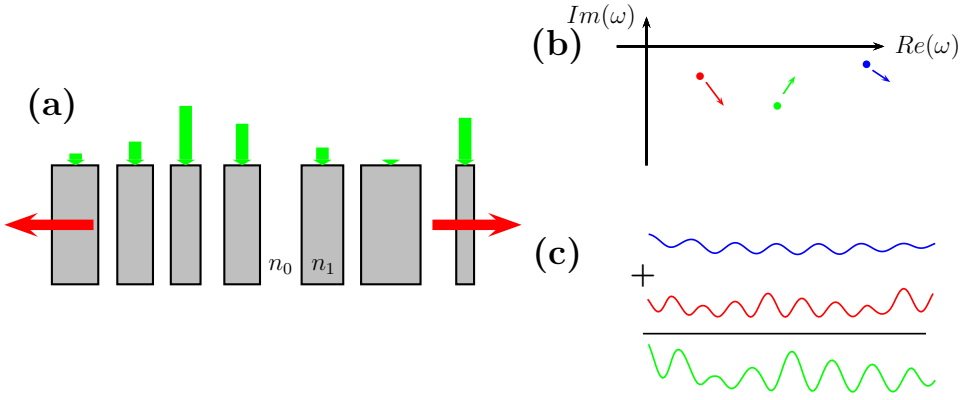

Figure 7.11: **(a)** A 1D random laser below threshold with a non-uniformly pumping. **(b)** Complex frequencies when the pumping is uniform. The arrows mimic their evolution when the pump profile is modified. **(c)** The spatial distribution results from a linear mixing of modes obtained for a uniform pumping.

A non-uniform profile f_E, as sketched in Fig. 7.11, is responsible for new coefficients V_{pq}. These new coefficients induce a new linear mixing of the passive modes. As shown in Fig. 7.11**(a)** and **(b)**, the complex frequencies and spatial distribution of the active modes are changed. Therefore, an adapted pump profile consists in finding the "good" coefficient V_{pq} to change the active mode toward a certain criterion.

7.3.2 Threshold optimization

Localized regime

In the localized regime, the spatial overlap between modes is weak

$$V_{pq} \propto \delta_{pq} \tag{7.17}$$

System described by eq. (7.13) has no off-diagonal terms, the coupling between passive modes is null. Hence, according to eq. (7.16), the spatial distribution of the active modes is identical to the passive one

$$\tilde{\Phi}_p = \Phi_p \tag{7.18}$$

In the localized regime, active modes are similar to passive modes and are not affected by the pump profile (as expected from Chapter 6). This absence of mode coupling is also observed in Fig. 7.5**(a)**, where the different modes are not frequency shifted.

Performing a derivation proposed in Chapter 6, the threshold of each mode can be derived from eq. (7.15)

$$\Delta N_{0p,th} \approx -\frac{\Gamma_p}{\mathrm{Im}\left(\Omega_p \chi_g(\Omega_p) \int f_E(u)\Phi_p^2(u)du\right)} \tag{7.19}$$

For localized modes, because the losses are weak, both the passive complex frequencies and the spatial distributions are almost real. Thus, equation (7.19) reads

$$\Delta N_{0p,th} \approx -\frac{1/Q_p}{\left(\int f_E(u)\Phi_p^2(u)du\right)\mathrm{Im}\left(\chi_g(\Omega_p)\right)} \tag{7.20}$$

Eq. (7.20) emphasizes the fact that in the localized regime, the threshold of the mode is directly triggered by the correlation between the pump profile $f_E(x)$ and the intensity of the mode Φ_p^2. The energy is transferred from the pump to the mode via the intensity of the field. As a result, because modes do not overlap, the optimization of one specific threshold consists in correlating the pump profile with the intensity of the mode. For instance, during optimization in the localized regime of section 7.2 (see Fig. 7.7), the correlation of the pump profile with Mode_2 intensity increases to a value close to one. In the same time, the correlation of mode profile with other modes converges to zero.

Weakly scattering regime

In the weakly scattering regime, the presence of spatial overlap induces a coupling of the passive modes responsible for non zero V_{pq}. This coefficients ensure a mixing of passive modes to build-up active modes. The spatial distributions of the active modes read

$$\tilde{\Phi_p} = \Phi_p + \Delta N_0 \sum_{q \neq p} \frac{\Omega_q^2}{\Omega_q^2 - \Omega_p^2} \chi_g(\omega_p) V_{pq} \Phi_q(r) \tag{7.21}$$

Hence, when the pump profile is modified, the mixing between the passive modes changes. For instance, as shown in Fig. 7.5**(b)** in section 7.2, during the optimization of Mode_2 the shape of its spatial distribution is strongly altered.

Like in the localized regime, the threshold of the different active modes reads

$$\Delta N_{0p,th} \approx -\frac{\Gamma_p}{\text{Im}\left(\Omega_p \chi_g(\Omega_p) \int f_E(u) \Phi_p^2(u) du\right)} \tag{7.22}$$

However, unlike localized case, the passive modes have important leakage in the weakly scattering regime. As a result, spatial distributions and complex frequencies of passive modes are complex. If we consider the example proposed in section 7.2, the quality factors of the passive modes are ≈ 10 and $\Omega_p \approx \omega_p$. Assuming modes are close to the center of the gain curve $\chi_g(\omega) \approx -i|\chi_g(\omega_a)|$. Threfore, the thresholds read

$$\Delta N_{0p,th} \approx \frac{1/Q_p}{|\chi_g(\Omega_p)| \text{Re}\left(\int f_E(u) \Phi_p^2(u) du\right)} = \frac{1/Q_p}{|\chi_g(\Omega_p)| \int f_E(u) \text{Re}(\Phi_p^2(u)) du} \tag{7.23}$$

The threshold of active mode in the weakly scattering regime is triggered by the overlap between the pump profile and the real part of the complex intensity $\text{Re}(\Phi_p^2) = \text{Re}(\Phi_p)^2 - \text{Im}(\Phi_p)^2$ instead of the intensity itself ($|\Phi_p|^2 = \text{Re}(\Phi_p)^2 + \text{Im}(\Phi_p)^2$). The RR of Mode_p in the weakly scattering regime reads

$$RR_p \propto \frac{\text{Re}\left(\int f_E(u) \Phi_i^2(u) du\right)}{\text{Re}\left(\int f_E(u) \Phi_p^2(u) du\right)} \tag{7.24}$$

where Mode_i is the mode with the lowest threshold apart from Mode_p. Eq. (7.24) highlights the complexity of the optimization. In the same time the pump profile must correlate with $\text{Re}(\Phi_p^2(u))$ and decorrelate with $\text{Re}(\Phi_q^2(u))$. Moreover, in the numerical experiment we presented in section 7.2, this optimization is complicated by the presence of a non-uniform gain curve.

Future work

Sections 7.3.2 and 7.3.2 provide preliminary observations made via the formalism introduced in Chapter 6. In these two sections, we only aimed to propose some analytical insights. In particular we wanted to stress the difference between the optimization of quasi-hermitian modes (localized system) and highly non-hermitian modes (weakly scattering system).

In future work, we will try to adapt this approach to 1D and 2D optimizations. This analytical approach, could be helpful to address reverse problems and thus achieve a strong control of random laser properties. We could also try to investigate the minimal number of "pixels" (the discretization steps in the numerical pump profile of section 7.2) which are needed in order to optimize a pump profile. Otherwise, more exotic optimizations could be tried (e.g. two modes, a single-mode laser with a control of the frequency of the mode).

7.3.3 Directivity optimization

When modifying the mode coupling, the pump does not only affect the complex frequencies of active modes, it also affects its spatial distribution. According to eq. (7.16), the spatial distribution of mode reads

$$\tilde{\Phi}_p = \Phi_p + \Delta N_0 \sum_{q \neq p} \frac{\Omega_q^2}{\Omega_q^2 - \Omega_p^2} \chi_g(\omega_p) \left(\int f_E(u) \Phi_p(u) \Phi_q(u) du \right) \Phi_q(r) \tag{7.25}$$

In a similar way to threshold optimization, the pump profile can be adapted to select a specific spatial emission. Hence f_E can be iteratively shaped to constrain the spatial distribution $\tilde{\Phi}_p$, via the coupling terms $\int f_E(u) \Phi_p \Phi_q$.

Such control of the emission directivity was achieved in 2013 by Hisch *et al.* [179]. Using Finite Element Method computation, they iteratively shaped emission pattern of a specific mode (see Fig. 7.12) and consequently forced emission in a given direction.

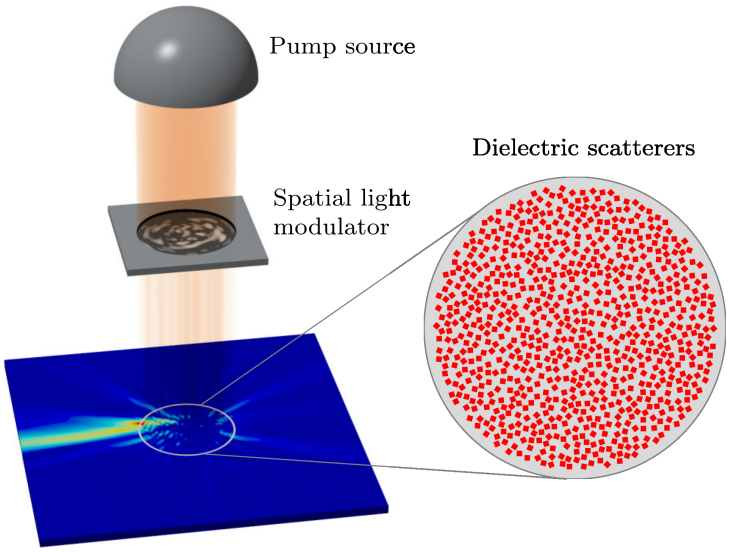

Figure 7.12: Schematic view of the directivity optimization of a random laser emission: A 2D circular random laser is modelled via FEM computation (below threshold computation). The linear mixing of modes modifies the emission pattern to emit in a particular direction [179].

7.4 Summary

We have demonstrated numerically the possibility of controlling random laser properties by adaptive shaping of the pump profile.

Starting from early observations relative to local pumping, we have stressed the possibility of controlling the linear-mixing between the modes of the passive system. By iteratively shaping the pump profile, different properties of random lasing emission can be tuned and controlled. We have applied this approach in a numerical experiment, where a 1D multimode random laser has been computed using a Transfer Matrix Approach. We have

investigated the possibility of achieving a single-mode emission via a control of mode thresholds based on an optimization routine. For localized modes, we have obtained pump profiles overlapping with the spatial extent of the selected mode. In the weakly scattering regime, despite the strong spatial overlap between modes, we have demonstrated that such optimization is still possible. Nevertheless, the adapted pump profile is rather complex. We have brought an analytical insight to this mechanism by inserting the pump profile within the modal description of random laser proposed in Chapter 6. As expected from numerical observations, the optimization of localized mode consists in correlating with its spatial distribution. In the weakly scattering regime, the pump profile results in a subtle mechanism.

Chapter 8

Adaptive pumping for the control of random lasers: Experimental investigation

Table of Contents

The modes of random lasers result from a mixing/combination of the modes of the passive system (see Chapter 6). Chapter 7 shown that a non-uniform distribution of the gain affects the mode mixing. The influence of the pump profile on mode mixing was used to control the active modes (*i.e.* below threshold) in a numerical experiment. In particular, an adapted pump profile can be designed to force single-mode emission of a random laser. This control can be extended to other characteristics of the modes, offering meanwhile interesting prospects and potential applications. We aim in the present chapter at demonstrating this laser control in an actual experiment.

Nevertheless, this optimization faces many challenges in practice and differs from the numerical approache developed in Chapter 7. For instance, the single-mode optimization will be performed on spectral peaks of the intensity rather than on mode thresholds. The optimization algorithm used in Chapter 7 cannot be used here. Indeed, in addition to experimental fluctuations, the intensity peaks naturally fluctuate because of the chaotic nature of random lasers [180]. Moreover, we must propose a solution to achieve a robust and precise modulation of the pump excitation. We also have to ensure that the laser is above threshold, whatever the pump profile. From a theoretical point of view, the modes observed experimentally differ from the ones considered numerically. Indeed, Chapter 6 hightlights the difference between active and lasing modes, below and above threshold, respectively. We stated that above threshold, the lasing modes result from complex linear and non-linear mixing of the passive modes. Therefore, the optimization that we intend to perform here relies on a different mechanism, where non-linear effects play a major role.

In this chapter, the control of spectral and spatial emissions is achieved using an optofluidic random laser similar to the laser described in Chapter 5. First, we perform the spectral control of a 1D random laser by modulation of the pump intensity via a spatial light modulator (SLM) [181]. By actively shaping the optical pump within the random laser, single-mode operation at any selected wavelength is achieved with spectral selectivity down to 0.06 nm and more than 10 dB side-lobe rejection. The analytical development of Chapter 6 is used to give a simple description of the optimization and to highlight the crucial quantities to consider for further investigations. Finally, we present preliminary experimental results concerning the control of the directivity of a 2D optofluidic source. Using similar approach, we force the direction of the emission.

8.1 1D optimization

The purpose of this section is to achieve the control of the spectral emission of a 1D microfluidic random laser. We show that the method proposed in the case of the numerical optimization presented in Chapter 7 is adapted to experimental conditions. First, the experimental setup and the numerical routine of optimization are presented. Then, we show an experimental optimization and discuss the reliability of the method. Finally, the description of Chapter 6 is used to offer an insight of the mechanism involved in the optimization.

8.1.1 Experimental Setup

1D random laser

We consider the optically pumped one-dimensional (1D) random laser described in Fig. 8.1. This laser is inspired from the device introduced in Chapter 5 and published in [120] for an easy integration of lasers into complex optofluidic structures [182]. The gain medium is a 2.5×10^{-3} M ethanolic solution of Rhodamine 6G circulating in a 2.8 mm-long PDMS microchannel made of a linear chain of randomly distributed rectangular pillars (see Fig. 8.1). This alternation of 70 layers, with two different indices of refraction ($n_{polymer}$ =1.42 and n_{dye} =1.36), provides multiple scattering and necessary feedback to achieve random lasing emission. As sketched in Fig. 8.1**(c)**, the microchannel is 80 μm wide and 15 μm deep. The pillars are 12 μm thick and 40 μm long. Their random positions are uniformly chosen in the range $\pm$6 μm around an arrangement having a period of 40 μm. Actually, this spatial disorder is not mandatory and artificial: Indeed, the limited accuracy of the photolithographic process results in a 1 μm tolerance in the position and thickness of the pillars, providing the necessary disorder at the optical scale (as explained in Chapter 5 and [120]). Because the random structure is static and the dye solution flows continuously within the microfluidic channel, dye-bleaching is reduced, making the lasing modes stable and the results reproducible over several hours. An auxiliary microchannel circulated by another dye (5.0×10^{-3} M ethanolic solution of Nile Blue) serves to image laser radiation scattered out by the structured channel (see Fig. 8.1**(d)** and **(e)**). The small index contrast between the polydimethylsiloxane (PDMS) pillars and the dye solution, Δn = 1.42 - 1.36 = 0.06, results in weak scattering. From numerical simulations (see Chapter 2) we find a localization length ξ = 22 mm at 560 nm, much longer than the sample size (2.8 mm). In this regime, modes are extended over the whole system and therefore strongly overlap with each other. This is confirmed in Fig. 8.1**(e)**, in which light is emitted all along the structure. Therefore, we are investigating optimization of random lasing emission in the weakly scattering regime.

Pump modulation and acquisition

As sketched in Fig. 8.2, the pumping is achieved by a laser beam from a frequency-doubled Q-switched Nd:YAG laser (Quantum Ultra: @532 nm, 10 ns pulse duration, maximum output energy 30 mJ, repetition rate 10 Hz). The pump beam is expanded to uniformly illuminate the surface of the SLM (Holoeye LC 2002), in order to perform

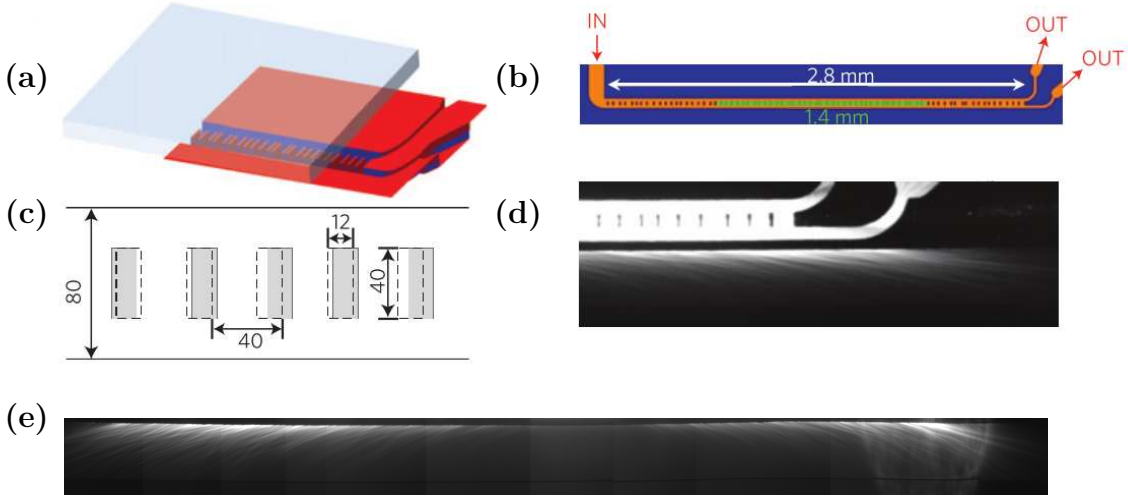

Figure 8.1: **(a)** 3D partial view of the microchannel device, **(b)** complete top view. **(c)** The microchannel is structured into a 1D-random distribution of 12 μm-thick rectangular pillars separated on average by 28 μm gaps. Geometrical dimensions are given in μm. A dye solution (Rhodamine 6G in ethanol) flows through the structured PDMS microchannel, which is plasma-bonded on a glass slide partially represented in **(a)**. A pressure differential at the two outlets forces dye flow between the scattering pillars and prevents dye bleaching. The structure is pumped by a Q-switched Nd:YAG laser at 532nm shaped into a 1.4mm-long stripe line (green line in **(b)**). **(d)** Imaging of the in-plane scattered laser emission. Dye (Nile blue) solution circulates in an 80 μm-wide auxiliary microchannel parallel to and at a distance of 10 μm from the structured channel and fluoresces at the laser emission wavelength. **(e)** Laser emission along the whole auxiliary channel.

spatial modulation of the excitation. The SLM itself, which sits between crossed polarizers to work in amplitude modulation, is placed in the object plane of a telescope with 5× reduction and is imaged on the sample after compression through a cylindrical lens with focal length $f = 6$ mm. This setup provides a 1.4 mm-long, 4 μm-thick laser stripe line with nearly diffraction-free modulation down to 1 μm-large rectangular pixels (see Fig. 8.1**(b)**).

We chose to tightly focus the pump beam to a narrow line in order to enforce single transverse mode laser operation. The length of 1.4 mm has been chosen to limit the amplified spontaneous emission (ASE) and to provide a manageable modal density. We checked experimentally that doubling the length increases the ASE by a factor of three and the number of modes by a factor of two. The microchannel is precisely aligned with the laser stripe line under a Zeiss Axioexaminer microscope and imaged using a Hamamatsu Orca-R2 silicon CCD camera microscope. The laser emission is collected via an optical fiber connected to a Horiba iHR550 imaging spectrometer equipped with a 2,400 l.mm^{-1} grating and a liquid nitrogen-cooled Symphony II camera (sampling rate 1MHz, 1,024×56 pixels, 26 μm pixel pitch). The entrance slit is 50 μm for a resulting spectral resolution of 20 pm and the integrating time is 1 s. An example of emission spectrum is illustrated in Fig. 8.4. Measured spectral linewidth is 0.03 nm (full-width at half-maximum) and not limited by the 20 pm-resolution of the imaging spectrometer.

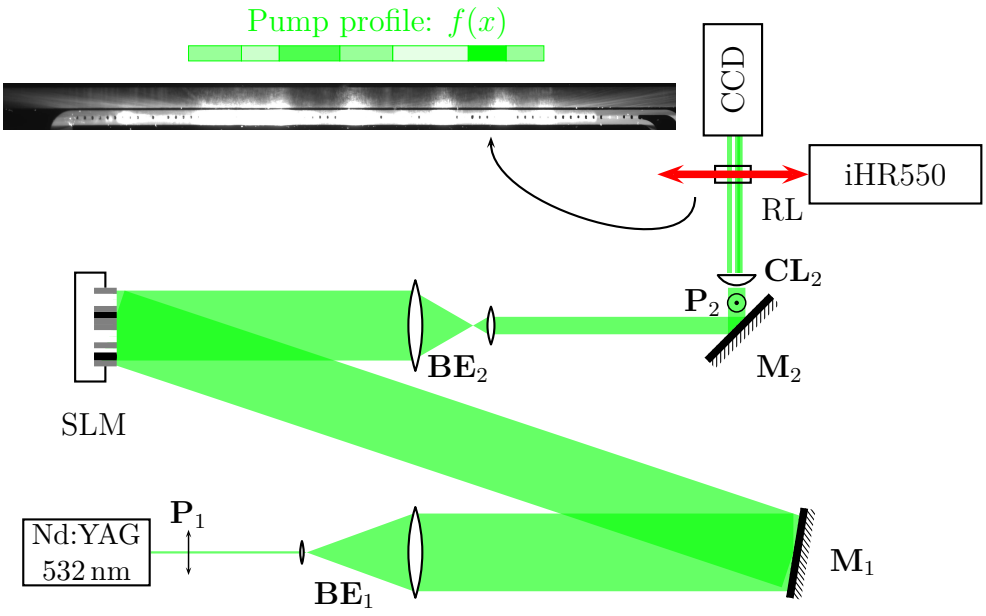

Figure 8.2: Experimental setup: The pump laser is polarized ($\mathbf{P}_1$) and expanded on the SLM by a beam expander ($\mathbf{BE}_1$). The SLM is imaged into the sample via a second beam expander ($\mathbf{BE}_2$). A second polarized ($\mathbf{P}_2$) performs the amplitude modulation. A cylindrical lens ($\mathbf{CL}_2$) is used to compress the image in 1D and achieves the pump profile $f_E(x)$. Random lasing light (Red arrows) is guided by the 1D structure, collected by the monochromator (iHR550) and the sample is imaged via a CCD camera protected by a notch filter (@ 532 nm) mounted on a Zeiss microscope.

Optimization method

In this work, we control the random lasing emission by enforcing a single mode emission and therefore confirm the numerical optimization proposed in Chapter 7. The 1D pump profile, $f_E(x)$, is made up of 32 lines (as sketched in Fig. 8.2). Each line is grey-scale-coded on 256 levels and imaged onto the sample to form a 46 μm-long, 4 μm-thick pixel. We chose the 32-column vectors X_i of the 32×32 binary Hadamard matrix [183] as the initial vertices to initiate the optimization procedure (see Fig. 8.3 and Appendix D). Consequently, the pump profile is expressed as a linear combination of 32 basis elements proposed in Fig. 8.3. Starting from any other basis on which an arbitrary pump profile can be decomposed should lead to convergence. We tested the alternate "stripe basis" with vectors formed by contiguous on-pixels, all others being off. The algorithm also converges, but to a different solution. Our choice of the Hadamard basis is practical, as all elements (except the first one) have the same mean amplitude. Therefore, they require a constant and reasonable pump fluence to reach threshold. Furthermore, to preclude any below threshold pumping, we set a minimum uniform background illumination (α_0). The pump profile is written as

$$f_E(x) = \frac{1}{255}\left[\alpha_0 + \sum_{1\to 32} \alpha_i X_i\right] \tag{8.1}$$

where the α_i take discrete values in the range [0,135] and the uniform background $\alpha_0 = 120$. Each vector $(X_i)_{i\in[1,32]}$ corresponds to a particular pump profile associated with a particular emission spectrum $I(\lambda)$.

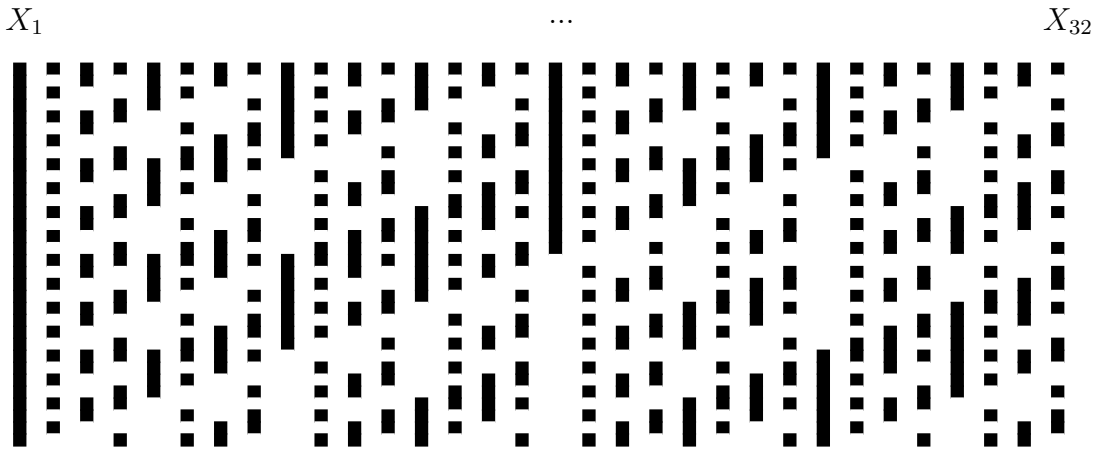

Figure 8.3: The Hadamard basis: Each column stands for a vector of the basis, X_i. For each pixel of the X_i, black squares stand for unitary value and white for zero value.

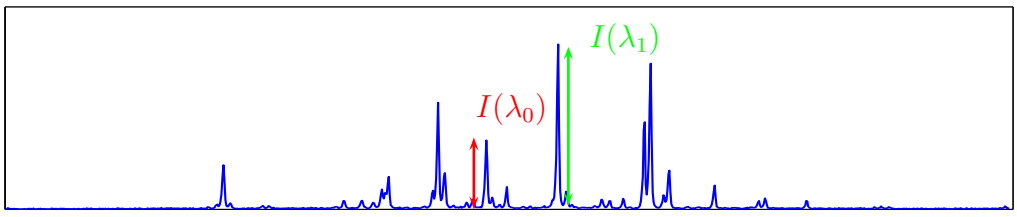

Figure 8.4: Rejection rate definition $R(\lambda_0)$: The intensity of targeted mode $I(\lambda_0)$ is divided by the highest other intensity $I(\lambda_1)$.

To achieve single-mode operation at a targeted wavelength, λ_0, we need to find the coefficients $(\alpha_i)_{i\in[1,32]}$ which maximize the rejection rate defined as

$$\alpha_i \rightarrow R(\lambda_0) = \frac{I(\lambda_0)}{I(\lambda_1)} \tag{8.2}$$

where λ_1 corresponds to the wavelength of the lasing mode with highest intensity, apart from the mode at λ_0 (an illustration is proposed in Fig. 8.4).

To perform optimization of eq. (8.2), we use the Nelder-Mead simplex (direct search) method implemented in the **fminsearch** function of Matlab (see Appendix D). We modified this function by setting the initial step (**usual_delta** parameter in **fminsearch**) to 0.5 to explore a large region of the 32-dimensional space. Because of inherent strong fluctuations of the random lasing emission, we chose this derivative-free algorithm to preclude any derivative computation. The number of pixels (32) has been determined for the best trade-off between sensitivity and computation time. A power of two has to be chosen for the definition of the Hadamard basis.

8.1.2 Optimization results

Optimization procedure

Experimentally, five spectra integrayed over ten shots are acquired every second and then averaged for a given pump profile $f_E(x)$. The typical shot-to-shot variance of the lasing peaks is around 10%. Hence, averaging over 50 shots reduces spectrum fluctuations to roughly 1.4. Such accuracy is needed when the denominator in

$$R(\lambda_0) = \frac{I(\lambda_0)}{I(\lambda_1)} \tag{8.3}$$

becomes small. Between successive acquisitions, the system is uniformly pumped ($f_E(x)$ =1) to "clean up" the gain medium from any memory effect due to possible residual thermal perturbation from previous pump profiles. A typical optimization lasts 20 min.

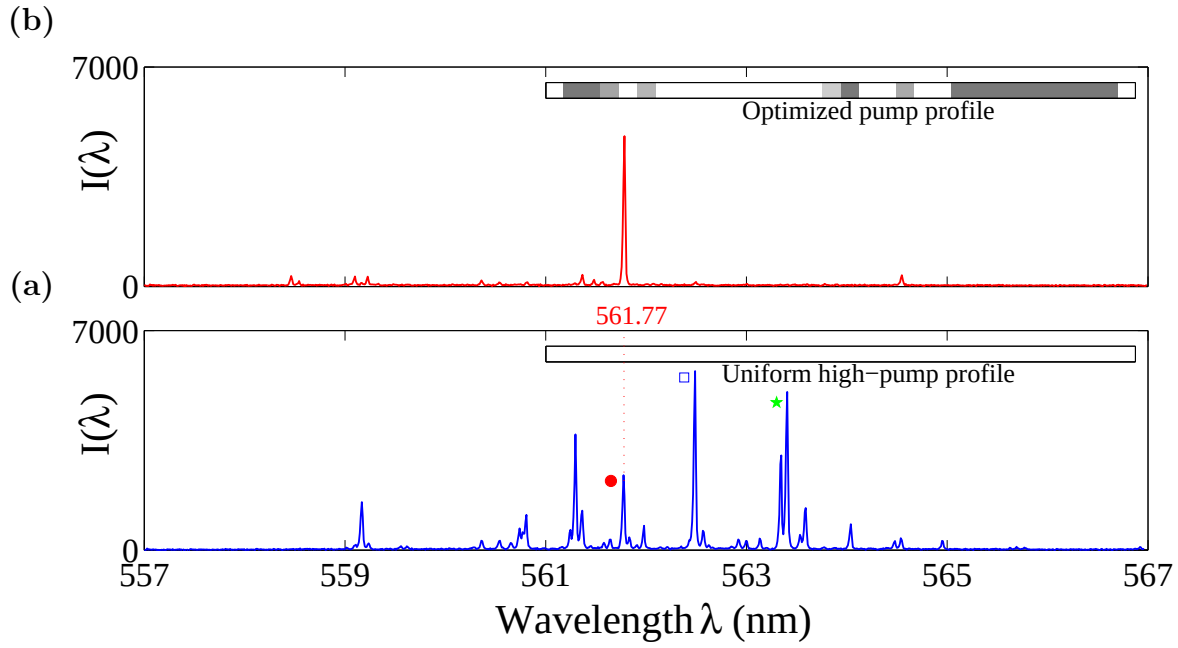

Figure 8.5: **(a)** Laser emission spectrum for uniform pumping above threshold. Symbols correspond to the modes shown in Fig. 8.4. **(b)** Emission spectrum after the optimization process to select laser emission at $\lambda_0 = 561.77nm$. Single-mode operation is achieved after 228 iterations. The corresponding non-uniform pump profile as displayed on the spatial light modulator (SLM) is shown in the inset. The grey scale ranges from 0 (black) to 255 (white).

The random laser is initially pumped uniformly in the multimode regime. The spectrum is shown in Fig. 8.5**(a)**. The optimization algorithm is then performed on the targeted mode λ_0 = 577.11 nm marked by a red dot in Fig. 8.5**(a)**. This lasing mode is not the first to lase under an uniform pumping, $R(\lambda_0)_{init}$ =0.4.

After 228 iterations (see Fig. 8.5**(b)**), the algorithm has converged to an optimized pump profile. We obtain $R(\lambda_0)$ = 13.1 after optimization, which corresponds to a sideband rejection of 11.4 dB.

We also check that no mode-hoping between laser lines occurs during the optimization process. Therefore, we ensure that the mode selected corresponds to the mode initially targeted at $\lambda = 577.11$ nm (see Fig. 8.6). Indeed, because the optimization procedure constantly explores new regions of the parameter space, it is not possible to assert that no other mode has been selected instead of the mode initially targeted. Starting from the final pump profile of Fig. 8.5**(b)**, we progressively increase the baseline value α_0. Therefore, we obtain the spectral emission from optimized to uniform pumping. The evolution of the modes (marked by dots in the plan frequency/peak intensity) is plotted in Fig. 8.6. The crosses stand for the uniform profile and the red marks for the optimized one. The targeted mode is clearly progressively optimized without any frequency shift, precluding any mode hoping. Actually, it is possible by this method to optimize almost any of the lasing modes present in the multi-mode spectrum measured with uniform pumping.

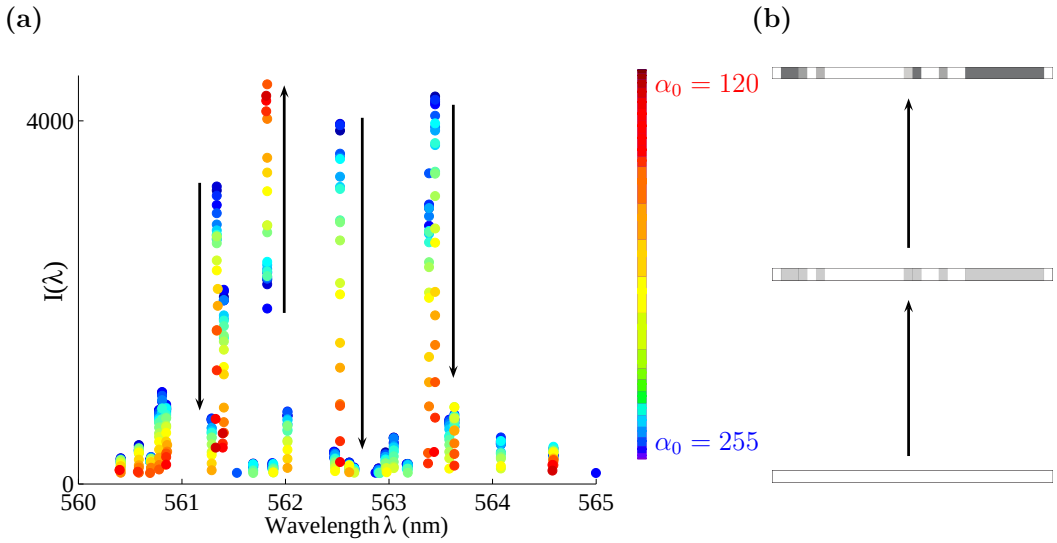

Figure 8.6: **(a)** Intensity of modes when the pump profile baseline decreases from $\alpha_0 = 255$ (blue) to 120 (red): The pump profile is shaped from uniform profile to adapted profile (optimization presented in Fig. 8.5). The arrows point out that the intensity of the targeted mode increases, while other intensities progressively decrease. **(b)** The different pump profiles when the baseline is decreased (down, $\alpha_0 = 255$) (up, $\alpha_0 = 120$).

Convergence and reliability

In Fig. 8.7**(a)**, we plot the evolution of $R(\lambda_0)$ and the correlation of the pump profile during the optimization proposed in section 8.1.2. The correlation is measured between the pump profile at the current iteration i and the previous iteration $i-1$. A unitary correlation means that convergence has been reached. During the optimization, the algorithm explores the parameter space and progressively moves in the direction of highest $R(\lambda_0)$. At iteration $i = 103$, a large value of $R(\lambda_0)$ is reached. The corresponding pump profile is chosen and progressively shaped to increase the rejection rate. Beyond 200 iterations, the optimization has converged.

To test the reliability of our method, we perform optimization over the whole emission bandwidth (see Fig. 8.7**(b)**). After several hours, ethanol infiltrates the PDMS and spec-

tral shift becomes significant relative to the spectral precision of the measurement. This explains why different data sets are collected in Fig. 8.7**(b)**. Remarkably enough, high $R(\lambda_0)$ are found in the whole spectrum. Optimization is efficient even away from the centre of the Rhodamine gain curve (typically ≈ 562 nm), where modes are provided with less gain. Moreover, even with extremely small initial amplitude for uniform pumping ($R_{init} \approx 0.3$ %), modes are optimized significantly (see Fig. 8.7**(b)**).

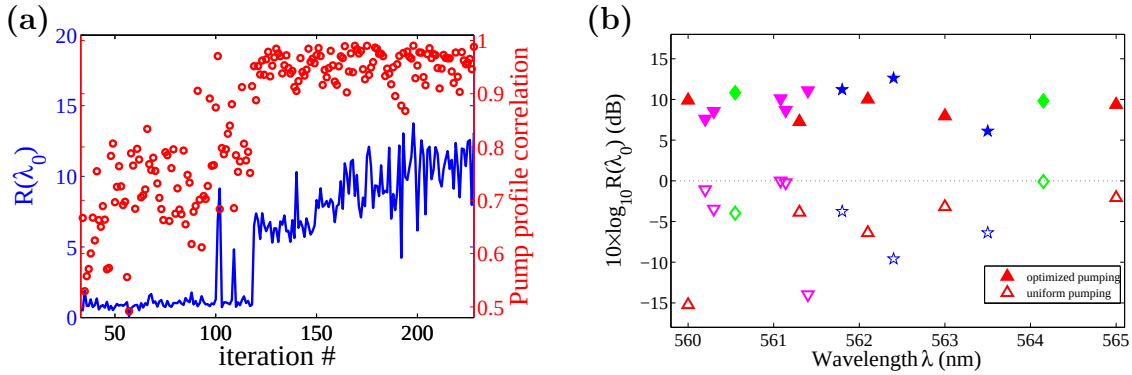

Figure 8.7: **(a)** Convergence characteristics of optimization presented in Fig. 8.5: Solid blue curve is the evolution of the criterion $R(\lambda_0)$ and red dots stand for correlation between two successive pump profiles. **(b)** $R(\lambda_0)$ versus wavelength before (open symbols: $R(\lambda_0) < 1$) and after (full symbols: $R(\lambda_0) \gg 1$) optimization of 15 lasing modes. The logarithmic representation gives $R(\lambda_0)$ in dB. The different symbols correspond to different sets of experiments.

Spectral selectivity

The optimization procedure allows to address the modes individually as soon as a mode is associated to a distinct peak in the spectrum. Hence, spectrally, the technique is only limited by the resolution of the spectrometer. To illustrate the spectral selectivity of

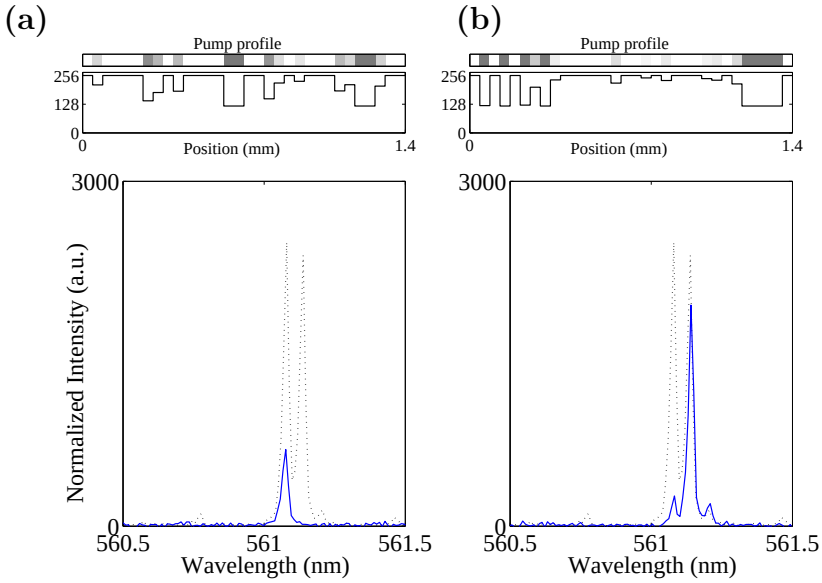

Figure 8.8: Optimizations at respectively $\lambda_0 = 561.08$ nm **(a)** and $\lambda_0 = 561.14$ nm. **(b)** The corresponding optimized pump profile is plotted versus position and the pattern displayed on the spatial light modulator is shown on a grey scale.

our method, we independently select two lasing modes separated only by 0.06 nm, as shown in Fig. 8.8. The optimization process clearly leads to two distinct pump profiles, associated with two different modes at $\lambda_0 = 561.08$ nm and $\lambda_0 = 561.14$ nm. This example emphasizes that all the modes can be addressed individually.

8.1.3 Optimization mechanism

The complexity of optimization mechanism: Influence of non-linear mixing

In Chapter 7, similar optimization was investigated with a numerical approach below threshold. We neglected gain non-linearities (also referred to as non-linear mode mixing) and restricted the description to linear mixing of modes. In this case, optimization was expressed in terms of mode threshold. To emphasize the difference between our previous numerical work and the current experimental optimization, we plot in Fig. 8.9 the thresholds characteristics for both a uniform pump profile and the pump profile obtained from the optimization presented in Fig. 8.5**(b)**.

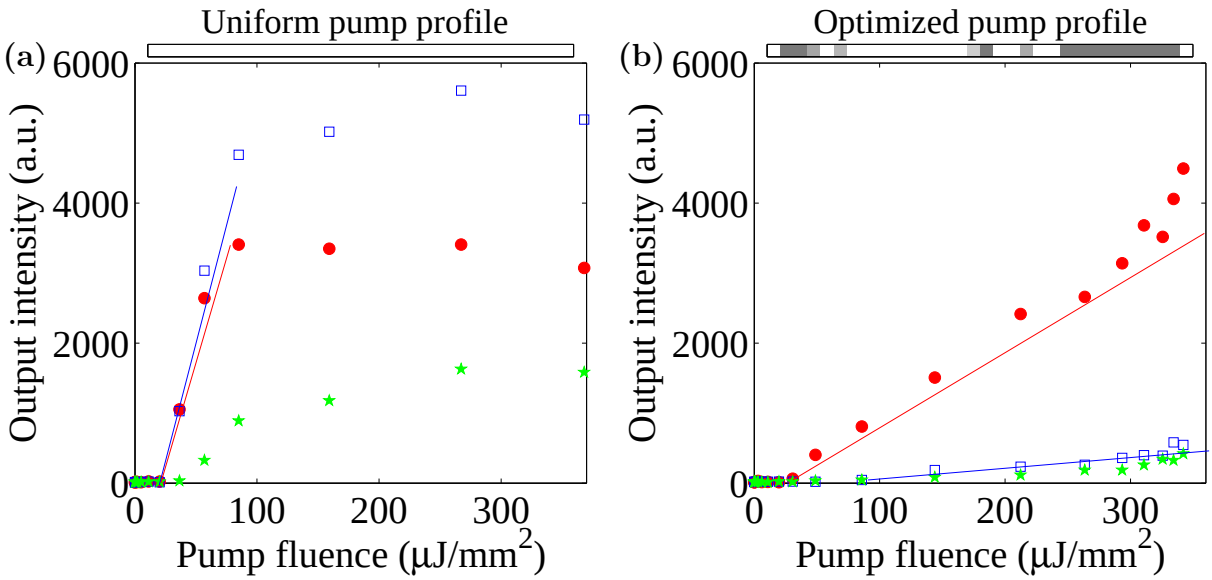

Figure 8.9: Uniform pumping **(a)** and optimized pumping **(b)** for the optimization routine carried out at $\lambda_0 = 561.77$ nm. The pump profile as displayed on the spatial light modulator is shown above each plot. For the targeted mode at $\lambda_0 = 561.77$ nm (full red circles), the threshold increased slightly from 21 to 28 μJ.mm^{-2}. For the mode which lases first under uniform pumping at $\lambda_1 = 562.50$ nm (blue squares), the threshold doubled from 21 to 50 μJ.mm^{-2}. Green stars indicate another mode at $\lambda_2 = 563.4$ nm. Lines are a linear fit to the stimulated regimes. **(b)** The x-axis shows the actual fluence impinging on the sample (which is different from the fluence of the incident pump beam when pumping is not uniform).

As expected from our numerical investigation, the threshold of the optimized modes remains at similar value while others are significantly increased. Threshold of the targeted mode (red dots, $\lambda_0 = 561.77$ nm) increases from 21 to 28 μJ and threshold of the highest intensity mode apart from λ_0 (blue dots, $\lambda_1 = 562.20$ nm) is increased from 21 μJ to

50 μJ. Nevertheless, the mode selection is rather due to slope efficiency than threshold inversion. As stated in Chapter 6, this slope efficiency is imposed by non-linear mixing provided by the hole burning effect. Moreover, it is worth noting the influence of adapted pump profile on cross-saturation. In Fig. 8.9**(a)** all the modes saturate more or less simultaneously close to 100 μJ.mm^{-1}. This effect is totally removed for an adapted pumping in Fig. 8.9**(b)**.

The observations made in Fig. 8.9 highlight the difference between below threshold optimization and the present case. The optimization achieved in the present experiment cannot be explained exclusively in terms of linear mixing. The non-uniform pump profile has an important influence on non-linear mode mixing.

Analytical investigation

Here, we give preliminary theoretical insights on the physics of non-linear mode mixing involved in the optimization. Chapter 6 approached this issue analytically. The model below is more qualitative than quantitative and paves the road to further investigations.

For uniform pumping, the intensity of the modes can be derived from a non-linear problem (see Chapter 6)

$$\begin{bmatrix} D_{11} & \dots & D_{1N_l} \\ \vdots & \ddots & \vdots \\ D_{N_l1} & \dots & D_{N_lN_l} \end{bmatrix} \begin{bmatrix} I_1 \\ \vdots \\ I_{N_l} \end{bmatrix} = \begin{bmatrix} B_1 - \frac{\Gamma_1}{2\Delta N_0} \\ \vdots \\ B_{N_l} - \frac{\Gamma_{N_l}}{2\Delta N_0} \end{bmatrix} \tag{8.4}$$

where linear coupling terms B_p read

$$B_p = Re\left(\Omega_p \frac{i\chi_g(\omega_p)}{2} V_{pp}\right) \tag{8.5}$$

non-linear coupling terms D_{pq} read

$$D_{pq} = Re\left(\Omega_p \frac{i\chi_g(\omega_p)}{\hbar} A_{ppqq}\right) \tag{8.6}$$

and ΔN_0 is proportional to the pump fluence. In a similar way to the optimization below threshold (developed in Chapter 7), the non uniform pump (f_E) modulates the spatial overlap between passive modes. This overlap is expressed in terms of linear mixing

$$V_{pp} = \int f_E(u)\Phi_p(u)^2 du \tag{8.7}$$

and non-linear mixing coefficients

$$A_{ppqq} = \int f_E(u)\Phi_p(u)^2|\Phi_q(u)|^2 Im(\chi_g(\omega_q)^*) du \tag{8.8}$$

where $\Phi_p(u)$ are passive mode spatial distributions, ω_q frequency of the passive mode and $\chi_g(\omega)$ the medium susceptibility. For sake of simplicity we will consider two lasing modes. Their intensities read (see Chapter 6)

$$I_1 \approx \frac{1}{\Delta} \frac{D_{22}B_1 - D_{12}B_2}{\Delta N_{th,1}} (\Delta N_0 - \Delta N_{th,1}) = \frac{1}{2\Delta} \frac{D_{22}\Gamma_1 - D_{12}\Gamma_2}{\Delta N_{th,1}^2} (\Delta N_0 - \Delta N_{th,1}) \tag{8.9}$$

$$I_2 \approx \frac{1}{\Delta}\frac{D_{11}B_2 - D_{21}B_1}{\Delta N_{th,2}}\left(\Delta N_0 - \Delta N_{th,2}\right) = \frac{1}{2\Delta}\frac{D_{11}\Gamma_2 - D_{21}\Gamma_1}{\Delta N_{th,2}^2}\left(\Delta N_0 - \Delta N_{th,2}\right) \quad (8.10)$$

where the threshold $\Delta N_{th,i_{i\in[1,2]}}$ read

$$\Delta N_{th,1} = \frac{D_{22}\Gamma_1 - D_{12}\Gamma_2}{2(D_{22}B_1 - D_{12}B_2)} \quad (8.11)$$

$$\Delta N_{th,2} = \frac{D_{11}\Gamma_2 - D_{21}\Gamma_1}{2(D_{11}B_2 - D_{21}B_1)} \quad (8.12)$$

and

$$\Delta = D_{11}D_{22} - D_{12}D_{21} \quad (8.13)$$

In this two-mode regime, we assume I_1 to be the intensity of the optimized mode (targeted mode $\lambda_0 = 561.77$ nm in Fig. 8.5) and I_2 the intensity of another mode (for instance $\lambda_1 = 562.50$ nm in Fig. 8.5).

First, eq. (8.9 - 8.12) highlight that the threshold and the slope of each mode are strongly related. When the slope is increased (or decreased), the threshold is decreased (or increased). Therefore, this confirms the validity of the numerical optimization made in Chapter 7. The mode with the lowest threshold will give rise to the highest intensity.

Nevertheless, the optimization cannot be restricted to a linear description. We observed in Fig. 8.9**(b)** that the optimization strongly decreases the slope of I_2. This diminution cannot be explained by the simple increase of threshold. Indeed, the slope of I_2 is reduced by approximatively a factor 20 and its threshold is only doubled. Therefore, the pump profile satisfies

$$D_{11}B_2 - D_{21}B_1 \to 0 \quad (8.14)$$

From eq. (8.14) we deduce that the slope reduction responsible for the optimization is driven by a subtle relation between non-linear coupling terms (D_{ij}) and linear ones (B_{ij}). As a result, we cannot separate the influence of linear and non-linear effects in the optimization process.

Finally, we observed in Fig. 8.9 **(b)** the absence of break in the slope of I_1. These breaks result from cross-saturation effects (see Chapter 6). When a mode starts lasing, it uses part of the gain and reduces the slopes of already lasing modes. Therefore, the cross-saturation of I_2 on I_1 is zero (see eq. (8.9))

$$D_{12} \approx 0 \quad (8.15)$$

This absence of cross-saturation leads to an "important" slope for I_1.

To summarize, the pump profile is shaped to satisfy eq. (8.14) in order to decrease I_2. Simultaneously, it fulfils eq. (8.15) in order to ensure a large intensity I_1. As a result, the pump profile disymmetrizes the cross-saturation terms which read $D_{12} \approx 0$ and $D_{21} \approx D_{11}B_2/B_1$, respectively.

In future works, we will aim at pursuing this preliminary investigations. For instance, we wish to use a numerical model above threshold (e.g. FDTD) to confirm the evolution of the different coupling terms.

8.2 2D optimization

Below threshold, the control of the directivity of the emission was demonstrated numerically by Hisch *et al.*[179]. In this section, we briefly present a work in progress, where we aim at performing similar optimization in 2D optofluidic random laser (see Chapter 5). First, we explain the experimental setup and the pump modulation that we perform. Then we present some preliminary results of optimization.

8.2.1 Experimental setup

2D optofluidic random laser

Here, we consider the 2D random laser introduced in Chapter 5 (see Fig. 8.10). The sample is composed of a 500 μm central part, where 201 pillars of radius 10 μm are embedded for a filling fraction of $\Phi = 0.32$. The scattering forces an in plane lasing [161] and the problem can be assumed 2D. The gain is provided by an ethanolic solution of Rhodamine 6G dye at concentration 2.5×10^{-3}M. The bulk is made of a resin of index $n_{resin} = 1.60$ and the resulting index contrast between dye flow and pillars is $\Delta n = n_{resin} - n_{dye} = 1.54 - 1.36 = 0.18$. The central part of the sample is surrounded by two auxiliary channels filled with Nile blue dye at concentration 2.5×10^{-3}M to perform imaging of the emission pattern (see explanation in Chapter 5). The index contrast and

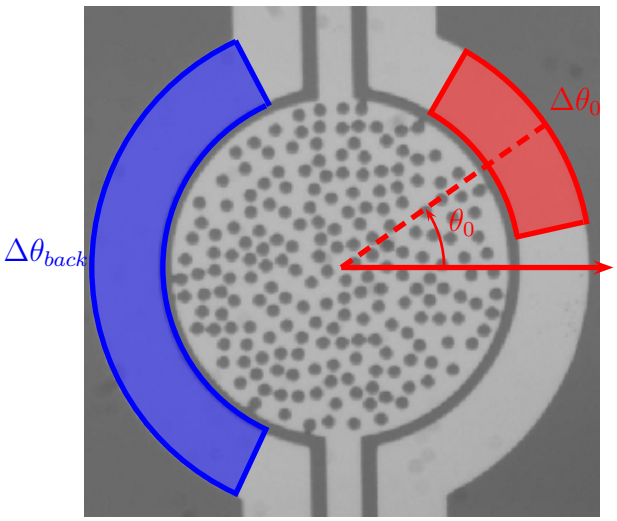

Figure 8.10: 2D microfluidic random laser: The central part of the sample is filled with Rhodamine, while Nile blue dye circulates into auxiliary channels. These channels are used to image the emission path. We define two angular domains, respectively $\Delta\theta_0$ and $\Delta\theta_{back}$. $\Delta\theta_0$ is direction where the emission must be enforced. $\Delta\theta_{back}$ serves to preclude obvious solutions.

the 2D geometry ensure that the system is operating in the weakly scattering regime. In the present section, we aim at completing control performed below threshold in [179] and presented in Chapter 7.

Pump modulation and acquisition

For 2D samples, the losses are significantly increased and modes have higher thresholds. Hence, the pump excitation is performed by a picosecond source providing higher instantaneous power: 532 nm Q-switched Nd:YAG laser (30 ps pulsewidth, 50 Hz repetition rate). The modulation of the pump is achieved by a similar setup as the one proposed in Fig. 8.2 in section 8.1.1, in which the cylindrical length used to compress the SLM image in 1D has been removed. The sample, as well as the auxiliary channels, are imaged by a Hamamatsu Orca-R2 silicon CCD camera fixed on a Zeiss Axioexaminer microscope.

Optimization method

To perform the directivity optimization of our 2D system, the pump profile is modulated using a set of 100 Zernike polynomials (see Fig. 8.11). This basis is used to study optical aberrations in 2D lenses [184]. Unlike Hadamard basis used in 1D, Zernike polynomials are continuous functions particularly adapted to the "circular" shape of the problem. Thus, the pump profile is a linear combination of these 100 vectors grey-scale-coded on 256 levels. To ensure the lasing emission for all the different modulations, we enforce a

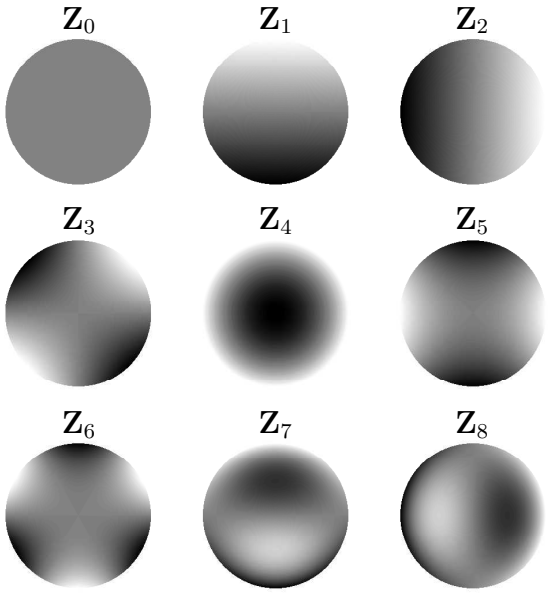

Figure 8.11: Zernike basis vector: The nine first elements of the basis. Their circular symmetry is used to modulate efficiently the pump profile.

background illumination (α_0). As a result, the pump profile reads

$$f(r) = \alpha_0 + \sum_{1\to 100} \alpha_i Z_i(r) \tag{8.16}$$

where r is the 2D spatial coordinate.

We aim at selecting the set of coefficients α_i enforcing the emission in a specific angular direction $\Delta\theta_0$ (see Fig. 8.10). For that matter, we define a directivity criterion D, reading

$$\alpha_i \to D(\theta_0) = \frac{I_{\Delta\theta_0}}{I_{2\pi}} - \frac{I_{2\pi}}{I_{\Delta\theta_{back}}} \tag{8.17}$$

where $I_{\Delta\theta_0}$ is the emission in the angular range $\Delta\theta_0$ and $I_{\Delta\theta_{back}}$ in the range $\Delta\theta_{back}$ (see Fig. 8.10). The intensity $I_{2\pi}$ corresponds to the intensity integrated over the whole angular space and is used to normalize the different intensities. In eq. (8.16) the presence of $I_{\Delta\theta_{back}}$ precludes obvious solutions (e.g. stripe line or any symmetric solution).

The optimization of eq. (8.17) is achieved using the Nelder-Mead simplex (direct search) method proposed in section 8.1 for 1D optimization. Like in the 1D optimization, the number of polynomials used for the optimization results from a trade-off between computation time and sensitivity.

8.2.2 Experimental results

Experimentally, images are integrated over 1 second and averaged over 10 times. Between two consecutive pump profiles, we apply a uniform pumping to clean up any undesired effects. Optimizations are performed for angular range of 30° and take approximatively 15 minutes.

We first consider the uniform pumping of Fig. 8.12. The pump diameter is voluntarily

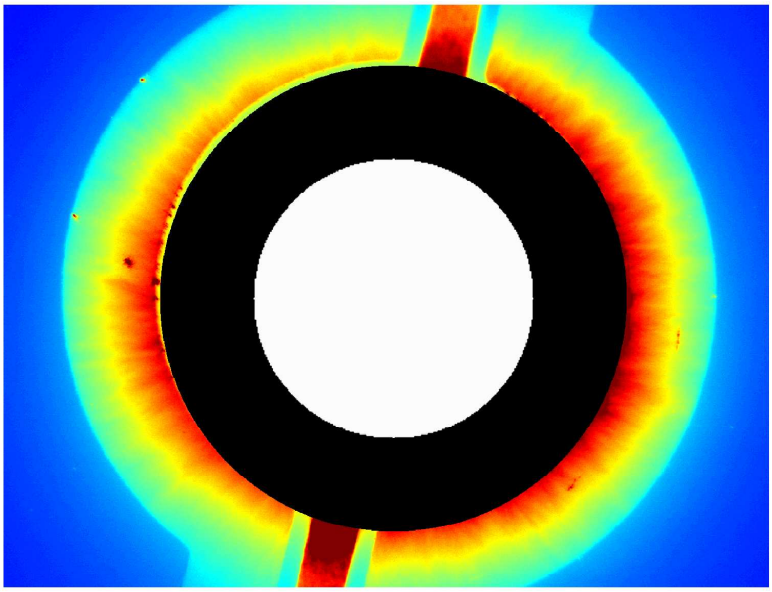

Figure 8.12: 2D random laser emission for a uniform pump profile: The central part of the image has been removed and replaced by the pattern printed onto the SLM.

chosen smaller than random laser size to preclude the obvious solution of a local pumping close to the edge. We define the criterion function $D(\theta_0)$ of eq. (8.17) to enforce the emission around θ_0 = - 45°. The final pump profile and the resulting emission pattern are provided by Fig. 8.13**(a)**. As expected, the optimization is forced in the angular range imposed by the criterion. In Fig. 8.14**(a)** and **(b)**, we plot respectively the criterion evolution and the correlation for the pump profile during the optimization. The correlation is defined as the correlation product between two successive pump profile patterns. The optimization converges after approximatively 250 iterations.

Remarkably enough, the final pump profile is non trivial. The pumping energy is spread

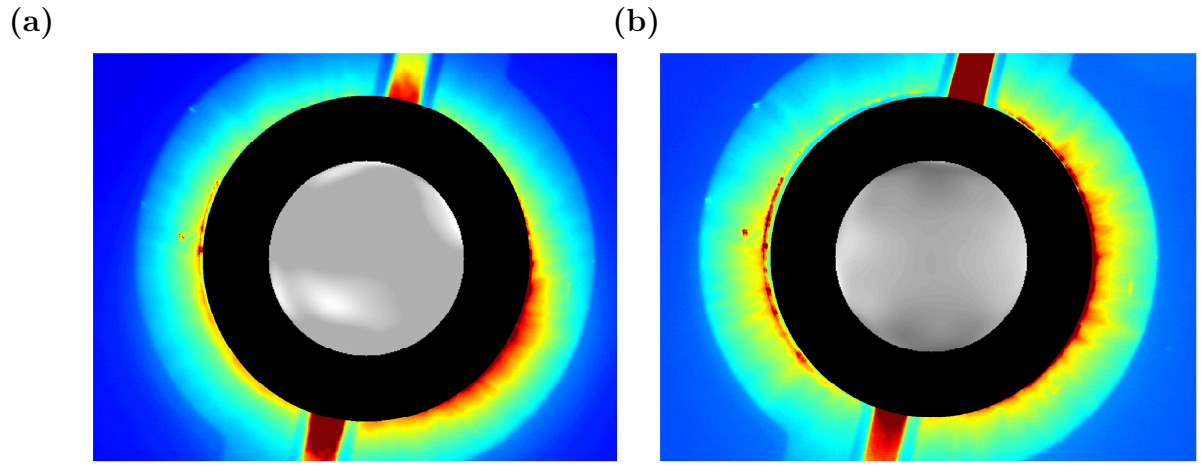

Figure 8.13: **(a)** Emission for an adapted pettern to for $\theta_0 = -45°$ and $\Delta\theta_0 = 30°$. **(b)** Emission for an adapted pettern to for $\theta_0 = 0°$ and $\Delta\theta_0 = 30°$

over the whole system. The pumping along the edges does not create emission in specific direction. This suggests that the emission pattern results from mixing of the modes.

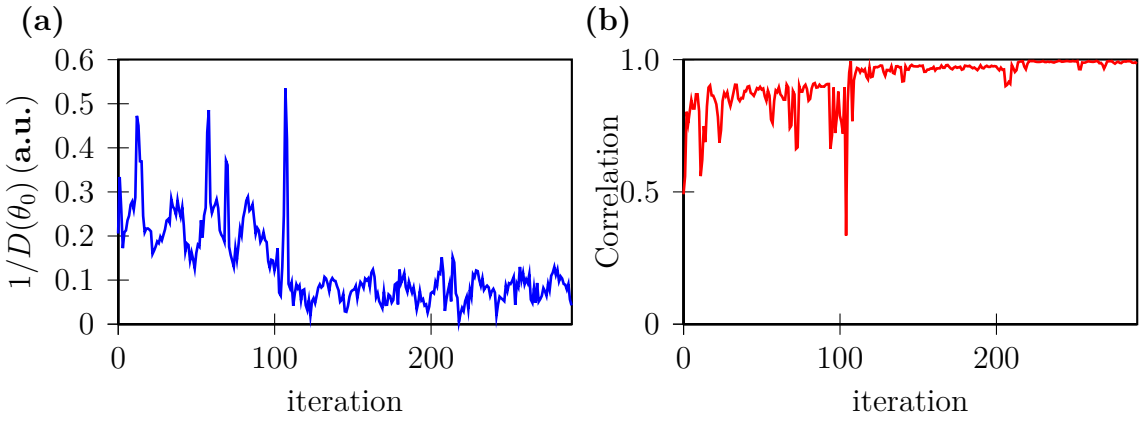

Figure 8.14: **(a)** Inverse criterion evolution during the optimization: The criterion progressively converges. **(b)** Evolution of the correlation between two successive pump profile. A unitary correlation points out the convergence of the optimization.

Fig. 8.13**(b)** shows another optimization performed for θ_0 =0° with an angular range $\Delta\theta_0$ =30°

8.2.3 Remarks and further work

In the work of Hisch *et al.* [179], the optimization was performed for a single mode emission and below threshold. In the present experiment, the random laser is multimode. Therefore, in further work we will record the evolution of the spectrum during the optimization. In particular, we wish to understand if the spatial distribution of the modes is modified by the pump profile as in [179]. We want to investigate the mode mixing as expected from Chapter 6 and aim at exploring the role played by non-linearities. Finally we wish to investigate the performances of the method (e.g. the minimal angular range, the required number of modes).

8.3 Summary

Here, we have performed experimental optimization of the emission of microfluidic based random lasers.

For 1D devices, we have developed an experimental setup, in which the pump excitation is modulated via a SLM and a simple cost function is defined from spectral acquisition. The optimization of the cost function turns the multimode random laser into single mode with more than 10 dB sideband rejection. This method is efficient, reliable and applicable over the whole spectrum. We have also investigated the relation between the actual experiment and the numerical optimization of Chapter 7. The threshold characteristics of uniform and adapted pump profiles highlight the complexity of the mechanism. From these observations, we have deduced that the linear description of Chapter 7 does not provide a complete understanding of the optimization. The analytical model developed in Chapter 6 emphasizes the simultaneous effect of linear and non-linear mixing. We wish to investigate this subtle mechanism in a future work. Finally, our preliminary results show that this method can be extended to 2D devices. Using two auxiliary channels, the spatial emission of lasing light is recorded by a camera. The pump is modulated by a different spatial decomposition and a simple cost function is defined from camera acquisition. From isotropic for a uniform pumping, the random lasing emission is forced into a particular angular range for an adapted profile.

The method proposed here is very general. We demonstrated its application to spectral and spatial control. However, it could be extended to other random laser characteristics (e.g. brightness or pulse duration). Moreover, this method could find nice applications in regular lasers. For instance it could reduce filamentation problem in broad-area lasers in which strong injection leads to filamentation issue [185]. Finally, it is noteworthy that our approach has already been applied for the control of semiconductor microdisk lasers [186].

Conclusion

In this thesis, we have developed theoretical, numerical and experimental approaches to address few issues on light-matter interaction in open random media. The light in such systems is supported by modes, either localized or extended according to the strength of the disorder. Based on the non-hermitian nature of these systems, we have explored both regimes and demonstrated that the modes provide an interesting platform to manage light-matter interaction in disordered media. Here, we summarize the main results and present some perspectives and potential applications.

- In Chapters I and II, we have recalled basic notions of light-matter interaction in the semiclassical description. More precisely, we have introduced the concept and the properties of modes in non-hermitian systems. In particular, we have focused on open systems and proposed a method to derive their modes. The complete biorthogonal formalism related to these modes as well as its application conditions have been reviewed. This approach can be applied to the specific case of disordered media. In such systems, since random multiple scattering may confine spatially all or part of the field, the resulting modes are either Anderson-localized or extended.

- In Chapter III, we have shown that the light-matter interaction in disorder media can be controlled by local manipulations. For that matter, a theory predicting the mode-coupling induced by any variation of the permittivity in open systems has been developed. This theory has been applied in the particular case of Anderson-localized modes, in which the merging of two states can be forced at a specific position called an exceptional point. Remarkably, this coalescence results from a complex multi-mode interaction. In the parameter space, the modes are characterized by a singular topology in the vicinity of an exceptional point. The density of exceptional points provided by this system offers interesting perspectives. Spectrally, the repulsion close to an exceptional point could be used to match the mode frequency with an emitter or to enhance mode confinement. Spatially, the hybridization of modes could serve to create necklace states and reach non-trivial transport regimes. The generality of the theory paves the road towards an experimental achievement.

- In Chapter IV, it has been shown that Anderson-localized modes could be used as high-Q cavities and induce regime of strong light-matter interaction. For small intensity of the electric field, the strong coupling regime can be reached between a two-level atom and a mode. Based on the biorthogonal formalism, we have derived both the strong coupling condition and the amplitude of resulting linear Rabi oscillations of the polarization. For high intensity, the electric field induces Stark shifts

in the energy levels of the atom and the apparition of a triplet in the polarization. Using an external source to excite the modes, we have derived the condition of observation and the amplitude of the corresponding non-linear Rabi oscillations. Conditions of simultaneous observation of both regimes being not incompatible, we have predicted different oscillations in an experiment confirmed by FDTD simulations. If strong coupling with Anderson-localized modes was expected, the formation of a triplet originating from Strak shifts is a major result. This observation confirms that Anderson-localized modes can serve as a playground to study strong light-matter interaction problems. For instance, purely quantum-mechanical effects such as resonance fluoresence (characterized by a Mollow triplet) should be achieved using such modes. This paves the road to many practical applications since the sidebands of the Mollow triplet are known to behave like non-classical sources. As a perspective, the manipulation of Anderson-localized modes proposed in Chapter III could be used to create controllable non-classical light. More generally, this theoretical work suggests that Anderson-localized modes may replace high-Q cavities, with the main advantage of being intrinsically disorder-robust.

- In Chapter V, lasers based on disordered systems, the so-called random lasers, have been presented. The concept of random lasers has been introduced in parallel to the academic description of conventional lasers. A model based on diffusion in gain medium has been derived and explains the presence of a threshold in the random laser emission. We have presented a particular laser developed in collaboration with Xavier Noblin in Nice: the microfluidic random laser. 1D and 2D geometries have been characterized and appear to be interesting platforms for the study of emission properties. The diffusion model of the random laser has been completed to consider the saturation of the amplifying medium. From observations of microfluidic random lasers, it has been deduced that a complete understanding requires a modal expansion of the electric field.

- In Chapter VI, a modal description of random laser based on semiclassical description has been proposed. In random lasers, like in conventional lasers, the presence of a threshold in the emission requires to consider two distinct regimes, namely below and above threshold. Below threshold, the modes of the random laser satisfy a system of equations derived from the linear coupling of the passive modes. We have performed a perturbation expansion to derive their complex frequency and spatial distribution in term of mixing of passive modes. Above threshold, the modes result from combination of linear and non-linear mixing of passive modes, described by a non-linear Schrödinger system of equations. Using a perturbation expansion has allowed us to obtain the complex frequency and spatial distribution of the modes and to highlight the role of saturation terms. Finally, a method to derive the intensity of lasing modes has been proposed and applied to the case of single-mode and two-mode lasers.

- In Chapter VII, the control of the random lasing emission has been achieved via an adapted profile of the pump excitation. We have considered a numerical 1D random laser, in which the gain is spatially modulated. An optimization has been performed to select one mode by increasing the difference between its threshold and others.

This routine has been successfully applied to random laser in both localized and weakly scattering regime. In the localized regime, in which the spatial overlap is weak, the mode is selected when the pump profile matches the spatial distribution of the mode. In the more challenging case of extended modes, optimization remains possible but the optimal pump profile is rather unpredictable. We have proposed preliminary interpretations in term of linear mode-mixing based on the model of Chapter VI.

- In Chapter VIII, the numerical method proposed in Chapter VII has been experimented on microfluidic random lasers introduced in Chapter V. A spatial light modulator has been used to shape the intensity profile of the pump laser. This pump profile has been iteratively modulated to drive the multimode random laser to single-mode lasing. This mode selection can be achieved for all modes of the multimode spectrum. Remarkable spectral discrimination is achieved between very close-by modes. The two-mode model of Chapter VI has been used to identify the origin of the process. It points out a subtle compromise between linear and nonlinear mixing of the passive modes. Further investigations are needed for a complete understanding. We have also presented preliminary results concerning the control of spatial distributions of the modes. Similar shaping of the pump for 2D optofluidic devices allows to control the directivity of the emission. We believe that this method could be extrapolated in many applications for different laser sources. For instance, in high energy lasers, filamentation of the gain medium may be hindered by a non-uniform pumping.

In passive media, the theory developed in Chapter III and its application to localized modes offer nice perspectives. From a fundamental point of view, this theory is an interesting playground to investigate the influence of exceptional point in Anderson's localization. Thus, different questions can be addressed: Does the density of exceptional points influence the confinement by disorder? Could we obtain exceptional point for weak disorder and extended modes? What is the role of coupling in localization? For practical applications, the exceptional point repulsion in complex frequency plane could be used either to increase Q-factor of modes or match the frequency of a mode with the resonance of an emitter. Hybridization resulting from multiple exceptional points could create necklace states, open channels in highly disordered media and reach non-trivial light transport regimes. The observation of a triplet originating from Strak effect is another application of Anderson-localized modes in passive media. We stated that disorder should be used to achieve interesting source of light. In further work, we will investigate the development of a pure quantum approach to demonstrate the possibility of creating a Mollow triplet emission with Anderson-localized modes.

In active media, the control of random lasers also offers theoretical and practical prospects. It could be used to optimize different properties of random lasers (e.g. brightness, temporal response) and could be extended to any kind of laser. In terms of theoretical question, a controlled pump profile would allow us to investigate the influence of non-linearities on Anderson-localized modes. We might achieve mode locking between modes, by controlling their spectral positions. Moreover, it could be used to explore non-hermitian physics (e.g.

exceptional points in random lasers). In further work, we aim at investigating the role played by pump profile on non-linearities (cross and self-saturations). We will also pursue our experimental work related to directivity optimization in 2D random media.

Appendices

Appendix A

Polarizability and susceptibility of a particle in 2D

In Chapter 1, we explained that the dipole moment $\mathbf{p}$ of a particle at microscopic scale and the polarization density $\mathbf{P}$ at macroscopic scale read respectively

$$\mathbf{p}(\omega) = \epsilon_0 \alpha_0(\omega) \mathbf{E}(\omega) \tag{A.1}$$

$$\mathbf{P}(\omega) = n\mathbf{p}(\omega) = \epsilon_0 \chi_S(\omega) \mathbf{E}(\omega) \tag{A.2}$$

where n is the total number of particles, $\alpha_0(\omega)$ the polarizability of the particle and $\chi_S(\omega)$ the material susceptibility. However, we stressed that eq. (A.2) is only true in the static limit ($\omega \to 0$).

In this appendix we aim at deriving the dynamic polarizability $\alpha(\omega)$ of the particle and the dynamic susceptibility $\chi_s(\omega)$ of a material composed of such particles. We consider a 2D problem with a TE electric field (similar to the system studied in Chapter 4). We know from the Lorentz's oscillator model introduced in Chapter 1 that the polarizability reads

$$\alpha(\omega) \propto \frac{1/\omega}{\omega_0^2 - \omega^2 - i\Gamma\omega} \tag{A.3}$$

In the Rotating Wave Approximation, we assume the optical frequency ω close to the resonant frequency of the particle ω_0

$$\omega_0^2 - \omega^2 \approx 2\omega(\omega_0 - \omega) \tag{A.4}$$

Hence, eq. (A.3) reads

$$\alpha(\omega) \propto \frac{1}{\omega^2(\omega_0 - \omega - i\frac{\Gamma}{2})} \tag{A.5}$$

If we consider the specific case of a two-level atom in a 2D problem with a TE electric field excitation, we can complete eq. (A.5) [187, 188] and the polarizability reads

$$\alpha(\omega) = \frac{2\Gamma_S^R}{\omega^2(\omega_0 - \omega - i\frac{\Gamma_S}{2})} \tag{A.6}$$

where $\Gamma_S = \Gamma_S^R + \Gamma_S^{NR}$ is the atomic linewidth, Γ_S^R the radiative part of this linewidth and Γ_S^{NR} the non-radiative part (see Chapter 1).

In the dynamic regime, the static assumption made in eq. (A.2) must be corrected, this is the so-called "radiative correction" [187, 188]. In our 2D problem with a TE electric field, the dynamic version of eq. (A.2) reads

$$\mathbf{P}(\omega) = n\epsilon_0 \frac{\alpha_0(\omega)}{1 - i\frac{\omega^2}{4}\alpha_0(\omega)}\mathbf{E}(\omega) = n\epsilon_0\alpha(\omega)\mathbf{E}(\omega) \quad \& \quad \alpha_0(\omega) \propto \chi_S(\omega) \tag{A.7}$$

From eq. (A.6) and (A.7), we derive

$$\omega^2 \left(\omega_0 - \omega - i\frac{\Gamma_S}{2}\right)\chi_S(\omega) = \left(1 - i\frac{\omega^2}{4}\chi_S(\omega)\right) 2\Gamma_S^R \tag{A.8}$$

We can recast eq. (A.8) in the form

$$\chi_S(\omega)\left(\omega^2\left(\omega_0 - \omega - i\frac{\Gamma_S}{2}\right) + i\frac{\omega^2}{4}2\Gamma_S^R\right) = 2\Gamma_S^R \tag{A.9}$$

Eq. (A.9) reads

$$\chi_S(\omega)\omega^2\left(\omega_0 - \omega - i\frac{\Gamma_S^{NR}}{2}\right) = 2\Gamma_S^R \tag{A.10}$$

Therefore, the susceptibility of the material reads

$$\chi_S(\omega) = \frac{2}{\omega^2}\frac{\Gamma_S^R}{\omega_0 - \omega - i\frac{\Gamma_S^{NR}}{2}} \tag{A.11}$$

Appendix B

Transfer Matrix Approach: Stationary and Travelling components

In this appendix, we present a method which enables to decompose numerically modes into stationary and travelling components. The stationary wave stands for the part of the mode remaining trapped inside the system. The travelling wave stands for the leaky part of the mode.

To introduce this method, we consider the case of a 1D open passive system (without pumping) shown in Fig. B.1**(a)**. It can be very easily extended to active medium by considering a complex index of refraction. We know from Chapter 2 that each mode (Ω_n, Ψ_n) reads

$$\Psi_n(x) = p_n(x)e^{i\Omega_n n(x)x} + q_n(x)e^{-i\Omega_n n(x)x} \tag{B.1}$$

where x is direction of propagation, $n(x) = n$ or $n + \Delta n$ the refractive indices and p_n and q_n respectively the forward and backward propagation coefficients. Let us consider the field within a single layer and fix the index of refraction arbitrarily to 1 in order to simplify the notation. The following results will be valid within any layer. Inside the layer the forward and backward coefficients p_n and q_n are constant and eq. (B.1) reads

$$\Psi_n(x) = p_n e^{i\Omega_n x} + q_n e^{-i\Omega_n x} \tag{B.2}$$

We now introduce

$$p_n = P_n e^{i\phi} \tag{B.3}$$
$$q_n = Q_n e^{i\psi} \tag{B.4}$$

where P_n/Q_n are the real amplitudes and ϕ/ψ the phases of p_n and q_n, respectively. Hence, eq. (B.2) reads

$$\Psi_n(x) = e^{i\Phi}\left(P_n e^{i(\Omega_n x+\Delta)} + Q_n e^{-i(\Omega_n x+\Delta)}\right) \tag{B.5}$$

where $\Phi = (\phi + \psi)/2$ and $\Delta = (\phi + \psi)/2$. Within each layer, we can fix arbitrarily the phase and enforce $\Phi = 0$ in order to simplify notation. As a result, eq. (B.5) reads

$$\Psi_n(x) = e^{\frac{\Gamma_n}{2}x}P_n e^{i(\omega_n x+\Delta)} + Q_n e^{-\frac{\Gamma_n}{2}x}e^{-i(\omega_n x+\Delta)} \tag{B.6}$$

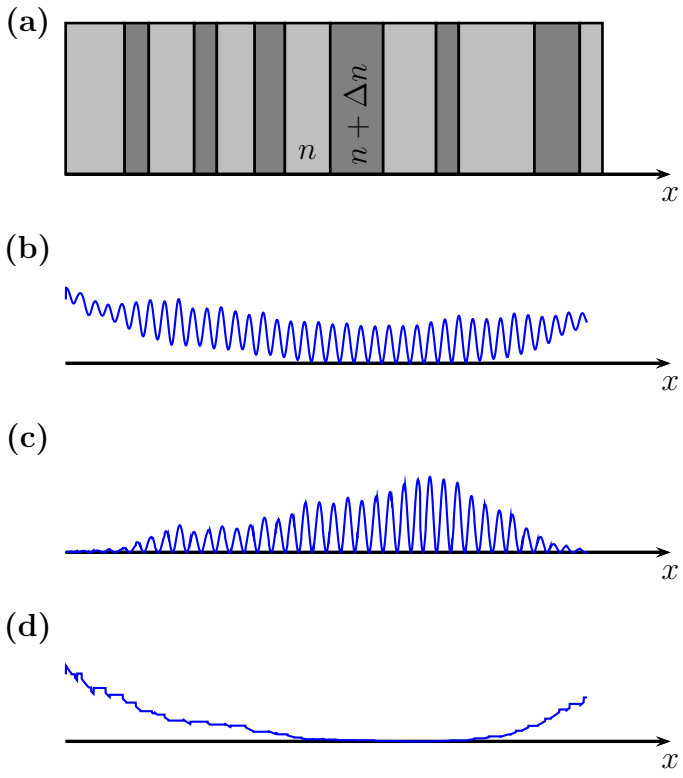

Figure B.1: **(a)** Schematic description of the 1D random system: Superposition of slabs of indices n and $n + \Delta n$. **(b)** Spatial mode distribution in the weakly scattering regime ($\Delta n = 0.1$). **(c)** The stationary part of the mode. **(d)** The travelling part of the mode.

The first term of the right-hand side of eq. (B.6), namely $e^{\frac{\Gamma_n}{2}x} P_n e^{i(\omega_n x+\Delta)}$ diverges at $x \to +\infty$. The second term diverges at $x \to -\infty$.

We can artificially define two standing components from eq. (B.6), namely

$$\Psi_{s,p_n} = P_n e^{\frac{\Gamma_n}{2}x} \left(e^{i(\omega_n x+\Delta)} + \left(e^{i(\omega_n x+\Delta)} \right)^* \right) = 2P_n e^{\frac{\Gamma_n}{2}x} \cos(\omega_n x + \Delta) \quad \text{(B.7)}$$

$$\Psi_{s,q_n} = Q_n e^{-\frac{\Gamma_n}{2}x} \left(e^{-i(\omega_n x+\Delta)} + \left(e^{-i(\omega_n x+\Delta)} \right)^* \right) = 2Q_n e^{-\frac{\Gamma_n}{2}x} \cos(\omega_n x + \Delta) \quad \text{(B.8)}$$

In a similar way, we can define travelling components as the remaining part of the mode

$$\Psi_{t,p_n} = \Psi_n - \Psi_{s,p_n} = \left(Q_n e^{-\frac{\Gamma_n}{2}x} - P_n e^{\frac{\Gamma_n}{2}x} \right) e^{-i(\omega_n x+\Delta)} \quad \text{(B.9)}$$

$$\Psi_{t,q_n} = \Psi_n - \Psi_{s,q_n} = \left(P_n e^{\frac{\Gamma_n}{2}x} - Q_n e^{-\frac{\Gamma_n}{2}x} \right) e^{i(\omega_n x+\Delta)} \quad \text{(B.10)}$$

We see that eq. (B.9) stands for a left-going propagation, while eq. (B.10) stands for a right-going one. Consequently, to numerically build the travelling part of the mode (*i.e.* exiting the system), we consider the left-going propagation when the backward amplitude coefficient Q_n prevails over the forward amplitude P_n and *vice versa*. Simultaneously we deduce the corresponding stationary part.

Appendix C

Perturbation Expansion of non-hermitian eigenvalue problem

In the scope of Chapter 6, we need to perform perturbation expansion of linear and non-linear eigenvalue problems. In this appendix we derive the perturbation expansion in both cases.

C.1 Perturbation expansion in the below threshold regime: Linear eigenvalue problem

For a broad gain curve, the below threshold regime is described by a linear eigenvalue problem reading

$$\lambda^2 = \begin{bmatrix} \lambda_1^2 & \dots & 0 \\ \vdots & \ddots & \vdots \\ 0 & \dots & \lambda_N^2 \end{bmatrix} + \begin{bmatrix} \lambda_1^2 V_{11}\Delta\tilde{N}_0 & \dots & \lambda_1^2 V_{1N}\Delta\tilde{N}_0 \\ \vdots & \ddots & \vdots \\ \lambda_N^2 V_{N1}\Delta\tilde{N}_0 & \dots & \lambda_N^2 V_{NN}\Delta\tilde{N}_0 \end{bmatrix} \tag{C.1}$$

Eq. (C.1) can be understood as a passive system perturbed by a matrix resulting from the coupling between the passive modes. We assume this perturbation to be weak $\tilde{N}_0 \ll 1$. For sake of notation compactness we note $\lambda_i^2 = X_i$, and eq. (C.1) reads

$$X = \begin{bmatrix} X_1 & \dots & 0 \\ \vdots & \ddots & \vdots \\ 0 & \dots & X_N \end{bmatrix} + \Delta\tilde{N}_0 \begin{bmatrix} X_1 V_{11} & \dots & X_1 V_{1N} \\ \vdots & \ddots & \vdots \\ X_N V_{N1} & \dots & X_N V_{NN} \end{bmatrix} = H_0 + \Delta\tilde{N}_0 H_1 \tag{C.2}$$

We are looking for the eigenvalues of the matrix

$$H = H_0 + \Delta\tilde{N}_0 H_1 \tag{C.3}$$

The set of eigenvalues and eigenvectors in perturbation expansion read

$$|\Psi_n\rangle = |\Psi_n^{(0)}\rangle + \Delta\tilde{N}_0|\Psi_n^{(1)}\rangle + \Delta\tilde{N}_0^2|\Psi_n^{(2)}\rangle + ... \tag{C.4}$$

$$X_n = X_n^{(0)} + \Delta\tilde{N}_0 X_n^{(1)} + \Delta\tilde{N}_0^2 X_n^{(2)} + ... \tag{C.5}$$

where $n \in [1, N]$. Eigensolutions satisfy

$$(H_0 + \tilde{N}_0 H_1)|\Psi_n\rangle = X_n|\Psi_n\rangle \tag{C.6}$$

Using the perturbation expansion, eq. (C.6) reads

$$\begin{aligned}&(H_0+\tilde{N}_0H_1)(|\Psi_n^{(0)}\rangle+\tilde{N}_0|\Psi_n^{(1)}\rangle+\tilde{N}_0^2|\Psi_n^{(2)}\rangle+...)\\&=(X_n^{(0)}+\tilde{N}_0X_n^{(1)}+\tilde{N}_0^2X_n^{(2)}+...)(|\Psi_n^{(0)}\rangle+\tilde{N}_0|\Psi_n^{(1)}\rangle+\tilde{N}_0^2|\Psi_n^{(2)}\rangle+...)\end{aligned}\tag{C.7}$$

By expanding eq. (C.7), the identification of different $\tilde{N}_0$ orders read

$$\tilde{N}_0^0:\quad H_0|\Psi_n^{(0)}\rangle=X_n^{(0)}|\Psi_n^{(0)}\rangle\tag{C.8}$$

$$\tilde{N}_0^1:\quad (H_0-X_n^{(0)})|\Psi_n^{(1)}\rangle=-H_1|\Psi_n^{(0)}\rangle+X_n^{(1)}|\Psi_n^{(0)}\rangle\tag{C.9}$$

$$\tilde{N}_0^2:\quad (H_0-X_n^{(0)})|\Psi_n^{(2)}\rangle=-H_1|\Psi_n^{(1)}\rangle+X_n^{(1)}|\Psi_n^{(1)}\rangle+X_n^{(2)}|\Psi_n^{(0)}\rangle\tag{C.10}$$

First order $\tilde{N}_0^1$:

Using $\tilde{N}_0^1$ relation of eq. (C.8) and the biorthogonal projection along $\langle\Psi_{n'}^{(0)*}|$

$$\forall n'\quad \langle\Psi_{n'}^{(0)*}|H_0-X_n^{(0)}|\Psi_n^{(1)}\rangle=-\langle\Psi_{n'}^{(0)*}|H_1|\Psi_n^{(0)}\rangle+X_n^{(1)}\langle\Psi_{n'}^{(0)*}|\Psi_n^{(0)}\rangle\tag{C.11}$$

Moreover, the left eigenvectors $\langle\Psi_{n'}^{(0)*}|$ fulfil

$$\langle\Psi_{n'}^{(0)*}|H_0=X_{n'}^{(0)}\langle\Psi_{n'}^{(0)*}|\tag{C.12}$$

Hence, if $n=n'$, eq. (C.11) reads

$$\langle\Psi_n^{(0)*}|H_0-X_n^{(0)}|\Psi_n^{(1)}\rangle=0=-\langle\Psi_{n'}^{(0)*}|H_1|\Psi_n^{(0)}\rangle+X_n^{(1)}\langle\Psi_{n'}^{(0)*}|\Psi_n^{(0)}\rangle\tag{C.13}$$

As a result

$$\boxed{X_n^{(1)}=\langle\Psi_n^{(0)*}|H_1|\Psi_n^{(0)}\rangle}\tag{C.14}$$

Otherwise, if $n'\neq n$, eq. (C.11) reads

$$(X_{n'}^{(0)}-X_n^{(0)})\langle\Psi_{n'}^{(0)*}|\Psi_n^{(1)}\rangle=-\langle\Psi_{n'}^{(0)*}|H_1|\Psi_n^{(0)}\rangle+X_n^{(1)}\langle\Psi_{n'}^{(0)*}|\Psi_n^{(0)}\rangle=-\langle\Psi_{n'}^{(0)*}|H_1|\Psi_n^{(0)}\rangle\tag{C.15}$$

Therefore

$$\forall n'\neq n\quad \langle\Psi_{n'}^{(0)*}|\Psi_n^{(1)}\rangle=\frac{\langle\Psi_{n'}^{(0)*}|H_1|\Psi_n^{(0)}\rangle}{X_n^{(0)}-X_{n'}^{(0)}}\tag{C.16}$$

Using the biorthogonal normalization

$$\begin{aligned}\langle\Psi_n^*|\Psi_n\rangle=1&=\langle\Psi_n^{*(0)}+\tilde{N}_0\Psi_n^{*(1)}+...|\Psi_n^{(0)}+\tilde{N}_0\Psi_n^{(1)}+...\rangle\\&=1+\tilde{N}_0(\langle\Psi_n^{*(0)}|\Psi_n^{(1)}\rangle+\langle\Psi_n^{*(1)}|\Psi_n^{(0)}\rangle)+\tilde{N}_0^2+...\end{aligned}\tag{C.17}$$

Noting the symmetry of the biorthogonal product

$$\langle\Psi_n^{*(0)}|\Psi_n^{(1)}\rangle=\int\Psi_n^{(0)}\Psi_n^{(1)}=\int\Psi_n^{(1)}\Psi_n^{(0)}=\langle\Psi_n^{*(1)}|\Psi_n^{(0)}\rangle\tag{C.18}$$

Hence, eq. (C.17) reads

$$1\approx 1+2\tilde{N}_0\langle\Psi_n^{*(1)}|\Psi_n^{(0)}\rangle\tag{C.19}$$

and we deduce

$$\langle\Psi_n^{*(0)}|\Psi_n^{(1)}\rangle=0\tag{C.20}$$

We obtain the first order component of the eigenvector

$$\boxed{\Psi_n^{(1)}=\textstyle\sum_{n'\neq n}\frac{\langle\Psi_{n'}^{(0)*}|H_1|\Psi_n^{(0)}\rangle}{X_n^{(0)}-X_{n'}^{(0)}}|\Psi_{n'}^{(0)}\rangle}\tag{C.21}$$

Second order $\tilde{N}_0^2$:

Projecting the second order eq. (C.11) along $\langle\Psi_n^{(0)*}|$ reads

$$\langle\Psi_n^{(0)*}|(H_0 - X_n^{(0)})|\Psi_n^{(2)}\rangle = -\langle\Psi_n^{(0)*}|H_1|\Psi_n^{(1)}\rangle + X_n^{(1)}\langle\Psi_n^{(0)*}|\Psi_n^{(1)}\rangle + X_n^{(2)}\langle\Psi_n^{(0)*}|\Psi_n^{(0)}\rangle \quad \text{(C.22)}$$

Using definition of left eigenvectors

$$0 = -\langle\Psi_n^{(0)*}|H_1|\Psi_n^{(1)}\rangle + X_n^{(1)}\langle\Psi_n^{(0)*}|\Psi_n^{(1)}\rangle + X_n^{(2)} \quad \text{(C.23)}$$

Using previous expression of $|\Psi_n^{(1)}\rangle$ in eq. (C.23) reads

$$X_n^{(2)} = \langle\Psi_n^{(0)*}|H_1 \sum_{n'\neq n} \frac{\langle\Psi_{n'}^{(0)*}|H_1|\Psi_n^{(0)}\rangle}{X_n^{(0)} - X_{n'}^{(0)}}|\Psi_{n'}^{(0)}\rangle \quad \text{(C.24)}$$

As a result

$$\boxed{X_n^{(2)} = \sum_{n'\neq n} \frac{\langle\Psi_{n'}^{(0)*}|H_1|\Psi_{n'}^{(0)}\rangle\langle\Psi_n^{(0)*}|H_1|\Psi_{n'}^{(0)}\rangle}{X_n^{(0)} - X_{n'}^{(0)}}} \quad \text{(C.25)}$$

And corresponding eigenvector reads

$$\boxed{|\Psi_n^{(2)}\rangle = \sum_{n'\neq n} \frac{\langle\Psi_{n'}^{(0)*}|H_1|\Psi_n^{(1)}\rangle}{X_n^{(0)} - X_{n'}^{(0)}}|\Psi_{n'}^{(0)}\rangle} \quad \text{(C.26)}$$

For sake of clarity, we will only consider eigenvector at first order.

C.2 Perturbative approach above threshold: non-linear case

In the above threshold regime, for a broadband gain curve, the lasing modes are the eigenvalues of a non-linear eigenvalue problem. This problem is equivalent to a Non-Linear Schrödinger equation system, which reads

$$\lambda^2 = \begin{bmatrix} \lambda_1^2 & \dots & 0 \\ \vdots & \ddots & \vdots \\ 0 & \dots & \lambda_N^2 \end{bmatrix} + \Delta\tilde{N}_0 \begin{bmatrix} \lambda_1^2 V_{11} & \dots & \lambda_1^2 V_{1N} \\ \vdots & \ddots & \vdots \\ \lambda_N^2 V_{N1} & \dots & \lambda_N^2 V_{NN} \end{bmatrix}$$
$$- \Delta\tilde{N}_0 \frac{2}{\hbar} \begin{bmatrix} \lambda_1^2 \sum_p |a_p|^2 A_{11pp} & \dots & \lambda_1^2 \sum_p |a_p|^2 A_{1Npp} \\ \vdots & \ddots & \vdots \\ \lambda_N^2 \sum_p |a_p|^2 A_{N1pp} & \dots & \lambda_N^2 \sum_p |a_p|^2 A_{NNpp} \end{bmatrix} \quad \text{(C.27)}$$

where $\tilde{N}_0 = N_0\chi_g(\omega)$. Noting $X_i = \lambda_i^2$, eq. (C.27) reads

$$X = \begin{bmatrix} X_1 & \dots & 0 \\ \vdots & \ddots & \vdots \\ 0 & \dots & X_N \end{bmatrix} + \Delta\tilde{N}_0 \begin{bmatrix} X_1 V_{11} & \dots & X_1 V_{1N} \\ \vdots & \ddots & \vdots \\ X_N V_{N1} & \dots & X_N V_{NN} \end{bmatrix}$$
$$- \Delta\tilde{N}_0 \frac{2}{\hbar} \begin{bmatrix} X_1 \sum_p |a_p|^2 A_{11pp} & \dots & X_1 \sum_p |a_p|^2 A_{1Npp} \\ \vdots & \ddots & \vdots \\ X_N \sum_p |a_p|^2 A_{N1pp} & \dots & X_N \sum_p |a_p|^2 A_{NNpp} \end{bmatrix} \quad \text{(C.28)}$$

Eq. (C.28) is equivalent to

$$H = H_0 + \tilde{N}_0(H_1 + H_3(\sum |\Psi_n\rangle)) = X \tag{C.29}$$

The perturbation reads

$$\left(H_0 + \Delta\tilde{N}_0\left(H_1 + H_3(\sum_q |\Psi_q^{(0)}\rangle + \tilde{N}_0|\Psi_q^{(1)}\rangle + \tilde{N}_0^2|\Psi_q^{(2)}\rangle + ...)\right)\right)$$

$$\left(|\Psi_n^{(0)}\rangle + \tilde{N}_0|\Psi_n^{(1)}\rangle + \tilde{N}_0^2|\Psi_n^{(2)}\rangle + ...\right)$$

$$= \left(X_n^{(0)} + \tilde{N}_0 X_n^{(1)} + \tilde{N}_0^2 X_n^{(2)} + ...)(|\Psi_n^{(0)}\rangle + \tilde{N}_0|\Psi_n^{(1)}\rangle + \tilde{N}_0^2|\Psi_n^{(2)}\rangle + ...\right) \tag{C.30}$$

By expanding eq. (C.30), the identifiaction of different $\tilde{N}_0$ orders read

$$\tilde{N}_0^0 : \quad H_0|\Psi_n^{(0)}\rangle = X_n^{(0)}|\Psi_n^{(0)}\rangle \tag{C.31}$$

$$\tilde{N}_0^1 : \quad (H_0 - X_n^{(0)})|\Psi_n^{(1)}\rangle = -(H_1 + H_3^{(0)}|\Psi_n^{(0)}\rangle + X_n^{(1)}|\Psi_n^{(0)}\rangle \tag{C.32}$$

where

$$H_3^{(0)} = H_3(\sum_p |\Psi_q^{(0)}\rangle) \tag{C.33}$$

First order $\tilde{N}_0^1$:

Performing the projection of eq. (C.32) along $\langle\Psi_n^{(0)*}|$ reads

$$\langle\Psi_n^{(0)*}|H_0|\Psi_n^{(1)}\rangle + \langle\Psi_n^{(0)*}|H_1|\Psi_n^{(0)}\rangle + \langle\Psi_n^{(0)*}|H_3^{(0)}|\Psi_n^{(0)}\rangle = X_n^{(1)} + X_n^{(0)}\langle\Psi_n^{(0)*}|\Psi_n^{(1)}\rangle \tag{C.34}$$

Leading to:

$$\boxed{X_n^{(1)} = \langle\Psi_n^{(0)*}|H_1 + H_3^{(0)}|\Psi_n^{(0)}\rangle} \tag{C.35}$$

In the scope of this manuscript, we do not use the eigenvectors.

Appendix D

Optimization via Simplex Algorithm

Here, we introduce the non-linear Simplex algorithm used in Chapter 8 for the optimization of random laser emission. This algorithm aims at minimising or maximising a non-linear function f, which reads

$$\mathbf{x} \rightarrow f(\mathbf{x}) \quad | \quad \mathbb{R}^N \rightarrow \mathbb{R} \tag{D.1}$$

where $\mathbf{x}$ is the parameter space of dimension N. Main advantage of this algorithm, also called Nelder-Mead algorithm, is to be derivative free. Deriving the gradient or computing its estimate is not required. As a result, this routine is often used in optimization procedure in which the noise is important. As guideline example, we will consider the function f provided by Fig. D.1**(a)**. In this example, we aim at maximising f.

The Simplex relies on $N+1$ initial vertices, namely $\mathbf{x}^{(0)}_{i\in[1,N+1]}$. For instance, in Fig. D.1**(a)**, three vertices $\mathbf{x}^{(0)}_{i\in[1,3]}$ are distributed in the parameter space. At each iteration the function f is evaluated for all the vertices. These evaluations are sorted and the smaller value is removed (for a maximization). Then, the algorithm derives a new vertex to replace the previous one (Fig. D.1**(a)**). As a result, the algorithm converges in the direction of the vertices providing the highest values of f.

The cornerstone of the method is the choice of the new vertex at each iteration. For instance, we carry on the example of Fig. D.1**(a)** and consider the distribution provided in Fig. D.1**(b)**. The vertices are sorted to fulfil

$$f(\mathbf{x}_1) > f(\mathbf{x}_2) > f(\mathbf{x}_3) \tag{D.2}$$

Hence, $\mathbf{x}_3$ is the vertex to be replaced. Now, we introduce $\mathbf{x}^*$, the barycentre of the N best vertices, which reads

$$\mathbf{x}^* = \frac{1}{N} \sum_{i\in[1,N]} \mathbf{x}_i \tag{D.3}$$

In our guideline example, $\mathbf{x}^*$ is placed at mid-distance between $\mathbf{x}_1$ and $\mathbf{x}_2$. If the new vertex is chosen along the line $(\mathbf{x}_3\mathbf{x}^*)$, four operations (positions) are possible

- The Reflection: $\mathbf{x}_3 \rightarrow \mathbf{x}_R = 2\mathbf{x}^* - \mathbf{x}_3$
- The Expansion: $\mathbf{x}_3 \rightarrow \mathbf{x}_E = 3\mathbf{x}^* - 2\mathbf{x}_3$
- The External Contraction: $\mathbf{x}_3 \rightarrow \mathbf{x}_{EC} = \frac{3}{2}\mathbf{x}^* - \frac{1}{2}\mathbf{x}_3$

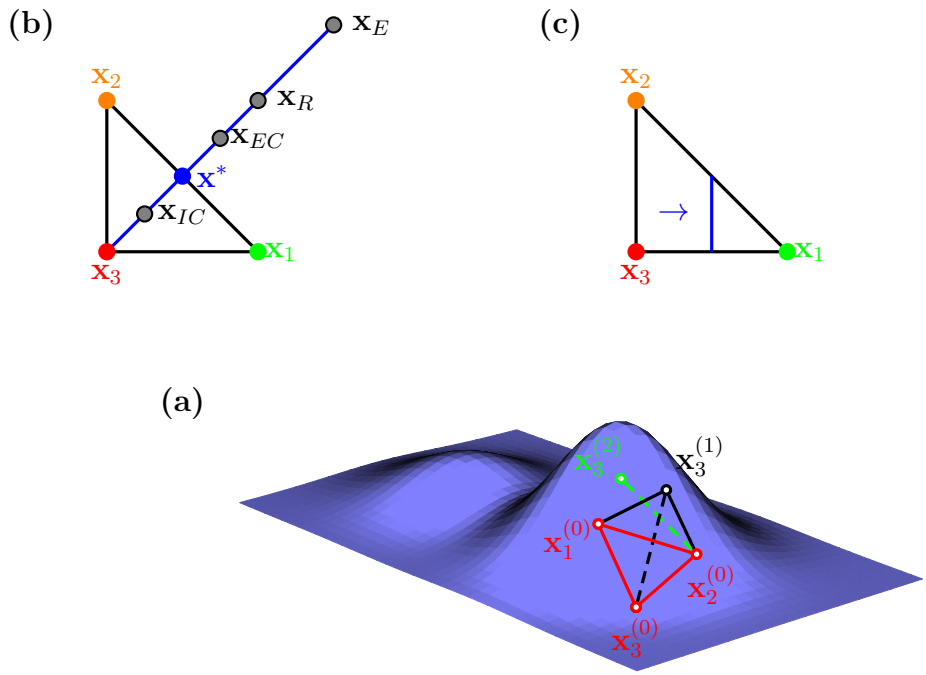

Figure D.1: **(a)** Example of optimization procedure. **(b)** Different transformations used to compute the new vertex. **(c)** When no choice of vertex is satisfying, the distribution is shrink.

- The Internal Contraction: $\mathbf{x}_3 \rightarrow \mathbf{x}_{IC} = \frac{1}{2}\mathbf{x}^* + \frac{1}{2}\mathbf{x}_3$

Otherwise, because no new vertex offers an increase of f, the initial vertex distribution $\mathbf{x}_{i\in[1,N+1]}$ is shrink as sketched in Fig. D.1**(c)**. The distribution is shrink in the direction of the best position $\mathbf{x}_1$. This transformation reads

$$\text{Shrink}: \forall i \in [1, N+1] \quad \mathbf{x}_i \rightarrow \mathbf{x}_i - \frac{\mathbf{x}_i - \mathbf{x}_1}{2}$$

We note n the current iteration of the algorithm, τ the convergence required and n_{max} the maximal number of iteration. At each iteration, the new vertex is chosen among the four positions previously introduced. The algorithm can be written formally

Initialization of the Simplex: Choice of $\mathbf{x}_{i\in[1,N+1]}^{(0)}$;
while *iteration* $n < n_{max}$ *and* $f(\boldsymbol{x}_{N+1}^{(n)}) - f(\boldsymbol{x}_1^{(n)}) > \tau$ **do**
  if $f(\boldsymbol{x}_R^{(n)}) < f(\boldsymbol{x}_1^{(n)})$ **then**
    if $f(\boldsymbol{x}_E^{(n)}) < f(\boldsymbol{x}_R^{(n)})$ **then**
      $\mathbf{x}_{N+1}^{(n+1)} = \mathbf{x}_E^{(n)}$
    else
      $\mathbf{x}_{N+1}^{(n+1)} = \mathbf{x}_R^{(n)}$
    end
    if $f(\boldsymbol{x}_1^{(n)}) \leq f(\boldsymbol{x}_R^{(n)}) < f(\boldsymbol{x}_N^{(n)})$ **then**
      $\mathbf{x}_{N+1}^{(n+1)} = \mathbf{x}_R^{(n)}$
    end
    if $f(\boldsymbol{x}_N^{(n)}) \leq f(\boldsymbol{x}_R^{(n)}) < f(\boldsymbol{x}_{N+1}^{(n)})$ *and* $f(\boldsymbol{x}_{EC}^{(n)}) \leq f(\boldsymbol{x}_R^{(n)})$ **then**
      $\mathbf{x}_{N+1}^{(n+1)} = \mathbf{x}_{EC}^{(n)}$
    end
    if $f(\boldsymbol{x}_R^{(n)}) \geq f(\boldsymbol{x}_{N+1}^{(n)})$ *and* $f(\boldsymbol{x}_{IC}^{(n)}) < f(\boldsymbol{x}_{N+1}^{(n)})$ **then**
      $\mathbf{x}_{N+1}^{(n+1)} = \mathbf{x}_{IC}^{(n)}$
    end
  else
    Shrink
  end
end

Algorithm 1: Non-linear Simplex algorithm

Bibliography

[1] R. Carminati, Optique Lumiere et Matiere, ESPCI (2011).

[2] Jean-Jacques Greffet, Electromagnetisme, Ecole Centrale (2008).

[3] J. Maxwell, *A treatise on electricity and magnetism* (1881).

[4] G. Russakoff, *Am. J. Phys.* (1970).

[5] L. Novotny and B. Hecht, *Principles of nano-optics* (2012).

[6] A. Ishimaru, *Wave propagation and scattering in random media*, volume 2, Academic press New York (1978).

[7] A. Ishimaru, *Proc. IEEE* **65**, 1030–1061 (1977).

[8] N. Bohr, *Philos. Mag. Ser. 6* **26**, 1–25 (1913).

[9] A. E. Siegman, Lasers. Mill Valley (1986).

[10] R. Menzel, *Photonics: Linear and Non Linear Interactions of Laser Light and Matter*, volume 24, Springer (2001).

[11] W. P. Risk, *J. Opt. Soc. Am. B* **5**, 1412 (1988).

[12] A. Einstein, *Phys. Z* (1917).

[13] B. Fain and P. W. Milonni, *J. Opt. Soc. Am. B* **4**, 78 (1987).

[14] D. Wiersma and A. Lagendijk, *Phys. Rev. E. Stat. Phys. Plasmas. Fluids. Relat. Interdiscip. Topics* **54**, 4256–4265 (1996).

[15] E. Fermi, *Rev. Mod. Phys.* **4**, 87–132 (1932).

[16] H. Rigneault, J. Capoulade, J. Dintinger, J. Wenger, N. Bonod, E. Popov, T. Ebbesen, and P.-F. Lenne, *Phys. Rev. Lett.* **95**, 117401 (2005).

[17] J. Wenger, D. Gérard, J. Dintinger, O. Mahboub, N. Bonod, E. Popov, T. W. Ebbesen, and H. Rigneault, *Opt. Express* **16**, 3008 (2008).

[18] P. Mühlschlegel, H.-J. Eisler, O. J. F. Martin, B. Hecht, and D. W. Pohl, *Science* **308**, 1607–9 (2005).

[19] B. Rolly, B. Stout, and N. Bonod, *Opt. Express* **20**, 1473–1478 (2012).

[20] Y. Akahane, T. Asano, B. Song, and S. Noda, *Nature* **425**, 4–7 (2003).

[21] T. Yoshie, J. Vuckovic, A. Scherer, H. Chen, and D. Deppe, *Appl. Phys. Lett.* **79**, 4289 (2001).

[22] G. Gamow, *Zeitschrift fur Phys.* **51**, 204–212 (1928).

[23] M. Berry, *Czechoslov. J. Phys.* **54**, 1039–1047 (2004).

[24] A. P. Seyranian, O. N. Kirillov, and A. A. Mailybaev, *J. Phys. A. Math. Gen.* **38**, 1723–1740 (2005).

[25] M. V. Berry and M. Wilkinson, *Proc. R. Soc. A Math. Phys. Eng. Sci.* **392**, 15–43 (1984).

[26] M. V. Berry, *Proc. R. Soc. A Math. Phys. Eng. Sci.* **392**, 45–57 (1984).

[27] R. Chiao and Y.-S. Wu, *Phys. Rev. Lett.* **57**, 933–936 (1986).

[28] A. Tomita and R. Chiao, *Phys. Rev. Lett.* **57**, 937–940 (1986).

[29] H.-M. Lauber, P. Weidenhammer, and D. Dubbers, *Phys. Rev. Lett.* **72**, 1004–1007 (1994).

[30] I. Rotter and A. Sadreev, *Phys. Rev. E* **71**, 036227 (2005).

[31] T. Kato, *Perturbation Theory for Linear Operators* (1966).

[32] R. Whitney and Y. Gefen, *Phys. Rev. Lett.* **90**, 190402 (2003).

[33] A. Carollo, I. Fuentes-Guridi, M. Santos, and V. Vedral, *Phys. Rev. Lett.* **90**, 160402 (2003).

[34] B. Dietz, H. L. Harney, O. N. Kirillov, M. Miski-Oglu, A. Richter, and F. Schäfer, *Phys. Rev. Lett.* **106**, 150403 (2011).

[35] Y. Choi, S. Kang, S. Lim, W. Kim, J.-R. Kim, J.-H. Lee, and K. An, *Phys. Rev. Lett.* **104**, 153601 (2010).

[36] S.-Y. Lee, *Phys. Rev. A* **80**, 042104 (2009).

[37] W. Heiss, *Eur. Phys. J. D - At. Mol. Opt. Phys.* **7**, 1–4 (1999).

[38] M. Kammerer, F. Merz, and F. Jenko, *Phys. Plasmas* **15**, 052102 (2008).

[39] W. Heiss and M. Müller, *Phys. Rev. E* **66**, 016217 (2002).

[40] O. Zaitsev and L. Deych, *J. Opt.* **12**, 024001 (2010).

[41] A. Fox, *IEEE J. Quantum Electron.* **4**, 460–465 (1968).

[42] A. Siegert, *Phys. Rev.* **56**, 750–752 (1939).

[43] S. Dutra and G. Nienhuis, *Phys. Rev. A* **62**, 063805 (2000).

[44] H. Türeci, A. Stone, and B. Collier, *Phys. Rev. A* **74**, 043822 (2006).

[45] O. Tolstikhin, V. Ostrovsky, and H. Nakamura, *Phys. Rev. Lett.* **79**, 2026–2029 (1997).

[46] O. Tolstikhin, V. Ostrovsky, and H. Nakamura, *Phys. Rev. A* **58**, 2077–2096 (1998).

[47] Zeldovich, *Scattering, Reactions and Decay in Nonrelativistic Quantum Mechanics*, Israel Program for Scientific Transactions, Jerusalem (1969).

[48] N. Moiseyev, *Non-Hermitian Quantum Mechanics*, cambridge edition (2011).

[49] T. Berggren, *Nucl. Phys. A* **109**, 265–287 (1968).

[50] P. Leung, S. Liu, and K. Young, *Phys. Rev. A* **49**, 3057–3067 (1994).

[51] P. Leung, S. Liu, S. Tong, and K. Young, *Phys. Rev. A* **49**, 3068–3073 (1994).

[52] P. Leung, W. Suen, C. Sun, and K. Young, *Phys. Rev. E* **57**, 6101–6104 (1998).

[53] E. Ching, P. Leung, A. Maassen van den Brink, W. Suen, S. Tong, and K. Young, *Rev. Mod. Phys.* **70**, 1545–1554 (1998).

[54] P. M. Morse and H. Feshbach, *Int. Ser. Pure Appl. Physics, New York McGraw-Hill, 1953* **1** (1953).

[55] N. Moiseyev, P. Certain, and F. Weinhold, *Mol. Phys.* **36**, 1613–1630 (1978).

[56] P. W. Anderson, *Phys. Rev.* **109**, 1492–1505 (1958).

[57] G. Feher and A. Kip, *Phys. Rev.* **98**, 337–348 (1955).

[58] S. John, *Phys. Rev. Lett.* **53**, 2169–2172 (1984).

[59] M. Albada and A. Lagendijk, *Phys. Rev. Lett.* **55**, 2692–2695 (1985).

[60] A. Ishimaru and L. Tsang, *J. Opt. Soc. Am. A* **5**, 228 (1988).

[61] P.-E. Wolf and G. Maret, *Phys. Rev. Lett.* **55**, 2696–2699 (1985).

[62] H. Hu, A. Strybulevych, J. H. Page, S. E. Skipetrov, and B. a. van Tiggelen, *Nat. Phys.* **4**, 945–948 (2008).

[63] F. Jendrzejewski, A. Bernard, K. Müller, P. Cheinet, V. Josse, M. Piraud, L. Pezzé, L. Sanchez-Palencia, A. Aspect, and P. Bouyer, *Nat. Phys.* **8**, 398–403 (2012).

[64] S. E. Skipetrov and I. M. Sokolov, *Phys. Rev. Lett.* **112**, 023905 (2014).

[65] S. John, *Phys. Today* **44**, 32 (1991).

[66] X. Jiang and C. Soukoulis, *Phys. Rev. E* **65**, 025601 (2002).

[67] J.-P. Berenger, *J. Comput. Phys.* **114**, 185–200 (1994).

[68] A. Taflove and S. Hagness, *Computational Electrodynamics*, Artech House, Boston, 3rd edition (2005).

[69] W. D. Heiss and A. L. Sannino, *J. Phys. A. Math. Gen.* **23**, 1167–1178 (1990).

[70] M. Liertzer, L. Ge, A. Cerjan, a. D. Stone, H. E. Türeci, and S. Rotter, *Phys. Rev. Lett.* **108**, 173901 (2012).

[71] S. Klaiman, U. Günther, and N. Moiseyev, *Phys. Rev. Lett.* **101**, 080402 (2008).

[72] a. Guo, G. J. Salamo, M. Volatier-Ravat, V. Aimez, G. a. Siviloglou, and D. N. Christodoulides, *Phys. Rev. Lett.* **103**, 093902 (2009).

[73] S.-B. Lee, J. Yang, S. Moon, S.-Y. Lee, J.-B. Shim, S. Kim, J.-H. Lee, and K. An, *Phys. Rev. Lett.* **103**, 134101 (2009).

[74] V. Milner and A. Genack, *Phys. Rev. Lett.* **94**, 073901 (2005).

[75] J.-K. Yang, H. Noh, M. J. Rooks, G. S. Solomon, F. Vollmer, and H. Cao, *Appl. Phys. Lett.* **98**, 241107 (2011).

[76] L. Sapienza, H. Thyrrestrup, S. r. Stobbe, P. D. Garcia, S. Smolka, and P. Lodahl, *Science* **327**, 1352–5 (2010).

[77] J. Gao, S. Combrie, B. Liang, P. Schmitteckert, G. Lehoucq, S. Xavier, X. Xu, K. Busch, D. L. Huffaker, A. De Rossi, and C. W. Wong, *Sci. Rep.* **3**, 1994 (2013).

[78] L. Labonté, C. Vanneste, and P. Sebbah, *Opt. Lett.* **37**, 1946–8 (2012).

[79] J. Bertolotti, S. Gottardo, D. Wiersma, M. Ghulinyan, and L. Pavesi, *Phys. Rev. Lett.* **94**, 113903 (2005).

[80] P. Sebbah, B. Hu, J. Klosner, and A. Genack, *Phys. Rev. Lett.* **96**, 183902 (2006).

[81] J. B. Pendry, *J. Phys. C Solid State Phys.* **20**, 733–742 (1987).

[82] J. B. Pendry, *Adv. Phys.* **43**, 461–542 (1994).

[83] O. Bendix, R. Fleischmann, T. Kottos, and B. Shapiro, *Phys. Rev. Lett.* **103**, 030402 (2009).

[84] H. Vemuri, V. Vavilala, T. Bhamidipati, and Y. N. Joglekar, *Phys. Rev. A* **84**, 043826 (2011).

[85] O. Vázquez-Candanedo, J. C. Hernández-Herrejón, F. M. Izrailev, and D. N. Christodoulides, *Phys. Rev. A* **89**, 013832 (2014).

[86] F. Riboli, P. Barthelemy, S. Vignolini, F. Intonti, A. De Rossi, S. Combrie, and D. S. Wiersma, *Opt. Lett.* **36**, 127–9 (2011).

[87] H. Morse, Philip M and Feshbach, *Methods of theoretical physics*, McGraw-Hill, New York, internatio edition (1953).

[88] Rachid Touzani, OFELI, An Object Oriented Finite Element Library (2013).

[89] V. Hernandez, J. E. Roman, and V. Vidal, *ACM Trans. Math. Softw.* **31**, 351–362 (2005).

[90] D. Laurent, O. Legrand, P. Sebbah, C. Vanneste, and F. Mortessagne, *Phys. Rev. Lett.* **99**, 253902 (2007).

[91] J. P. Reithmaier, G. Sek, A. Löffler, C. Hofmann, S. Kuhn, S. Reitzenstein, L. V. Keldysh, V. D. Kulakovskii, T. L. Reinecke, and A. Forchel, *Nature* **432**, 197–200 (2004).

[92] A. Majumdar, A. Rundquist, M. Bajcsy, V. D. Dasika, S. R. Bank, and J. Vuckovic, *Phys. Rev. B* **86**, 195312 (2012).

[93] F. Riboli, N. Caselli, S. Vignolini, F. Intonti, K. Vynck, P. Barthelemy, A. Gerardino, L. Balet, L. H. Li, A. Fiore, M. Gurioli, and D. S. Wiersma, *Nat. Mater.* pages 1–6 (2014).

[94] E. M. Purcell, *Phys. Rev.* **69**, 681 (1946).

[95] K. Drexhage, *J. Lumin.* **1-2**, 693–701 (1970).

[96] J.-M. Gérard, *Solid-State Cavity-Quantum Electrodynamics with Self-Assembled Quantum Dots*, volume 327 (2003).

[97] D. Englund, A. Majumdar, M. Bajcsy, A. Faraon, P. Petroff, and J. Vučković, *Phys. Rev. Lett.* **108**, 093604 (2012).

[98] A. Faraon, A. Majumdar, H. Kim, P. Petroff, and J. Vučković, *Phys. Rev. Lett.* **104**, 047402 (2010).

[99] R. P. Feynman, *Int. J. Theor. Phys.* **21**, 467–488 (1982).

[100] S. Lloyd, *Science (80-.).* **273**, 1073–1078 (1996).

[101] S. Buckley, K. Rivoire, and J. Vučković, *Rep. Prog. Phys.* **75**, 126503 (2012).

[102] M. Bajcsy, A. Majumdar, A. Rundquist, and J. Vučković, *New J. Phys.* **15**, 025014 (2013).

[103] H. Thyrrestrup, S. Smolka, L. Sapienza, and P. Lodahl, *Phys. Rev. Lett.* **108**, 113901 (2012).

[104] A. Cazé, R. Pierrat, and R. Carminati, *Phys. Rev. Lett.* **111**, 053901 (2013).

[105] B. Mollow, *Phys. Rev. A* **5**, 2217–2222 (1972).

[106] R. W. Boyd, *Nonlinear optics* (2007).

[107] J. STARK, *Nature* **92**, 401–401 (1913).

[108] B. Mollow, *Phys. Rev.* **188**, 1969–1975 (1969).

[109] C. Vanneste and P. Sebbah, *Phys. Rev. Lett.* **87**, 183903 (2001).

[110] P. Sebbah and C. Vanneste, *Phys. Rev. B* **66**, 144202 (2002).

[111] C. Vanneste and P. Sebbah, *Phys. Rev. A* **79**, 041802 (2009).

[112] A. Aspect, G. Roger, and S. Reynaud, *Phys. Rev. Lett.* **45** (1980).

[113] C. Schrama, G. Nienhuis, and H. Dijkerman, *Phys. Rev. A* **45** (1992).

[114] G. Nienhuis, *Phys. Rev. A* **47**, 510–518 (1993).

[115] E. B. Flagg, a. Muller, J. W. Robertson, S. Founta, D. G. Deppe, M. Xiao, W. Ma, G. J. Salamo, and C. K. Shih, *Nat. Phys.* **5**, 203–207 (2009).

[116] A. Ulhaq, S. Weiler, S. Ulrich, and R. Roß bach, *Nat. ...* **6**, 238–242 (2012).

[117] V. Letokhov, *Sov. J. Exp. Theor. ...* **26** (1968).

[118] H. Cao, Y. Zhao, S. Ho, E. Seelig, Q. Wang, and R. Chang, *Phys. Rev. Lett.* **82**, 2278–2281 (1999).

[119] H. Cao, *Waves in Random Media* **13**, R1–R39 (2003).

[120] B. N. Shivakiran Bhaktha, N. Bachelard, X. Noblin, and P. Sebbah, *Appl. Phys. Lett.* **101**, 151101 (2012).

[121] R. Carminati and P. Sebbah, *Photoniques* pages 34–39 (2014).

[122] C. Gouedard, D. Husson, C. Sauteret, F. Auzel, and A. Migus, *J. Opt. Soc. Am. B* **10**, 2358 (1993).

[123] N. M. Lawandy, R. M. Balachandran, A. S. L. Gomes, and E. Sauvain, *Nature* **368**, 436–438 (1994).

[124] A. Z. Genack and J. M. Drake, *Nature* **368**, 400–401 (1994).

[125] D. S. Wiersma, M. P. van Albada, and A. Lagendijk, *Nature* **373**, 203–204 (1995).

[126] H. Cao, Y. G. Zhao, H. C. Ong, S. T. Ho, J. Y. Dai, J. Y. Wu, and R. P. H. Chang, *Appl. Phys. Lett.* **73**, 3656 (1998).

[127] A. F. Ioffe and A. R. Regel, *Prog. Semicond* **4**, 237–291 (1960).

[128] P. W. Anderson, *Philos. Mag. Part B* **52**, 505–509 (1985).

[129] B. Davison, J. B. Sykes, and E. R. Cohen, *Phys. Today* **11**, 30 (1958).

[130] D. S. Wiersma, *Nat. Phys.* **4**, 359–367 (2008).

[131] M. Noginov, *Solid-state random lasers*, Springer (2005).

[132] Z. Li and D. Psaltis, *Microfluid. Nanofluidics* **4**, 145–158 (2007).

[133] C. Monat, P. Domachuk, and B. Eggleton, *Nat. Photonics* **1** (2007).

[134] Y. Xia and G. M. Whitesides, *Annu. Rev. Mater. Sci.* **28**, 153–184 (1998).

[135] C. Beenakker, J. Paasschens, and P. Brouwer, *Phys. Rev. Lett.* **76**, 1368–1371 (1996).

[136] a. Burin, M. Ratner, H. Cao, and R. Chang, *Phys. Rev. Lett.* **87**, 215503 (2001).

[137] C. Beenakker, *Phys. Rev. Lett.* **81**, 1829–1832 (1998).

[138] R. Pierrat and R. Carminati, *Phys. Rev. A* **76**, 023821 (2007).

[139] R. M. Balachandran, N. M. Lawandy, and J. a. Moon, *Opt. Lett.* **22**, 319–21 (1997).

[140] J. Gordon, H. Zeiger, and C. Townes, *Phys. Rev.* **99**, 1264–1274 (1955).

[141] A. Schawlow and C. Townes, *Phys. Rev.* **112**, 1940–1949 (1958).

[142] A. Javan, *Phys. Rev. Lett.* **3**, 87–89 (1959).

[143] J. Sanders, *Phys. Rev. Lett.* **3**, 86–87 (1959).

[144] T. Maiman, *Phys. Rev. Lett.* **4**, 564–566 (1960).

[145] T. H. Maiman, *Nature* **187**, 493–494 (1960).

[146] H. Haken and H. Sauermann, *Zeitschrift fur Phys.* **173**, 261–275 (1963).

[147] W. Lamb, *Phys. Rev.* **134**, A1429–A1450 (1964).

[148] R. Lang, M. Scully, and W. Lamb, *Phys. Rev. A* **7**, 1788–1797 (1973).

[149] X. Jiang and C. Soukoulis, *Phys. Rev. Lett.* **85**, 70–3 (2000).

[150] C. Soukoulis, X. Jiang, J. Xu, and H. Cao, *Phys. Rev. B* **65**, 041103 (2002).

[151] B. Liu, A. Yamilov, Y. Ling, J. Xu, and H. Cao, *Phys. Rev. Lett.* **91**, 063903 (2003).

[152] L. Deych, *Phys. Rev. Lett.* **95**, 043902 (2005).

[153] O. Zaitsev and L. Deych, *Phys. Rev. A* **81**, 023822 (2010).

[154] J. Andreasen, P. Sebbah, and C. Vanneste, *J. Opt. Soc. Am. B* **28**, 2947 (2011).

[155] P. Stano and P. Jacquod, *Nat. Photonics* **7**, 66–71 (2012).

[156] H. E. Türeci, L. Ge, S. Rotter, and a. D. Stone, *Science* **320**, 643–6 (2008).

[157] R. C. Polson and Z. V. Vardeny, *Appl. Phys. Lett.* **85**, 1289 (2004).

[158] B. Redding, M. A. Choma, and H. Cao, *Nat. Photonics* **6**, 355–359 (2012).

[159] D. S. Wiersma and S. Cavalieri, *Nature* **414**, 708–9 (2001).

[160] K. Lee and N. M. Lawandy, *Opt. Commun.* **203**, 169–174 (2002).

[161] S. Gottardo, S. Cavalieri, O. Yaroshchuk, and D. Wiersma, *Phys. Rev. Lett.* **93**, 263901 (2004).

[162] S. Gottardo, R. Sapienza, P. D. García, A. Blanco, D. S. Wiersma, and C. López, *Nat. Photonics* **2**, 429–432 (2008).

[163] H. K. Liang, S. F. Yu, and H. Y. Yang, *Appl. Phys. Lett.* **96**, 101116 (2010).

[164] R. G. S. El-Dardiry and A. Lagendijk, *Appl. Phys. Lett.* **98**, 161106 (2011).

[165] R. Bardoux, A. Kaneta, M. Funato, K. Okamoto, Y. Kawakami, A. Kikuchi, and K. Kishino, *Opt. Express* **19**, 9262–8 (2011).

[166] S. Frolov, Z. Vardeny, K. Yoshino, A. Zakhidov, and R. Baughman, *Phys. Rev. B* **59**, R5284–R5287 (1999).

[167] Y. Ling, H. Cao, A. Burin, M. Ratner, X. Liu, and R. Chang, *Phys. Rev. A* **64**, 063808 (2001).

[168] X. Wu, W. Fang, A. Yamilov, A. Chabanov, A. Asatryan, L. Botten, and H. Cao, *Phys. Rev. A* **74**, 053812 (2006).

[169] M. Patra, *Phys. Rev. E* **67**, 016603 (2003).

[170] V. Apalkov and M. Raikh, *Phys. Rev. B* **71**, 054203 (2005).

[171] J. Andreasen, C. Vanneste, L. Ge, and H. Cao, *Phys. Rev. A* **81**, 043818 (2010).

[172] X. Wu, J. Andreasen, H. Cao, and A. Yamilov, *J. Opt. Soc. Am. B* **24**, A26 (2007).

[173] R. Polson and Z. Vardeny, *Phys. Rev. B* **71**, 045205 (2005).

[174] C. Gmachl, *Science (80-.).* **280**, 1556–1564 (1998).

[175] A. D. Stone, *Nature* **465**, 696–7 (2010).

[176] D. Naidoo, T. Godin, M. Fromager, E. Cagniot, N. Passilly, A. Forbes, and K. Aït-Ameur, *Opt. Commun.* **284**, 5475–5479 (2011).

[177] N. Bachelard, J. Andreasen, S. Gigan, and P. Sebbah, *Phys. Rev. Lett.* **109**, 033903 (2012).

[178] J. Andreasen, a. a. Asatryan, L. C. Botten, M. a. Byrne, H. Cao, L. Ge, L. Labonté, P. Sebbah, a. D. Stone, H. E. Türeci, and C. Vanneste, *Adv. Opt. Photonics* **3**, 88 (2010).

[179] T. Hisch, M. Liertzer, D. Pogany, F. Mintert, and S. Rotter, *Phys. Rev. Lett.* **111**, 023902 (2013).

[180] S. Mujumdar, V. Türck, R. Torre, and D. Wiersma, *Phys. Rev. A* **76**, 033807 (2007).

[181] N. Bachelard, S. Gigan, X. Noblin, and P. Sebbah, *Nat. Phys.* pages 1–6 (2014).

[182] R. Won, *Nat. Photonics* **7**, 3–3 (2012).

[183] N. J. Sloane and M. Harwit, *Appl. Opt.* **15**, 107–14 (1976).

[184] J. Wyant and K. Creath, *Appl. Opt. Opt. Eng.* **Xl** (1992).

[185] S. Takimoto, T. Tachikawa, R. Shogenji, and J. Ohtsubo, *IEEE Photonics Technol. Lett.* **21**, 1051–1053 (2009).

[186] S. F. Liew, B. Redding, L. Ge, G. S. Solomon, and H. Cao pages 2–5 (2014).

[187] H. C. van de Hulst, *Light scattering by small particles*, John Wiley & Sons, New York (1957).

[188] P. de Vries, D. van Coevorden, and A. Lagendijk, *Rev. Mod. Phys.* **70**, 447–466 (1998).